DEVELOPMENT OF A CRYOGENIC FAR-INFRARED POST-DISPERSED POLARIZING FOURIER-TRANSFORM SPECTROMETER

MATTHEW ANDREW BUCHAN
Bachelor of Engineering, Aerospace, Carleton University, 2022

A thesis submitted
in partial fulfilment of the requirements for the degree of

MASTER OF SCIENCE

in

PHYSICS

Department of Physics and Astronomy
University of Lethbridge
LETHBRIDGE, ALBERTA, CANADA

DEVELOPMENT OF A CRYOGENIC FAR-INFRARED POST-DISPERSED POLARIZING FOURIER-TRANSFORM SPECTROMETER

MATTHEW ANDREW BUCHAN

Date of Defence: 12th June 2024

David A. Naylor	Professor Emeritus	PhD
Locke D. Spencer	Associate Professor	PhD
Thesis Co-supervisors		
Chad A. Povey	Instructor	PhD
Thesis Examination Committee Member		
Alexandra J. Tetarenko	Assistant Professor	PhD
Thesis Examination Committee Member		
Kenneth J. E. Vos	Associate Professor	PhD
Chair, Thesis Examination Committee		

Abstract

The next generation of far-infrared space observatories will feature large (2 m to 3 m class), actively cooled (4.5 K) telescopes and high resolution spectroscopic capabilities provided by a Fourier-transform spectrometer (FTS). In the absence of telescope self-emission and with access to ultra-sensitive detectors, the multiplex advantage of an FTS becomes a disadvantage if instantaneous broad spectral measurements are attempted as the photon noise associated with the astronomical source now determines the spectral noise density. The only way to reduce the photon noise is by reducing the instantaneous spectral bandwidth observed by a single detector, typically to a fraction of one percent, using some form of post-dispersing element. While there are many approaches to post-dispersion, it is widely regarded that reflection diffraction gratings are the preferred method. The efficiency of a diffraction grating varies with wavelength. At the high angles of incidence required to achieve the necessary resolving power of $R \sim 100$, reflection diffraction gratings operate with high and uniform efficiency ($\sim 80\,\%$) for transverse magnetic (TM) polarized light, but lower and variable efficiency (10 % to 40 %) for transverse electric (TE) polarized light. The polarizing encoding properties of a Martin-Puplett interferometer can exploit this strong polarization dependence by ensuring that the interferometer output presents the TM mode to the grating. The hybrid post-dispersed polarizing Fourier transform spectrometer (PDPFTS) concept is the leading candidate for a future far-infrared astronomy mission. A fully cryogenic far-infrared PDPFTS has been developed in our laboratory to gain a better understanding of the challenges presented by this novel hybrid instrument. The results obtained from this PDPFTS will be valuable in guiding the development of such hybrid spectrometers being proposed for future far-infrared space observatories.

Acknowledgements

Foremost, I want to express my deepest gratitude towards my supervisor, Professor Emeritus David Naylor, for his invaluable mentorship and for providing me with the opportunity to work on the cutting edge of far-infrared space astronomy. What started as an undergraduate engineering internship within your research group has transformed into a career-shaping academic journey.

This thesis would not have been possible without the significant contributions from Brad Gom. You trained me in the design and operation of cryogenic instrumentation, machined many of the countless parts of which I had designed for this project, and developed the bolometer detector that played a crucial role in obtaining the data necessary for this thesis.

I would like to thank Professor Lock Spencer for taking on the role of co-supervisor during the latter part of my studies following David's retirement, for always having an open office door which led to many valuable conversations, and for providing an alternative viewpoint to discuss my research.

I want to thank the countless members of the Astronomical Instrumentation Group (AIG) who have made contributions to this project. Alicia Anderson, for her work designing the diffraction grating spectrometer incorporated into this thesis. Adam Christiansen, for allowing me to collect data using his laser position metrology system and for his aid in the triage of said data. Anthony Huber for exploring the operation of a polarization encoding source module to generate realistic astronomical spectra. Rebecca Sirota and Mason Remmer for providing electronics support. The late Gregory Tompkins for designing the detector preamplifier. Holden Holzer, Maher Dyayn, Jaden Ingleton, Ethan Predinchuk, and Daniel Yang, the many co-op students who provided assistance during their time with the AIG.

Thank you to Blue Sky Spectroscopy for providing many of the cryostat components and an insurmountable amount of the supporting test kit. Thank you to my old colleagues at Blue Sky Spectroscopy. Dr Sudhakar Gunuganti, for helping me run tests and collect data with some of my first cryogenic experiments. Ben Louwerse, for your support in the design of a few key aspects of the Large Facility Cryostat, namely the external frame. Trevor Fulton, for writing the diffraction grating spectrometer control software.

Un gros merci à Alain Cournoyer et à tous mes collègues chez ABB pour l'opportunité d'utiliser leur FTSM afin de concevoir la prochaine génération d'instrumentation pour les télescope spatial dans l'infrarouge. Ce fut un plaisir de travailler avec vous durant ce projet. À bientôt.

This research was funded in part by ABB Inc., Alberta Innovates, Blue Sky Spectroscopy Inc., Canada Foundation for Innovation, Canadian Microelectronics Corporation, Canadian Space Agency, Natural Sciences and Engineering Research Council of Canada, New Technologies for Canadian Observatories, Netherlands Institute for Space Research, Cardiff University, the University of Groningen, and the University of Lethbridge.

Lastly, I would like to express a heartfelt thank you to my family, especially my parents, Andy and Susan, for their unwavering support and encouragement in following my interests. A loving thank you to my partner, Ariane, for her constant support and her physicist's perspective.

Contents

List of Tables

List of Figures

List of Abbreviations

AIG	Astronomical Instrumentation Group
ALMA	Atacama Large Millimeter/submillimeter Array
CAD	computer-aided design
CFRP	carbon fiber reinforced polymer
CNC	computer numerical control
COC	cyclic olefin copolymer
CSA	Canadian Space Agency
CTE	coefficient of thermal expansion
DLATGS	deuterated L-alanine doped triglycene sulphate
EDU	engineering development unit
EFL	effective focal length
ESA	European Space Agency
ETP	electrolytic tough pitch
FDM	fused deposition modeling
FEA	finite element analysis
FYST	Fred Young Submillimeter Telescope
FTS	Fourier-transform spectrometer
FTSM	Fourier-transform spectrometer mechanism
FTSO	Fourier-transform spectrometer optics
FWHM	full width half maximum
GFRP	glass fiber reinforced polymer
GSFC	Goddard Space Flight Center
Herschel	Herschel Space Observatory
ID	inside diameter
IRAS	Infrared Astronomical Satellite
ISO	Infrared Space Observatory

JAXA	Japan Aerospace Exploration Agency
JCMT	James Clerk Maxwell Telescope
JFET	junction field effect transistor
JPL	Jet Propulsion Laboratory
LFC	Large Facility Cryostat
MKID	microwave kinetic inductance detector
MLI	multilayer insulation
NASA	National Aeronautics and Space Administration
NEP	noise-equivalent power
OAP	off-axis parabolic
OD	outside diameter
OFHC	oxygen free high conductivity
OPD	optical path difference
OVC	outer vacuum chamber
PCB	printed circuit board
PDPFTS	post-dispersed polarizing Fourier transform spectrometer
PRIMA	PRobe far-Infrared Mission for Astrophysics
PTC	pulse tube cryocooler
RMS	root mean square
RRR	residual resistance ratio
SAFARI	SpicA FAR-infrared Instrument
SI	Système International
SMA	Submillimeter Array
SOFIA	Stratospheric Observatory For Infrared Astronomy
SPICA	SPace Infrared telescope for Cosmology and Astrophysics
SPIRE	Spectral and Photometric Imaging REceiver
SPT	South Pole Telescope
SRF	spectral response function
SWIR	short-wavelength infrared
TE	transverse electric

TES transition edge sensor
TFC Test Facility Cryostat
TM transverse magnetic
TRL technology readiness level

ZPD zero path differnce

List of Notations

A	area
$A\Omega$	étendue
α	incident angle
b	offset
B	spectral radiance
β	diffracted angle
d	slit spacing
c	speed of light
CT	lens center thickness
δ	dihedral deviation angle
E_b	emissive power
ε	emissivity
η	index of refraction, optical efficiency
F	view factor
h	Planck constant
I	measured signal intensity
J	radiosity
K	thermal conductivity
k_B	Boltzmann constant
l	grating length
L	length
$\Delta L/L$	total linear contraction
λ	wavelength

$\Delta\lambda$ spectral resolution

m order of diffraction, slope

N number of insulating layers
ν frequency

ϕ deviation angle

$\dot{Q}$ heat transfer rate

r entrance focal length
r' exit focal length
R radius of lens surface, resolving power, thermal resistance

σ Stefan-Boltzmann constant, wavenumber

T temperature
θ angle of incidence minus deviation angle
θ_B blaze angle

w entrance slit width
w'' exit slit width
W grating width

X separation of two crosshair images

Chapter 1

Introduction

> "I can't lie to you about your chances, but... you have my sympathies."
>
> Ash
> Alien

The instrument concept that is widely considered by the European Space Agency (ESA), the Japan Aerospace Exploration Agency (JAXA), and the National Aeronautics and Space Administration (NASA) to be the leading candidate for a future far-infrared space astronomy mission is a post-dispersed polarizing Fourier transform spectrometer (PDPFTS). The science case and motivation for why the PDPFTS is the future of far-infrared astronomy is covered in this chapter. The Astronomical Instrumentation Group (AIG) at the University of Lethbridge, and their industrial partners, have been leading the development of the PDPFTS to show its operation under the critical parameters for a far-infrared space telescope, namely a high vacuum and cryogenic temperature (4 K) environment. A complete end-to-end laboratory demonstration of the PDPFTS is a stepping stone on the path-to-flight for this hybrid spectrometer. This thesis covers the development of the Large Facility Cryostat (LFC), a large volume 4 K cryogenic test facility, and the integration of a far-infrared PDPFTS in said cryostat to obtain first light results from this instrument concept.

1.1 The PDPFTS Science Case

The earliest stages of star and planetary formation can only be observed at far-infrared wavelengths. Terrestrial observations are limited due to the fact that the Earth's atmosphere

is opaque to nearly all far-infrared radiation. Water vapour in the atmosphere is the principal cause of absorption in the far-infrared [1], with only a few narrow atmospheric windows transparent at these wavelengths. Figure 1.1 shows the atmospheric opacity of the Earth across the electromagnetic spectrum. To avoid atmospheric extinction, ground-based observatories are located at high altitudes to get above the majority of the atmospheric water vapour, such as the James Clerk Maxwell Telescope (JCMT) [2] and the Submillimeter Array (SMA) [3] on Mauna Kea, Hawaii [4], the Atacama Large Millimeter/submillimeter Array (ALMA) [5] and the Fred Young Submillimeter Telescope (FYST) [6] in the Atacama Desert, Chile, and the South Pole Telescope (SPT) [7], Antartica. Even in such locations, the residual absorption due to water vapour precludes astronomical observations in certain wavelength regions. For unimpeded access, the ideal far-infrared observatory necessitates the use of space-borne platforms.

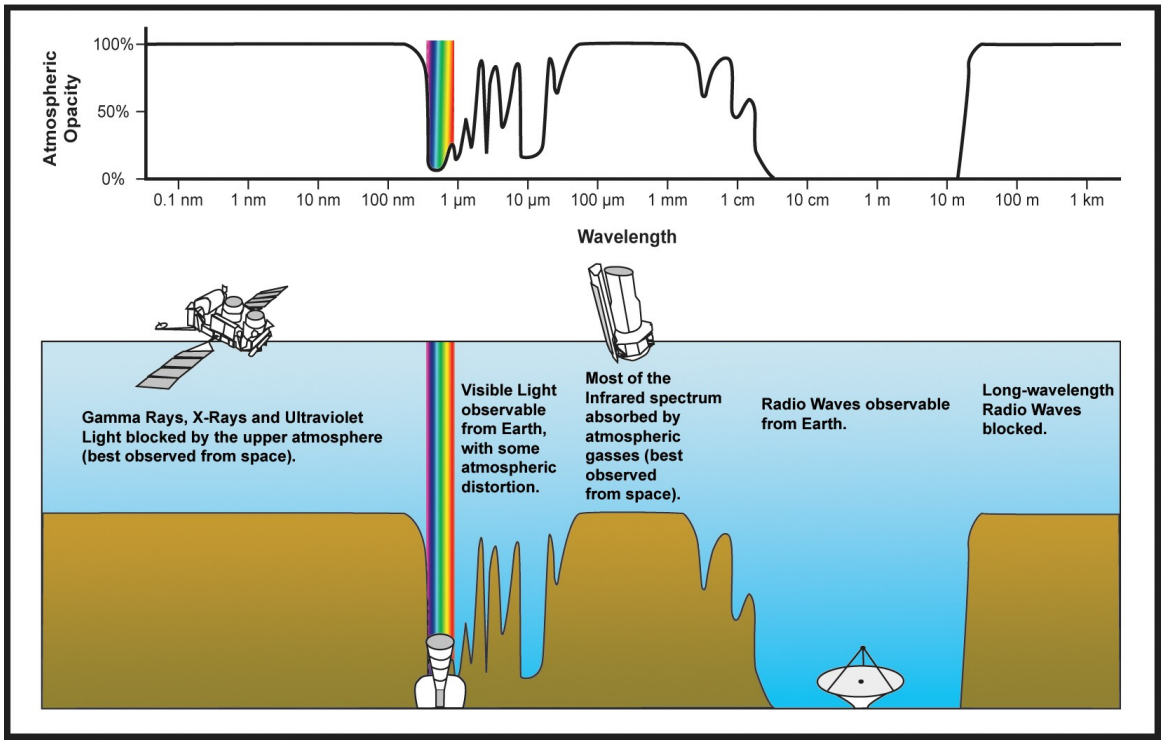

Figure 1.1: Atmospheric opacity of the Earth across the electromagnetic spectrum. While there are a few transparent windows in the near- and mid-infrared wavelength bands, the atmosphere is opaque to almost all far-infrared radiation. Image taken from [8].

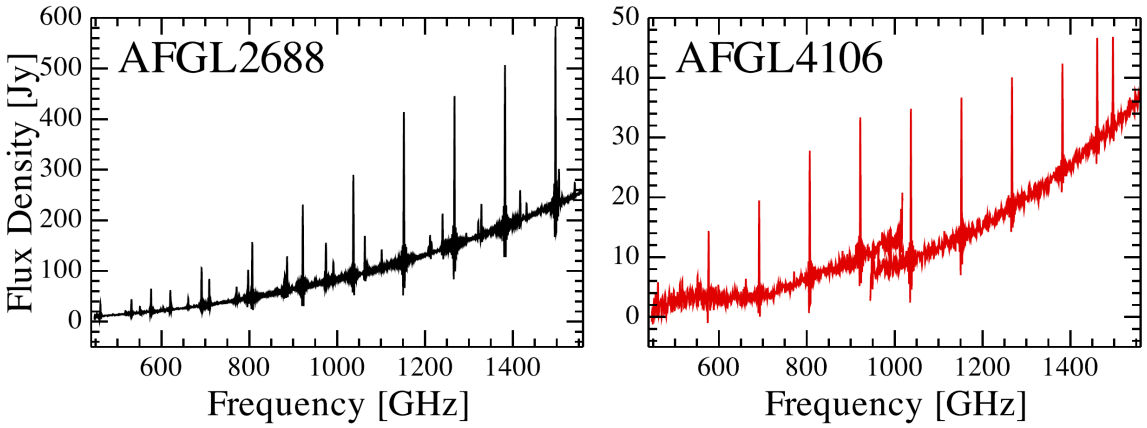

Figure 1.2: Herschel far-infrared spectra showcasing a broad continuum with many unresolved line features. Left: Spectrum of the protoplanetary nebula AFGL 2688. Right: Spectrum of the post-red supergiant AFGL 4106 [9]

The roots of far-infrared space astronomy can be traced back to the Infrared Astronomical Satellite (IRAS) [10] launched in 1983, the Infrared Space Observatory (ISO) [11] launched by ESA in 1995, and the AKARI mission [12] launched by JAXA in 2006, leading to the launch of the Herschel Space Observatory (Herschel) [13] by ESA in 2009. Herschel is widely regarded as the most successful far-infrared astronomy mission to date. The Herschel instrument suite was able to observe obscured regions in our galaxy and measure the emission of distant galaxies at high redshift. Herschel made fundamental contributions to our understanding of the evolution of stars and galaxies over cosmic time scales.

Despite its success, the sensitivity of Herschel was limited by the fact that the telescope was passively cooled, only reaching temperatures of around 85 K. The next generation of far-infrared space observatories will feature large (2 m to 3 m class), actively cooled (4.5 K) telescopes with high resolution spectroscopic capabilities provided by a Fourier-transform spectrometer (FTS). During the decade and a half since the launch of Herschel, there has been continued development and refinement of far-infrared detectors, with modern day microwave kinetic inductance detectors (MKIDs) achieving noise-equivalent powers (NEPs) in the few $10^{-20}\,\mathrm{W}/\sqrt{\mathrm{Hz}}$ [14]. In the absence of telescope self-emission and with access to ultra-sensitive detectors, the multiplex advantage of an FTS [15] becomes a disadvantage if instantaneous broad spectral measurements are attempted as the photon noise associated

with the astronomical source now determines the spectral noise density. Examples of broad spectral observations from Herschel that consist of a continuum and line features can be seen in Figure 1.2 [9]. These spectra depict two different stars at distinct stages of their life cycles: a protoplanetary nebula (AFGL 2688) and a post-red supergiant (AFGL 4106). Far-infrared astronomical observations require broad spectral coverage with high spectral resolution while employing state-of-the-art detectors.

With the new generation of ultra-sensitive detectors, a broad spectral observation using an FTS as seen above in Figure 1.2 would reach the photon background limit where the photon noise is greater than the detector noise. The photon noise arising from the quantized nature of radiation, $\mathrm{NEP_{Ph}}$, can be expressed as [16]:

$$\mathrm{NEP_{Ph}}^2 = \frac{4A\Omega(k_B T_s)^5}{c^2 h^3} \int_0^\infty \frac{\eta\varepsilon x^4}{e^x - 1}\left[1 + \frac{\eta\varepsilon}{e^x - 1}\right] dx, \quad [\mathrm{W}/\sqrt{\mathrm{Hz}}] \quad (1.1)$$

where $A\Omega$ [m^2 sr] is the étendue and T_s [K] is the temperature of the source being viewed. ε, the emissivity of the source, η, the optical efficiency of the instrument, and x are dimensionless. The dimensionless quantity x is equal to $h\nu/k_B T_s$, where ν [Hz] is the frequency of electromagnetic radiation and c, h, and k_B are the physical constants; the speed of light, the Planck constant, and the Boltzmann constant, respectively. The only meaningful way to reduce the photon noise in this equation is to restrict the instantaneous spectral bandwidth $d\nu$. Since x is a function of ν, Equation (1.1) can be rewritten as:

$$\mathrm{NEP_{Ph}}^2 = \frac{4A\Omega(k_B T_s)^5}{c^2 h^3} \int_0^\infty \frac{\eta\varepsilon x^4}{e^x - 1}\left[1 + \frac{\eta\varepsilon}{e^x - 1}\right] \frac{h}{k_B T_s} d\nu. \ [\mathrm{W}/\sqrt{\mathrm{Hz}}] \quad (1.2)$$

The photon noise can be reduced by restricting $d\nu$. This is accomplished by coupling some form of post-dispersion element to the output of the FTS. When observing far-infrared astronomical sources, the instantaneous spectral bandwidth needs to be reduced to a fraction of one percent. For this thesis, the FTS output beam is post-dispersed by a single diffraction grating with a resolving power of $R \sim 100$.

The efficiency of a diffraction grating varies with wavelength. At the high angles of incidence required to achieve $R \sim 100$, reflection diffraction gratings operate with high and uniform efficiency ($\sim 80\,\%$) for transverse magnetic (TM) polarized light, in the dispersion direction from the grating, but lower and variable efficiency ($10\,\%$ to $40\,\%$) for transverse electric (TE) polarized light, parallel to the grating grooves. The polarizing encoding properties of a Martin-Puplett interferometer [17] can exploit this strong polarization dependence by ensuring that the interferometer output presents the TM mode to the grating.

The hybrid PDPFTS concept was adopted for the SpicA FAR-infrared Instrument (SAFARI) aboard the joint ESA and JAXA M5 mission candidate, the SPace Infrared telescope for Cosmology and Astrophysics (SPICA) [18]. The SPICA mission was unfortunately removed from consideration in late October 2020 [19]. On November 4$^{\text{th}}$ 2021, the US National Academies of Sciences, Engineering, and Medicine released the Decadal Survey on Astronomy and Astrophysics for the 2020s [20]. The three broad science themes of this survey were: Worlds and Suns in Context, New Messengers and New Physics, and Cosmic Ecosystems. Specific science cases include the formation of planetary systems [21] and cosmological spectrophotometric surveys of black holes and star formation at the cosmic noon [22]. A more diverse set of science objectives has been developed in support of the PRobe far-Infrared Mission for Astrophysics (PRIMA) proposal [23]. A far-infrared probe class mission would provide unique and critical contributions to all three of these science themes. The survey concluded that due to this change in landscape from the cancellation of SPICA, a properly scoped far-infrared probe to advance high-priority science is an extremely timely and compelling opportunity. In light of this survey, a PDPFTS instrument has been adopted for the PRIMA. PRIMA is a NASA Goddard Space Flight Center (GSFC)/Jet Propulsion Laboratory (JPL)-led observatory [24, 25]. The PDPFTS will provide orders of magnitude more sensitivity compared to previous far-infrared space observatories, while maintaining the high resolution spectroscopic capabilities of an FTS. This instrument concept is widely regarded as the next step in far-infrared space astronomy.

1.2 Thesis Outline

This thesis opens with a discussion on the design, development, and verification of the LFC. Since the Test Facility Cryostat (TFC) previously developed by Veenendaal [26] for testing smaller far-infrared instrumentation could not accommodate the size of the PDPFTS presented in this thesis, it was necessary to develop a larger volume 4 K cryogenic facility. The following chapters cover the design, integration, and testing of the fully cryogenic far-infrared PDPFTS. The first light results obtained from this instrument are analyzed and presented. These results are broken into two chapters: a room temperature implementation of the PDPFTS, and the fully cryogenic integration of the instrument into the LFC. The final chapter provides a summary of the results obtained in this thesis and an outlook of the PDPFTS concept being flown on a space observatory in the coming decade. The work performed in this thesis is outlined as follows:

Chapter 1 presents the science case and motivation for the development of the PDPFTS and outlines the work performed in this thesis.

Chapter 2 covers the development, assembly, and testing of the LFC. This cryogenic test facility was purpose-built for the development of far-infrared astronomical instrumentation within the AIG at the University of Lethbridge.

Chapter 3 provides the design of the fully cryogenic far-infrared PDPFTS. The four modules that make up the instrument are covered: the source module, the FTS module, the diffraction grating module, and the detector module.

Chapter 4 presents the room temperature implementation of the PDPFTS. Preliminary results were obtained at room temperature while the construction of the LFC was underway.

Chapter 5 covers the integration of the PDPFTS into the LFC and presents the first light results obtained from the first ever fully cryogenic PDPFTS.

Chapter 6 concludes with a summary of the results obtained in this thesis. This project makes a significant contribution to the ongoing development of modern astronomical instrumentation. Furthermore, with the PRIMA mission adopting a PDPFTS and currently being under review by NASA, there is a potential path-to-flight for this instrument concept.

1.3 A Note Regarding Author's Contributions

The PDPFTS covered in this thesis is a complex hybrid spectrometer with many individual components being integrated. This thesis builds upon the work of others and represents the culmination of efforts spanning multiple decades. Throughout this thesis, I will present my contributions to this project while also acknowledging and calling attention to the many contributions of others.

1.4 A Note Regarding Units

Industry in North America has a large crossover between using the Système International (SI) d'unités and the Imperial Measurement System. In this thesis, Imperial units are presented with their SI conversion only when the natural units or designed units are in Imperial; SI units are used otherwise. The natural units used in astronomy vary greatly depending on what band of electromagnetic radiation you are observing, and what type of instrument is used in the observation. This thesis involves two different spectrometers, a reflection diffraction grating that operates in units of angle [°] and wavelength [µm] and an FTS that operates in reciprocal space with units of wavenumber [cm^{-1}]. Throughout this thesis, I will adopt the natural spectral unit most appropriate to the module being discussed, providing a conversion to wavenumber where applicable.

Chapter 2

The Large Facility Cryostat

> "I am putting myself to the fullest possible use, which is all I think that any conscious entity can ever hope to do."
>
> HAL 9000
> 2001: A Space Odyssey

The design of the Large Facility Cryostat (LFC) builds upon the work of Veenendaal [26] and the Test Facility Cryostat (TFC). The LFC features a 650 mm × 650 mm × 250 mm 4 K volume. If a future experiment requires additional space, the height of this volume can be expanded from 250 mm to 400 mm. The overall increase in volume when compared with the TFC allows larger and more complex far-infrared space telescope instrumentation to be fully integrated and tested at cryogenic temperatures. Beyond volume, attention has been paid to the usability and ease of operating the LFC which influenced aspects of the mechanical design. I will outline my involvement in the design process of the LFC covering the mechanical and thermal analysis, construction and assembly, and verifying the performance of the cryostat. The manufacturing part drawings for the LFC which I created or made contributions to can be found in Appendix A.

2.1 LFC Design

The term cryostat originates from the Greek words *kryos* meaning cold, and *stat*, meaning stable. The design of a cryostat revolves around maintaining a stable operating cryogenic temperature through the management of heat transfer. Heat transfer concerns the rate at which energy can move from one thermodynamic system to another as a result of a tem-

perature gradient. This energy transfer can arise from three basic mechanisms: conduction, convection, and radiation. Minimizing heat transfer between the outer structure, maintained at room temperature, to the internal cold structure of the cryostat whose coldest parts are at 0.3 K is critical. Each of these heat transfer modes introduces specific design challenges that must be addressed. There is an art to the science of cryogenics as the properties that define these heat transfer modes are difficult to characterize explicitly over the temperature ranges a cryostat is operated over, requiring empirical data and many rules of thumb. I direct the reader towards a book by Ekin [27] as a valuable resource for cryostat design.

Since cryostats are typically designed to be operated under vacuum, convection can be ignored leaving only the conductive and radiative heat transfer modes to be considered. The outer vacuum chamber (OVC) of the cryostat must be designed to withstand the 1 atm pressure differential.

To reduce heat transfer from thermal radiation into the interior cold structure of a cryostat, concentric layers of radiation shields are used. These shields are typically made of materials with low emissivity and therefore high reflectivity. Low emissivity leads the outer warmer shield to emit less radiation while allowing the colder inner shield to reflect incoming radiation instead of absorbing it. Emissivity is a wavelength dependent material property influenced by both the material used and its surface finish. A well polished surface will have a lower emissivity than a coarse rough surface. The emissivity value of polished metallic surfaces will have values approaching zero, while a fully oxidized and coarse surface can have an emissivity that approaches one [27]. To prevent oxidation, any copper shields must be gold plated while polished aluminum, despite its lower thermal conductivity, can be used as is. In practice, this dictates the use of copper surrounding the inner 4 K working volume. These shields are thermally anchored at intermediate cold stages to efficiently dissipate any absorbed radiation.

The cold structures of a cryostat are typically made using highly conductive materials with low heat capacities. Between room temperature and temperatures approaching abso-

lute zero, thermal properties of materials tend to be temperature dependent and non linear, requiring numerical integration using experimentally determined values over the desired temperature gradient. The type of material and purity have a significant impact on the thermal conductivity. For nonconductive materials, reducing temperature causes a decrease in thermal conductivity as this reduces phonon vibrations that act as carriers of heat within a material. However, with highly conductive metals, heat transfer is dominated by the free movement of conduction electrons in the crystalline lattice of the material. As temperature decreases, there is an increase in thermal conductivity as electron scattering with phonons is reduced. As the temperature is decreased further past liquid nitrogen temperatures (77 K), the scattering mechanism between the conduction electrons and impurities in the material becomes the dominant factor and the thermal conductivity decreases [27]. The thermal conductivity behaviour of pure metallic materials at cryogenic temperatures lends itself to using high purity copper and aluminum to make up the cold structure of a cryostat. For the choice of high purity copper, electrolytic tough pitch (ETP) copper (99.9 % pure) and oxygen free high conductivity (OFHC) copper (99.99 % pure) perform nearly identically. ETP copper is the economical choice as OFHC is more expensive, harder to acquire, and more difficult to machine. Increasing the purity of copper to 99.999 % improves the thermal conductivity by a factor of 20 at liquid helium temperatures (4 K) compared to both ETP and OFHC copper [27]. The low temperature performance of higher purity coppers must be weighed against the increase in cost and reduced availability.

Careful consideration must be given not only to the thermal conductivity through the cold structure of a cryostat but also to thermal contact conduction when joining these structures. The heat transfer through bolted joints is highly dependent on the surface properties on either side of the joint and the clamping pressure of the bolt.

The different cold stages of a cryostat need to be supported, but thermally isolated from each other. The supports that separate the cold structures from room temperature are made from insulating materials with low thermal conductivity, such as carbon fiber reinforced

polymer (CFRP), glass fiber reinforced polymer (GFRP), or stainless steel tubing. These materials offer both high tensile strength and low thermal conductivity, making them well suited for insulating the cold stages of a cryostat. By effectively managing parasitic conductive and radiative heat transfer, cryogenic test facilities can achieve and maintain low operating temperatures.

Historically, cryostats have been designed around the latent heat of evaporation where cooling power was generated by a liquid cryogen, such as nitrogen or helium, evaporating. This approach has become increasingly expensive with the rising cost of liquid helium, and it comes with heightened risks of cold-related hazards and asphyxiation. Modern cryocoolers have emerged as closed-cycle systems designed to address these challenges. This emergence of closed-cycle cryocoolers not only eliminates the need for a costly and finite supply of liquid cryogens, but also significantly reduces the associated safety risks [27].

The design process for the LFC started with an analysis of the TFC [26]. Following this analysis, a list of what worked well and areas for improvement was compiled to guide the design direction for the LFC. The key difference between the two cryostats was an increase in the 4 K working volume. The original specifications for the LFC were based on developing a prototype of the SAFARI instrument for the SPace Infrared telescope for Cosmology and Astrophysics (SPICA) mission [29, 18]. A computer-aided design (CAD) rendering showcasing the proposed 4 K working volume of the LFC can be seen in Figure 2.1. This rendering presents the initial conceptual layout of the prototype SAFARI instrument. The corresponding initial design specifications for the LFC are detailed in Table 2.1.

The as-designed working volume of the LFC is 650 mm $\times$ 650 mm $\times$ 250 mm. The originally conceived layout of the SAFARI instrument required a height of 400 mm but as the project evolved, we were able to better integrate the prototype post-dispersed polarizing Fourier transform spectrometer (PDPFTS) instrument concept covered in this thesis in a volume with a height of 250 mm. With some modification, the height of the 4 K volume can be extended to match the originally proposed specification.

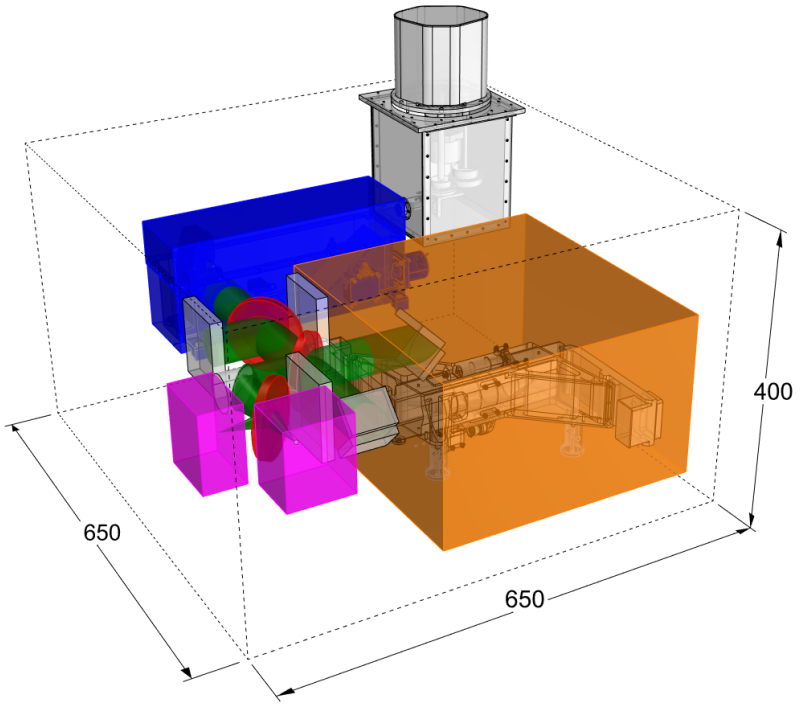

Figure 2.1: The originally proposed LFC 4 K working volume containing a conceptual layout of the prototype SpicA FAR-infrared Instrument (SAFARI) instrument. The SAFARI mechanism space envelope is shown in orange, with the ABB scanning mechanism occupying most of this space. The post-dispersion grating mechanism is shown in blue, coupled to the 0.3 K refrigerator and bolometer system in grey. The Fourier-transform spectrometer (FTS) includes polarizers from QMC Instruments shown in red. The blackbody continuum and photomixer line source modules are shown in magenta. Image taken from [28].

Table 2.1: Proposed LFC specifications [28].

Specification	**Requirement**
Mass	Not applicable.
Volume	Must fit either assembled or disassembled through the facility doors.
4 K Volume	650 mm × 650 mm × 400 mm (L×W×H), approximate.
Material	Stainless steel chamber, CFRP internal support structure, gold plated copper cold surfaces.
Shielding	MLI covered aluminum panels for 45 K shielding, gold plated copper panels for 4 K shielding.
Viewports	To be determined.
Electrical ports	To be determined.
Cryocooler	Compatible with Cryomech PT415 pulse tube cryocoolers (PTCs), with ability to operate with one or two installed coolers.
Cold cycling time	24 h.

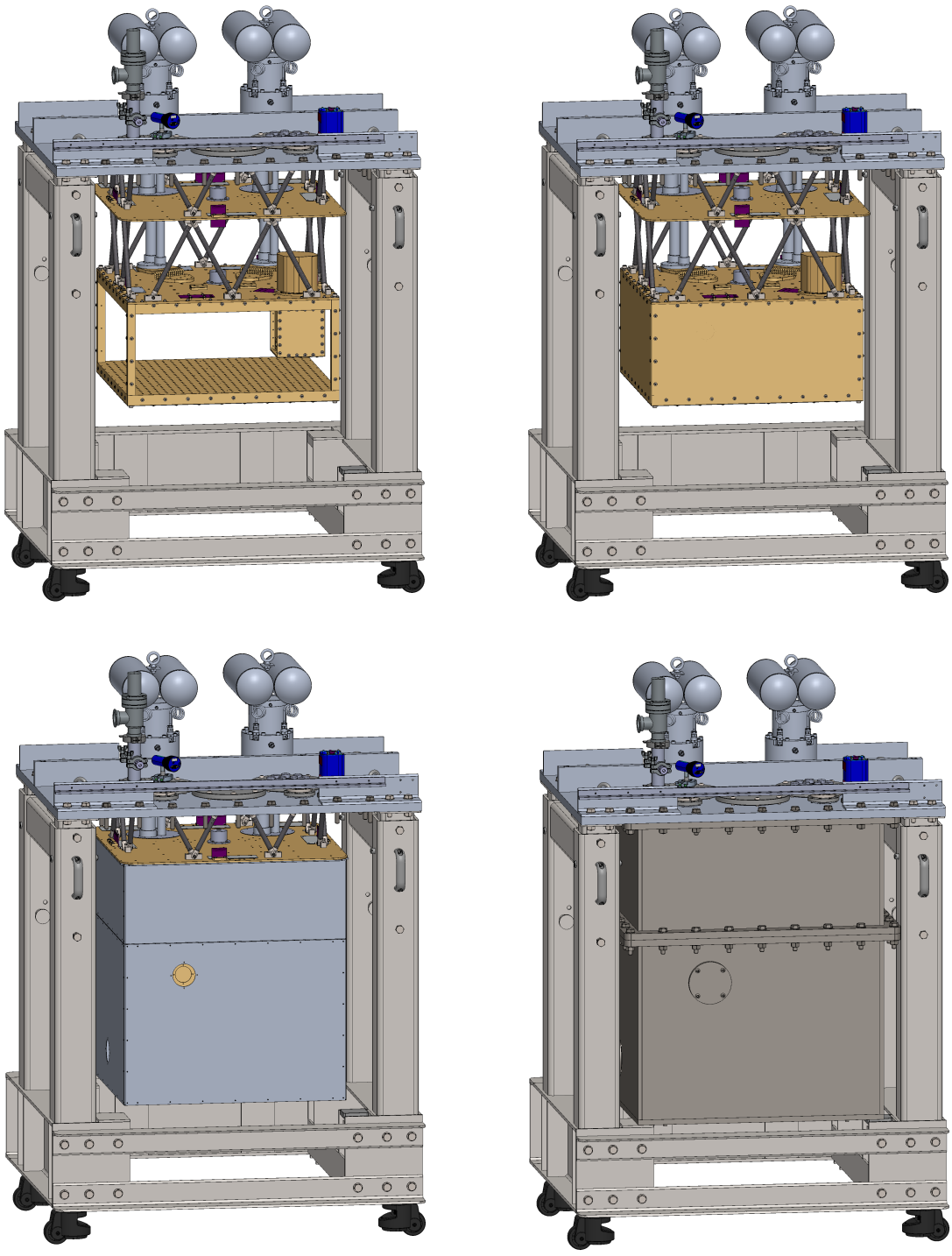

Figure 2.2: CAD rendering showing an overview of the LFC. Two Cryomech PT415 PTCs provide cooling capacity while CFRP struts and concentric layers of radiation shielding reduce parasitic heat transfer. Top Left: Fully open. Top Right: 4 K radiation shielding. Bottom Left: 45 K radiation shielding. Bottom Right: OVC.

The LFC design draws significant inspiration from the TFC [26]. The LFC retains a rectangular shape and consists of a 45 K intermediate stage, a large 4 K working volume, and a small 0.3 K sub-volume. In order to improve the overall structural rigidity and functionality, several key modifications were implemented. These included a redesign of the external frame, the incorporation of CFRP tubes to form a triangular space frame like support structure, and the adoption of a torsion box design for the 4 K cold plates. Figure 2.2 shows a CAD overview of the LFC, with its various layers of radiation shielding and outer vacuum chamber removed to show the concentric layers and the internal framework. The following subsections cover the design work for the LFC.

2.1.1 External Frame

The external framework of the LFC draws inspiration from the design of container cranes and gantry cranes. It consists of a robust welded steel frame with two telescoping legs connected by an aluminum top plate to create a portal frame. Suspended from this top plate are the cold structures of the cryostat and the vacuum chamber sections. This configuration allows for the efficient operation of the LFC. When in its lowered position, the cryostat height is short enough to allow it to be wheeled around on four levelling plate castors through the facility doors within the Astronomical Instrumentation Group (AIG) at the University of Lethbridge. Once in its desired position, the levelling pads on each caster are extended to provide a stable platform for the cryostat and prevent inadvertent movement. To access the internal structure of the LFC, the telescopic frame is raised to create an open space beneath the cryostat. The vacuum chamber sections are subsequently lowered onto a lift cart and removed from the open side of the portal frame, allowing easy access to the cold structure of the cryostat and facilitating the installation and modification of experiments. Figure 2.3 shows the external frame of the cryostat in the lowered and raised positions. While I contributed to the initial conceptualization and early iterations of the telescopic frame, Ben Louwerse refined the design into its final form.

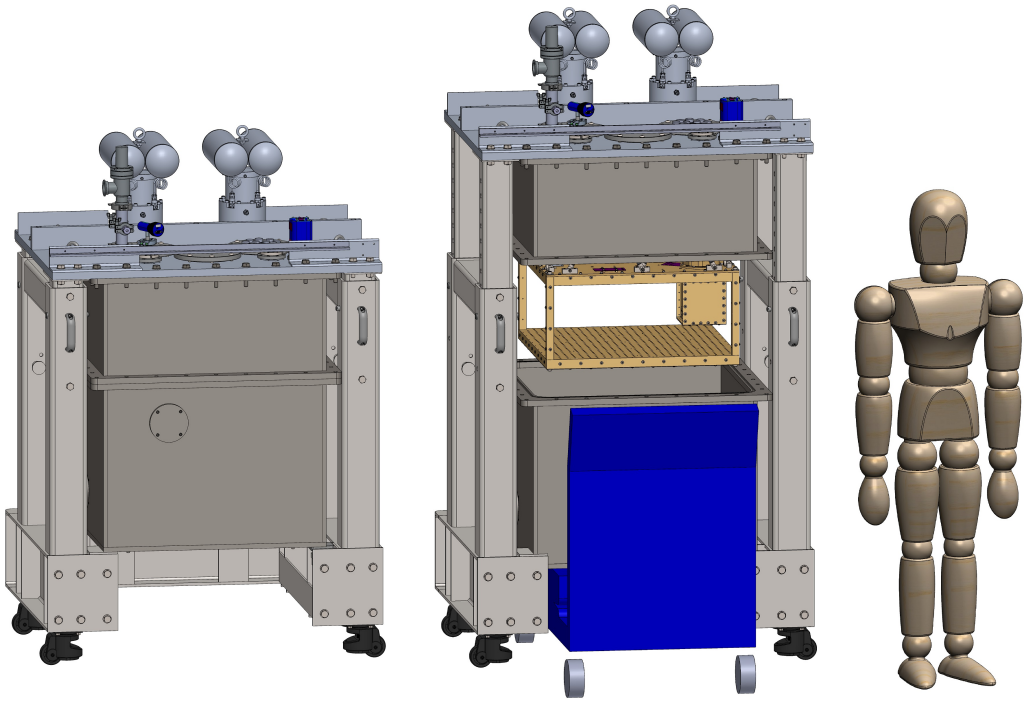

Figure 2.3: CAD rendering showing the external frame of the LFC in the lowered and raised position with an average size human figure for reference. Left: Frame lowered. Right: Frame raised with a vacuum chamber section lowered onto a blue lift cart.

2.1.2 Vacuum Chamber

The design of the LFC was strongly guided by the lessons learned from the TFC [26]. This led to the use of stainless steel for the main vacuum chamber sections and aluminum for the top plate. This choice was driven by practical considerations: stainless steel is easier to weld, while aluminum is more suitable for machining. This decision had cost-saving implications, especially since the top plate required intricate passthroughs for the vacuum manifold, PTCs, and various electrical and optical fiber connections. To increase the future usability of the cryostat, four viewports were incorporated into the lower vacuum chamber section to allow light from external instrumentation to be passed through to the 4 K volume. These viewports were blanked off and not used for any of the measurements made in this thesis to eliminate all sources of stray light. While the primary goal of the LFC is to integrate entire far-infrared instrument concepts at 4 K without windows looking out to the room temperature lab, the inclusion of these four viewports was considered a prudent investment, resulting in a small overall increase in cost in anticipation of future use cases.

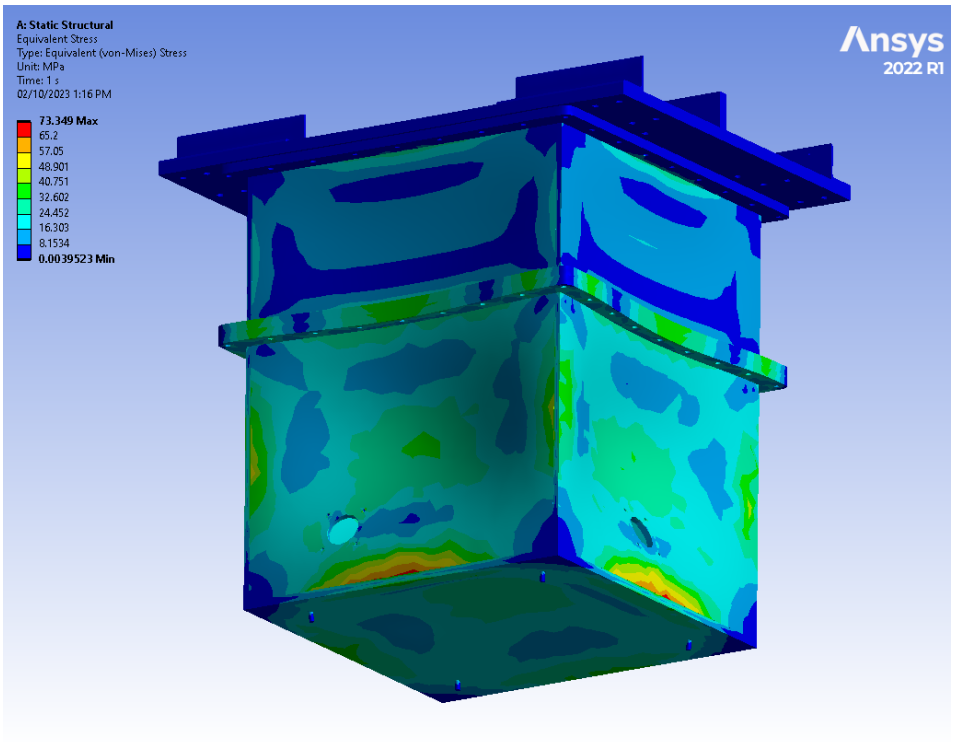

Figure 2.4: FEA model showing the equivalent von-Mises stress on the LFC vacuum chamber walls resulting from a 1 atm pressure differential.

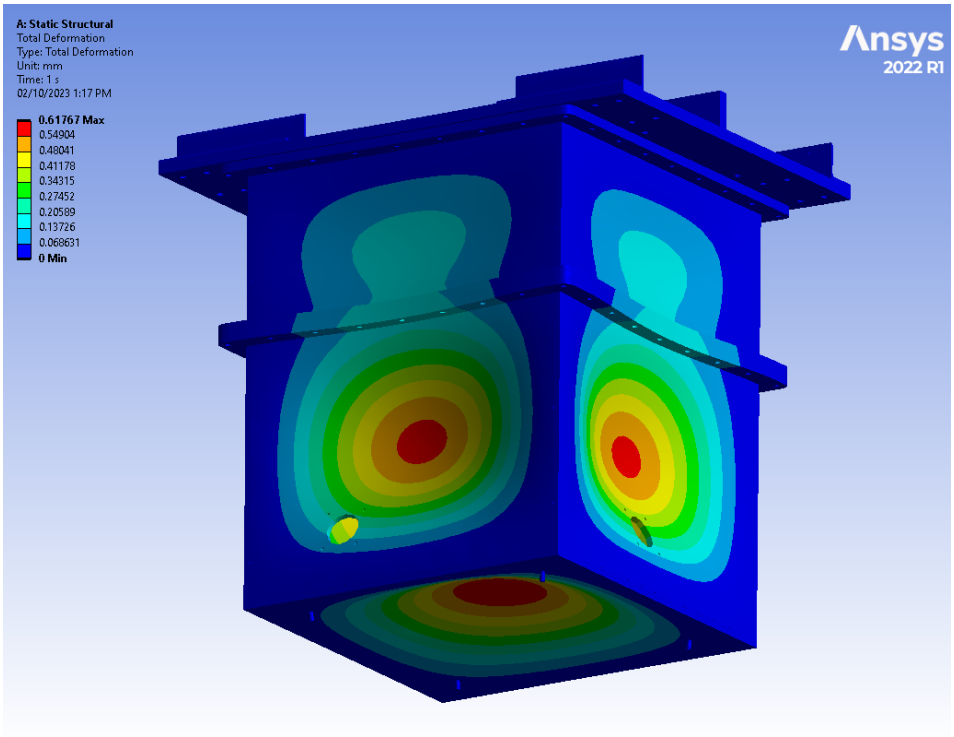

Figure 2.5: FEA model showing the deformation of the LFC vacuum chamber walls resulting from a 1 atm pressure differential.

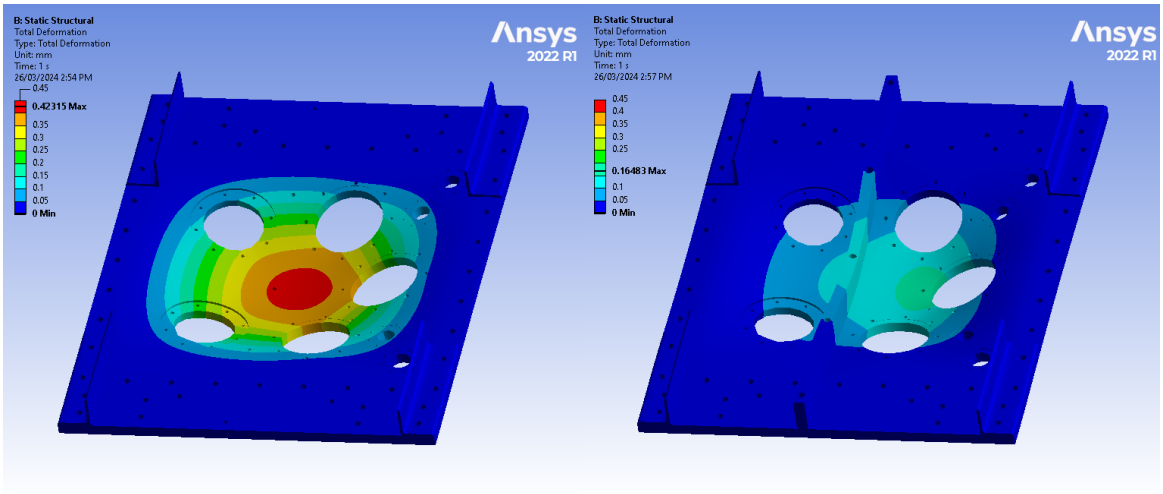

Figure 2.6: FEA models comparing the deformation of the LFC vacuum chamber top plate before and after the addition of an aluminum stiffening bar.

Several iterations of the chamber were analyzed using Ansys Mechanical™ finite element analysis (FEA) software to determine the optimal chamber wall and flange thicknesses. This balanced the increased cost of manufacturing against the reduction of stress and deformation of the chamber as increasing the thickness of the chamber walls offers increased stiffness, thereby lowering stress and deformation while raising the material cost. Ultimately, the upper and lower vacuum chamber sections were manufactured from 304 stainless steel. The chamber features side walls that are $1/2$ in (12.7 mm) thick, a bottom plate measuring $5/8$ in (15.9 mm) , and 1 in (25.4 mm) flanges. The top plate of the vacuum chamber was manufactured from 1 in (25.4 mm) thick 6061 aluminum. Figure 2.4 shows the equivalent von-Mises stress while Figure 2.5 shows the plastic deformation that is expected to occur when a 1 atm pressure differential is applied to the vacuum chamber. The maximum stress that occurs is 73 MPa, which is well below the 215 MPa tensile yield strength of stainless steel [30]. As 6061 aluminum has a notably lower Young's modulus of 68.9 GPa [31] when compared with the Young's modulus of 304 stainless steel of 193 GPa [30], an additional 1 in $\times$ 3 in (25.4 mm $\times$ 76.8 mm) aluminum bar was bolted across the top plate of the vacuum chamber to increase its stiffness. This reduced the deformation of the top plate from 0.42 mm to 0.16 mm. Figure 2.6 shows the effects of this bar on the stiffness of the vacuum chamber top plate.

2.1.3 CFRP Struts

The LFC has 16 CFRP tube struts separating the 45 K stage from the OVC, and 16 CFRP tube struts separating the 4 K stage from the 45 K stage. CFRP was chosen to limit the parasitic heat transfer between stages as CFRP has a relatively low thermal conductivity when compared to other available materials, such as stainless steel. The CFRP struts were cut from lengths of 0.500 in (12.7 mm) inside diameter (ID), 0.570 in (14.5 mm) outside diameter (OD) CFRP tube available from Clearwater Composites [32]. This gives each CFRP strut a cross-sectional area of approximately 38 mm^2. The struts separating the 45 K stage from the OVC are 108 mm long while the struts separating the 4 K stage from the 45 K stage are 221 mm long. Stainless steel knuckles extend 10 mm into both ends of each CFRP tube and are epoxied in place using LOCTITE© STYCAST 2850FT epoxy cured with CAT 24LV catalyst [33]. Ventilation holes were drilled through the CFRP tubes so that any trapped air would vent from the sealed cavity. As a safety measure, pins extend through the CFRP tubes and stainless steel endcaps to prevent catastrophic failure should the epoxy joint fail.

Heat transfer calculations through the CFRP struts assume that the stainless steel knuckles and endcaps are isothermal at both ends of the temperature gradient. As these endcaps extend into the CFRP tubes, the overall lengths used in heat transfer calculations were reduced by 20 mm. Thermal conductivity tends to be non-linear at cryogenic temperatures, as such, temperature dependent thermal conductivity values for CFRP were obtained from Chen et al. [34] and the thermal conductivity integral over the desired temperature gradient was numerically calculated. The temperature dependent thermal conductivity was obtained for integer temperature values over the chosen gradient by fitting a cubic spline to the 4 point neighbourhood surrounding each interval. The tabular data were then numerically integrated with segments being processed in groups of four using a 5 point Newton-Cotes integration formula [35] to give the thermal conductivity integral. This was combined with

the above CFRP strut geometry to determine the net heat transfer of 3.9 W through the 45 K struts and 18.2 mW through the 4 K struts.

2.1.4 Cold Structure

The cold structure of the LFC is comprised of an intermediate 45 K stage and a 4 K working volume. The 45 K stage consists of a single cold plate while the 4 K working volume is split between an upper and lower cold plate connected at the corners by four 1 in $\times$ 1 in (25.4 mm $\times$ 25.4 mm) square bar posts. All cold structure components are made from gold plated C110 ETP copper. The as-assembled configuration of the LFC provides a 650 mm $\times$ 650 mm $\times$ 250 mm 4 K working volume. The height of this volume can be extended from 250 mm to 400 mm by replacing the four 1 in $\times$ 1 in (25.4 mm $\times$ 25.4 mm) square bar posts with longer equivalent posts, and by installing taller 4 K radiation shields. The cold plates of the cryostat form two breadboards with a 25 mm spacing hole grid on the lower breadboard and a 50 mm spacing hole grind on the upper breadboard to allow flexibility in experiment design and installation. To prevent the galling of threads in the soft copper, M3 and M4 Yardley©stainless steel press-fit threaded inserts were installed in the breadboards. M3 Heli-Coil©inserts were installed on the sides of the plates to which the radiation shields are fastened.

With the increased size of the 4 K volume relative to the TFC, a torsion box design was employed for the upper and lower cold plates to increase the stiffness of the breadboard to prevent sagging. Maintaining a rigid 4 K structure had two requirements. A composite bolometer detector housed within the 0.3 K sub-volume drove vibration considerations. It was critical to keep the fundamental vibration mode for the structure of the cryostat well above the detector cutoff frequency of around 10 Hz. Increasing the rigidity of the structure increases the fundamental vibration mode frequency. Maintaining a flat and rigid breadboard is also critical when installing high-precision optical systems within the cryostat. It was determined that a single plate was insufficient to maintain a rigid 4 K structure and a torsion box design was necessary.

The torsion box design allowed the creation of a rigid, lightweight breadboard by sandwiching a grid of ribs between two parallel skins. Two design philosophies were explored when looking at creating torsion boxes: a top and bottom skin bolted together with individual spars, and a skin with integrated spars being machined from a billet block of copper which is then bolted to a plate acting as the second skin. The billet design philosophy was ultimately adopted as this approach both saved on manufacturing costs and improved thermal conduction through the cold structure due to a reduction of bolted joints. Bolted connections introduce unpredictable contact conduction and heat transfer across a joint when compared with a homogeneous material. Eliminating bolted connections where possible and opting for a billet design provides improved conduction.

Ansys Mechanical™ FEA was used in the design iteration process to study the vibration modes and how the 4 K breadboards deform under load. Figure 2.7 shows the deformation of the internal structure of the LFC while under standard Earth gravity. The first two vibration modes are a pendulum-like motion of the structure in either of the two major rectangular axes occurring at 38 Hz. Figure 2.8 shows an example of one of these two vibration modes. The results for the second pendulum mode are similar. The modal analysis computes only the frequency and shape of the vibration modes but the magnitude of deformation has no physical meaning as no load is applied and should be ignored.

The PTCs that provide the cooling power to the 4 K volume are bolted onto the upper 4 K plate through flexible thermal braids. These braids provide a thermal link between the PTCs cold heads and the 4 K plate while isolating mechanical vibrations from being transmitted into the cryostat. The design of these thermal braids is discussed further in Section 2.2.4. For the lower 4 K plate to cool, conduction needs to occur across these braids connecting the PTCs to the 4 K plate, then conduction needs to occur across the four square posts at the corners connecting the upper and lower plates of the 4 K volume. Bolted connections are present between the mating surfaces of these braids and posts. Calculating conduction through bolted connections at cryogenic temperatures presents challenges due

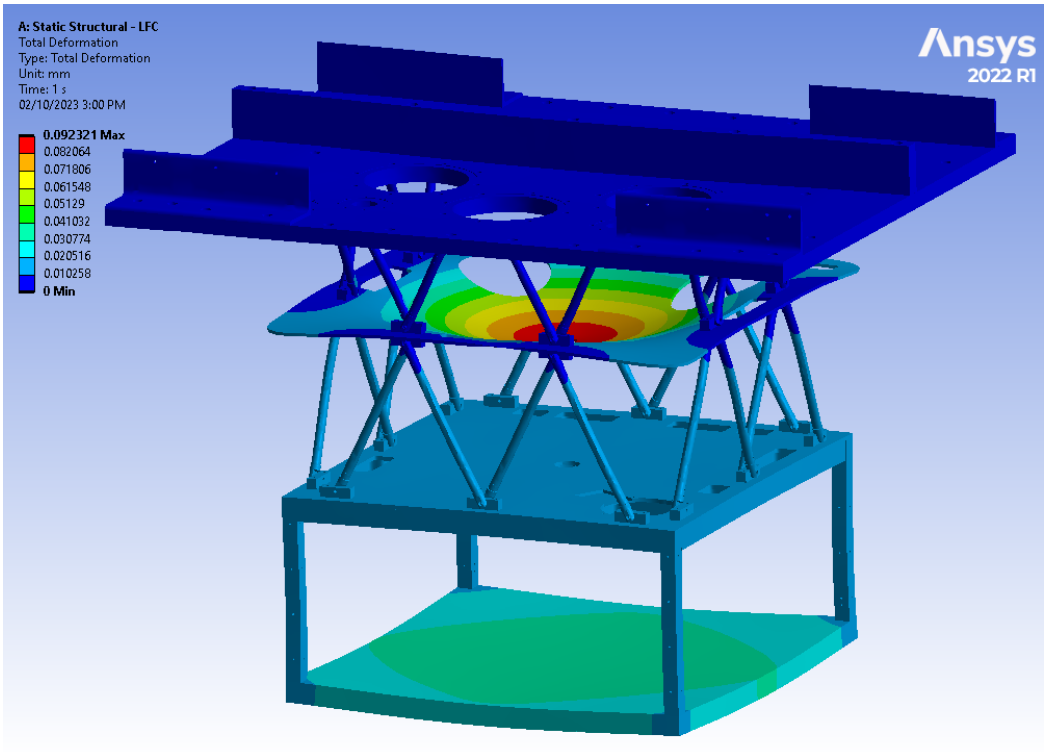

Figure 2.7: FEA model showing how the internal structure of the LFC deforms under standard Earth gravity.

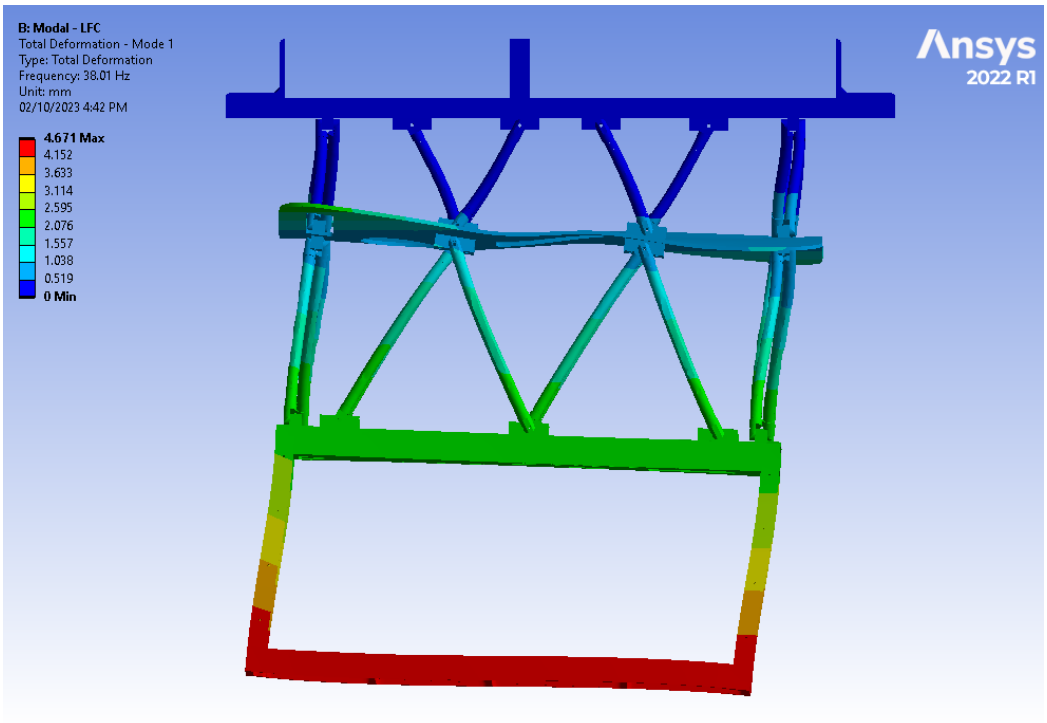

Figure 2.8: FEA model showing the pendulum like motion of the fundamental vibration mode for the internal structure of the LFC. The oscillation occurs at 38 Hz.

to numerous variables that are challenging to control. Factors such as flatness, surface roughness, cleanliness, and material influence the contact conduction through a mated joint. Contact conduction is generally empirically determined, using equations that are a function of bolt clamping force instead of the cross-sectional area of a joint [27]. At a microscopic level, peaks and valleys given by the surface roughness of a joint will mean that the only appreciable contact occurs in a small region around each bolt. Increasing the clamping force at a bolted connection causes these microscopic peaks and valleys to deform, increasing the contact conduction in the local area around the bolt.

An analysis was conducted to determine the optimal size for the corner posts and fasteners. Larger bolts will enable a higher clamping pressure, improving contact conduction between the cold plates and the posts, while larger posts will improve the conduction from the side mated to the bottom plate to the side mated to the upper plate. If the corner posts are undersized relative to the bolts, heat transfer from the lower plate to the upper plate will be restricted by the conduction through the posts, and if the bolts are too small with a low clamping pressure, the heat transfer will be limited by the contact resistance of the bolted connections. Striking a balance between these two factors and the available cooling power from the cryocooler is crucial to prevent either from becoming a bottleneck.

Bolted copper joints at cryogenic temperatures have been empirically shown to follow a power law over a 0.1 K to 20 K temperature range. The prefactor is a function of clamping force and the exponent is based on the two materials of the joint [27]. For a 3 kN force, gold-gold contact thermal conductance is given by the following equation [36]:

$$K \approx 0.1161 T^{1.11}, \qquad [\mathrm{W\,K^{-1}}] \quad (2.1)$$

where T is the average joint temperature.

Scaling the prefactor for a 9.9 kN clamping force from an M8 bolt gives a contact thermal conductance of:

$$K \approx 0.3831 T^{1.11}. \qquad [\mathrm{W\,K^{-1}}] \quad (2.2)$$

Assuming a joint temperature of 4 K yields a contact conductance of $1.785\,\mathrm{W\,K^{-1}}$. Based on copper with a residual resistance ratio (RRR) of 100 having a thermal conductivity of $642.3\,\mathrm{W\,m^{-1}\,K^{-1}}$ at 4 K [37], 280 mm long 1 in × 1 in (25.4 mm × 25.4 mm) square bar stock yields a conductance of $1.480\,\mathrm{W\,K^{-1}}$. With the four corner posts, and 1.5 W of cooling power at 4.2 K [38] provided by each of the two cryocoolers, M8 bolts paired with 1 in × 1 in (25.4 mm × 25.4 mm) square post were chosen.

To validate the design decisions, Ansys Mechanical™ steady-state thermal FEA simulations were conducted to determine the heat flow from the lower to the upper 4 K plates, using the above conductance values. Joint contact conductance values were applied to the posts, a static temperature was set at the location of the cryocoolers on the upper 4 K plate, and power was applied to the lower 4 K plate. The resulting thermal gradient can be seen in Figure 2.9.

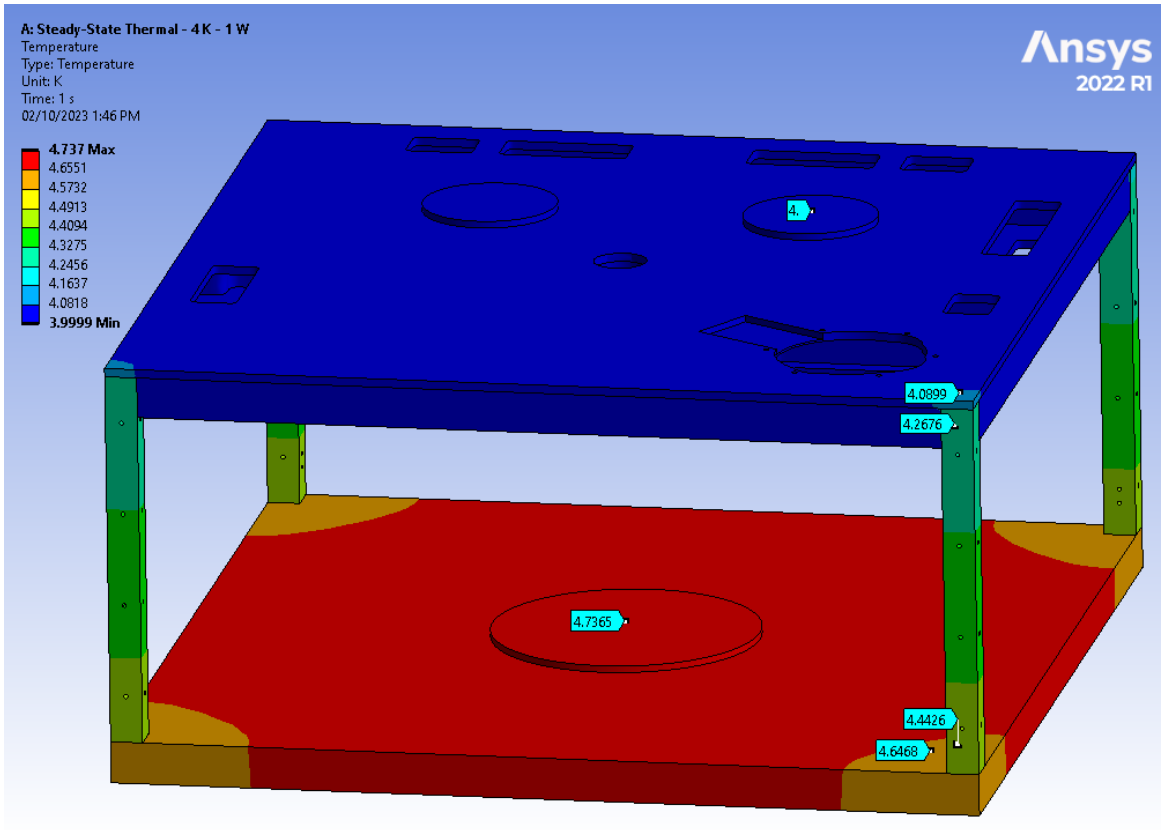

Figure 2.9: Steady-state thermal FEA model showing the thermal gradient in the 4 K as a result of 1 W applied to the lower 4 K plate. 1 in × 1 in (25.4 mm × 25.4 mm) corner posts were paired with the contact conductance value for gold-gold M8 bolted joint connections.

The coefficient of thermal expansion (CTE) for copper is greater than that of the stainless steel bolts. As the clamping force is a function of the elastic deformation of the bolt, the clamping force will be reduced as the bolted connection cools. To compensate for the CTE mismatch between the copper cold structure and the stainless fastener, molybdenum or invar washers are commonly used. Invar tends to be cheaper and requires a thinner washer to negate the CTE mismatch. The total linear contraction from room temperature (293 K) to the desired temperature T is defined as [27]:

$$\Delta L/L = (L_{293K} - L_T)/L_{293K} \tag{2.3}$$

$\Delta L/L$ values for various materials at key temperatures are provided by Ekin [27] and used to find the difference in thermal contraction between the stainless fasteners and the copper structure. Figure 2.10 plots the difference in thermal contraction between a stainless steel fastener and the copper through hole which forms the joint between the upper 4 K plate and the corner post. A 0.6 mm thick invar washer was used to compensate for the CTE mismatch at this bolted joint. All washers used to compensate for CTE mismatch in the LFC were machined in house.

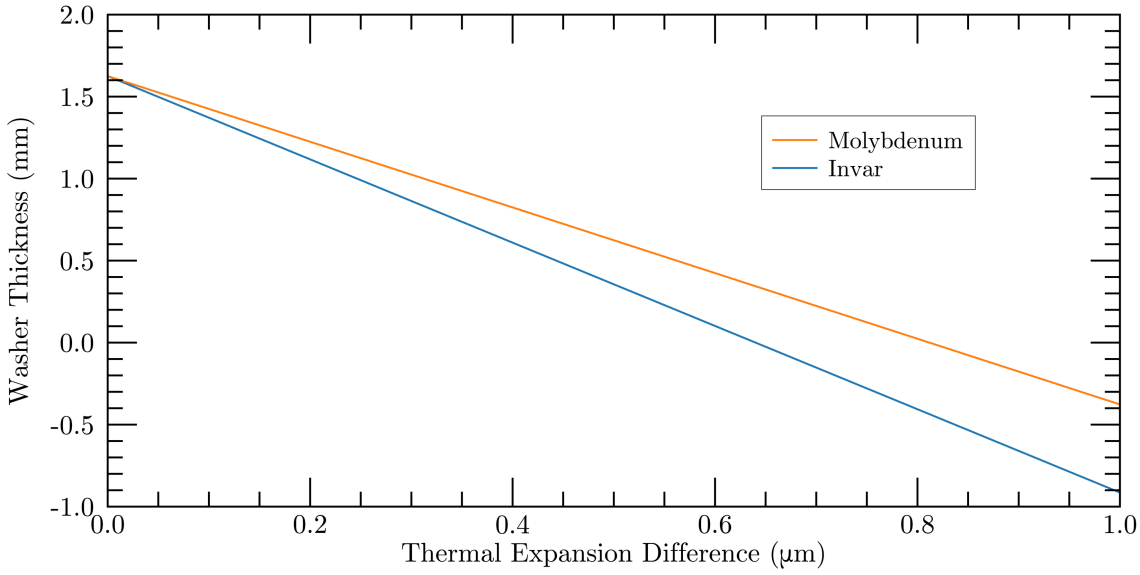

Figure 2.10: Difference in thermal contraction from 293 K to 4 K between a 6.35 mm long stainless steel fastener and a copper through hole. As a molybdenum (orange) or an invar (blue) washer increases in thickness, the difference in contraction is compensated.

2.1.5 Radiation Shielding

Radiative heat transfer tends to have the largest impact on the thermal constraints of a cryostat. To reduce the radiative power incident on the low-temperature stage of a cryostat, intermediate stages and concentric layers of radiation shielding are used to separate the cold structure from the warm room temperature side. The LFC is broken into four stages: the room temperature OVC, a 45 K stage, a 4 K stage, and a small 0.3 K sub-volume. As Stephen-Boltzmann's law scales to the fourth power with temperature, the majority of the radiative heat transfer in the LFC occurs between the room temperature OVC and the 45 K stage. To reduce this heat load, the 45 K stage radiation shielding is lined with multilayer insulation (MLI) blankets. These blankets effectively trap radiant heat within multiple layers of highly reflective material. The construction of the MLI blankets for the LFC is covered in Section 2.2.5. Other methods to reduce radiative heat transfer included lining the stainless steel vacuum chamber with an aluminum foil to reduce its emissivity, and gold plating the copper 4 K and 0.3 K radiation shielding to reduce their emissivity.

Radiative heat transfer calculations were performed to determine the radiative loading on the 45 K stage and the 4 K stage. Calculations assumed that both emitters and reflectors were diffuse (incoming and outgoing radiation is uniform over each surface), the surfaces were gray (independent of wavelength), opaque (nontransparent), and isothermal. Steady state heat transfer was assumed such that absorptivity equals emissivity. As a worst case scenario, all emissivities were assumed to be 10 % and the insulating properties of MLI between the OVC and 45 K stage were not taken into account. While the principles defining heat transfer through MLI are well understood, it is difficult to characterize the real-world performance of this insulation. Variations in construction, as well as intermediate contact between layers of MLI affect its insulating properties and are difficult to quantify. The addition of MLI on the 45 K shielding will reduce the radiative heat transfer and improve cool down time.

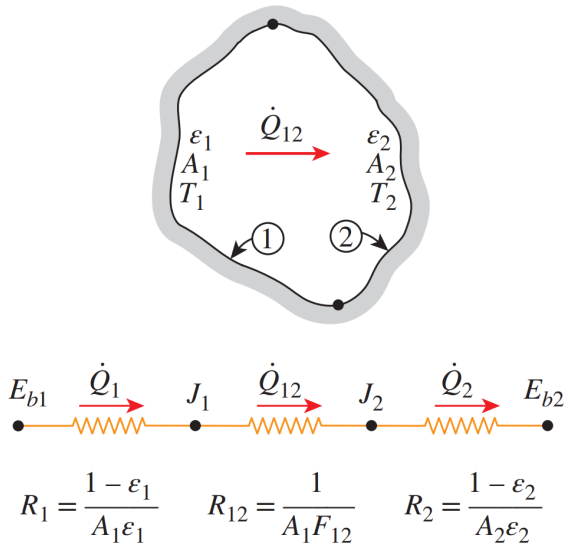

Figure 2.11: Diagram depicting a two-surface enclosure and its corresponding radiation network. Image taken from [39].

By treating the concentric layers of radiation shielding as two-surface enclosures where the emissivity, area, and temperature of each surface is known, a series of thermal resistances, R, can be defined and a resistance network approach as shown in Figure 2.11 can be used to solve the net radiative heat transfer from one surface to another. This resistance network is made up by placing a surface resistance on each surface of the enclosure and connecting them in series with a space resistance. For a two surface enclosure, this method is straightforward as the network remains quite simple.

From Figure 2.11, ε, A, and T represent the emissivity, area, and temperature of each surface. The emissive power and radiosity for the surfaces are given by E_b and J, respectively. The view factor, F, is a geometrical factor that defines how well one of the surfaces can see the other. With the emissivities, surface areas, and temperatures known, the net rate of radiative heat transfer between the two surfaces is going to equal the net rate of heat transfer for surface 1, which will also equal the net rate of heat transfer for surface 2. We can then determine the net rate of radiative heat transfer using the following equation [39]:

$$\dot{Q}_{12} = \frac{E_{b1} - E_{b2}}{R_1 + R_{12} + R_2} = \dot{Q}_1 = -\dot{Q}_2, \qquad \text{[W]} \quad (2.4)$$

which is equivalent to:

$$\dot{Q}_{12} = \frac{\sigma(T_1^4 - T_2^4)}{(1-\varepsilon_1)/A_1\varepsilon_1 + 1/A_1F_{12} + (1-\varepsilon_2)/A_2\varepsilon_2}, \qquad \text{[W]} \quad (2.5)$$

where σ is the Stefan-Boltzmann constant.

To find the view factor, the two surfaces of the radiation shielding will be treated as concentric spheres. This gives the inside surface looking towards the outside surface a view factor of unity. As the areas of the emitting surface i and reflecting surface j are known, the reciprocity relation shown below can be used to find the view factor of the outside surface looking towards the inside surface.

$$A_iF_{i\to j} = A_jF_{j\to i} \quad (2.6)$$

2.1.6 Crycooler

The LFC was designed to be cooled using a pair of Cryomech PT415 PTCs, each of which is accompanied by a CPA1110 compressor. The PT415 is a two stage cryocooler, providing a 45 K first stage and a 4 K second stage. Each PTC is rated to provide 1.5 W of cooling power at 4 K and 40 W of cooling power at 45 K and is capable of achieving a base temperature of 2.8 K. The available cooling capacity is dependent on the temperatures of both stages. Figure 2.12 shows the cooling capacity curve for the PT415 PTC. The matching compressors have a maximum power draw of up to 10.7 kW [38]. This maximum power draw occurs at the start of a cool down when the compressors are working the hardest. To manage the heat generated by these compressors, a water cooling system is employed.

To mitigate the transmission of vibrations generated during the pulsating refrigeration cycle of the PTCs, flexible thermal braids are used to connect the cold heads of each PTC to the cold plates of the cryostat. A more comprehensive discussion on the assembly of these thermal braids can be found in Section 2.2.4.

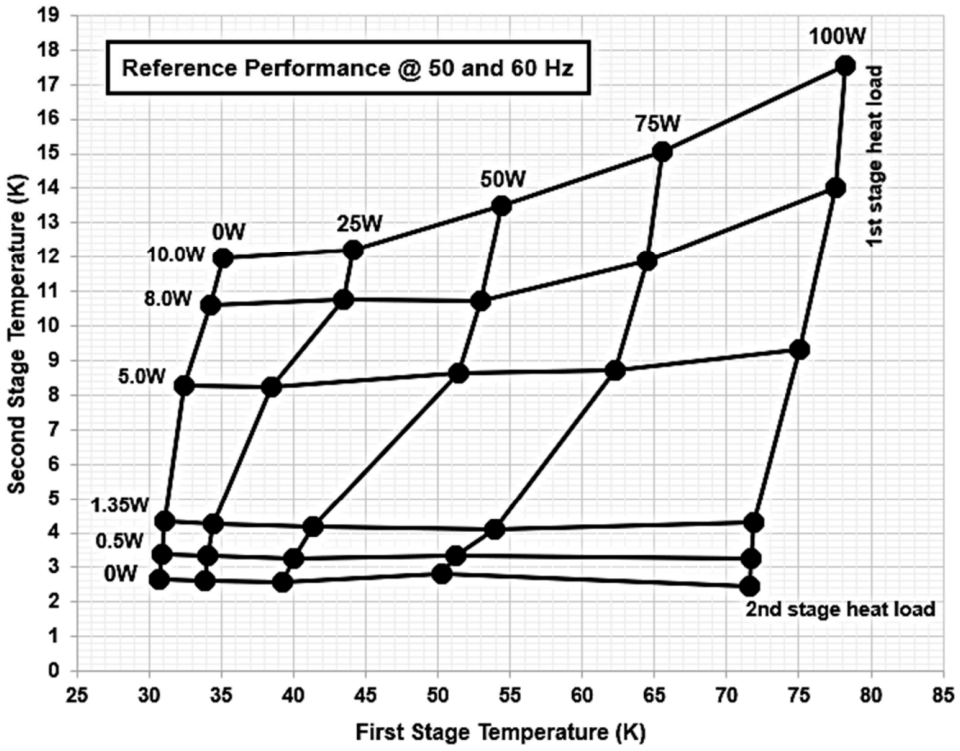

Figure 2.12: Cryomech PT415 PTC cooling capacity. Image taken from [38]

2.2 LFC Assembly

The design of a cryostat is only half the battle. Parts must be manufactured, either in house, or by sending drawings off to various machine shops. The AIG is fortunate that its project manager, Brad Gom, is an extremely skilled machinist who is able to manufacture many of these parts. Once the parts have been procured, the next step is to assemble the cryostat. The following subsections underline the process of assembling the LFC.

2.2.1 Gold Plating

Gold plating was applied to all copper components within the cryostat. This was done for two distinct yet crucial reasons: The copper cold structure of the LFC would oxidize over time without being gold plated increasing its emissivity, and the thermal contact conduction across bolted joints is improved with a gold-gold surface contact. The components that

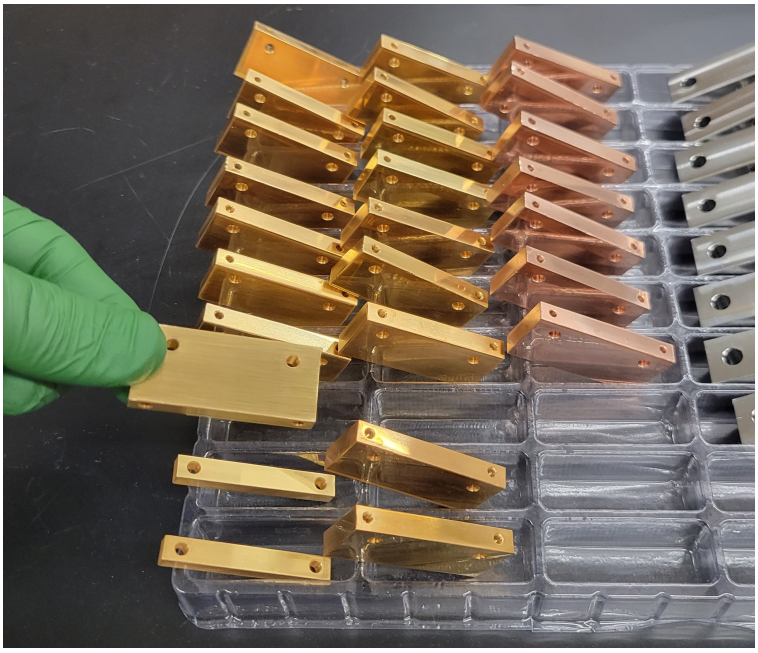

Figure 2.13: Gold plated copper wiring harness heat sinks.

were gold plated include the 45 K cold plate, 4 K cold plates, 4 K radiation shields, 0.3 K radiation shields, wiring harness heat sinks, and the flexible thermal braids. Figure 2.13 shows the gold plated copper wiring harness heat sinks. The two rows on the left show heat sinks that have already been gold plated while the row on the right shows bare copper heat sinks that have yet to be gold plated.

The gold plating process began by preparing the copper components for plating. All components were thoroughly degreased, cleaned, and deoxidized. Citric acid was used to remove oxide from the copper pieces as it was found to work effectively on heavily oxidized copper without damaging the base copper material while posing minimal exposure risks when compared to stronger acids such as hydrochloric acid. Immediately before gold plating, a dilute solution of acetic acid (2 % to 3 % by volume) was used to acid etch the copper. This was to remove any oxide that may have formed between the citric acid deoxidation process and gold plating. The copper piece was then thoroughly rinsed of acid using reverse-osmosis water before being submerged into the gold plating bath solution. The electroplating process for gold plating used a potassium aurocyanide based 24 carat

pure gold solution from Gold Plating Services [40] and platinum clad niobium anodes. A current density of $3\,\mathrm{mA\,cm^{-2}}$ over the gold plated part was chosen as the optimal current density for the solution falls in the $2\,\mathrm{mA\,cm^{-2}}$ to $5\,\mathrm{mA\,cm^{-2}}$ range [41]. During the plating process, replenisher was added to the bath solution in order to maintain a sufficiently high concentration of gold in the plating solution. As the concentration of gold drops below a threshold value, the uniformity of plating becomes more variable and the deposition rate of gold is reduced as the bath efficiency decreases [42]. A total of 6 gallons (22.7 L) of gold plating bath solution, alongside replenisher solution containing 20 g of gold were used, costing approximately $10 000 USD.

Gold coatings for thermal contact, such as those on the 4 K cold plates and thermal braids, should fall in the 2 µm to 5 µm range. In contrast, surfaces intended for gold plating to reduce emissivity, such as the 4 K radiation shielding, were plated to a thickness of 1 µm as this is significantly greater than the skin depth of gold at infrared wavelengths, which spans from 4.4 nm to 138 nm across the 1 µm to 1000 µm range of wavelengths [43]. For corrosion protection, a 0.5 µm thickness of gold plating is sufficient.

2.2.2 CFRP Strut Assembly

CFRP struts were assembled using a two part epoxy to bond the composite carbon fiber to the stainless steel endcaps. These endcaps are then bolted to the cold structure of the cryostat. Epoxies tend to have a higher CTE under cooling than most materials. To compensate for this higher CTE, glass-filled epoxies such as LOCTITE© STYCAST 2850FT [33] use low thermal contraction ceramic powder as an additive to achieve a lower average thermal contraction [27]. Reducing the differential thermal contraction reduces the stresses in the epoxy helping to prevent cracking and the joint from failing. Through destructive testing, it was found to improve epoxy joint integrity if both the CFRP tube and the stainless endcap were scuffed with sandpaper and thoroughly cleaned. While the use of epoxy to join stainless steel to composites has been shown to be reliable, the addition of pins going through

the CFRP tube and stainless endcaps were included as an additional factor of safety should an epoxy joint fail.

Each epoxy joint has a surface area of 2000 mm^2. Assuming that the expected load of 100 kg would act purely in tension across all 16 of the 45 K struts, the shear stress on the concentric lap joints would be 30.7 kPa. Epoxies are able to achieve a shear strength up to 25 MPa, however with metal aluminum parts, the shear strength tends to fall to around 6 MPa [44]. Using this lower value gives the epoxy joints a factor of safety close to 200. This substantial safety margin takes into account potential variations in load distribution, shock loading, the fact that the struts will experience forces other than tension, and any discrepancies in surface preparation before the epoxy bonding process.

The CFRP struts were epoxy-bonded in batches of eight, with one side of the struts being epoxied at a time. Care was taken during the assembly process to ensure that the ventilation holes in the CFRP tubes were not blocked with epoxy. Figure 2.14 shows the assembly process of the CFRP struts using a jig, as well as showcasing all the fully assembled struts.

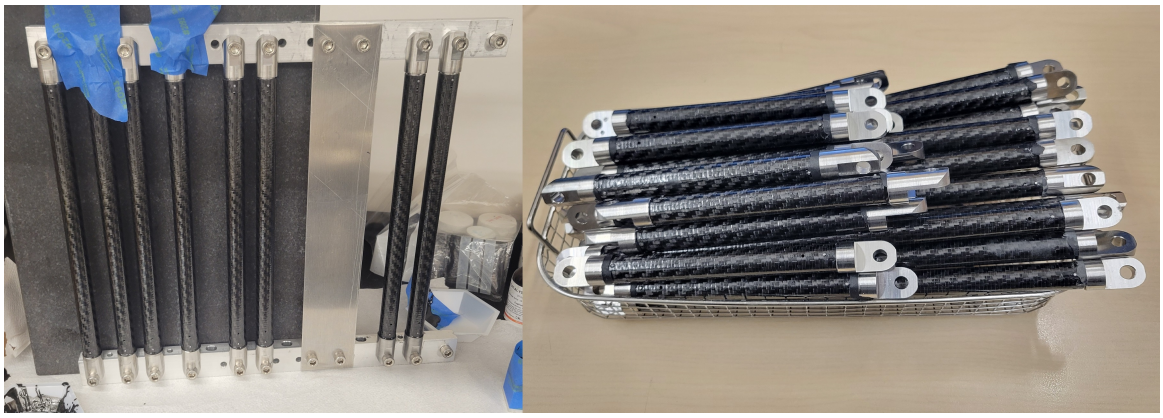

Figure 2.14: Assembly process of CFRP struts. Left: The assembly process using a jig to epoxy-bond eight CFRP struts at a time. Right: All fully assembled CFRP struts.

2.2.3 Cold Structure Assembly

Once the outer framework of the LFC was complete, the cold structure assembly could begin. The cold structure of the cryostat was assembled top down hanging from the top plate of the outer vacuum chamber. A hydraulic lift cart was used to raise sections of the cold stages such that the CFRP struts could be installed. Figure 2.15 shows the process of assembling the cold structure of the LFC.

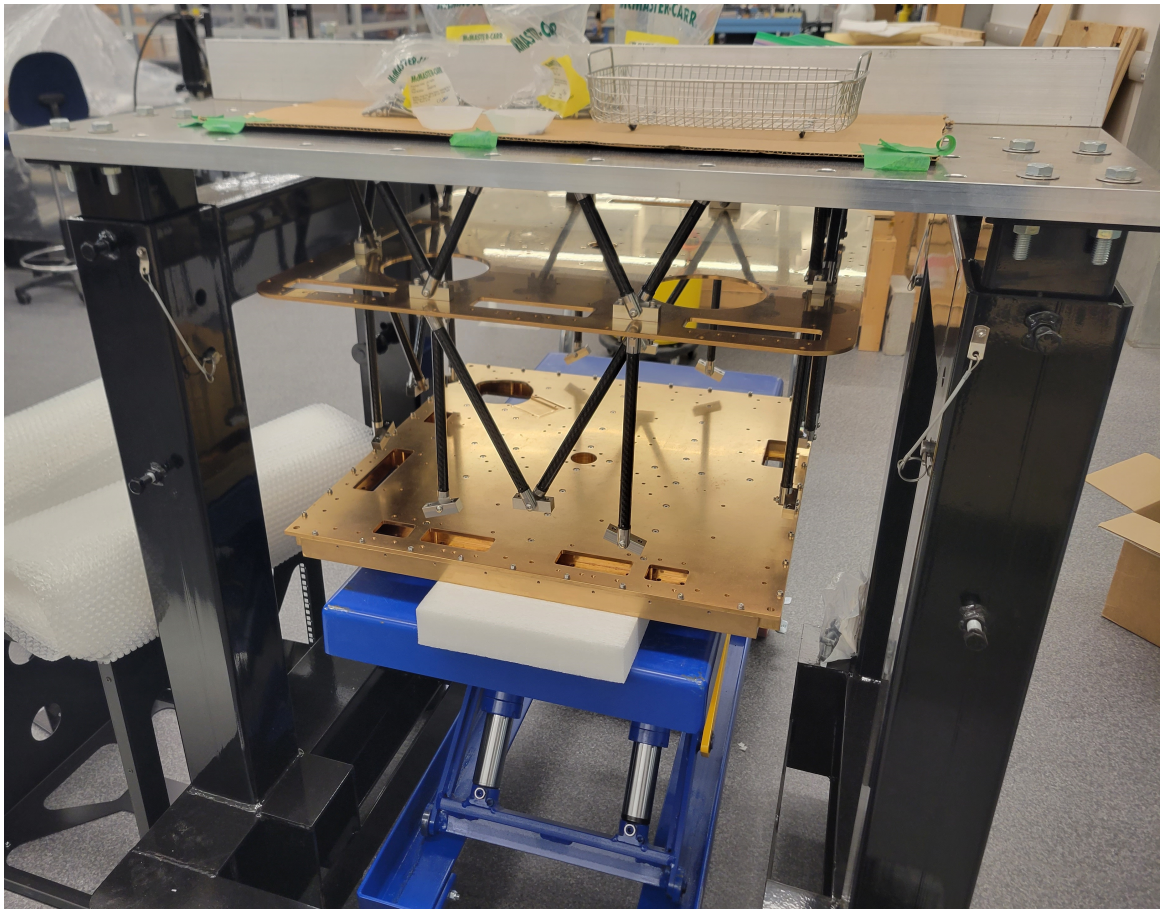

Figure 2.15: Assembly of the LFC cold structure. The 4 K upper cold plate is being raised using a hydraulic lift cart before being mounted to the hanging CFRP struts.

2.2.4 Thermal Braids

PTCs provide the cooling power necessary for the LFC to reach 4 K. Vibrations induced into the cold structure of the cryostat from the pulsing of the PTC refrigeration cycle must be effectively managed. Flexible thermal braids are employed, serving to thermally link the PTCs to the cold structure of the cryostat while mechanically isolating and damping vibra-

tions. These braids are made from thermally conductive material and must strike a balance between conductivity and flexibility to optimize performance. Longer braid cables provide more flexibility but have a negative impact on thermal conductivity while shorter braid cables improve thermal conductivity but will be less flexible and transmit more vibrations into the cryostat.

A comprehensive procedure for manufacturing the thermal braids in house was developed. The thermal braids used in the LFC consist of two copper plates interconnected with flexible copper cables. The plates are bolted to both the cold structure of the cryostat and the PTC cold heads, with the copper cables serving as the thermal link and providing mechanical isolation.

The braid plates were machined in house on a computer numerical control (CNC) mill from $^{3}/_{8}$ in (9.53 mm) copper plate. To accommodate the flexible cabling, two rows of offset holes were drilled into the edge of each plate. The flexible cabling, made from 10 AWG stranded OFHC copper cable, was cut to the desired length. A custom jig allowed the ends of the stranded copper cable to be welded together, preventing fraying during the braid assembly proccess. Once welded, the cable ends were cleaned up and a total of 36 cables were inserted into the holes drilled into the ends of the braid plates. A hydraulic press was used to deform the plate where the cables were inserted in order to create a cold weld connection between the plates and the cable braids. This cold weld ensures the greatest conduction between the cables and the cold plates. Figure 2.16 shows the process of using a hydraulic press to cold weld the flexible braids into the braid plates.

The process of achieving a desirable cold weld has a very fine line between insufficient deformation of the plate, and excessively deforming the plate. If too little pressure is applied to the joint, there will not be optimal conduction as there will be too little deformation to achieve optimal cold welds. If too great of pressure is applied, the joint will deform to the point where the flexible cables will start to be cut at the joint and the braid will have to be scrapped. Manufacturing thermal braids is a time intensive process and damaging a

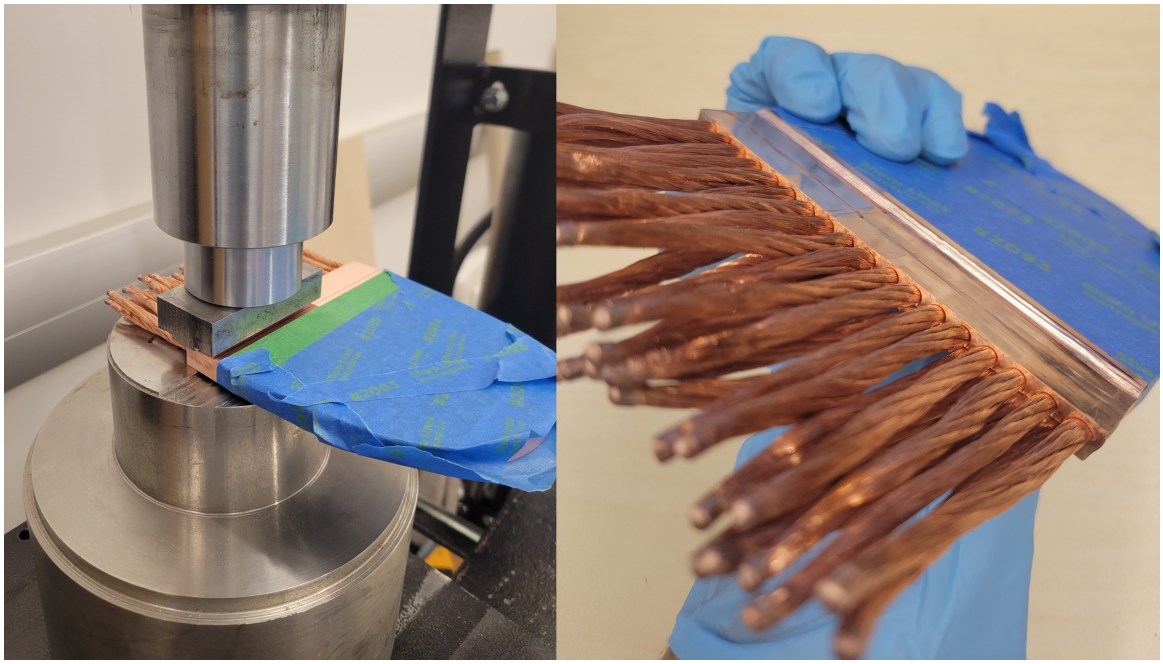

Figure 2.16: Process of manufacturing flexible thermal braids. Flexible copper cables are inserted into the ends of the braid plate. A hydraulic press is used to deform the braid plate and form a cold weld joint with the cables. Left: A hydraulic press is used to form the cold welds between a braid plate and flexible cables. Right: The results of the cold welding process on one end of the thermal braid.

thermal braid during the cold welding step would require a new set of cables to be prepped and welded, and new braid plates to be machined. Luckily, only a single thermal braid had to be scrapped during the construction of the LFC due to the author of this thesis being a bit overzealous with the hydraulic press.

To ensure optimal thermal contact conduction from the PTC to the thermal braid and from the thermal braid to the cold structure through the bolted joints, the cold plates on the braids were polished flat. The thermal braid plates were then gold plated to 2 µm thickness, and the cables were given a cosmetic plating to prevent oxidation. Figure 2.17 shows the 45 K and 4 K thermal braids after they have been pressed and gold plated.

The use of invar washers to compensate for the CTE mismatch between stainless fasteners and copper through holes was already explored in Section 2.1.4. This same concept was applied to the thermal braids. 1 mm thick invar washers were used for all braids to ensure clamping force remains constant, and that thermal contact conductance across the bolted

Figure 2.17: Flexible thermal braids after being pressed and gold plated. Left: 45 K braid. Right: 4 K braid.

joints does not decrease while cooling. As most of the thermal contraction occurs between room temperature and 45 K, the difference in washer thickness needed for the 45 K braids and the 4 K braids was negligible.

2.2.5 Multi-layer Insulation

The largest source of heat transfer within the LFC occurs due to radiation between the OVC held at room temperature, and the 45 K stage. To reduce the radiant loading on the 45 K stage, its aluminum radiation shield was lined with MLI blankets. These MLI blankets were manufactured in house using sheets of aluminized mylar.

MLI are made of many thin, low emissivity (high reflectivity) sheets. When under vacuum, the intermediate layers of an MLI radiation shield would have no contact such that the only mechanism for heat transfer to occur is from the radiation emitted from the low emissivity sheets. Assuming each layer is an infinite plane and all layers have the same emissivity, the heat transfer across the MLI is reduced by a factor of $1/(N+1)$, where N is the number of layers in the radiation shield [39]. This reciprocal relation means that increasing the number of layers in an MLI blanket will reduce the net heat transfer, but with diminishing returns.

The fabrication of MLI often leads to deviations from the ideal insulating properties. Achieving perfect control over the manufacturing and installation of processes of MLI to adhere strictly to the theoretical equation is impractical. Real world applications inevitably involve contact between layers, particularly around the edges where the blankets are secured, leading to conduction occurring within the blanket. Additionally, the geometries an MLI blanket must conform to can vary greatly and are often complex, deviating from the ideal infinite plane. Consequently, the insulating properties of MLI are typically characterized by empirical data as a function of the number of layers and layer density. Layer density impacts how tightly packed the reflective sheets are, thus affecting the contact and conduction between layers, while increasing the number of layers follows the above reciprocal relationship with diminishing returns.

Veenendaal explored the construction of MLI blankets for the TFC [26]. The MLI constructed for the TFC consisted of 8 layer and 12 layer double aluminized mylar blankets. These were deemed adequate for the operation of the TFC. As the LFC has a larger volume, and subsequently a larger area with more radiant energy on the 45 K stage, 20 layer MLI blankets were manufactured.

The MLI blankets for the LFC were constructed from NRC-2 Superinsulation [45], a specialized aluminized mylar specifically made for MLI applications. Templates were created for each blanket and the aluminized mylar was cut to match these templates. To allow

Figure 2.18: MLI blankets before they were installed onto the 45 K radiation shields.

trapped gases to escape when under vacuum, a fine tipped soldering iron was used to melt holes through the individual layers. Additionally, to prevent shifting of the intermediate layers within the blanket, selected points around the edges were melted together using a soldering iron. The edges of the blankets were taped and sealed to minimize the risk of tearing the aluminized mylar during the installation or removal of the radiation shields. Cutouts were made on the upper 45 K blanket to accommodate PTCs, electrical wiring harness, and fiber optic cables to pass through the insulation. Figure 2.18 shows the MLI blankets before they were installed onto the 45 K radiation shields.

2.2.6 Wiring Harness and Optical Fiber Harness

Attention was focused on improving the usability of the wiring harness within the LFC when compared to the TFC. While the wiring harness within the TFC was more than adequate, making changes to accommodate new experiments and troubleshooting electrical

issues posed considerable challenges. Consequently, the design of the wiring harness in the LFC aimed to improve both the flexibility of electrical connections and the accessibility of the wiring harness.

To allow the passage of 200 electrical connections through the OVC, 10 hermetically sealed Amphenol PT Series miniature cylindrical connectors [46] were installed on a custom machined ISO-160 flange. Within the cryostat, the wiring harness branches out to serve subsystems that have different electrical and thermal requirements. These subsystems are split into thermometry channels, 45 K wiring, 4 K wiring, a He-10 sorption fridge, a detector, and heaters. All sections of the wiring harness that extended into the 4 K volume break out into MDM-25 connectors [47]. If more electrical connections are needed at 4 K, two MDM-25 connectors dedicated to thermometry channels in the 4 K volume can be easily repurposed for other experiments. This allows freedom in designing the wiring harness for experiments interconnects with the LFC, and flexibility in placing thermometers. Two additional blank ISO-160 flanges on the top plate of the OVC allow for the existing wiring harness to be expanded in the future, or for a custom wiring harness to be installed with an experiment. The ability to pass multiple optical fibers through the OVC was also required. A KF-40 flange on the top plate was the OVC was dedicated for the use of optical fiber passthroughs. The PDPFTS relies on both 780 nm and 1550 nm optical fibers for use with a photomixer and recording the translation stage position with laser metrology. Details concerning the PDPFTS are discussed further in Chapter 3. Table 2.2 compares the key details of the electrical wiring harness and optical harness between the TFC and the LFC. A wiring diagram showing the complete wiring harness layout for the LFC can be found in Appendix B.

To reduce parasitic conduction through the wiring harness, a method of heat sinking needs to be implemented. This is typically achieved by clamping or varnishing wires to the cold plates of a cryostat. For the LFC, a custom solution was adopted, using tailor made printed circuit boards (PCBs) to act as passthrough at the 45 K stage and into the 4 K vol-

ume. These PCBs incorporate a series of interconnects, which allows the wiring harness to be soldered onto both sides of a PCB, providing continuous electrical connections through the intermediate stages of the LFC. To reduce parasitic heat transfer, these PCBs are heat sunk to the intermediate stages. MDM-25 connectors can also be soldered onto the PCBs to allow flexibility in how experiments integrate with the LFC wiring harness. All of the passthroughs that extend into the 4 K volume break out with MDM-25 connectors such that the thermometry and electrical requirements for any given experiment can be easily met. Figure 2.19 shows one of the PCB passthrough that extends into the 4 K with an MDM-25 connector.

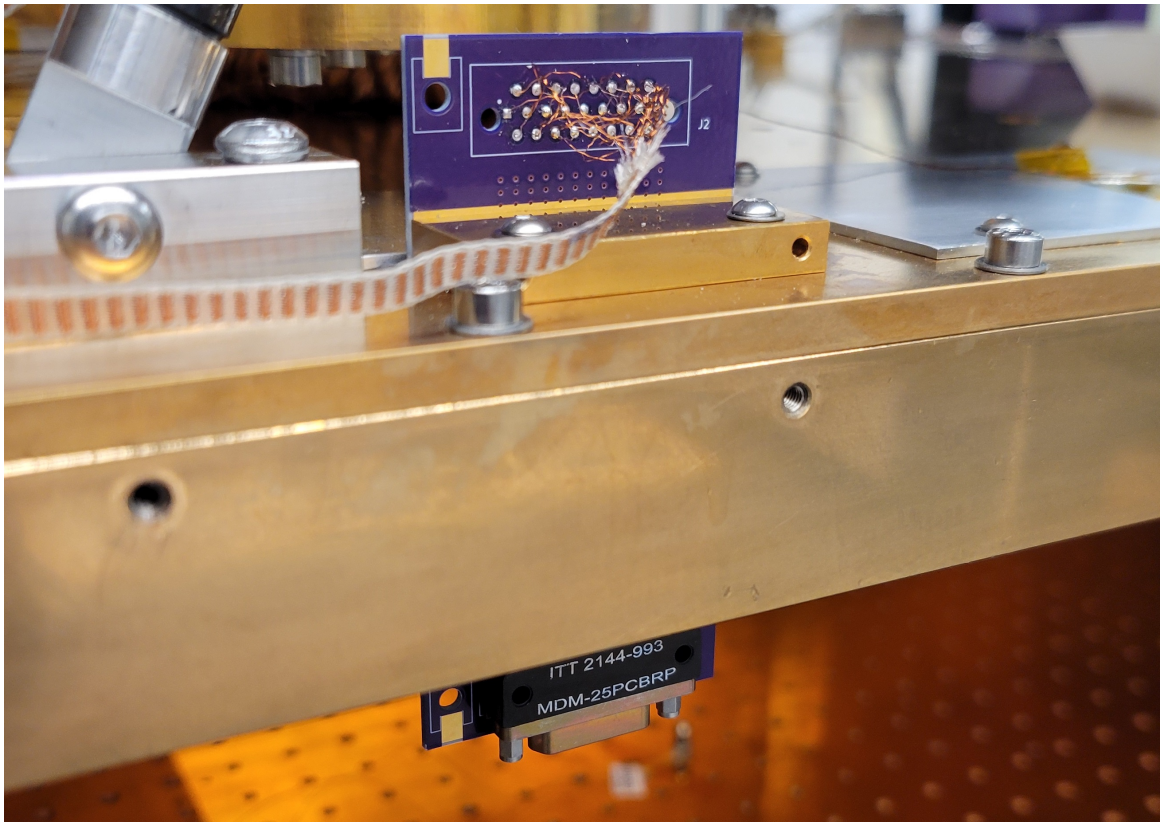

Figure 2.19: 4 K PCB wiring harness passthrough. A 12 twisted pair loom of 39 AWG copper wire is soldered onto one side of a PCB passthrough that extends into the 4 K volume. An MDM-25 connector is soldered onto the side of the PCB that extends into the 4 K volume.

Table 2.2: Comparison of the wiring harness between the TFC and the LFC.

Harness Specification	**TFC**	**LFC**
Thermometry Channels	15	16
Heaters	2×100 W heaters at 45 K 2×100 W heaters at 4 K	2×200 W heaters at 45 K 2×200 W heaters at 4 K
He-10 Sorption Fridge	Dedicated harness	Dedicated harness
Detector	Dedicated harness	Dedicated harness
Spare Electrical Harness	0 MDM-25 at 45 K 2 MDM-25 at 4 K	1 MDM-25 at 45 K 2 MDM-25 at 4 K
Optical Fiber Passthrough	Shared with vacuum manifold	Dedicated KF-40 flange

2.3 LFC Verification

With the construction of the LFC complete, the first step was to run the cryostat through a series of tests to verify that it performed as designed. Vacuum leak testing was performed as well as a series of cool downs to test the integrated subsystems and ancillary instrumentation. The following subsections go over the initial testing and validation of the LFC.

2.3.1 Vacuum Testing

With the cold structure of the LFC assembled, vacuum testing of the OVC was conducted to check for potential leaks. The vacuum chamber was pumped down using an Edwards-XDS35i dry scroll pump rated to achieve an ultimate pressure of 8 mTorr [48]. This phase of testing is essential prior to cooling down a cryostat as it involves understanding the pump down behaviour and creating a typical pump down curve, both crucial for monitoring the health of a vacuum chamber. If during the pump down process, the pressure lags behind the expected pump down rate or fails to reach a similar ultimate vacuum pressure, it indicates that there is a potential leak that must be investigated before proceeding with the cool down.

Before cooling down a cryostat, the vacuum chamber is pumped out to remove air as a mechanism of heat transfer. Leaks in the vacuum chamber of a cryostat pose significant

risks for several reasons. Once cooled down to 4 K, any gas leaking into the cryostat, with the exception of a few trace gases, will condense onto the cold surfaces. A rise in pressure will not be apparent as the gas leaking into the cryostat will condense. This can have an immediate effect of damaging experiments within the cryostat that contain sensitive optics and detectors. An additional concern arises during the warmup process. If enough gas has leaked into the cryostat and condensed unnoticed, there can be a rapid pressure increase during warmup as the condensed gas starts to evaporate. In the event of a sufficiently large leak and the absence of mechanisms to mitigate overpressure, such as an overpressure relief valve or burst disc, the vacuum chamber can rupture.

The OVC of the LFC was pumped down twice to confirm its vacuum integrity. As both pump downs were able to reach the rated base pressure of the vacuum pump, leak testing was not performed. Failure to reach the base pressure would have signalled a potential leak. In such a case, a helium mass spectrometer leak detector would have been employed to search the o-rings and seals of the OVC in order to locate any leaks. A typical pump down curve, shown in Figure 2.20, was generated during the first pump down to use as a reference for future pump downs. The LFC is equipped with two types of vacuum gauges: a convection gauge and an ion gauge. The convection gauge is able to operate at atmospheric pressure but is less accurate at low pressures, while the ion gauge is more accurate but cannot operate at pressures greater than 50 mTorr.

In the pump down curve shown in Figure 2.20, a change in the pump down rate can be seen at the 2 hour mark due to the gas ballast valve being partially closed on the vacuum pump. Air pumped from the OVC can often contain vapours from water, adhesives, solvents, and other volatiles. The gas ballast on a vacuum pump introduces outside air into the pump, limiting its ultimate pressure but inhibiting vapours from condensing inside the pump. Introducing gas ballast at the start of a pump down is key to extending the lifespan of seals within a mechanical vacuum pump. Reducing the gas ballast when it is no longer needed allows the pump to achieve a lower ultimate pressure.

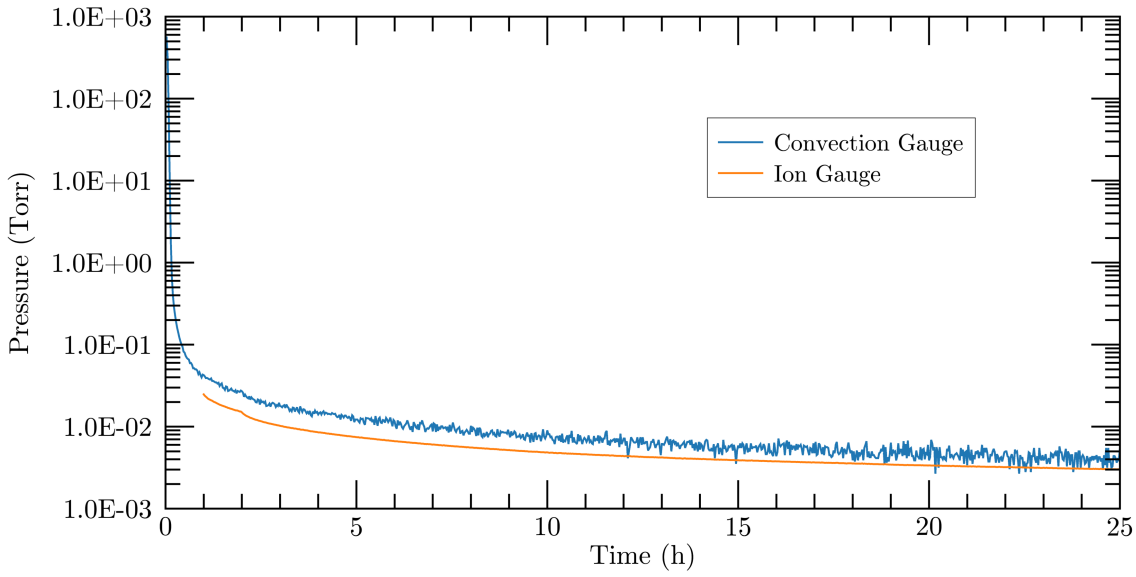

Figure 2.20: Typical vacuum chamber pump down curve for the LFC. A change in pump down rate can be seen at the 2 hour mark as the vacuum pump was switched from Ballast Setting 2 to Ballast Setting 1. The convection gauge pressure readout is shown in blue while the ion gauge pressure readout is shown in orange.

2.3.2 Initial Cool Downs

The first cool down of the LFC operated with a minimal setup; only a single PTC was installed alongside a basic wiring harness focusing on the essential thermometry. During cool down, there were no issues with the vacuum chamber, the wiring harness, or the brand new PTC. Furthermore, the performance of the thermal braids in the LFC matched the similar performance to the TFC and the cool down was faster than the worst case prediction. Due to the care that went into the design and assembly of the LFC, the first cool down was flawless.

Figure 2.21 shows the temperature log that was recorded during the first cool down of the LFC. After 36 hours, the 45 K plate reached a base temperature of 52 K with the 4 K plate reaching a temperature of 4.9 K. The 4 K plate continued to cool until its temperature plateaued at 4.5 K around the 48 hour mark. This first cool down demonstrated that the LFC is able to operate on a single PTC, albeit with a rather long cool down time.

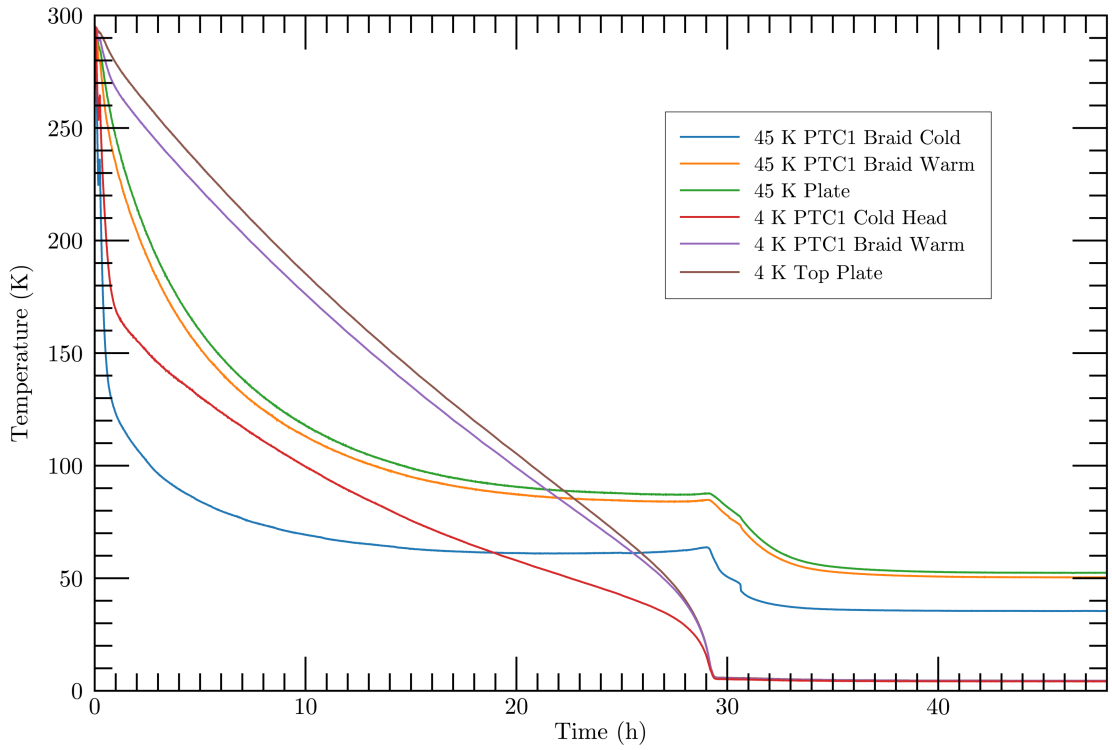

Figure 2.21: The first cool down log for the LFC while operating on a single PTC. The 45 K plate reached a base temperature of 52 K while the upper 4 K plate reached a base temperature of 4.5 K.

Following the successful first cool down, additional subsystems were integrated into the LFC. Between the first and second cool down, the entire wiring harness, the He-10 sorption fridge, and the detector junction field effect transistor (JFET) module were all installed. It is remarkable that in a wiring harness consisting of over 1000 solder joints, only a single failure was experienced. During the second cool down, a single electrical short in the He-10 sorption fridge wiring harness caused a fuse to blow in the He-10 fridge cycle control box. Upon warm up, the short was traced back to a tiny piece of solder that had fallen into an MDM-25 connector and bridged two solder cups on the backside of the connector. Once this electrical short was fixed, there have been no other issues with the LFC.

The next significant milestone for the LFC was its transition into utilizing two PTCs. With the LFC now serving as the primary large volume cryostat for the AIG, a PTC had to be removed from the TFC and transplanted into the LFC. Figure 2.22 shows the fully assembled LFC featuring both PTCs and all ancillary subsystems. This upgrade significantly

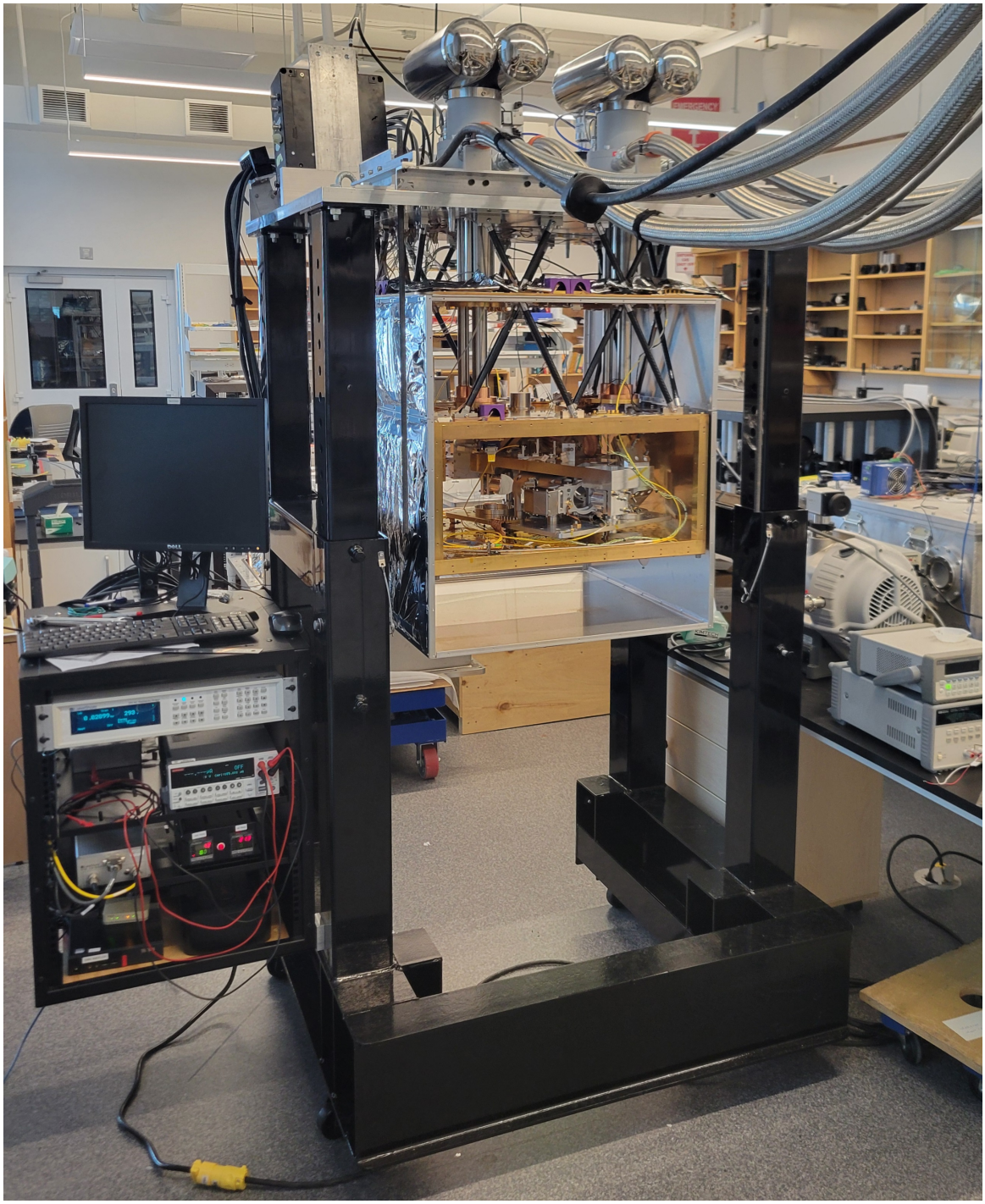

Figure 2.22: The completed LFC featuring two Cryomech PT-415 pulse tube cryocoolers, a 650 mm × 650 mm × 250 mm 4 K volume, and a He-10 sorption fridge providing a small 0.3 K sub-volume.

reduced the cool down time of the LFC, enabling the 4 K volume to reach 4.0 K in under 24 hours, with the majority of this cooling occurring in the first 17 hours. The 45 K plate reached a base temperature of 41.5 K during this time. Figure 2.23 shows the cool down log for the LFC operating with two PTCs. The temperatures of all thermometers matched their expected cool down rates, temperature gradients across the thermal braids matched their typical performance, and there was minimal difference in PTC cold head temperatures.

The performance of the LFC operating with two PTCs has been verified. The successes obtained from the first half-dozen cool downs stand as a testament to the quality of work and care put into the assembly of the LFC. This success is a reflection of the collective expertise, knowledge, and contributions of every member within the AIG.

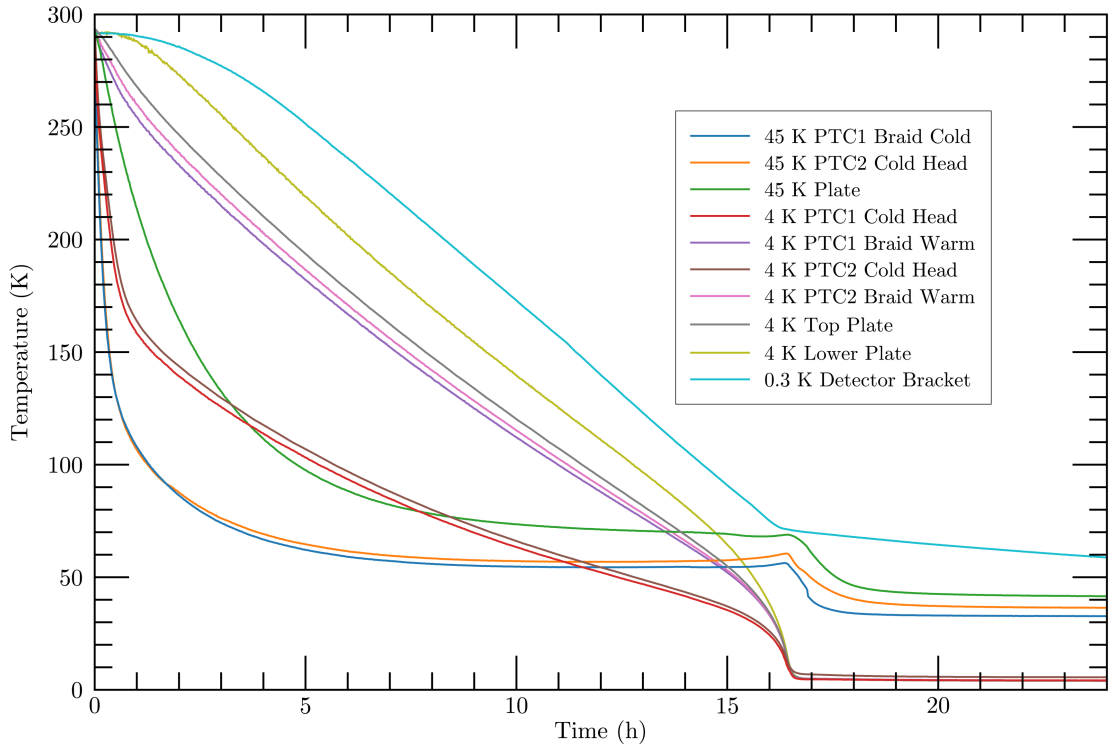

Figure 2.23: The LFC cool down log when operating with both PTCs installed. The 4 K volume reached a temperature of 4.0 K in under 24 hours. The temperature of the 0.3 K detector bracket plateaus around the 16 hour mark as the He-10 sorption fridge cool down cycle had not been started.

2.4 Summary

This chapter covered the design process, assembly, and verification of the LFC. This cryostat was purpose-built for the development of far-infrared astronomical instrumentation. With all subsystems now fully installed in the LFC, efforts swiftly moved towards integrating the PDPFTS into its 4 K volume. Following the positive trend, the sole cool down with the fully integrated PDPFTS proceeded flawlessly. The design of the PDPFTS and the first light results while operating the instrument at 4 K are covered in the following chapters.

Chapter 3

Design of the Post-Dispersed Polarizing FTS

> Optical and near-infrared astronomy has a mature and well-understood landscape in terms of technology development for different platforms. In contrast, far-infrared astronomy has more of the "wild west" about it.
>
> Duncan Farrah

The post-dispersed polarizing Fourier transform spectrometer (PDPFTS) is a hybrid spectrometer designed to operate over the wavelength range of 285 µm to 500 µm (35 cm^{-1} to 20 cm^{-1}), chosen to match available diagnostic test hardware, and consists of four separate modules: a cryogenic source module (4 K), a polarizing Fourier-transform spectrometer (FTS) (4 K) which is split into a Fourier-transform spectrometer optics (FTSO) assembly and a Fourier-transform spectrometer mechanism (FTSM) [49, 50, 51, 52], a reflection diffraction grating (4 K) [53, 54, 55], and a composite bolometer detector (0.3 K) [56, 57]. Figure 3.1 shows a schematic of the PDPFTS featuring the four separate modules. Red arrows in the schematic indicate the direction in which light travels between modules.

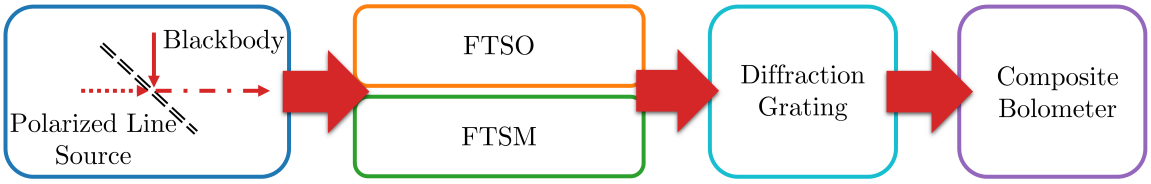

Figure 3.1: A schematic overview of the cryogenic PDPFTS highlighting the four principal modules.

Figure 3.2 shows a computer-aided design (CAD) rendering of the optomechanical layout of the fully integrated PDPFTS; subcomponents use the same colour coding as in Figure 3.1. This layout consists of a source module (blue) featuring a modified flight spare of SCAL [13], the blackbody calibration source of the Spectral and Photometric Imaging REceiver (SPIRE) instrument on the Herschel Space Observatory (Herschel) [58], and a tuneable cryogenic photomixer, capable of producing unresolved spectral features in the THz frequency range. The double-decker polarizing FTS produces an interferogram of the source spectrum and is split into two levels: the upper level consisting of the FTSO (orange) and the lower level consisting of the FTSM (green) [49, 50, 51, 52]. The diffraction grating module (cyan) [53, 54, 55] post-disperses the output from the FTS to produce a narrow band interferogram which is measured by the composite bolometer detector (purple). Figure 3.3 exposes the two arms of the FTS that are hidden by the optics breadboard of the FTSO. The white beam path shows the light that is transmitted through the beamsplitter while the black beam path shows light that is reflected by the beamsplitter.

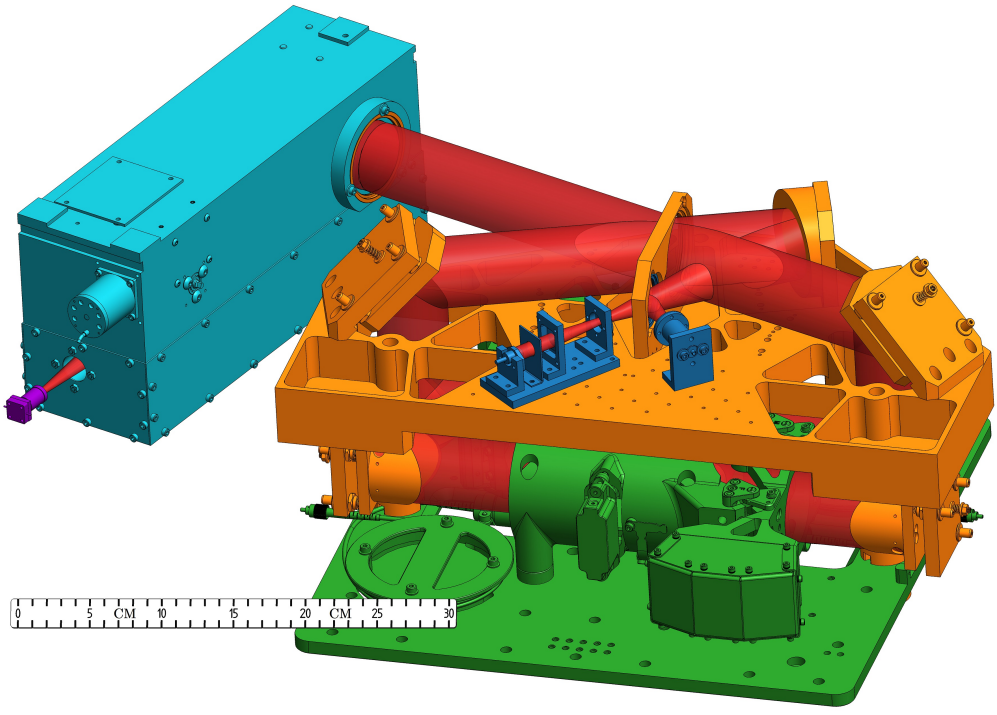

Figure 3.2: CAD rendering of the PDPFTS featuring all four modules of the prototype instrument. The colour coding shown in this rendering match the diagram in Figure 3.1.

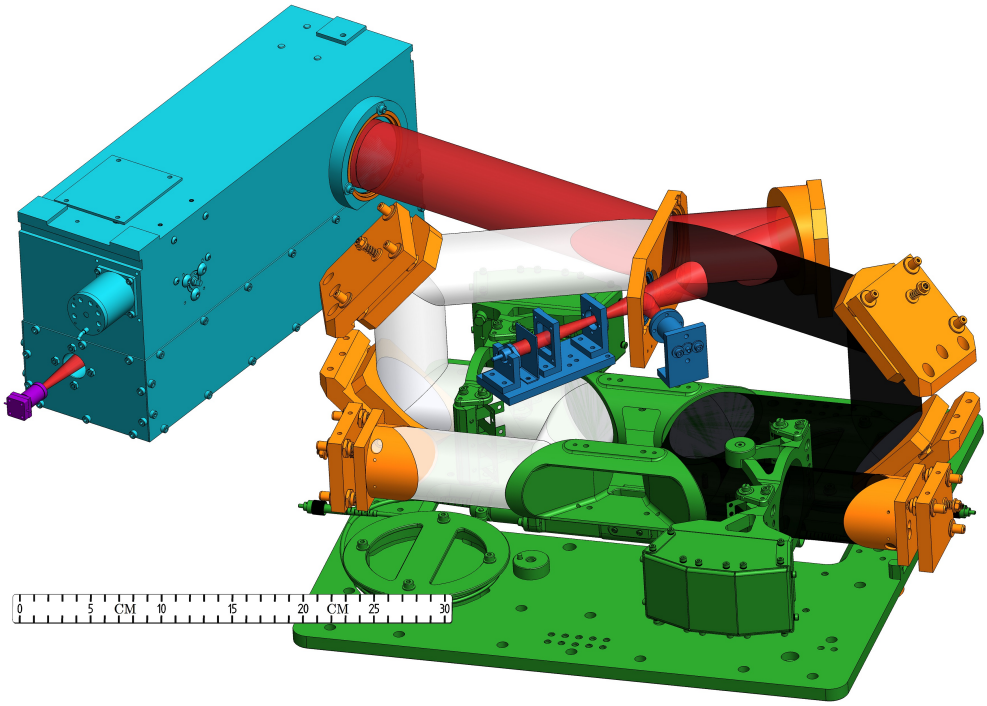

Figure 3.3: CAD rendering of the PDPFTS showing the two arms of the interferometer after the input beam encounters the polarizing beamsplitter. The white beam shows light that is transmitted through the beamsplitter while the black beam shows reflected light.

The use of two levels and fold mirrors results in a compact layout that fits within the volume constraints of the Large Facility Cryostat (LFC). The polarized light generated from the source module is collimated on the upper level of the FTS with the FTSO and is passed down to the scanning mechanism on the lower level through pairs of periscope mirrors. The FTSM scanning mechanism controls the optical path difference (OPD) between the two arms of the interferometer before the light returns along the same path and is recombined on the upper level. To optimally couple the output beam from the polarizing FTS with the grating module, the output analyzer is oriented such that the transverse magnetic (TM) polarization is vertical, in the dispersion direction from the grating. The polarization dependence of the grating is discussed further in Section 3.6. The TM polarized output beam is directed to the grating module where it is post-dispersed onto the detector. This design has an optical multiplier of 8, i.e. for a mechanical displacement of 3.6 cm provided by the FTSM, we achieve an OPD of 28.8 cm. Rooftop mirrors within the FTSO can be repositioned to change the single-sidedness of the scanned interferogram. The FTS

can be configured in a symmetric configuration with both sides of the interferogram having a 14.4 cm OPD around the zero path differnce (ZPD). This would provide the maximal amount of phase information at the cost of resolution. Reconfiguring the FTSO for higher resolution with a more single sided interferogram can achieve an OPD of $+21.2$ cm to -7.6 cm. Table 3.1 summarizes the design specifications of the PDPFTS. The manufacturing part drawings for the PDPFTS can be found in Appendix C.

The linear polarizers used within the PDPFTS are the first-of-their-kind and were manufactured by QMC Instruments [59]. The polarizers feature a 2 µm period (1 µm spacing) wire grid, deposited onto a thin polymer substrate through a standard mask process. QMC Instruments has developed a process enabling matching wire grids to be precisely aligned and deposited on both sides of the polarizer substrate. This design ensures that when one of the polarizers is used as a beamsplitter in the PDPFTS, the phase remains balanced in both arms of the FTS as the light in each arm travels through the polarizer substrate once. This contrasts with traditional linear polarizers, where the wire grid is deposited on only one side of the substrate. In such cases, the light in one arm of the FTS passes through the substrate once, while the light in the opposite arm passes through the substrate three times, introducing phase errors.

Table 3.1: Cryogenic PDPFTS specifications.

Parameter	**Value**
Mechanical displacement	3.6 cm
Reconfigurable OPD	$+14.4$ cm to -14.4 cm
	$+17.8$ cm to -11.0 cm
	$+21.2$ cm to -7.6 cm
Aperture	50 mm
Entrance slit width, w	2.1 mm
Exit slit width, w''	4.0 mm
Entrance focal length, r	163.34 mm
Exit focal length, r'	310.08 mm
Number of mirrors	15
Adjustable degrees of freedom	18
Power dissipation at 4 K	< 1.5 mW

3.1 Source Module

The PDPFTS source module is comprised of a blackbody broad band emission source (continuum) and an unresolved line source (spectral feature). To generate realistic astronomical spectra and demonstrate the performance of the PDPFTS, a spectral feature needs to be superimposed onto a continuum. This is achieved by exploiting the polarization encoding properties of a Martin-Puplett interferometer. When the line source is placed on the same side of the linear input polarizer as the blackbody, both sources will have the same polarization, resulting in an emission feature being superimposed onto a continuum. If the line source is placed on the opposite side of the linear input polarizer, the two sources will have opposite polarizations, resulting in an absorption feature being superimposed onto a continuum. This novel polarization encoding source module was conceptualized by Naylor and its operation at room temperature was initially explored by Huber [60]. I worked on the design of the cryogenic source module that would be integrated into the PDPFTS.

The continuum source for the PDPFTS uses a blackbody element from the flight spare of SCAL, the blackbody calibration source for Herschel SPIRE [58]. A blackbody element was rewired and enclosed in a custom baffle, the inside surfaces of which were coated with black LOCTITE© STYCAST 2850FT epoxy [33] and sprinkled with carborundum particles to reduce stray reflections. An entrance slit is placed on the open end of the baffle, which sits at the focus of the PDPFTS entrance optics. Figure 3.4 shows the flight spare of SCAL and the custom baffle designed to enclose one of the blackbody elements for use in the PDPFTS source module.

The blackbody elements used in SCAL are equipped with a calibrated Cernox® CX-1030-SD thermometer [61] and a Vishay® precision P0603 500 Ω ±0.01 % resistor [62] as a heater to allow precise temperature control of the blackbody. From Planck's law,

$$B(\nu, T) = \frac{2h\nu^3}{c^2} \frac{1}{\frac{h\nu}{\exp(k_B T)} - 1}, \qquad [\mathrm{W\,m^{-2}\,Hz^{-1}\,sr^{-1}}] \quad (3.1)$$

where ν is the frequency of the electromagnetic spectrum that is being radiated, h is the Planck constant, c is the speed of light, and k_B is the Boltzmann constant, as the temperature

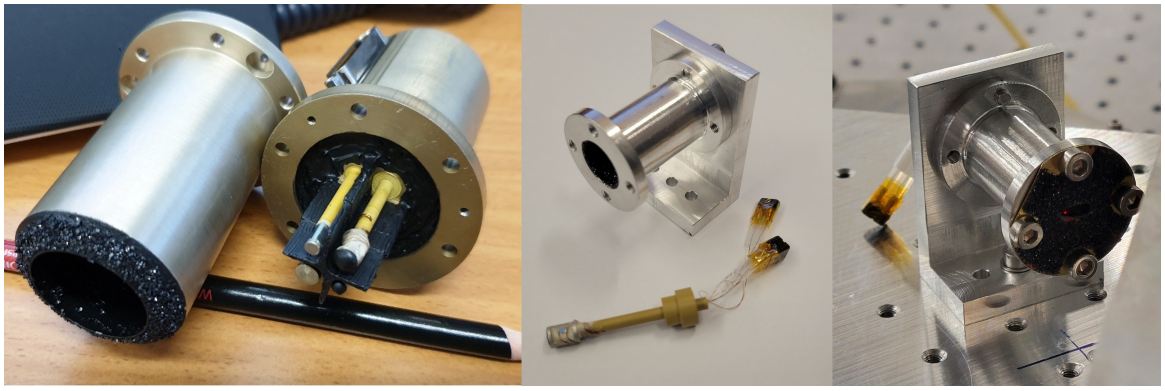

Figure 3.4: The blackbody source module for the PDPFTS. Left: The flight space of SCAL, the blackbody calibration source for Herschel [58]. Middle: The custom baffle and a blackbody element from SCAL. Right: The blackbody source as installed in the PDPFTS.

T increases, so does the spectral radiance of the body, B. By controlling the temperature of the blackbody in the PDPFTS source module, a variable continuum following Planck's law can be generated.

To generate spectral line features, a cryogenic THz photomixer was used. This photomixer employs two optical fiber coupled 780 nm continuous-wave laser diodes [63] and a semiconductor possessing a band gap smaller than the energy of 780 nm photons. The frequencies of the two lasers are tuned such that their difference, or beat frequency, falls within the THz regime. If a bias voltage is applied, when the light from these lasers is incident on the semiconductor, an alternating photocurrent is induced with the beat frequency of the lasers. By coupling the semiconductor to an antenna, free-space THz radiation is emitted [64].

For the PDPFTS, we present only the TM polarization mode to the diffraction grating module. A photomixer with a bow tie antenna that emits linearly polarized light would allow for optimal coupling and high efficiency. Unfortunately, there are no cryogenically rated photomixers with bow tie antennas. Consequently, we opted for a Bakman™ Technologies B1319 GaAs photomixer with a log-spiral antenna, due to their proven reliability operating at 4.5 K [65]. The output from our photomixer is approximately collimated and emits elliptically polarized light with the orientation of the semi-major axis varying with

wavelength.This characteristic would pose challenges to calibrations as the amplitude of the TM polarization component presented to the grating will change with wavelength, but is unimportant for the verification of the PDPFTS in this thesis as we do not need to know the line source intensity.

To couple the collimated beam from the photomixer to the FTSO, a custom made TOPAS® cyclic olefin copolymer (COC) biconvex lens focuses the output from the photomixer through an entrance slit before being collimated by the input off-axis parabolic (OAP) mirror. To magnify the output of the photomixer to match the 50 mm beam in the PDPFTS, the biconex lens should have an effective focal length (EFL) of 32.67 mm. Table 3.2 outlines the lens prescription.

Attempts were made to 3D print the lens using TOPAS® filament. While successful, the facet lines due to the process of fused deposition modeling (FDM) 3D printing were found to be unacceptable. A casting process using TOPAS® 5013S-04 COC [66] was instead developed by Brad Gom to produce a lens with more clarity. A two part negative mold of the lens was fabricated using a computer numerical control (CNC) milling machine. The mold was filled with TOPAS® pellets and was placed into a 525 K vacuum oven. Melting the pellets under vacuum allowed any trapped gasses to be evacuated, producing a clear and defect free lens. Figure 3.5 shows the custom made TOPAS® COC biconvex lens using the casting process.

Table 3.2: Custom made TOPAS® COC biconvex lens prescription. The image space and object space indices of refraction were set to unity as the lens will be operating in vacuum.

Parameter	**Value**
Radius of surface 1, R_1	34.1 mm
Radius of surface 2, R_2	-34.1 mm
Center thickness, CT	3 mm
Lens index of refraction, η	1.5258(2) [67]
EFL	32.67 mm

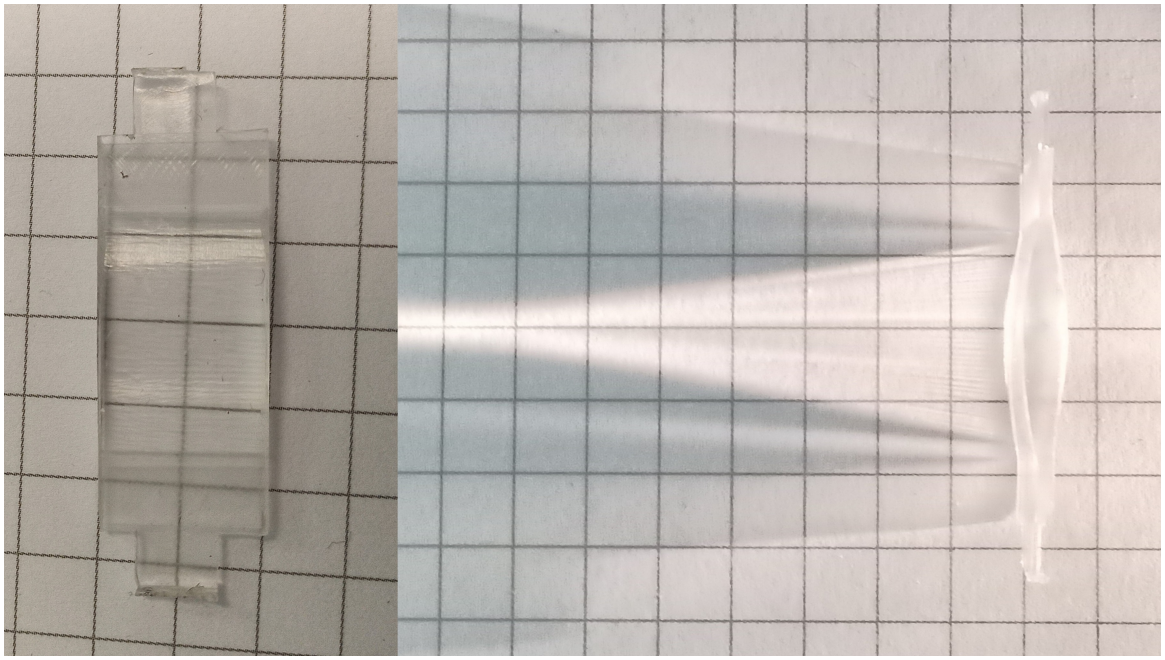

Figure 3.5: Custom made TOPAS® COC biconvex lens.

The line source assembly consists of the cryogenic photomixer, followed by a 12 mm aperture, the custom made biconvex lens, and the entrance slit. The flat surfaces of the aperture and entrance slit were coated with black LOCTITE© STYCAST 2850FT epoxy [33] and carborundum particles to reduce stray reflections. These four components were mounted onto a plate and aligned with the FTSO. Figure 3.6 shows the line source assembly.

When installed on the PDPFTS for cryogenic testing, the blackbody and photomixer line sources were configured to superimpose an absorption feature onto a continuum. Figure 3.7 shows the source module installed on the upper level of the FTS. The output from the blackbody is reflected off of the input polarizer towards the input OAP mirror while the output from the photomixer is transmitted through the input polarizer towards the input OAP mirror.

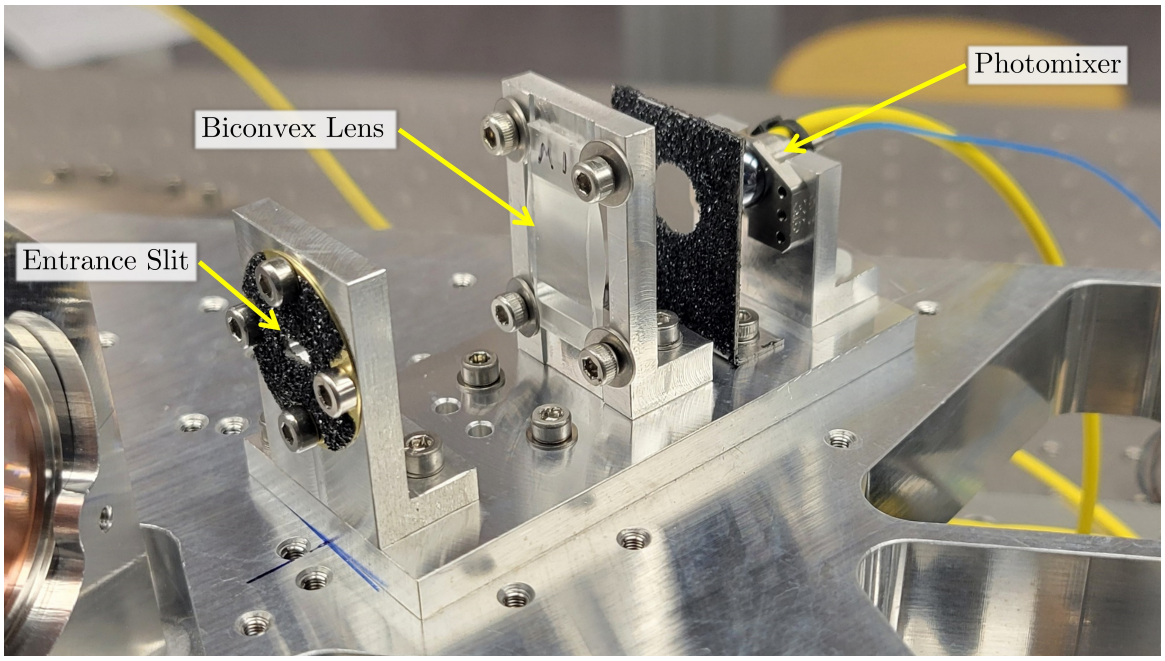

Figure 3.6: The line source module for the PDPFTS. A tuneable cryogenic photomixer generates an unresolved line feature. A custom made biconvex Topas lens focuses the output from the photomixer onto the entrance slit of the system.

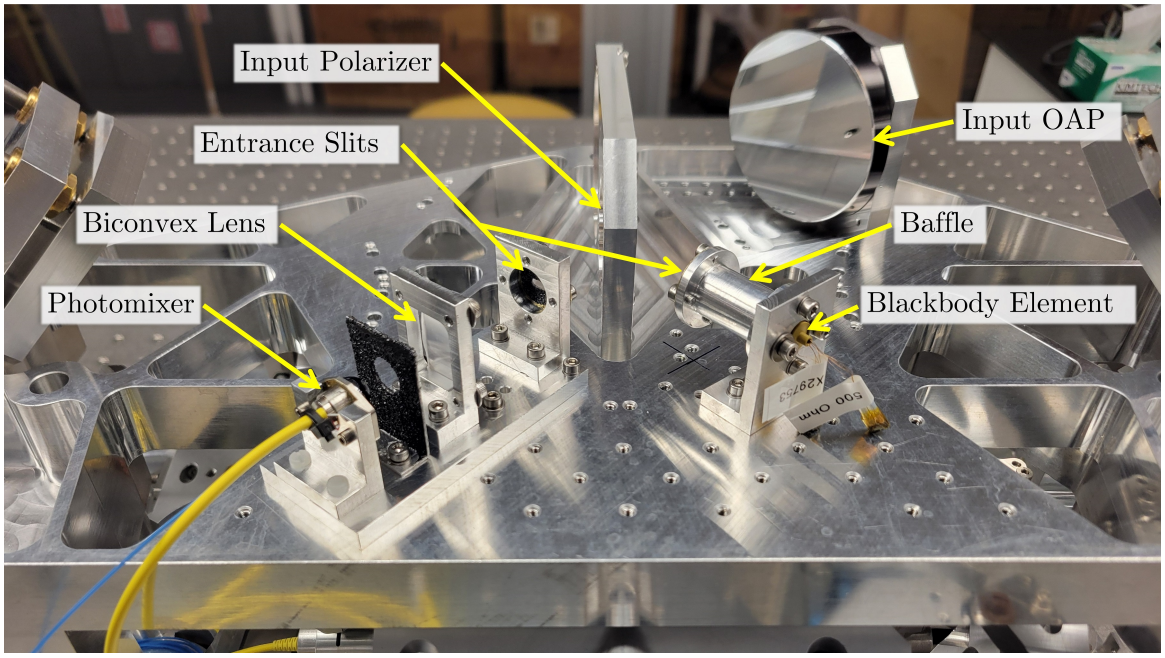

Figure 3.7: The PDPFTS source module consisting of a blackbody and an unresolved line source. The continuum produced by the blackbody is reflected off the input polarizer while the line feature produced by the photomixer is transmitted through the input polarizer. This configuration superimposes an absorption feature onto the continuum.

3.2 FTS Mechanism

The Measurements & Analytics Division of ABB has developed a novel stiffness compensated reactionless scan mechanism intended for a cryogenic far-infrared PDPFTS. The Fourier-transform spectrometer mechanism (FTSM) engineering development unit (EDU) demonstrates the technology readiness level (TRL) 5 requirements for a cryogenic scanning mirror mechanism intended for the SpicA FAR-infrared Instrument (SAFARI). This instrument would have been employed on the SPace Infrared telescope for Cosmology and Astrophysics (SPICA) M5 mission [18]. In October 2020, the European Space Agency (ESA) made the decision to remove SPICA from consideration as a candidate for the M5 mission [19]. Despite this late cancellation, a few months before the final mission selection review, the development and testing of the FTSM continued. The FTSM achieved a total stroke greater than 3.5 cm while dissipating less than 1.5 mW of power at 4 K. Figure 3.8 shows the FTSM EDU installed in the Test Facility Cryostat (TFC) during part of its cryogenic test campaign. Publications from Cournoyer et al. present the results of the development and cryogenic testing of the FTSM EDU [49, 50, 51, 52].

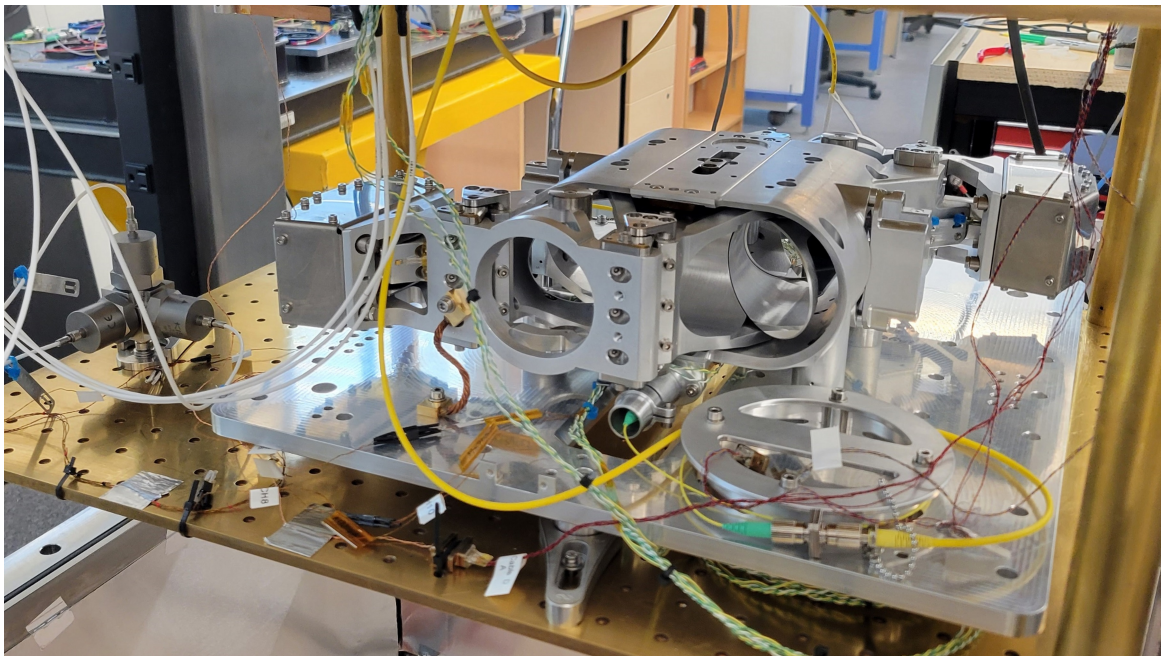

Figure 3.8: The ABB FTSM EDU installed in the TFC as a TRL-5 demonstration of a cryogenic scanning mirror mechanism. [49, 50, 51, 52].

I integrated the FTSM EDU as the scanning mechanism into the design of the cryogenic PDPFTS. Subsequent chapters will discuss the design of an optical breadboard and the additional optics necessary for integrating the FTSO around the FTSM.

3.3 FTS Optical Breadboard

The FTSO assembly consists of an optical breadboard onto which the source module and all auxiliary FTS optics can be mounted. Once the blackbody source, photomixer line source, input polarizer, polarizing beamsplitter, and mirrors are mounted onto this optical breadboard, the FTSO functions as a single unit. This assembly is then integrated with the ABB FTSM to form the PDPFTS source module and polarizing FTS module.

I designed the optical breadboard and auxiliary optics around the double-decker FTS concept, optimizing the use of the 4 K volume within the LFC. The mirrors and optics of the FTS are mounted on both sides of the breadboard before it is lowered onto the scanning mirror mechanism. The stiffness of the breadboard was optimized while minimizing its mass, decreasing the cool down time of the optics while ensuring alignment stability, particularly crucial due to the eight times multiplier effect on optical alignment tolerances resulting from folded optics in the PDPFTS.

During the design phase, finite element analysis (FEA) simulations were performed using Ansys Mechanical™ to analyze the deformation of the breadboard under load and study its vibration modes. The final iteration of the breadboard adopted a triangular honeycomb structure. Figure 3.10 shows the maximum deformation of the breadboard of 1.5 µm under standard Earth gravity, while Figure 3.9 shows the results of the modal analysis with the fundamental vibration mode occurring at ~ 430 Hz. While not visible in these renderings, all auxiliary optics that form the FTSO are present in the simulations but hidden from view to highlight the results affecting the breadboard only. It is important to note that the magnitude of deformation between the static structural simulation and the modal analysis should not be compared. The modal analysis computes the frequency modes and shape, but the magnitude of deformation has no physical meaning as no load is applied.

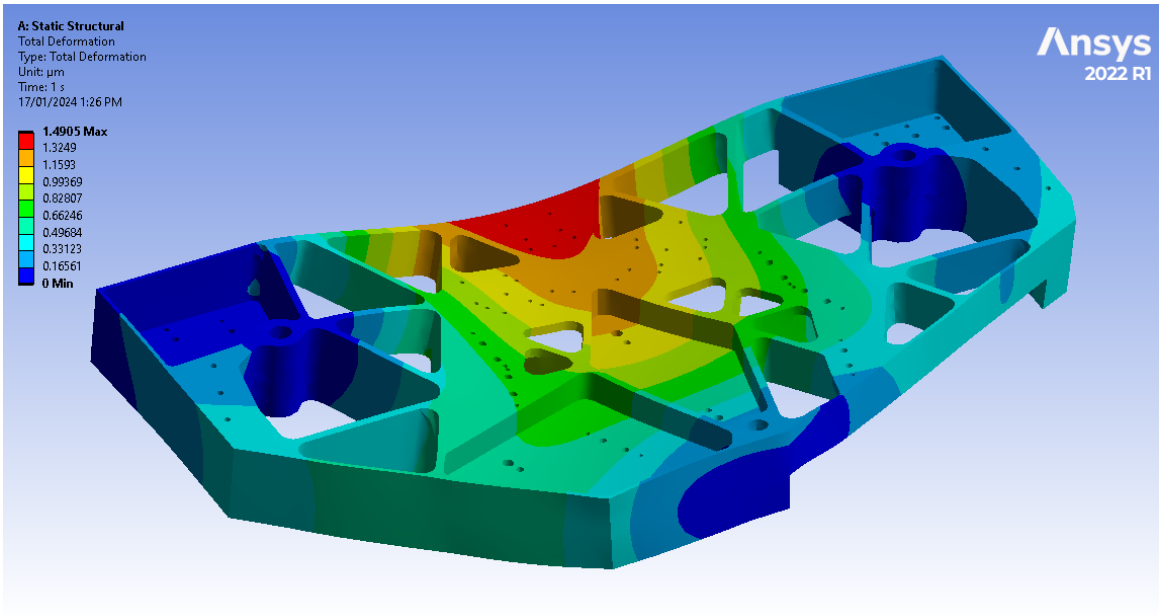

Figure 3.9: Deformation of the PDPFTS breadboard due to standard Earth gravity. All auxiliary optics mounted to the breadboard are included in the simulation but hidden from view for clarity.

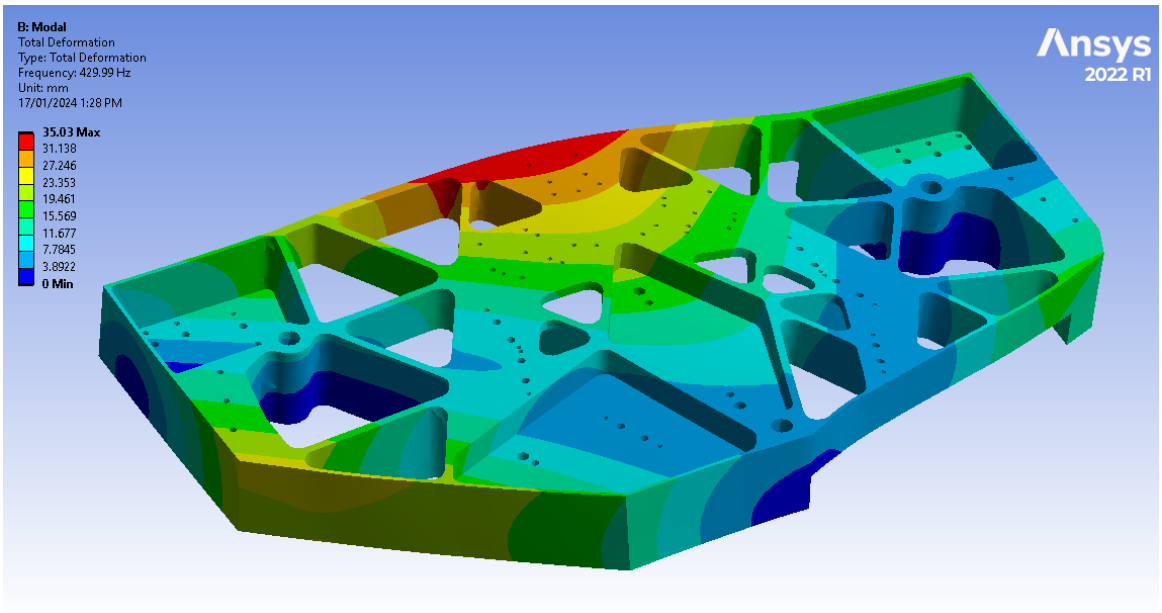

Figure 3.10: Modal analysis of the PDPFTS breadboard. The fundamental vibration mode occurs around 430 Hz. All auxiliary optics mounted to the breadboard are included in the simulation but hidden from view for clarity.

3.4 FTS Mirrors

The PDPFTS mirrors were manufactured by B-Con Engineering [68]. The PDPFTS mirrors were diamond turned to an optical quality surface finish to aid in alignment using a 632.8 nm HeNe laser and a 1550 nm infrared laser as discussed in the following section. An overall mirror flatness of $\lambda/10$ is sufficient for an interferometric system with a single reflecting surface, however, as each arm of the FTS has 10 reflections due to the folded optics, the constraint on surface roughness for any individual mirror would increase by a factor of $\sqrt{10}$. The reported root mean square (RMS) surface roughness for the mirrors ranged from 87 nm to 150 nm. Figure 3.11 shows a two part rooftop and a fold mirror used in the FTSO.

The dihedral angles on the initial batch of the two part rooftop mirrors received from B-Con were out of specification. Both rooftop dihedral angles were open (i.e. dehidral angle $> 90°$). To measure the dihedral angle in our lab, the inexpensive technique based on autocollimation outlined by Naylor and Schultz [69] was used. A telescope with a 500 mm

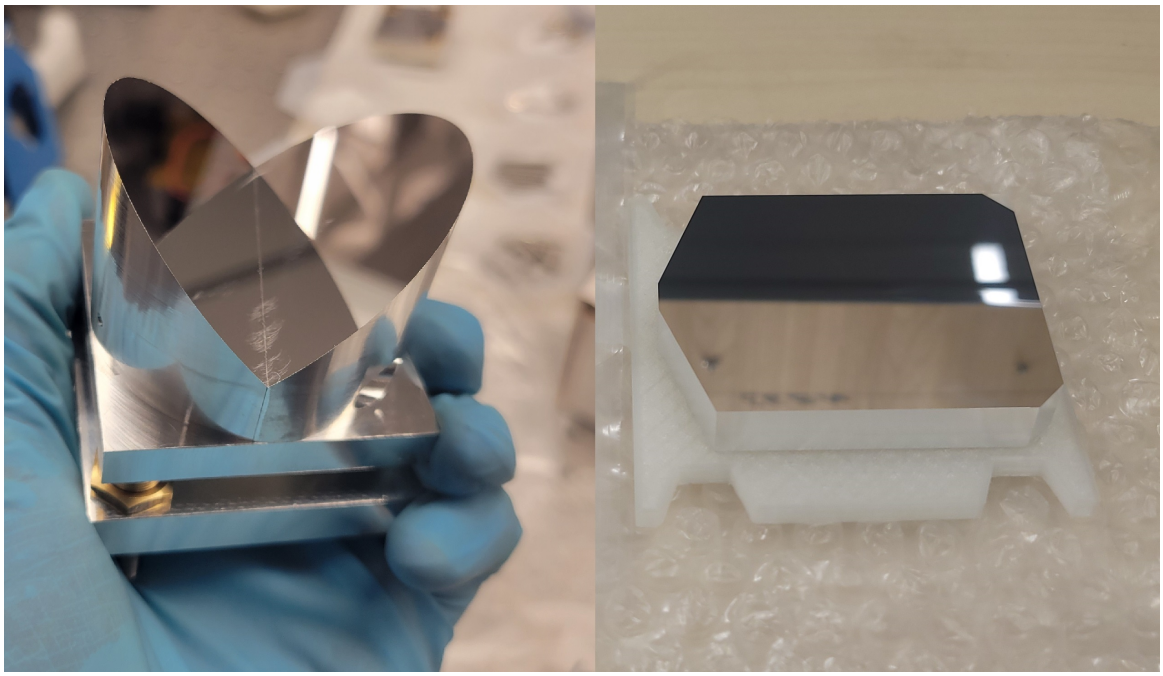

Figure 3.11: The mirrors used in the FTSO. Left: A two part rooftop mirror. Right: A fold mirror used in the sets of periscope mirrors.

focal length was used in conjunction with a 12 mm double crosshair reticule eyepiece. The double crosshair reticule had a 0.2 mm spacing with a line width of 20 µm. When the crosshairs are aligned with the roof line of the mirror, the separation X of the two images of the crosshair will occur in one axis only and is given by $X = 4\delta$, where δ is the deviation of the dihedral angle from 90°. Figure 3.12 shows the telescope setup used to measure the rooftop deviation angle.

Rooftop serial number pair 3, 4 was measured as having a dihedral angle of $90° + 8.36'$. Rooftop serial number pair 5, 6 was measured as having a dihedral angle of $90° + 7.24'$. As the folded optics in the PDPFTS provide an eight times multiplier to the optical path, the dihedral deviation angle needed to be less than one arc minute. These values were unacceptable and the mirrors were sent back to B-Con for repair. After repair, the deviation angle on rooftop pair 3, 4 measured $7.8''$ and rooftop pair 5, 6 measured $12''$, falling well below one arc minute. Figures 3.13 and 3.14 show pictures taken looking through the telescope before and after correction. Red arrows mark the separation X of the two images of the crosshair due to the dihedral deviation angle. After correction, the two images of the crosshair appear to overlap as the dihedral deviation angle is on the order of arcseconds.

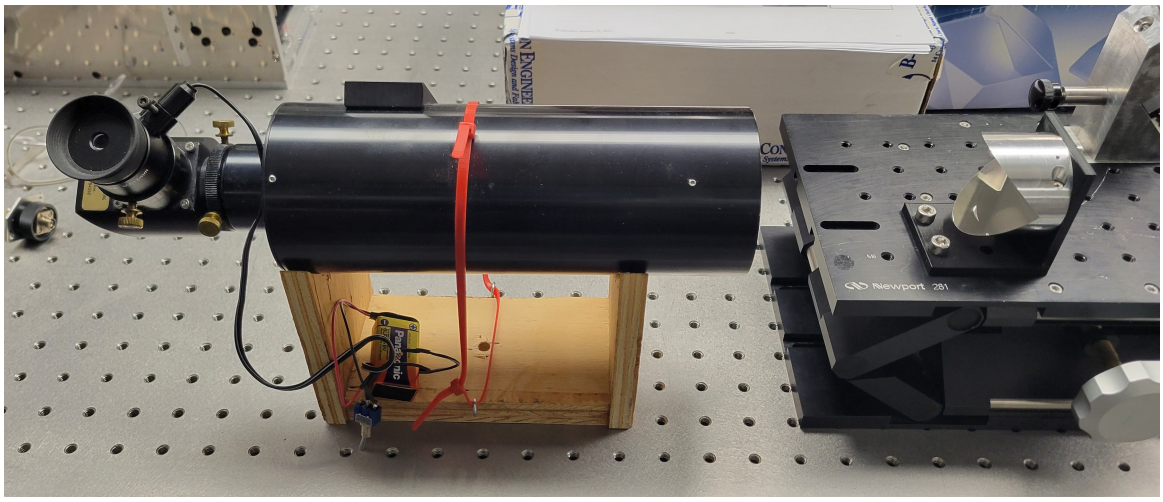

Figure 3.12: Experimental setup used to measure the rooftop mirror dihedral deviation angle. A 500 mm focal length telescope is used with a 12 mm eyepiec. The eyepiece features a double crosshair reticules that has a 0.2 mm spacing and a line width of 20 µm.

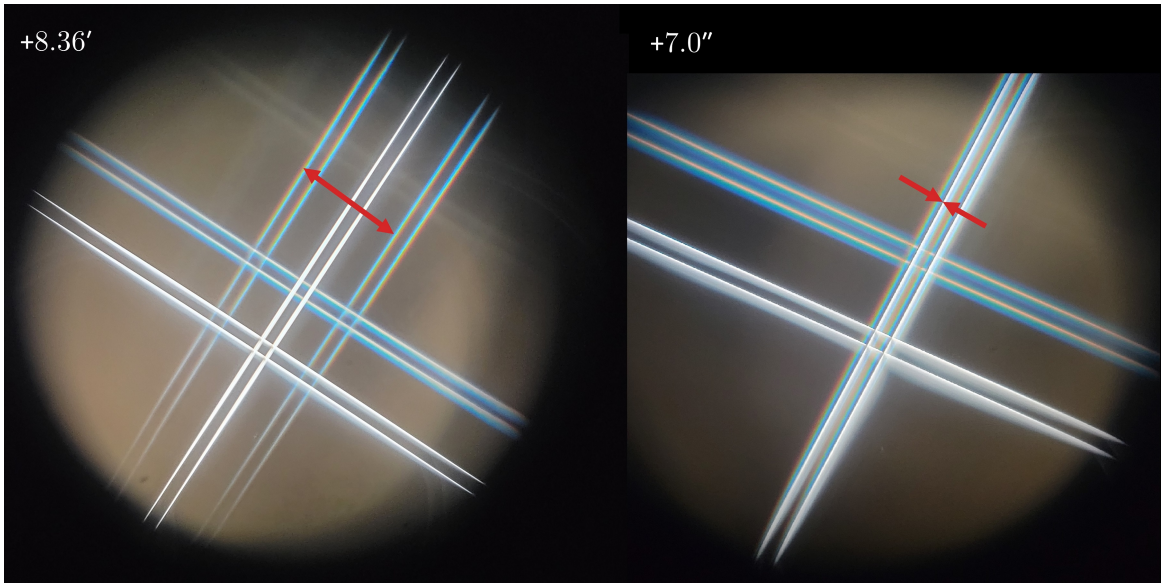

Figure 3.13: Measured dihedral angle deviation of rooftop mirror pair $3,4$ before and after correction. Left: Pre-correction dihedral deviation angle of $8.36'$. Right: Post-correction dihedral deviation angle of $7.0''$.

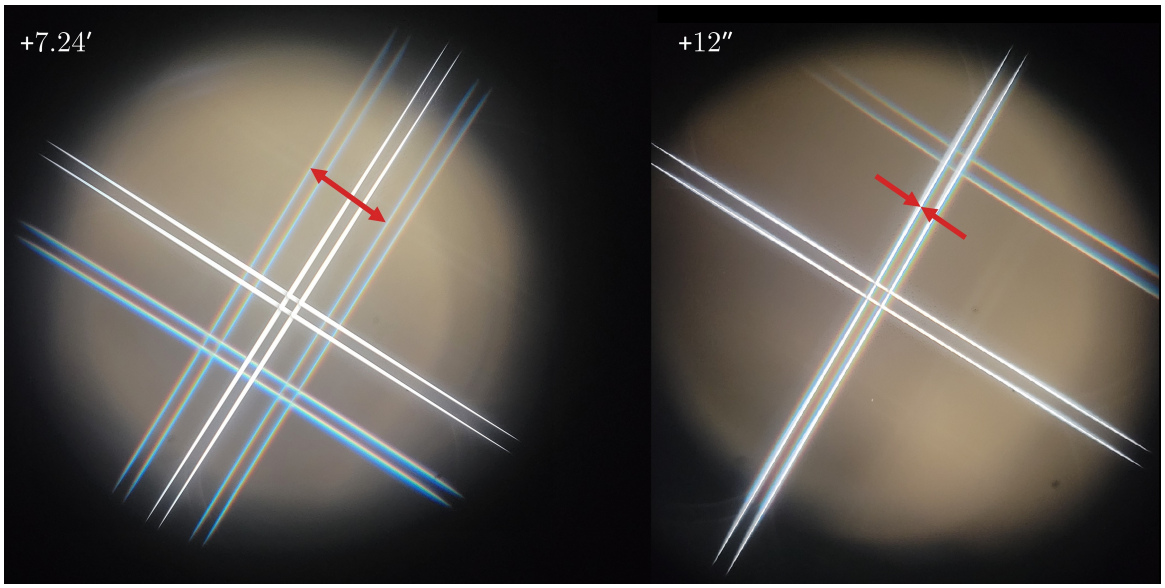

Figure 3.14: Measured dihedral angle deviation of rooftop mirror pair$5,6$ before and after correction. Left: Pre-correction dihedral deviation angle of $7.24'$. Right: Post-correction dihedral deviation angle of $12''$.

3.5 FTS Mirror Alignment

Three point adjustable mounts were designed to integrate the mirrors discussed in Section 3.4 into the FTSO. Adjustment screws with a thread pitch of 254 TPI were sourced from Newport [70] to provide the fold mirrors with $1.1''$ of adjustment per 1° of screw rotation and the rooftop mirrors with $1.4''$ of adjustment per 1° of screw rotation. The use of three adjustment screws per mount allows for the control of tip, tilt, and parallel translation of each mirror. Control over parallel translation was particularly critical for the periscope mirrors, ensuring alignment of the lower level beams of the FTS with the optical axis.

I performed the alignment of the FTS in two steps. The first step involved the alignment of the FTSO before integrating with the FTSM. Without the FTSM in place, a ring laser setup was used to align the periscope mirrors to ensure that the beam would remain on axis as it was passed from the upper level of the FTS to the lower level. Alignment targets

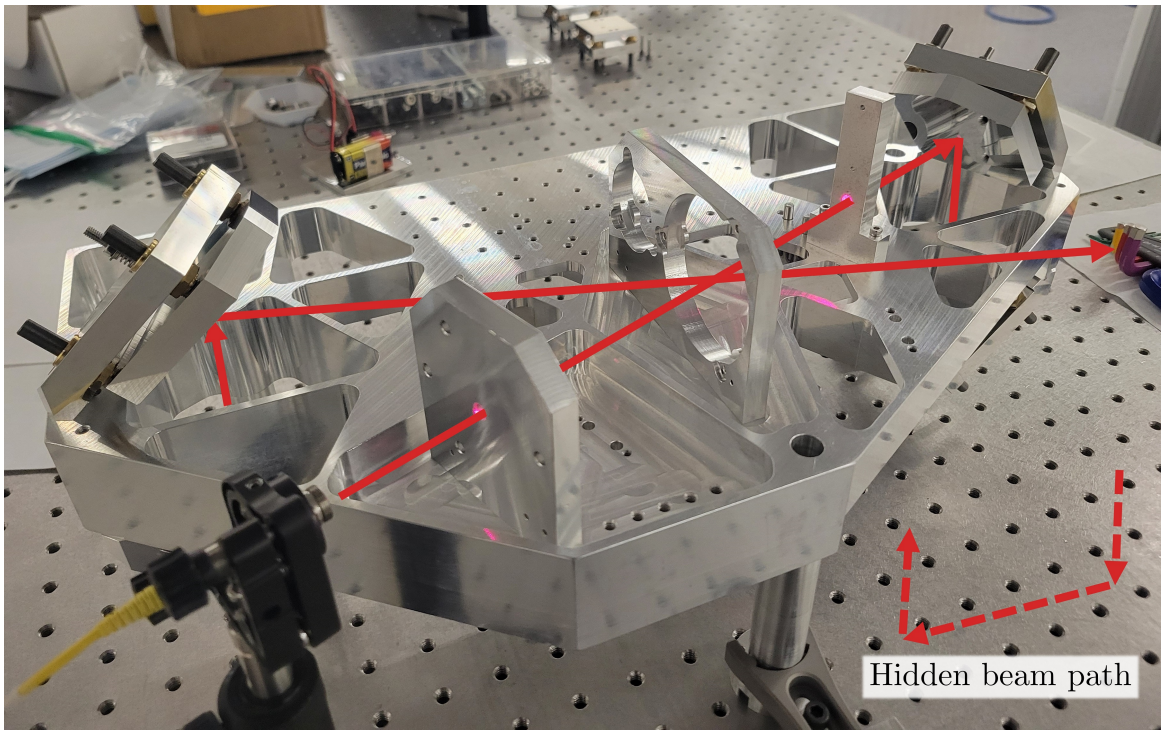

Figure 3.15: Alignment of the PDPFTS using a visible wavelength laser and alignment targets. The collimated output from the laser is fed through the optical axis of the FTSO. By placing alignment targets at set points, the mirror mounts can be adjusted such that the beam stays on axis throughout the instrument.

were placed at various points within the ring laser setup and adjustments were made to each mirror mount to keep the collimated laser beam on axis. Figure 3.15 shows the ring laser setup. The laser beam can be seen passing through the OAP mirror mount along the optical axis and through an alignment target on the upper level. Two sets of periscope mirrors pass the beam between the upper and lower levels.

The optical laser was then replaced with a 1550 nm Eblana laser [71] and a beamsplitter was installed in its mount. By placing a NIT short-wavelength infrared (SWIR) InGaAs camera [72] at the output of the ring laser setup, the alignment of the FTSO can be verified with 1550 nm spatial fringes. Figure 3.16 compares intentional misalignment of the FTSO to produce 1550 nm fringes with the aligned optics showing no fringes.

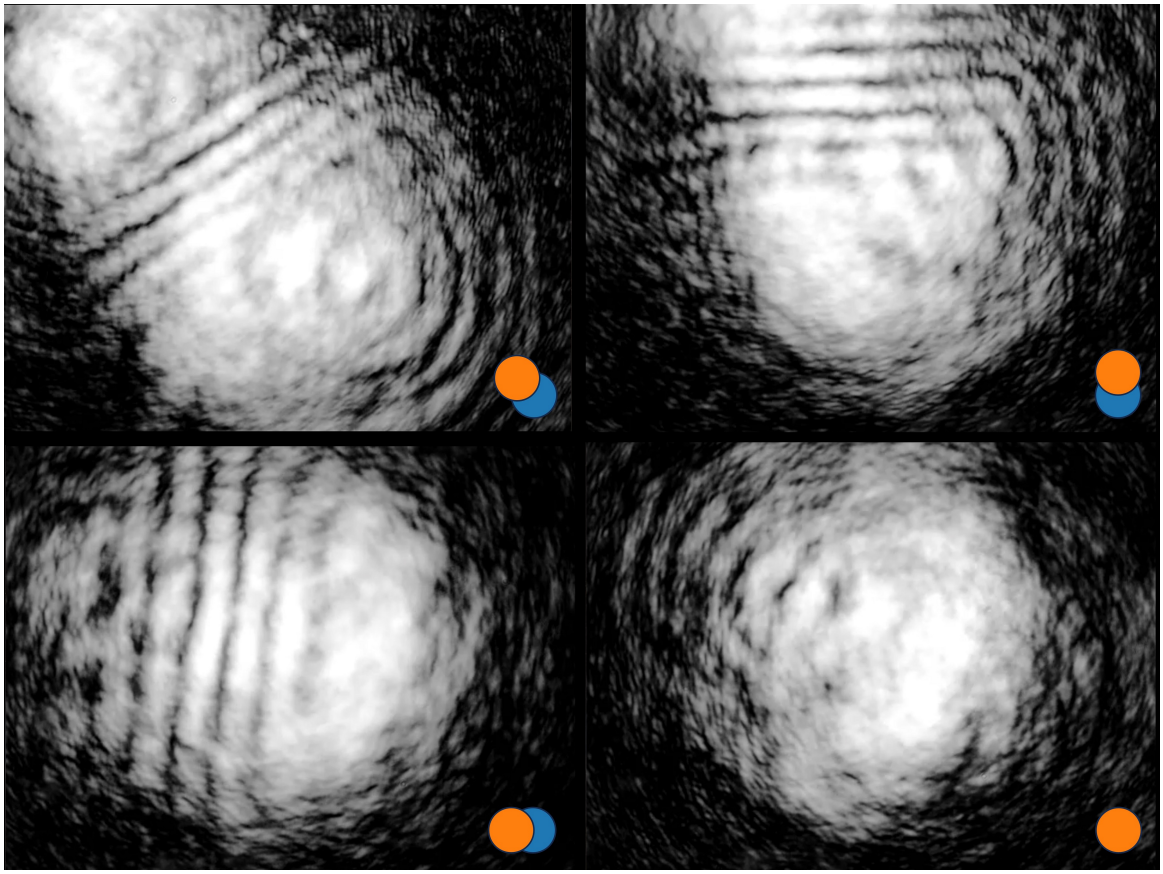

Figure 3.16: SWIR InGaAs camera showing the intentional misalignemnt of the FTSO to produce 1550 nm spatial fringes. The blue and orange circles in each image represent the positions of the two beams. Top left: Misalignment on both axis of a single mirror. Top right: Misalignment in the Y-axis of a single mirror. Bottom Left: Misalignment in the X-axis of a single mirror. Bottom right: FTSO optics aligned with no fringes visible.

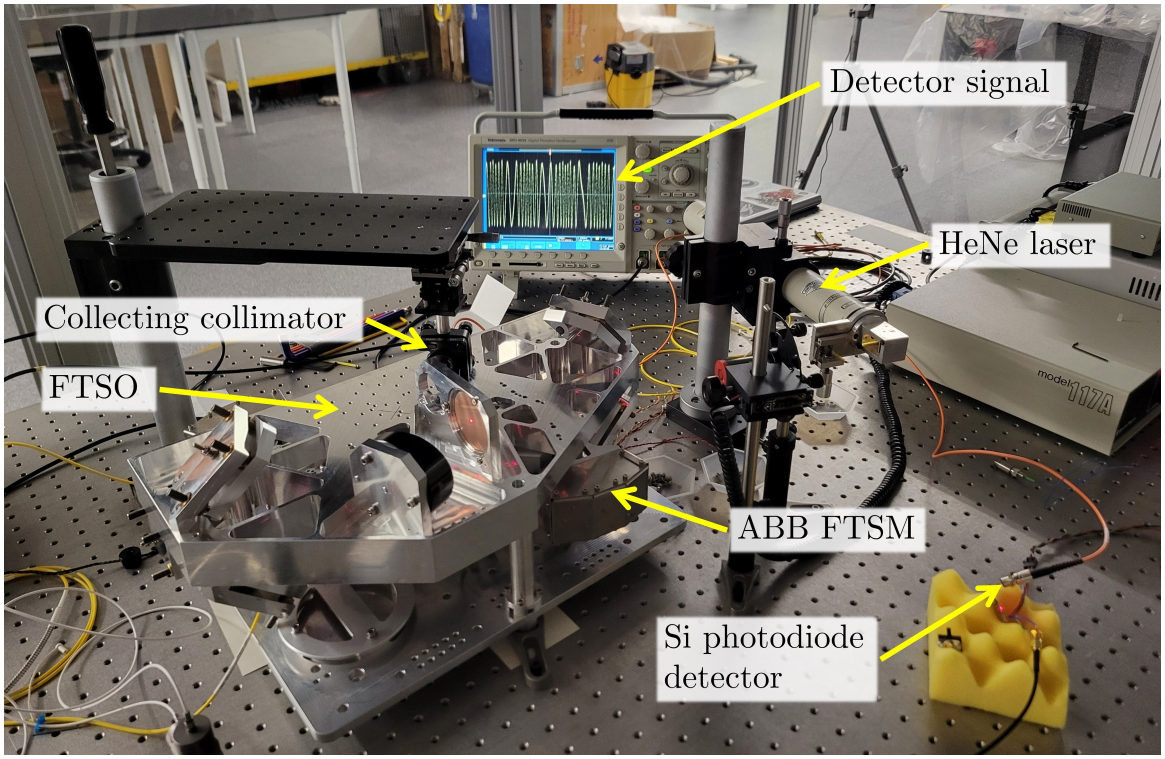

Figure 3.17: The experimental setup used to measured spectral fringes across the travel of the FTSM. A 632.8 nm HeNe laser was used as a source and a Si photodiode was used as the detector. Spectral fringes from interference in the FTS can be seen on the oscilloscope in the background.

The second step in alignment occurred after the FTSO was integrated with the FTSM. With the FTS assembled, a 632.8 nm HeNe laser beam was launched through the optical axis of the system. The rooftop mirrors were adjusted so that the returning beam in each arm of the FTS remained on axis. A collimator was placed at the output of the interferometer and was fiber coupled to a Si photodiode detector. With the FTSO aligned to the FTSM, the mechanism was scanned to introduce an OPD between the two arms of the interferometer. The detector signal was output to an oscilloscope, and 632.8 nm spectral fringes were measured from the FTSM scanning across its entire range of travel. Figure 3.17 shows the experimental setup used to check alignment of the FTS.

The linear polarizing beamsplitter used in this setup has a 2 µm period (1 µm spacing). At 632.8 nm, the FTS behaves as a Michelson interferometer, with the polarizer substrate acting as the beamsplitter. To configure the FTS as a Martin-Puplett interferometer, the

HeNe laser was replaced with a 1550 nm Eblana laser, and the Si photodiode was replaced with an InGaAs photodiode. An input polarizer and output analyzer were added to the FTS, and 1550 nm spectral fringes were measured across the entire range of the FTSM travel.

Spectral fringes with minimal apodization were observed across the entire range of travel at both 632.8 nm and 1550 nm. Although this experimental setup allowed for the alignment of the FTS at $\sim \lambda/200$ of its designed operating wavelength, the polarizing beam-splitter was inefficient due to the wire grid spacing being in the same wavelength regime as the 632.8 nm and 1550 nm lasers.

3.6 Diffraction Grating Module

The diffraction grating module for the PDPFTS was designed by Anderson [53, 54, 55]. I integrated this module into the cryogenic PDPFTS as the post-dispersing element. The grating for the PDPFTS was designed to operate over the wavelength range from 285 µm to 500 µm (35 cm^{-1} to 20 cm^{-1}). Assuming that the grating was slit width limited, the width of the exit slit, w'' was chosen to achieve a resolving power of $R \sim 100$ at 392.5 µm (25.48 cm^{-1}). The blaze angle of the grooves on the grating was set at 39.4° to maximize the efficiency at this wavelength. The specifications of the grating, designed to operate in the first order, are listed in Table 3.3. The grating was manufactured by B-Con Engineering [68] from RSA 6061 aluminum and ruled with single point diamond tooling under a specialized thermalization process to minimize internal stress.

The design of this grating spectrometer features the grating mounted in a monolithic aluminum enclosure on a pivot driven by a cryogenic stepper motor through worm gear reduction. The monolithic design and material choice for the enclosure ensures that the gear drive and optics maintain alignment as the system is cooled to cryogenic temperatures. As envisaged, a far-infrared PDPFTS on the PRobe far-Infrared Mission for Astrophysics (PRIMA) space telescope will incorporate several stationary diffraction gratings to distribute the signal from a polarizing FTS across different spectral bands of interest onto an array of ultra-sensitive detectors. However, since we did not have access to a detector array,

Table 3.3: Specifications for the grating spectrometer designed to operate over the range of 285 µm to 500 µm [53, 54, 55]. The parameters in bold were changed from the original design when integrating the grating module into the PDPFTS.

Parameter	Value
Grating width, W	105 mm
Grating length, l	50 mm
Order of diffraction, m	1
Slit spacing, d	312 µm
Deviation angle, 2ϕ	15°
Entrance focal length, r	**310 mm**
Exit focal length, r'	310.08 mm
Entrance slit width, w	**5.0 mm**
Exit slit width, w''	4.0 mm
Blaze angle, θ_B	39.4°

the grating needed to rotate to change the angle of incidence/diffraction and scan the wavelength range of interest using a single detector. This led to a Czerny-Turner monochromator configuration shown in Figure 3.18 being chosen for the grating spectrometer.

The monolithic enclosure that houses the grating is shown in Figure 3.19 alongside a CAD rendering cut-away view of the grating spectrometer. The cut-away view showcases the beam path of the Czerny-Turner monochromator configuration used in the rotating grating The grating is coupled to a cryogenic stepper motor through a worm-gear reduction, allowing the chosen wavelength to fall onto the detector. The inside surfaces of the enclosure were coated with black LOCTITE© STYCAST 2850FT [33] epoxy and sprinkled with carborundum particles to reduce reflectivity, thereby mitigating stray light. The output analyzer of the PDPFTS is mounted onto the entrance of the grating module.

A unique feature of the grating spectrometer is the inclusion of a plane mirror mounted to the rear side of the grating. This allowed the efficiency of the grating to be measured across its designed operating range and compared with theory. When the system is coupled to an FTS and the mirror is inserted into the optical path by rotating the grating 180°, a single measurement of the entire band is obtained which serves to calibrate the efficiency of the

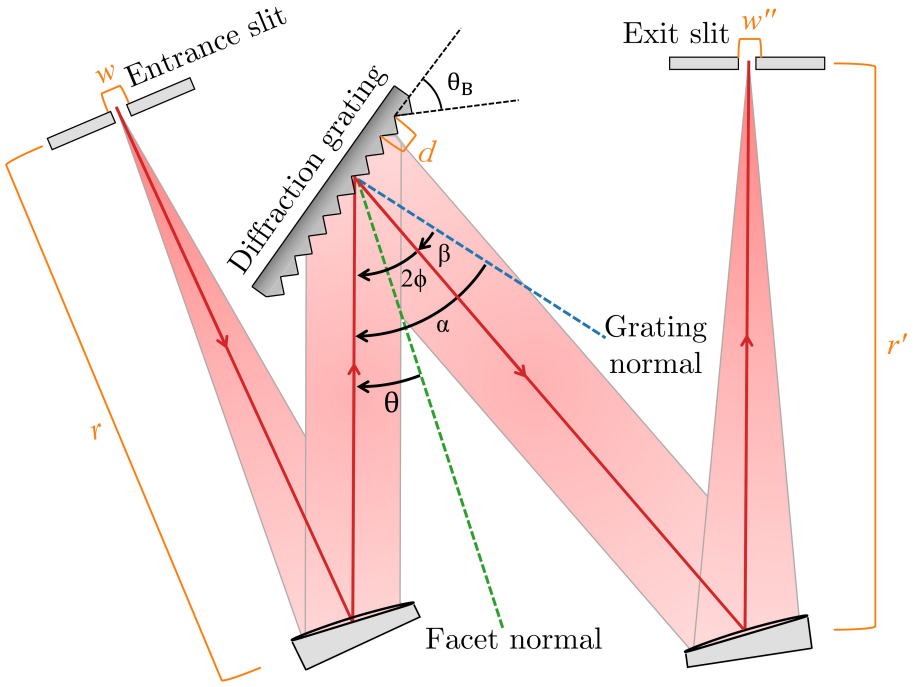

Figure 3.18: The Czerny-Turner monochromator configuration. α is the incident angle, β is the diffracted angle, the input and output collimating mirrors have focal lengths r and r', respectively. w and w'' are the widths of the entrance and exit slits.

grating as a function of wavelength. Anderson investigated the general trend of the grating efficiency across the operating range. The efficiency measurements shown in Figure 3.20 were calculated for each polarization state by comparing the amplitude of the grating scan to the signal amplitude of mirror data at the same wavelength position [54, 55]. The methods discussed in Li et al. [73] were used to produce a theoretical polarization-sensitive efficiency of the diffraction grating to compare with experimental measurements. The s-polarization (TM mode) diffraction efficiency is shown to be greater than the p-polarization (transverse electric (TE) mode) efficiency for a significant portion of the grating band. At high angles of incidence, reflection diffraction gratings operate with high and uniform efficiency ($\sim 80\,\%$) for TM polarized light, but lower and variable efficiency (10 % to 40 %) for TE polarized light. The polarizing encoding properties of a Martin-Puplett interferometer [17] can exploit this strong polarization dependence by ensuring that the interferometer output presents the TM mode to the grating.

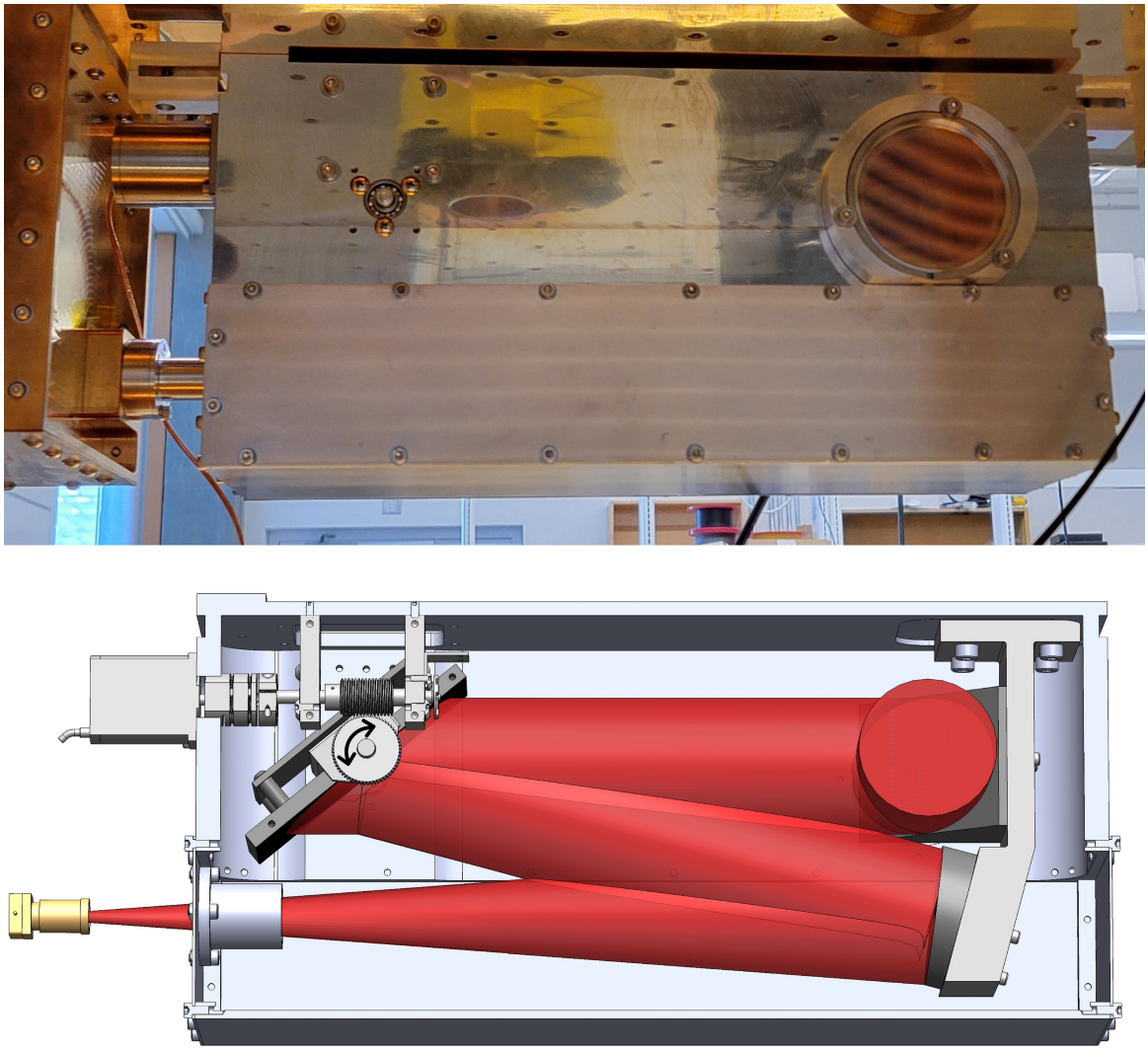

Figure 3.19: The monolithic diffraction grating module designed by Anderson [53, 54, 55]. A CAD rendering cutaway view shows the beam path and rotating diffraction grating within the monolithic enclosure.

The resolving power of the grating was measured across the wavelength range from 285 µm to 479 µm (35 cm^{-1} to 21 cm^{-1}). Figure 3.21 shows the resolving measurements and the data are compared with the theoretical slit-width limited resolving power. Even with a slightly lower resolving power, these measurements show that the grating succeeds as a post-dispersing module by restricting the spectral band of radiation viewed by the detector, achieving the target $R \sim 100$ at the band centre.

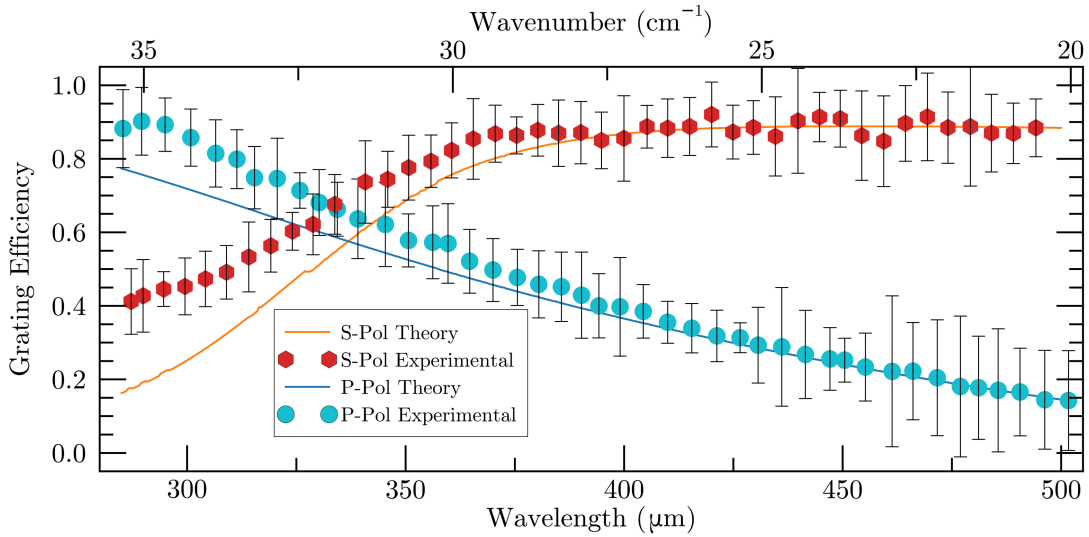

Figure 3.20: Diffraction efficiency measurements of s-polarized (red hexagons) and p-polarized (cyan circles) light. The measured data are compared to numerical calculations of the diffraction efficiency for s-polarized (orange) and p-polarized (blue) light using the coordinate-transform method [54, 55]. The s-polarization measurements agree with theory and confirm that the efficiency is both high and uniform over the wavelength range of interest.

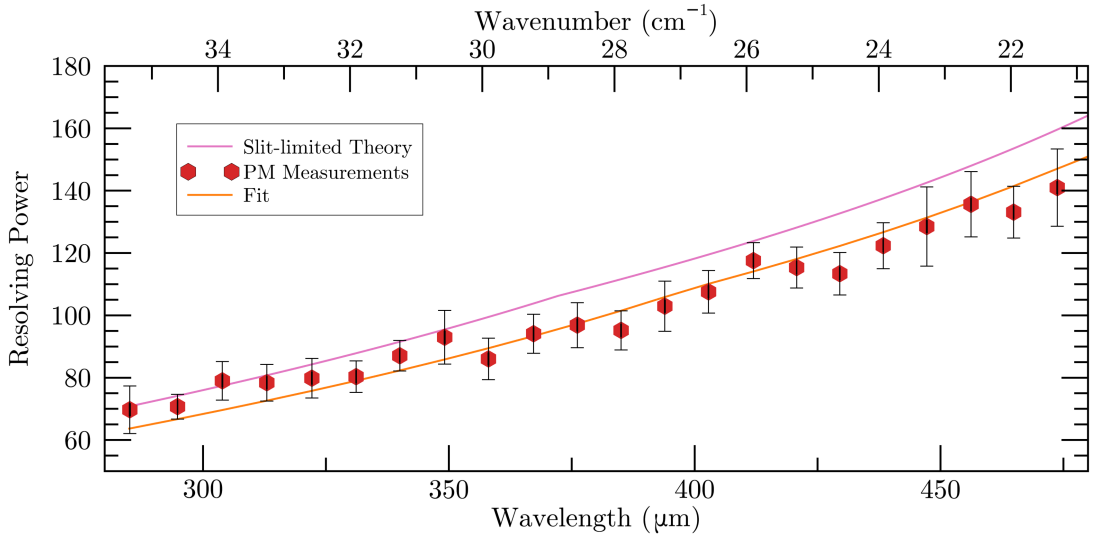

Figure 3.21: Experimental resolving power of the grating (blue) measured with the cryogenic photomixer (cyan circles). Measured data are compared with slit-limited theory (orange) [55].

3.7 Detector Module

The detector module for the PDPFTS consists of a cryogenic composite bolometer mounted onto the 0.3 K ultra-cold head of a three stage He-10 sorption fridge. The twin composite Ge:Ga bolometer used in the detector module was designed by Gom [56, 57] and was manufactured by QMC Instruments [59]. I designed the detector mounting bracket, exit slit, and routed all the wiring through the cryostat and sorption fridge to the detector. This bolometer was shown by Gom to have a typical noise-equivalent power (NEP) of $\sim 5 \times 10^{-16}\,\mathrm{W}/\sqrt{\mathrm{Hz}}$. Figure 3.22 shows the bolometer mounted onto the ultra-cold head of the He-10 sorption fridge installed in the LFC. The exit slit for the PDPFTS, along with a $35\,\mathrm{cm}^{-1}$ edge filter, are installed onto the feed horn of the bolometer.

The working principles of a bolometer rely on measuring a change in temperature due to radiation incident on the detector. By placing a semiconductor material with an electrical resistivity coefficient that is highly sensitive to temperature onto a radiation absorbing substrate, the temperature change of the detector due to incidence radiation will result in a comparatively large change in its resistance. By applying a known bias voltage across the bolometer, this change in resistance will result in a shift in the measured current.

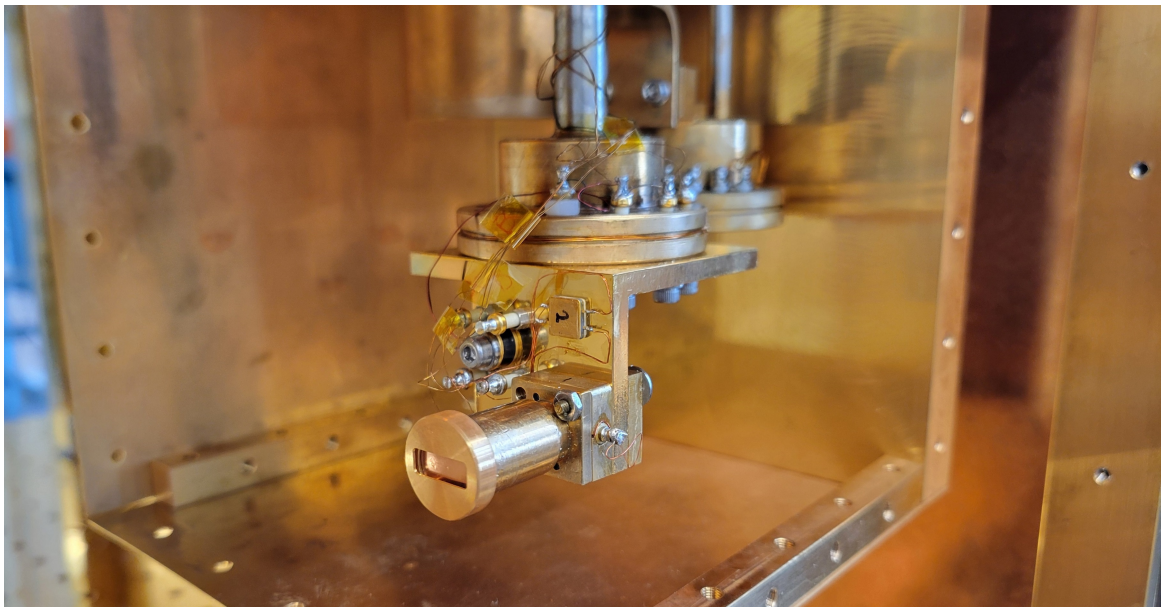

Figure 3.22: Composite Ge:Ga bolometer detector mounted onto the ultra-cold head of the He-10 sorption fridge. The exit slit of the PDPFTS can be seen on the feed horn of the detector.

This type of bolometer has been used in a number of far-infrared astronomical facilities. Notable examples include bolometers being used at ground based observatories such as the James Clerk Maxwell Telescope (JCMT) [74], airborne observatories such as the Stratospheric Observatory For Infrared Astronomy (SOFIA) [75], and spaceborne missions such as Herschel [58]. The next generation of far infrared observatories will utilize state-of-the-art microwave kinetic inductance detectors (MKIDs) due to their sensitivity being a few orders a magnitude greater than bolometers and transition edge sensors (TESs). In recent years, MKIDs have been shown to achieve an NEP in the few $10^{-20}\,\mathrm{W}/\sqrt{\mathrm{Hz}}$ [14]. The sensitivity of the bolometer used in this thesis is more than capable of demonstrating the performance of the fully cryogenic far-infrared PDPFTS.

3.8 Summary

A source module capable of producing a continuum with superimposed absorption features has been developed, a method to align the FTSO after installation on the ABB FTSM [49, 50, 51, 52] was implemented, the diffraction grating module was previously tested by Anderson [53, 54, 55], and the bolometer detector [56, 57] has been installed in the LFC. With all four modules built, the PDPFTS can be fully integrated. The following chapters cover the integration of the PDPFTS and the results obtained for a room temperature implementation of the instrument and the fully cryogenic integration in the LFC.

Chapter 4

Room Temperature Post-dispersed Polarizing FTS Results

Insufficient data for meaningful answer.

Isaac Asimov
The Last Question

4.1 Instrument Integration

While the construction of the Large Facility Cryostat (LFC) was underway, a room temperature implementation of the post-dispersed polarizing Fourier transform spectrometer (PDPFTS) was developed, marking progress towards achieving a fully cryogenic configuration. In this implementation, a less sensitive room temperature deuterated L-alanine doped triglycene sulphate (DLATGS) pyroelectric detector manufactured by QMC Instruments [59] was used in place of the cryogenic bolometer detector. While this pyroelectric detector ranks among the best room temperature infrared detectors, its sensitivity is six orders of magnitude lower than that of our cryogenic bolometer. This reduction in sensitivity drove the requirement for a higher power source module. Fortunately, the Astronomical Instrumentation Group (AIG) had available a Virginia Diodes tuneable line source [76]. This source operates on the principles of frequency multiplication and is capable of producing narrow banded spectral features within the 300 GHz to 400 GHz (10.0 cm^{-1} to 13.3 cm^{-1}) frequency range at an output power that is four orders of magnitude greater than the cryogenic source module. A schematic overview of this room temperature implementation is

shown in Figure 4.1, closely resembling the cryogenic configuration with modifications made to the detector and source modules. The photon path for the room temperature implementation matches that of the cryogenic design. Figure 4.2 shows the room temperature implementation of the PDPFTS.

As the room temperature implementation of the PDPFTS was being developed, it became evident that a new diffraction grating was required as the operating range of the cryogenic grating fell outside the emission range of the Virginia Diodes line source. A new diffraction grating was manufactured in house with a blaze angle of 45° and a 675 µm

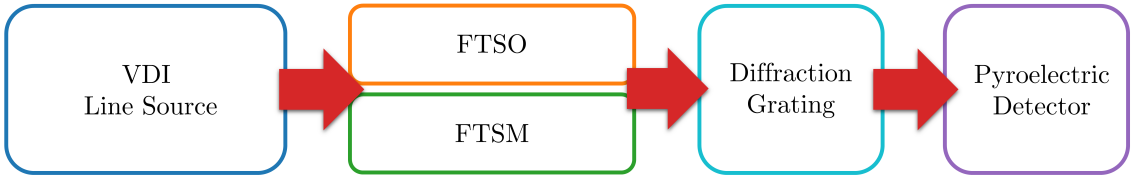

Figure 4.1: A schematic overview of the room temperature implementation of the PDPFTS highlighting the four principal modules. A lower sensitivity room temperature QMC Instruments pyroelectric detector [59] and a Virginia Diodes line source [76] were used in place of the cryogenic bolometer and cryogenic source module.

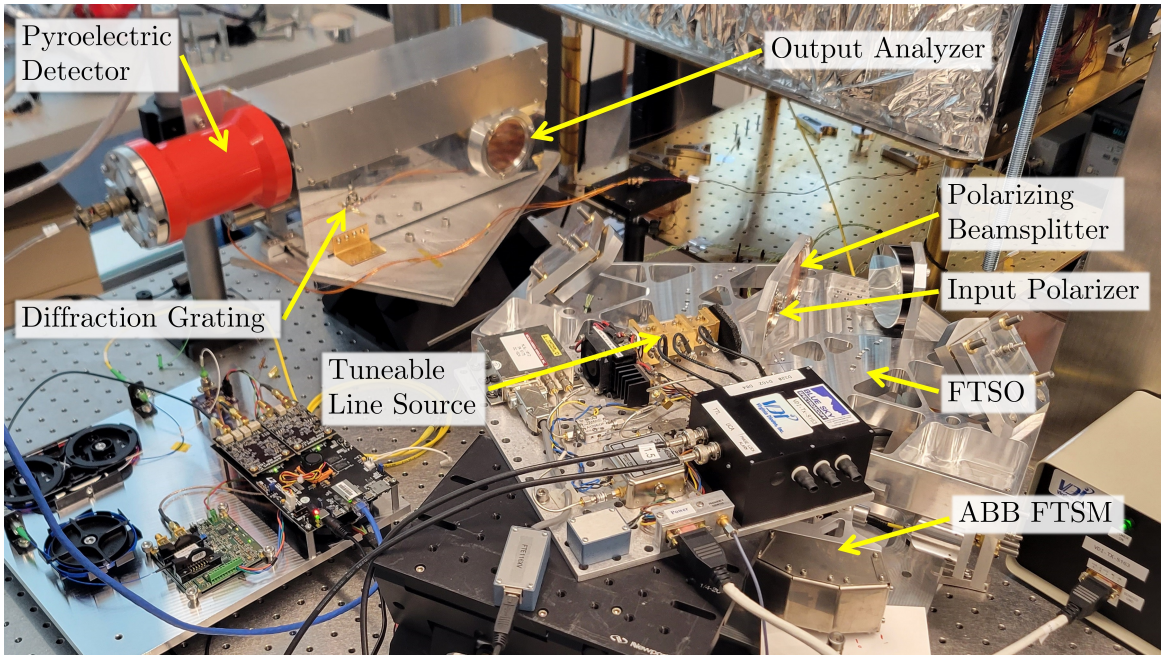

Figure 4.2: The room temperature implementation of the PDPFTS featuring a lower sensitivity pyroelectric detector and a higher power but longer wavelength length source.

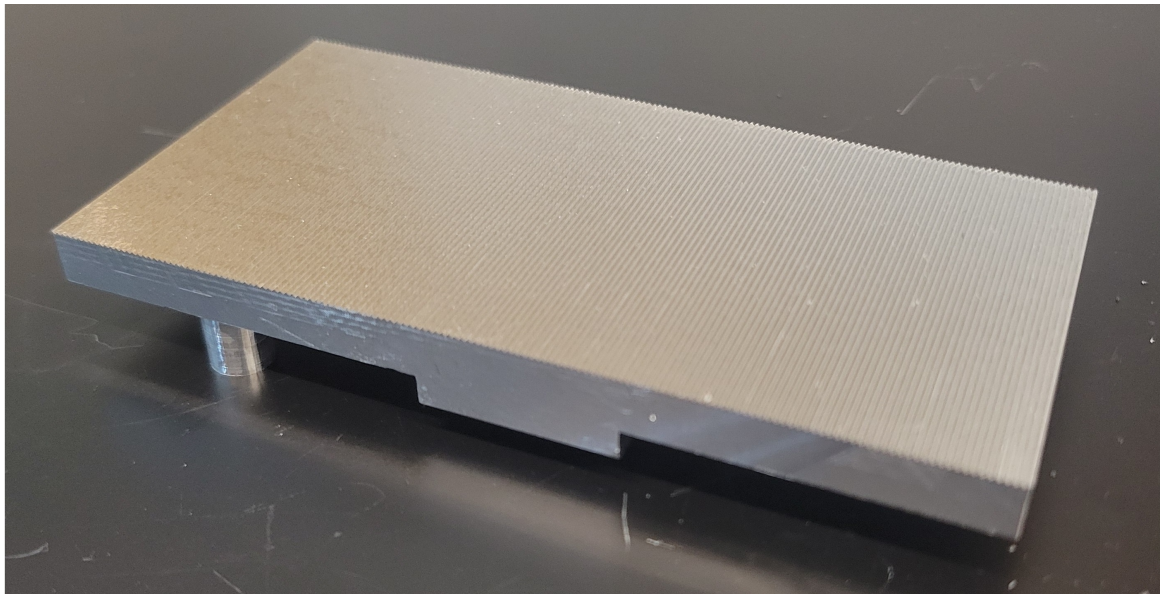

Figure 4.3: A custom diffraction grating manufactured in house to match the wavelength range of a Virginia Diodes line source. This grating was machined with a blaze angle of a 45° and a ruling spacing of 675 µm.

ruling spacing designed to match the available frequency range of the higher power line source. A blank of the existing grating was machined out of aluminum and computer numerical control (CNC) was used to mill the grating rulings. I would like to acknowledge the work of Brad Gom, the AIG project manager, for his invaluable contribution to machining this grating. The precision required for manufacturing high tolerance optics is considerable and Brad was able to machine a custom grating on short notice. Figure 4.3 shows the custom diffraction grating machined for the room temperature implementation of the PDPFTS. This grating was used exclusively for the room temperature PDPFTS testing, after which the original cryogenic grating was reinstalled.

4.2 Results

The room temperature implementation of the PDPFTS was tested in two operating modes: as a diffraction grating spectrometer and as a post-dispersed Fourier-transform spectrometer (FTS). When operating as a diffraction grating spectrometer, the Fourier-transform spectrometer mechanism (FTSM) introduced in Section 3.2 was held stationary at a large

optical path difference (OPD). The output from the Virginia Diodes line source [76] was amplitude modulated, and the detector signal was fed through a lock-in amplifier. With the photon path passing through the stationary FTS, the grating was rotated to measure the spectral response. When operating as the post-dispersed FTS, the diffraction grating was rotated so that the desired spectral band would fall onto the detector, while the FTSM scanned to provide modulation within the FTS module.

As a new diffraction grating was machined for room temperature testing, the spectral response of this grating was measured using the first of these two operating modes. At various line source tunings, the diffraction grating was rotated such that the $m = \pm 1$ and the zeroth grating order could be observed. From diffraction theory, using a Czerny-Turner monochromator configuration, when monochromatic light of wavelength λ is incident on a diffraction grating, the grating equation is given as:

$$m\lambda = 2d(\sin(\theta - \phi)\cos\phi) \tag{4.1}$$

where m is the order of diffraction, d is the spacing between adjacent grooves, ϕ is the deviation angle, and θ is the angle of incidence minus the deviation angle [77].

For a given order of diffraction, as the wavelength decreases, the angle of the grating relative to its zeroth order will decrease. This can be seen in Figure 4.4 with the results of the diffraction grating spectrometer scans. The $m = 1$ order in the top plot is highlighted and expanded in the bottom plot with the grating angle converted to wavelength.

The resolving power for the diffraction grating was also measured. Line source tunings were chosen for three closely spaced spectral features such that the resolving power of the grating would not be able to distinguish one from another. For a generic spectrometer, the spectral resolving power is given by:

$$R = \frac{\lambda}{\Delta\lambda} \tag{4.2}$$

where $\Delta\lambda$ is the spectral resolution, the separation needed to distinguish two wavelengths.While there are many ways to define resolving power, I have adopted the use of the full width half maximum (FWHM) as a practical method of measuring spectral resolution. The custom grating achieved a resolving power of 53.4(1) at 856.7 µm (11.66 cm^{-1}) and a resolving power of 57.8(4) at 938.1 µm (10.66 cm^{-1}). The close up of the $m = 1$ order in Figure 4.4 shows how the grating spectrometer is able to resolve the spectral feature at 856.7 µm (11.68 cm^{-1}), but would not be able to resolve the closely spaced features around 856.7 µm (10.77 cm^{-1}).

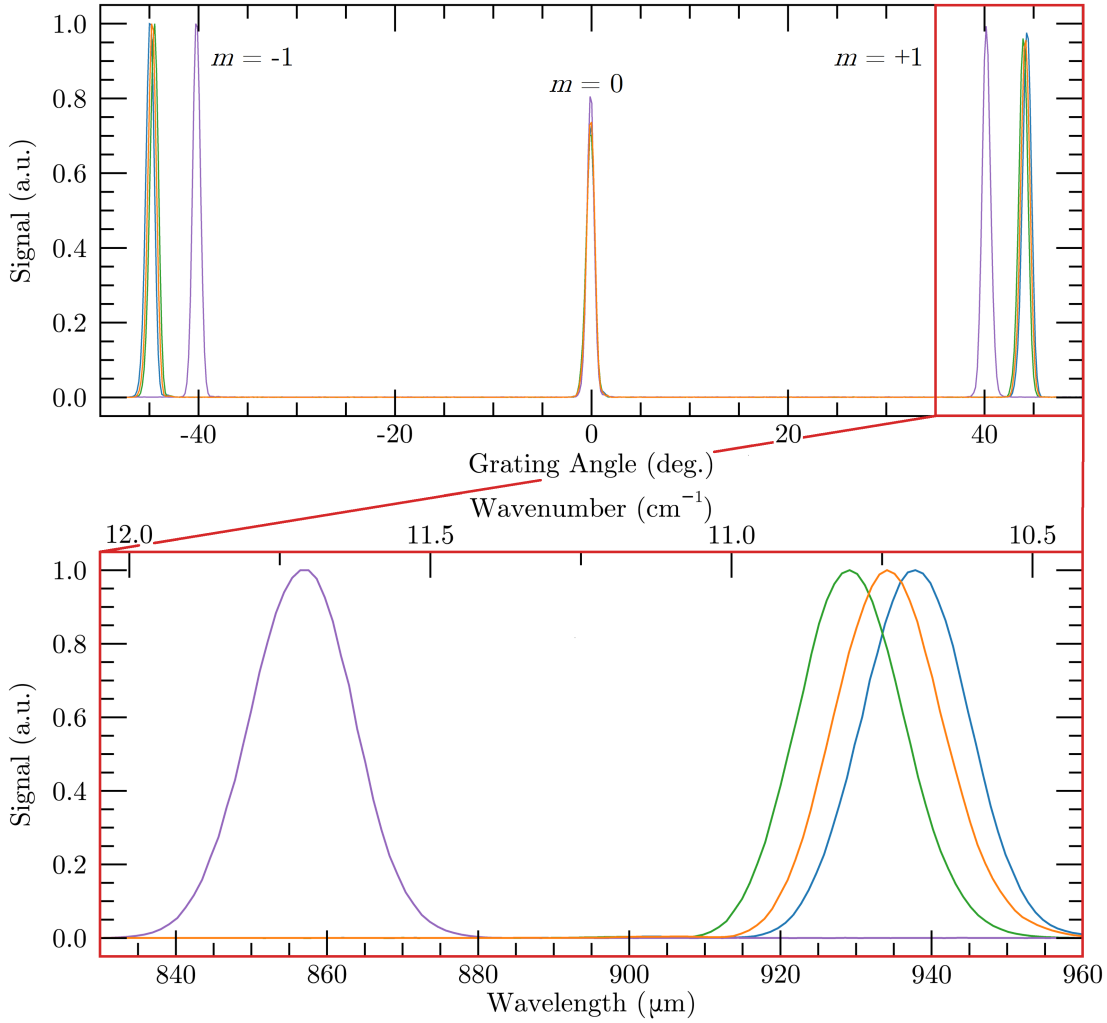

Figure 4.4: Room temperature diffraction grating spectrometer scan results. Top: Grating spectrometer scans showing the $m = \pm 1$ and zeroth order. As the wavelength decreases, the line features shift closer in grating angular position toward the zeroth order. Bottom: A close up of the $m = 1$ grating order. The diffraction grating alone with its lower resolving power ($R \sim 55$) would not be able to distinguish the closely spaced line features.

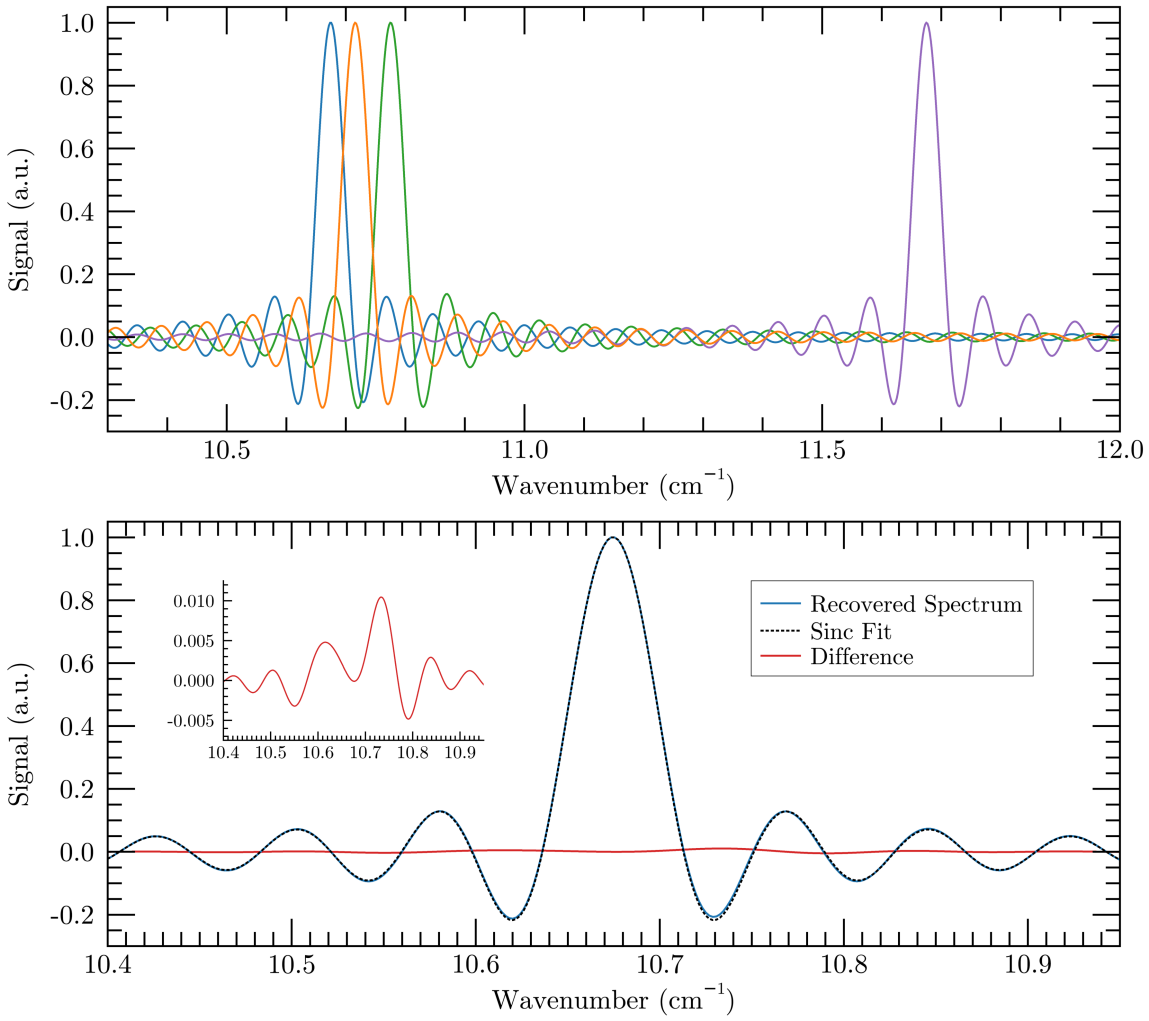

Figure 4.5: Top: Room temperature PDPFTS scan results. The higher resolving power of the FTS ($R \sim 300$), when compared to the grating ($R \sim 55$), can resolve the closely spaced spectral features. Bottom: One of the recovered spectra with a best fit sinc profile.

In the second series of tests, post-dispersed FTS scans were performed at the same line source tunings as the diffraction grating spectrometer scans. The Fourier-transform spectrometer optics (FTSO) were configured to scan a fully double-sided interferogram. The single-sided FTS scan length of 13.019 cm gave a theoretical spectral resolution of $0.038\,406\,\mathrm{cm}^{-1}$. For an FTS, the instrumental line shape is given by the cardinal sine function, defined as [15]:

$$\operatorname{sinc} x = \frac{\sin x}{x}. \tag{4.3}$$

The FWHM of the sinc function was used to find the spectral resolution of the FTS. The recovered FTS spectra are very well fit by sinc profiles and the measured scans achieved a spectral resolution of $0.038\,389(4)\,\mathrm{cm}^{-1}$. The results of the post-dispersed FTS scans can be seen in Figure 4.5. The higher resolving power of the FTS is able to resolve the closely spaced spectral features at $10.77\,\mathrm{cm}^{-1}$.

Comparing the grating spectra to the FTS spectra showcases the power of the PDPFTS. The diffraction grating spectrometer limits the spectral bandwidth, allowing the use of ultrasensitive detectors, but would not be able to resolve closely spaced line features; an FTS is needed to provide the higher resolving power.

The room temperature implementation of the PDPFTS allowed significant progress to be made toward fully integrating the instrument at cryogenic temperatures. While modifications had to be made to three out of the four modules, I was able to functionally test the polarizing FTS module, which had not previously undergone testing. The results obtained from these room temperature tests were used to set the stage for the fully cryogenic integration shown in the following chapter.

Chapter 5

Cryogenic Post-dispersed Polarizing FTS Results

> "It is a capital mistake to theorize before you have all the evidence. It biases the judgment."
>
> Sherlock Holmes
> A Study in Scarlet

5.1 Instrument Integration

With the construction of the Large Facility Cryostat (LFC) completed, the fully cryogenic post-dispersed polarizing Fourier transform spectrometer (PDPFTS) was integrated into the 4 K volume of the cryostat. The instrument integration follows the design outlined in Chapter 3. Figure 5.1 shows a computer-aided design (CAD) rendering of the PDPFTS alongside a photograph of the instrument installed within the 4 K volume of the LFC. The blackbody and photomixer can be seen on the Fourier-transform spectrometer optics (FTSO) breadboard. The Fourier-transform spectrometer mechanism (FTSM) [50, 51, 52] is seen on the lower level of the Fourier-transform spectrometer (FTS). The diffraction grating module [53, 54, 55] is inverted and mounted onto the LFC upper 4 K plate.The bolometer detector [56, 57] is mounted onto the ultra-cold head of a He-10 sorption fridge. The detector is hidden from view in the photograph due to the 0.3 K sub-volume radiation shields. This is the world's first fully cryogenic far-infrared PDPFTS. The spectroscopic results obtained from this hybrid spectrometer are presented in detail throughout this chapter.

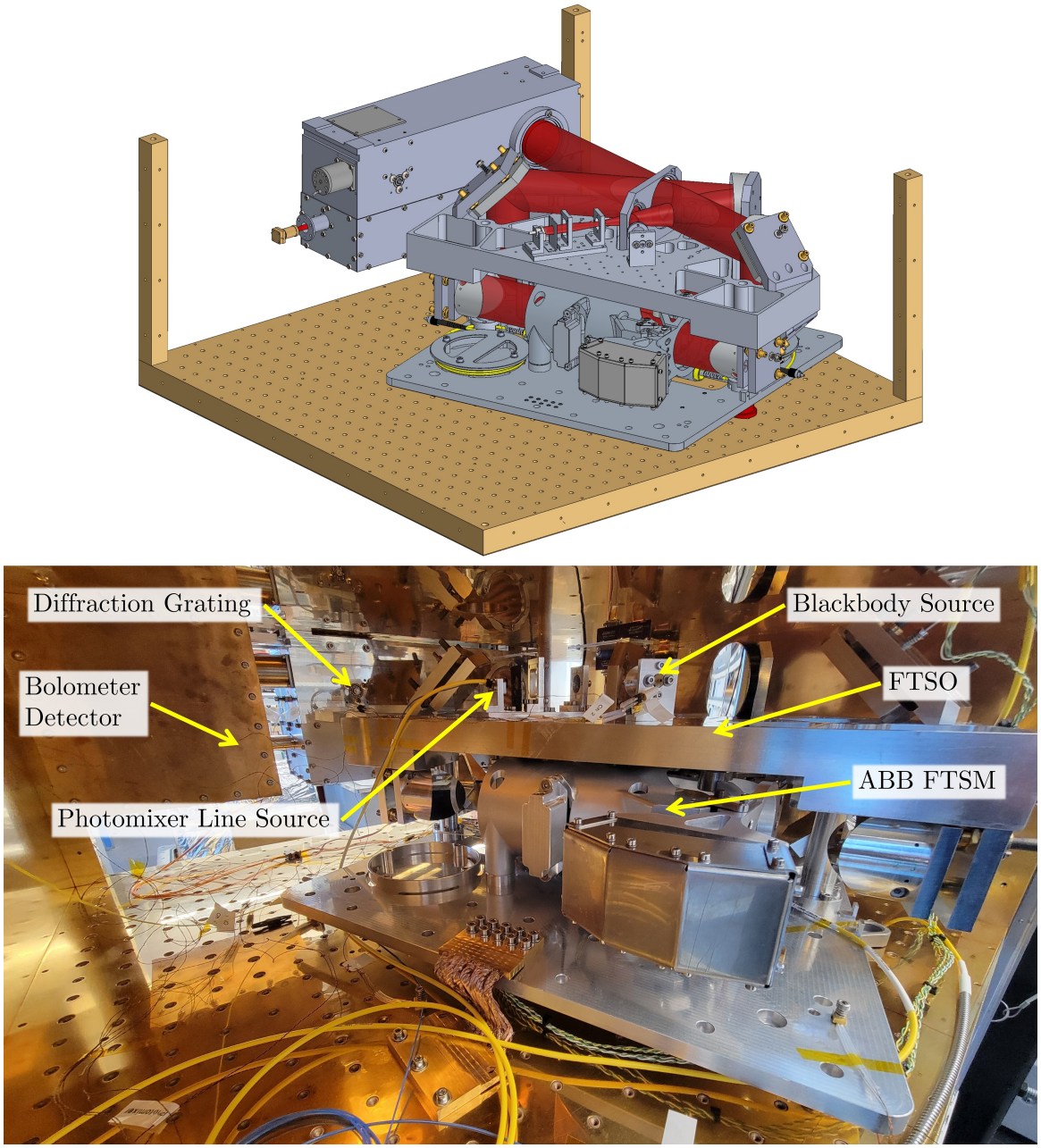

Figure 5.1: Cryogenic integration of the PDPFTS installed in the 4 K volume of the LFC. Top: CAD rendering of the cryogenic integration. Bottom: A photograph of the fully integrated PDPFTS before cool down.

5.2 Results

The intensity calibration of the PDPFTS was demonstrated with the entire instrument cooled to 4 K. Calibration data were collected using only the blackbody source to determine the spectral response function (SRF) of the instrument. Exceptional calibration accuracy was achieved due to having the entire PDPFTS cooled to 4 K with no photon path to the labora-

tory. Following the intensity calibration measurements, a series of absorption features were superimposed onto a continuum using the novel source module discussed in Chapter 3 to demonstrate the high resolution capabilities of the PDPFTS to resolve line features within the low resolution micro-spectra post-dispersed by the grating. The resolving power of the diffraction grating and the FTS were compared over the wavenumber range of $20\,\mathrm{cm}^{-1}$ to $35\,\mathrm{cm}^{-1}$ using both the continuum and line emission components of the source module.

For these measurements, the rooftop mirrors in the FTSO were positioned to offset the zero path differnce (ZPD) away from the midpoint of the scanning mechanism, resulting in an asymmetric interferogram measured from $+21.2\,\mathrm{cm}$ to $-7.6\,\mathrm{cm}$ optical path difference (OPD). This decision aimed to achieve a higher spectral resolution by measuring a longer single-sided OPD. However, during cryogenic measurements, the behaviour of the FTSM as it moved through its center of travel posed challenges. We believe that changes in the performance of the stiffness compensating flexure blades within the FTSM are a result of it having undergone extensive accelerated lifetime testing with a large number of scan cycles before being integrated into the PDPFTS. With this change in performance, the servo control was no longer able to scan the mechanism smoothly through the center of travel. As the FTSM approached the center of its travel, the stiffness of the flexures would increase before buckling, causing a sudden change in sign to the restoring force, a rapid acceleration, and velocities that exceeded the capabilities of the laser position metrology. This reduced the usable travel of the FTSM to half of its full stroke and limited the spectral resolution of the FTS to around one third of its theoretical maximum for these measurements. In hindsight, it was fortunate that the decision was made to offset ZPD. Due to the limited time available for testing, we were only able to cool down the fully integrated PDPFTS once before shipping the FTSM back to ABB so it could undergo shock and vibration testing. Had ZPD been left at the midpoint of the FTSM, the white light fringe would have remained in this problematic region of travel in the scanning mechanism and the measured interferograms would not have been capable of demonstrating the operation of the PDPFTS. Despite the

limited usable travel of the FTSM, which reduced the available spectral resolution of the PDPFTS, the quality of data was sufficient to demonstrate the hybrid spectrometer concept.

5.2.1 FTS Calibration

The initial set of calibration data were taken using a mirror in place of the diffraction grating, resulting in broad spectral measurements without a post-dispersing element. Data were collected for three blackbody temperatures: $132.70(5)\,\mathrm{K}$, $106.00(5)\,\mathrm{K}$, and $88.60(5)\,\mathrm{K}$. The instrumental SRF of the FTS was determined by comparing the measured signal intensity of the continuum spectra, I [V], to their theoretical spectral radiance, B [$\mathrm{W\,cm^{-1}\,sr^{-1}}$]. Theoretical spectral radiance values were determined using Planck's law. For a linear system, the spectral response consists of a slope, m [$\mathrm{V\,W^{-1}\,cm\,sr}$], and an offset, b [V]. The spectral radiance can then be related to the measured signal intensity as a function of temperature, T [K], and wavenumber, σ [$\mathrm{cm^{-1}}$]:

$$I(T,\sigma) = m(\sigma)B(T,\sigma) + b(\sigma) \tag{5.1}$$

As the slope and offset are only a function of wavenumber, the signal intensity from two of the recovered spectra, alongside the spectral radiance for their recorded blackbody temperatures, can be used to solve for the spectral response. The third remaining spectrum was treated as an unknown temperature. Calibrated spectra for all three temperatures were obtained by applying the SRF to their recovered spectra. These calibrated spectra should more closely resemble the Planck curve when compared to the recovered spectra. As the spectrum treated as an unknown temperature is independent of the SRF, it was used to establish the calibration accuracy.

Figure 5.2 shows the FTS calibration process. The top left plot shows an example of a measured interferogram. The dominant structure in this interferogram is the white light fringe centred at ZPD. The top right plot shows the recovered spectra for the three blackbody temperatures noted above. A noticeable drop in the signal intensity can be seen at $35\,\mathrm{cm^{-1}}$ due to the edge filter installed on the detector. The recovered spectra show

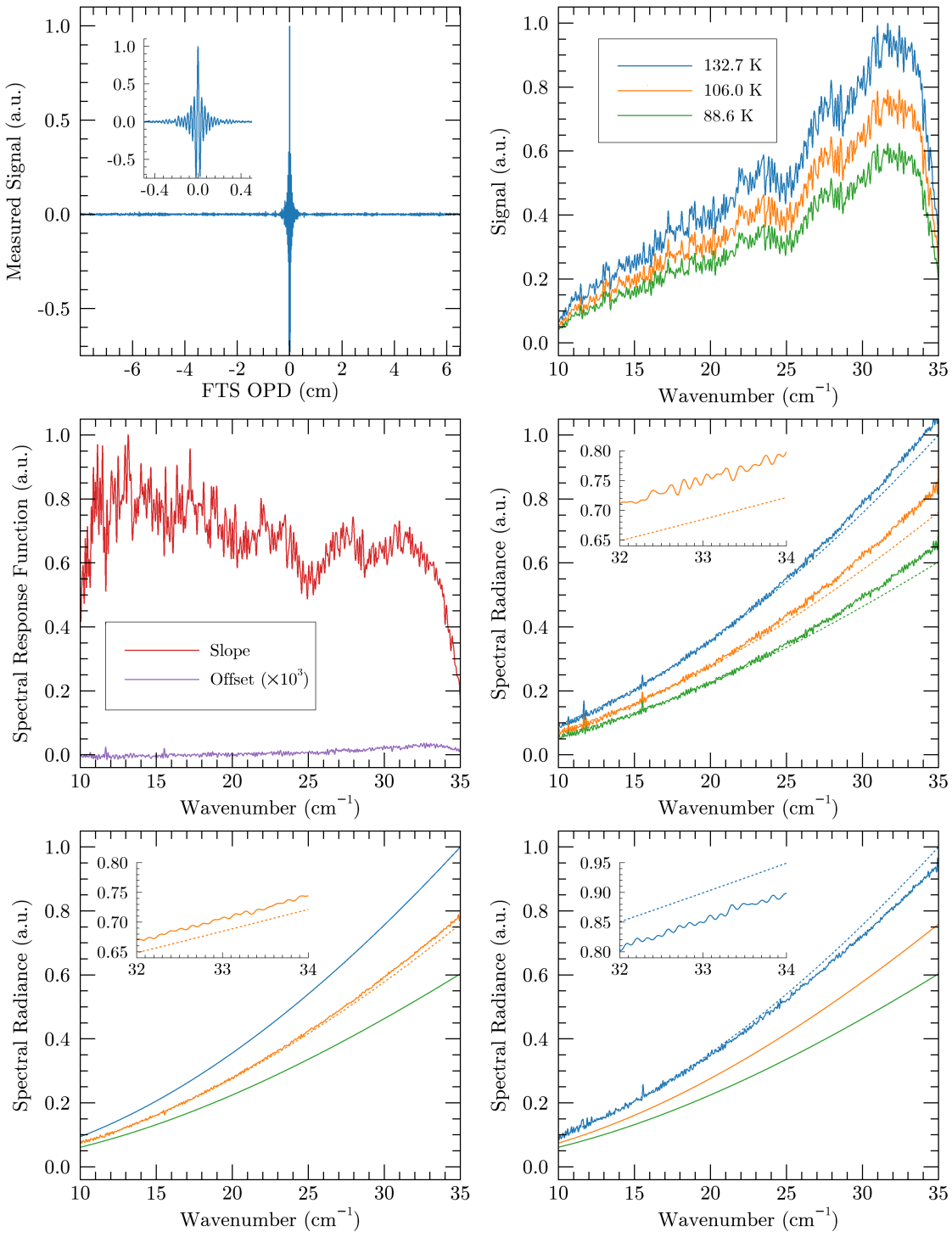

Figure 5.2: The FTS calibration process. Top Left: Example of a measured interferogram. Top Right: Recovered spectra for three blackbody temperatures. Middle Left: SRF based on two of the recovered spectra. Middle Right: Comparison of calibrated spectra (solid lines) and expected Planck curve (dashed lines) using only the SRF slope. Bottom Left: Calibrated spectra using both SRF slope and offset. Bottom Right: Calibrated spectra highlighting the non-linear detector response at higher blackbody temperatures.

similarities to the Planck curve with many channel fringes present. These channel fringes are believed to arise from unwanted reflective cavities with the many optical components required in the double decker FTS design. At this stage, and unlike the diffraction grating module where great efforts were made to reduce stray reflections [53, 54, 55], there was no baffling put in place within the FTS. Operating with a closed cryostat offers a significant benefit as the test environment is stable and one should be able to calibrate out these channel fringes. The middle left plot shows the SRF derived from the difference between two spectra and Planck's law. The three remaining plots show the results of applying different SRFs to the recovered spectra. Solid lines show the calibrated spectra while dashed lines show the expected Planck curve.

The first attempt at calibration assumed that because no room temperature photons were reaching the detector, the contributions from the 4 K background would be insignificant such that the offset of the SRF could be ignored. This SRF was calculated using the $133.70(5)$ K and $88.60(5)$ K spectra; only the slope from this SRF was applied to the recovered spectra. The middle right plot in Figure 5.2 shows the calibrated spectra from this initial attempt at calibration. The calibrated spectra for all three measurements deviate from the theoretical Planck curve and appear hotter than expected at shorter wavelengths. While the SRF offset is minimal, there is a slight rise at the shorter wavelengths which would indicate that self heating from the source module is making its way into the background. This first attempt at calibration showed that the SRF offset could not be ignored.

The second attempt at calibration accounted for the change in background due to self heating of the instrument by applying both the slope and offset of the SRF to the recovered spectra. This SRF was calculated using the 132.7 K and 88.6 K spectra. The bottom left plot in Figure 5.2 shows the calibrated spectra when both the slope and offset are considered in the calibration. While there is much better agreement between the calibrated spectra and the Planck curve, the $106.00(5)$ K spectrum treated as the unknown temperature is reading warmer than expected. This led to investigating the non-linearity of the detector. The bias

voltage across the bolometer detector varied as a result of black body temperature for these measurements, signifying that its spectral response was changing. As shown by Gom [56, 57], the spectral response of our bolometer has a non-linear dependency on the intensity of incident radiation. With a high radiant loading reaching the detector with the mirror in place instead of the grating, an increase in the blackbody temperature causes the bolometer to become increasingly non-linear in its spectral response. As the temperature of the blackbody is increased, the bolometer will measure a temperature lower than expected due to this non-linear response. As a result of using the hottest of the three temperatures to derive the SRF, which would see the most non-linearity, the middle temperature independent from the calibration reads hotter than expected.

The third attempt at calibration considered the non-linear effects of the detector by using the two colder temperatures of $106.00(5)$ K and $88.60(5)$ K for the SRF calculation as they would introduce the least amount of non-linear effects. The bottom right plot in Figure 5.2 shows the expected outcome as a result of calibrating with a non-linear detector response as the $133.70(5)$ K spectrum appears colder than its corresponding Planck curve.

The non-linear response of the detector is also evident due to the appearance of harmonics in the out-of-band portion of the recovered spectra [78]. Figure 5.3 shows recovered spectra with an extended x-axis to show the out-of-band energy in the second harmonic as a result of the detector non-linearity. The high sample rate provided by the laser position metrology designed by Christiansen [79] set our Nyquist wavenumber to 500 and allowed for these out-of-band harmonics to be probed. Unfortunately, there was insufficient detector information recorded during these measurements to perform a non-linear calibration. No further attempts were made to calibrate the FTS without a post-dispersing element as these measurements are not important for the PDPFTS. The cause of the non-linear response during these measurements is fully understood, and with the diffraction grating spectrometer post-dispersing the output from the FTS, the photon flux incident on the detector will be reduced by a factor of 100 and the detector will behave in the linear regime.

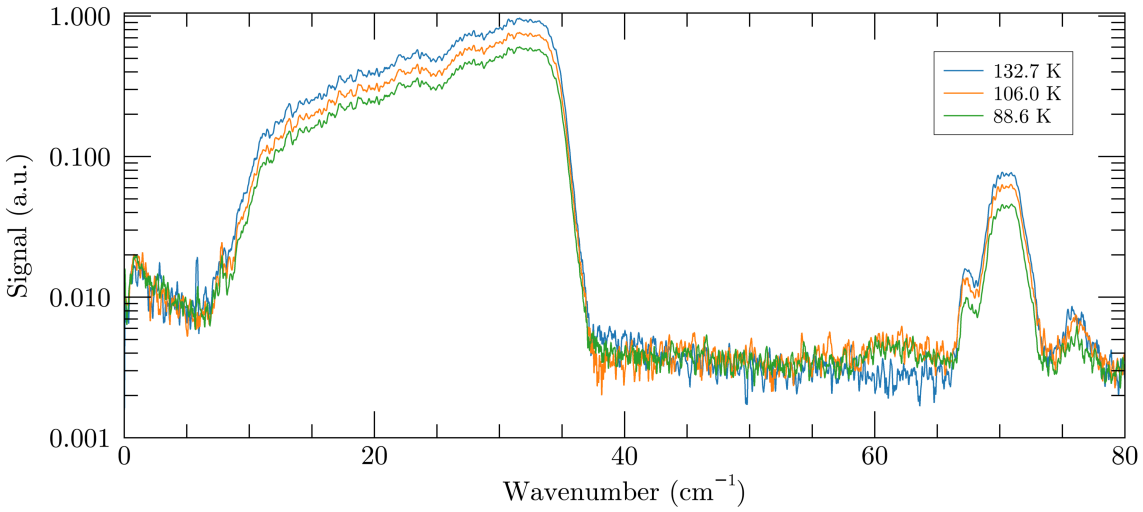

Figure 5.3: The recovered spectra for three blackbody temperatures indicate detector non-linearity with the out-of-band second harmonic.

5.2.2 Post-dispersed FTS Calibration

Attention was now turned to calibrating the PDPFTS. In this second set of calibration data, the diffraction grating was rotated back into the optical path instead of the mirror, and the output from the FTS was post-dispersed onto the detector. These data are the first measurements taken with a fully cryogenic PDPFTS. Data were collected for three blackbody temperatures: 133.50(5) K, 106.90(5) K, and 88.90(5) K. The same calibration process from Section 5.2.1 was used to derive the instrumental SRF for the PDPFTS where the recovered spectra from two of these three blackbody temperatures are treated as known measurements with the third temperature treated as an unknown to check to the accuracy of the calibration.

Figure 5.4 shows the PDPFTS calibration process at 32.9 cm^{-1} for a single detector at the post-dispersed output. A far-infrared space observatory flying a fully realized PDPFTS will employ arrays of detectors. Calibration products will have to be generated for every detector measuring small portions of the entire band. While the PDPFTS in this thesis only has a single detector and the desired wavenumber must be selected by rotating the diffraction grating spectrometer, the same calibration process would be employed for every detector in an array.

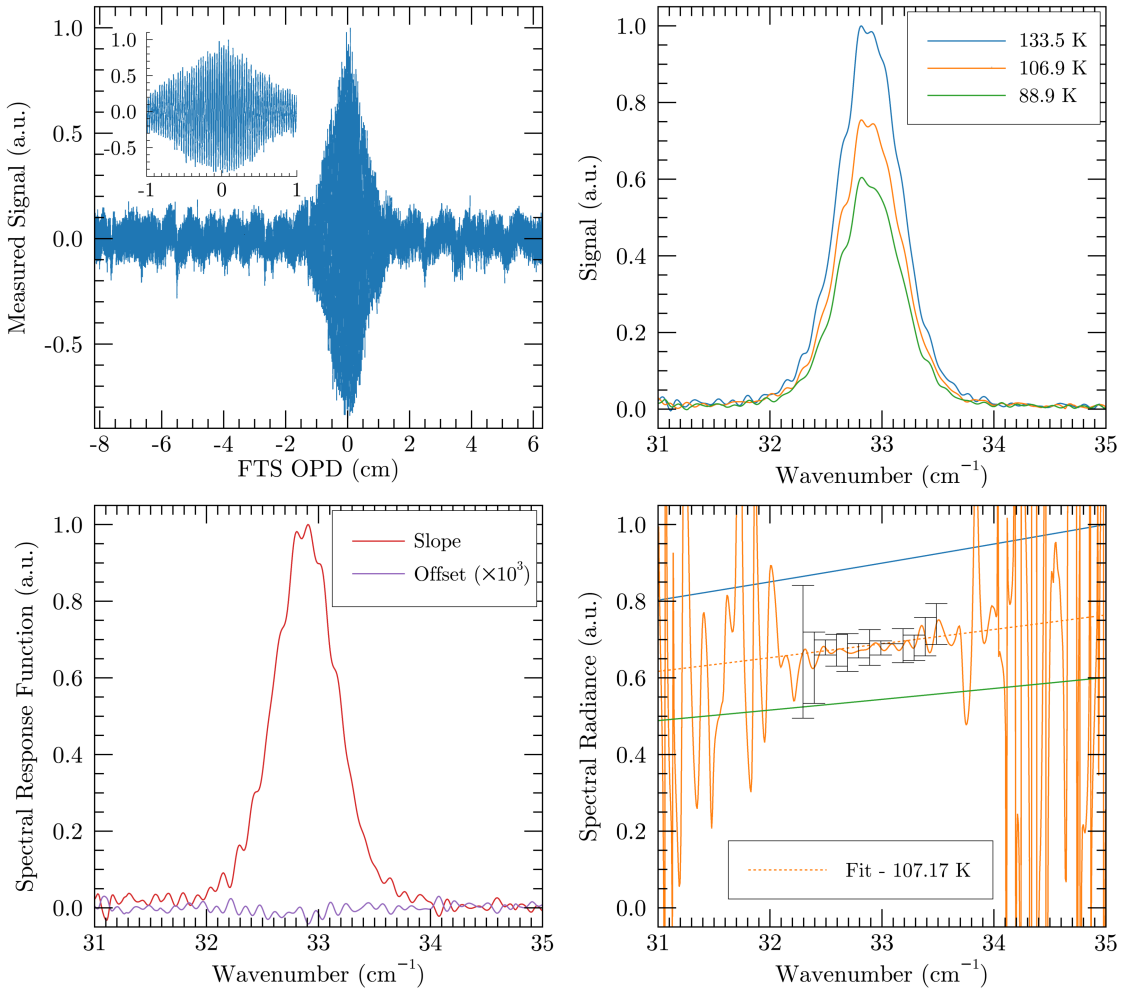

Figure 5.4: The PDPFTS calibration process. Top Left: Example interferogram. Top Right: Recovered spectra showing the grating profile at three different blackbody temperatures. Bottom Left: The SRF derived from two of the recovered spectra. Bottom Right: The calibrated spectra (solid lines) compared to their associated Planck curve (dashed lines). The calibrated spectra used to derive the calibration perfectly match the Planck curve. A Planck curve was fit to the unknown spectrum weighted by uncertainty values. A subset of error bars are plotted to show the uncertainty.

The top left plot in Figure 5.4 shows an example of a measured interferogram. With the grating restricting the spectral bandwidth measured by the detector, an increase in the coherence length can be seen in the reciprocal space as the interferogram is broadened around ZPD. The top right plot shows the recovered spectra for all three blackbody temperatures. The Gaussian-like grating profile can be seen in the recovered spectra with minor structure introduced from channel fringes within the instrument. The bottom left plot shows the SRF slope and offset derived from using the 133.50(5) K and 88.90(5) K recovered spectra. The

bottom right plot shows the calibrated spectra by applying the SRF to the recovered spectra. A Planck curve for the best-fit temperature was found for the unknown 106.90(5) K spectrum. This fit was weighted by uncertainty values where the signal strength was at least 10 % of the peak value. Outside of the grating profile, the spectrum is noise dominant and should not be considered as part of the spectral response. A subset of the uncertainty values are shown on the plot as error bars for reference. The best-fit Planck curve temperature had a value of 107.1680(6) K while the expected black body temperature was 106.90(5) K. This shows excellent PDPFTS intensity calibration with a 0.25 % difference. The non-linear effects seen in Section 5.2.1 were not present with the post-dispersion element limiting the amount of radiation incident on the detector.

For completeness, I searched for a harmonic in the post-dispersed spectra which would indicate detector non-linearity. Figure 5.5 shows the recovered post-dispersed spectra with an extended x-axis. For these spectra, a harmonic indicating detector non-linearity would occur at 66 cm^{-1}. With sufficient smoothing of the data, a feature of less than one percent can be found at the second harmonic. When compared to the prominent 10 % out-of-band signal in Figure 5.3, the small harmonic feature in the post-dispersed spectra is lost within the noise and indicates that the detector was behaving in the linear regime. One feature of note in these post-dispersed spectra is the smaller peak at 16.5 cm^{-1} arising from the second order of diffraction from the grating. From the grating equation, Equation (4.1), for a set angle of incidence the second order of diffraction will occur at twice the wavelength, or half the wavenumber. Other features can be seen arising from $1/f$ noise and the pulses transmitted from the pulse tube cryocoolers (PTCs). With the scan speed of the FTS set at 0.18 $\mathrm{cm\,s}^{-1}$, the $1/f$ noise has fully decayed by 10 cm^{-1} (1.8 Hz), and the sharp peak at $\sim 7.8\,\mathrm{cm}^{-1}$, alongside its harmonics, are correlated with the 1.4 Hz pulses from the PTCs.

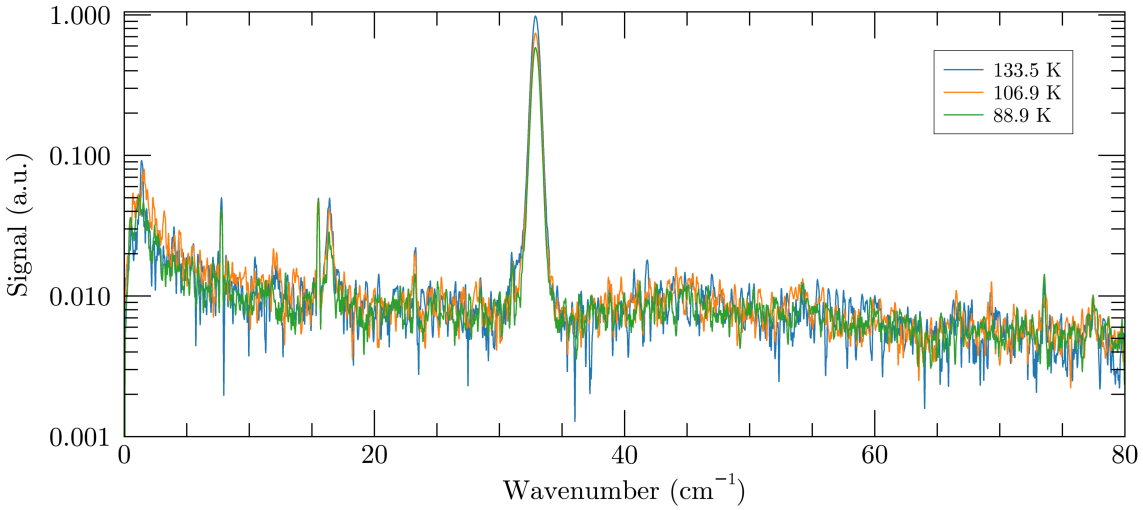

Figure 5.5: The recovered post-dispersed spectra for three blackbody temperatures show the detector operating in the linear regime with no evidence of a harmonic at 66 cm^{-1}.

5.2.3 Resolving Power

The next step in demonstrating the performance of the PDPFTS was to determine the spectral resolving power for both the diffraction grating module and the FTS. This was accomplished by simulating and measuring interferograms of realistic astronomical spectra consisting of a continuum and an unresolved absorption feature. The diffraction grating module post-disperses a narrow portion of the continuum onto the detector and the photomixer line source would be tuned to place an absorption feature into this narrow band.

At a given blackbody temperature, the diffraction grating was rotated such that the desired wavenumber of radiation would be incident on the detector and the FTS was scanned. The spectral resolving power of the diffraction grating was determined by measuring the continuum at three points across the band: 20.0 cm^{-1}, 24.9 cm^{-1}, and 33.9 cm^{-1}. A Gaussian fit was performed on the resulting continuum measurements with the full width half maximum (FWHM) of the fit being used to determine the resolving power. In Figure 5.6, a recovered spectrum at 32.9 cm^{-1} shows the grating profile and its Gaussian fit with minimal deviations due to channel fringes within the instrument. Of note, the wings of the grating profile are exceptionally clean, showing no stray reflections as seen in previous measurements with a room temperature FTS coupled to the grating [53, 54, 55].

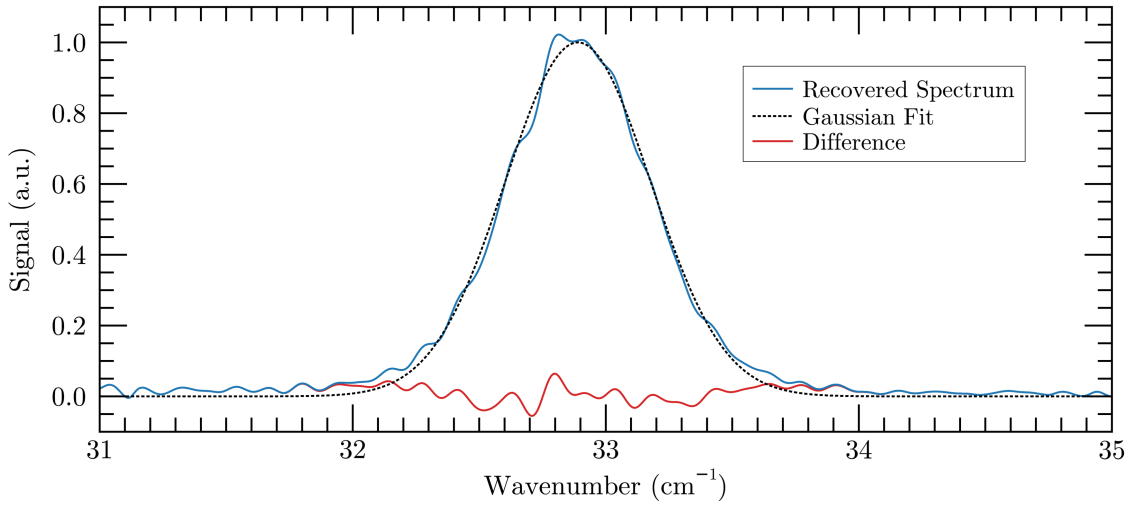

Figure 5.6: The recovered spectrum from a continuum measurement showing the diffraction grating profile and a Gaussian fit. The Gaussian fit was used to determine the spectral resolution of the diffraction grating.

To determine the resolving power of the FTS, an unresolved absorption feature was superimposed onto the continuum measurements mentioned above. The photomixer was tuned to place an absorption feature at the center of the grating profile and interferograms were measured. To find the spectral resolution of the FTS, the absorption feature was isolated from the continuum. The continuum contribution to the recovered spectrum was determined by multiplying the Planck curve for the recorded blackbody temperature with the instrumental SRF found using the calibration data from Section 5.2.2. By subtracting this continuum contribution from the recovered spectrum, the absorption feature can be isolated. The top plot in Figure 5.7 shows an example of the simulated astronomical spectrum measured at 32.9 cm^{-1} by the PDPFTS. The continuum contribution is superimposed on top of the recovered spectrum and the bottom plot shows the absorption feature isolated from the continuum using this calibration data. The isolated line feature is very well fit by the sinc profile canonical of an FTS [15]. The FWHM of the sinc profile was used to find the experimental spectral resolution of the FTS.

A slight asymmetry is evident in the isolated absorption feature when compared with the sinc profile. It is suspected that this asymmetry is introduced from the input polarizer. As discussed in Chapter 3, QMC Instruments [59] had manufactured a first-of-their-kind

polarizer with matching wire grids deposited on both sides of the substrate. While this was ideal for the polarizing beamsplitter in the FTS, it introduced a small phase imbalance in the source module. Given that the absorption feature is superimposed onto a continuum by encoding the two sources with opposite polarizations, the line source and blackbody are placed on opposite sides of the input polarizer. Light from the photomixer is transmitted through the polarizer and passes through its substrate once, while light from the blackbody is reflected and does not encounter the substrate. In cases where the transmitted and reflected light from the input polarizer or output analyzer are used, such as the case with the PRobe far-Infrared Mission for Astrophysics (PRIMA) [24, 25], wire grid polarizers with no underlying substrate should be used to avoid this calibration issue.

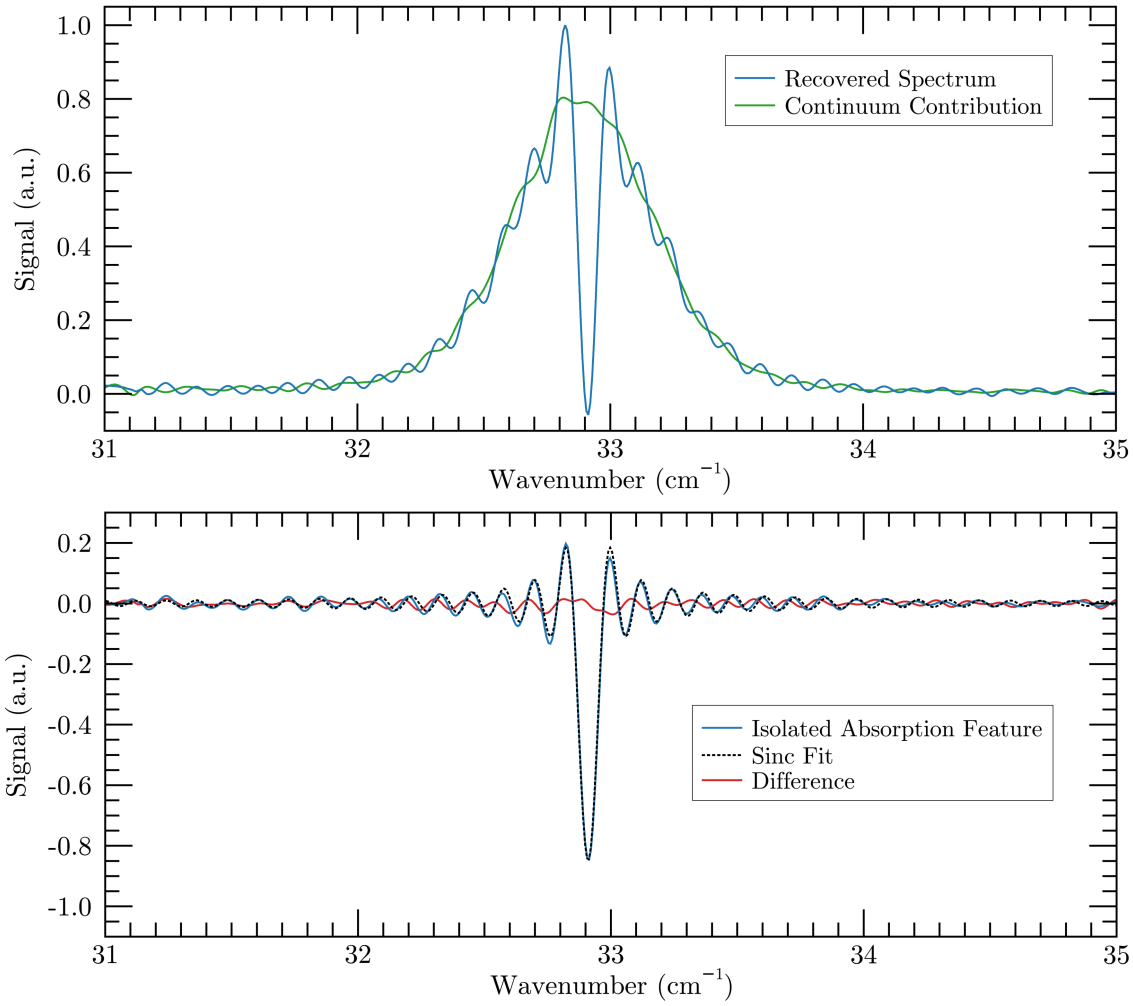

Figure 5.7: The line feature extraction process. Top: A recovered spectrum containing an absorption line feature and a calibrated grating profile representing a continuum only measurement. Bottom: The absorption feature isolated from the recovered spectrum.

The experimental resolving power for the diffraction grating and FTS were compared against theory over the wavenumber range of $20\,\mathrm{cm}^{-1}$ to $35\,\mathrm{cm}^{-1}$. The top plot in Figure 5.8 shows the experimental resolving power measurements and the middle plot shows the post-dispersed continuum measurements and superimposed absorption features used to determine the experimental resolving power following the steps outlined above.

The diffraction grating theory assumed slit-limited resolving power. The diffraction grating achieved a resolving power of $R\,121(1)$ at $20.0\,\mathrm{cm}^{-1}$, $R\,83.5(7)$ at $24.9\,\mathrm{cm}^{-1}$, and $R\,57.2(3)$ at $32.9\,\mathrm{cm}^{-1}$. The experimental resolving power for the diffraction grating was determined to be approximately 70 % of theory. As the SCAL [13] blackbody element used in the source is disk shaped and had to be positioned slightly away from the entrance slit, it is suspected that a convolution of the 5 mm diameter blackbody element and the 2.1 mm entrance slit is making the effective entrance slit size appear larger than expected. There were discussions about modifying the blackbody element into a linear shape mimicking the slit but the element was left unchanged for these first tests. To account for the path from either end of the source making its way through the entrance slit, I chose to model the slit-limited theory with a larger effective entrance slit size of 4.2 mm.

With respect to the resolving power of the FTS itself, the single-sided scan length for these measurements of $8.1(3)\,\mathrm{cm}$ gave a theoretical spectral resolution of $0.062(2)\,\mathrm{cm}^{-1}$. Due to the challenges associated with controlling the FTSM around its center of travel, the maximum OPD differed slightly from one observation to the next. Fourier analysis of the measured interferograms yielded a spectral resolution of $0.0639(8)\,\mathrm{cm}^{-1}$ at $20.0\,\mathrm{cm}^{-1}$, $0.0631(2)\,\mathrm{cm}^{-1}$ at $24.9\,\mathrm{cm}^{-1}$, and $0.0609(4)\,\mathrm{cm}^{-1}$ at $32.9\,\mathrm{cm}^{-1}$. In an ideal FTS, the scan length would not vary, the spectral resolution would remain unchanged for all measurements, and the resolving power would increase linearly with wavenumber. The experimental results shown in Figure 5.8 follow theory, achieving a resolving power of $R\,313(4)$, $R\,393(1)$, and $R\,540(3)$ at $20.0\,\mathrm{cm}^{-1}$, $24.9\,\mathrm{cm}^{-1}$, and $32.9\,\mathrm{cm}^{-1}$, respectively.

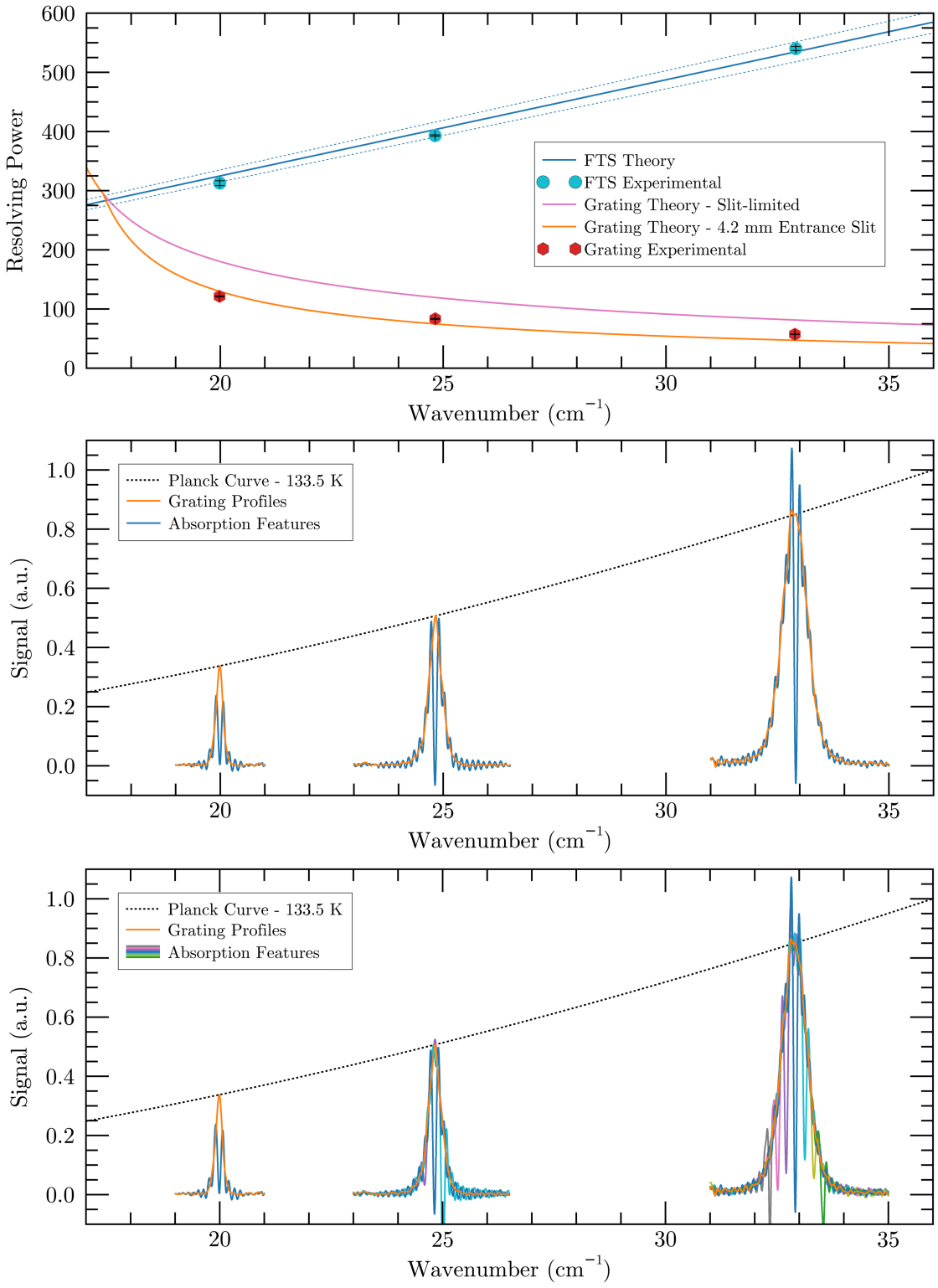

Figure 5.8: Top: Comparison between theoretical and experimental resolving power for the low resolution diffraction grating and high resolution FTS that form the PDPFTS. Middle: Recovered spectra showing the grating profiles and absorption features used to determine the experimental resolving power of the PDPFTS. Bottom: Recovered spectra with multiple absorption features tuned across the grating profile highlighting the difference in resolving power between the grating and FTS.

The three measurements made across the band shown in Figure 5.8 emphasize the difference in resolving power between the diffraction grating spectrometer and the FTS. The number of line features that can be superimposed within a post-dispersed continuum spectum is directly related to the ratio between the FTS resolving power and the grating resolving power. When looking at the top plot in Figure 5.8, the difference in resolving power is on the order of ~ 2.6 times at $20.0\,\mathrm{cm}^{-1}$. When looking at the bottom plot, only a single line feature was superimposed within the continuum spectrum. Moving onto the measurements at $32.9\,\mathrm{cm}^{-1}$, the difference in resolving power is around ~ 9.5 times. As a direct result, the number of line features that are superimposed with the continuum spectrum increases from one at $20.0\,\mathrm{cm}^{-1}$ to seven at $32.9\,\mathrm{cm}^{-1}$.

Figure 5.8 serves as the proof for the operation of a fully cryogenic far-infrared PDPFTS. While measurements were only made at three different wavenumbers due to the limited time available for tests, these data demonstrate the intensity and spectral calibration of the PDPFTS presented in this thesis. The high resolving power of the FTS is able to super resolve and isolate the line features from a continuum within the post-dispersed micro-spectra. A complete broadband spectrum can be reconstructed by stitching together many thousands of these micro-spectra, achieving the high resolution, the broad spectral coverage, and the ultra-high sensitivity necessary for the next generation of far-infrared space astronomy missions.

Chapter 6

Conclusion

> But that is the beginning of a new story – the story of the gradual renewal of a man, the story of his gradual regeneration, of his passing from one world into another, of his initiation into a new unknown life. That might be the subject of a new story, but our present story is ended.
>
> Fyodor Dostoevsky
> Crime and Punishment

This thesis presented the development of the Large Facility Cryostat (LFC), a large volume 4 K closed-cycle cryostat purpose built for the development and integration of far-infrared astronomical instrumentation. The design, assembly, and initial testing of the LFC are covered in Chapter 2. The hybrid post-dispersed polarizing Fourier transform spectrometer (PDPFTS) concept is the largest instrumental configuration that the Astronomical Instrumentation Group (AIG) at the University of Lethbridge has integrated. It was necessary to build a new cryostat so that the entirety of the PDPFTS that forms the basis of my thesis could be cooled to 4 K. This cryostat is unique in Canada and was essential for the work covered in this thesis. The PDPFTS integrated into this cryostat consists of four separate modules: the source module, the Fourier-transform spectrometer (FTS) module, the diffraction grating module, and the detector module. The design of these four modules is covered in Chapter 3. While the previously mentioned LFC was under construction, results were obtained for a preliminary room temperature implementation of the instrument. These preliminary results are presented in Chapter 4.

With the construction of the LFC completed, the culmination of this work is presented in Chapter 5 with the fully cryogenic integration of the PDPFTS. The first light intensity and spectral measurements for a fully cryogenic far-infrared PDPFTS are the key results of this thesis. Figure 5.4 highlights the exceptional calibration accuracy as a result of operating the PDPFTS in a closed cryostat with a 4 K background. The spectral calibration and resolving power for both the low resolution diffraction grating and high resolution FTS that form the PDPFTS are presented in Figure 5.8. Despite the issues that are not uncommon with testing an instrument for the first time, the PDPFTS concept demonstrates how a complete broadband spectrum can be reconstructed from many post-dispersed micro-spectra to achieving high spectral resolution, broad spectral coverage, and exploit the sensitivity of modern detectors that are necessary for future far-infrared space astronomy missions.

The work presented in this thesis builds upon the shoulders of earlier students, the expertise within the University of Lethbridge AIG, and our industrial partners. The Test Facility Cryostat (TFC) designed by Veenendaal [26], the precursor cryostat that informed a lot of decisions around the development of the LFC, was a Master's thesis. The bolometer detector used in the PDPFTS was designed by Gom [56, 57] as a Master's thesis. The diffraction grating spectrometer designed by Anderson [53, 54, 55] used to post-disperse the output of the FTS was a Master's thesis. The laser metrology system designed by Christiansen [79] used to record the position of the PDPFTS scanning mechanism was a PhD thesis. A novel source module was developed at the AIG to simulate realistic astronomical spectra in order to demonstrate the performance of the PDPFTS. The cryogenic Fourier-transform spectrometer mechanism (FTSM) designed by ABB [49, 50, 51, 52] provided the phase delay in the FTS. My contributions to this effort were to bring all these separate components together, build the necessary cryogenic test facility, design the Fourier-transform spectrometer optics (FTSO) around the FTSM, integrate the source, FTS, diffraction grating, and detector into the LFC, and perform the first light measurements. With these measurements, I demonstrated the intensity and spectral calibration for a fully cryogenic far-infrared PDPFTS.

6.1 Outlook

The work performed in this thesis and the lessons learned will be valuable in guiding the development of such hybrid spectrometers being proposed for future far-infrared space observatories. The reconstruction of a broadband spectrum from thousands of micro-spectra will require a well thought out calibration strategy, that in all likelihood will employ a source module similar to the one presented in this thesis. The design of instrumentation that operates at 4 K is challenging due to the change in thermal, electrical, and mechanical material properties that occur when cooled to temperatures approaching absolute zero. Optimizing the servo control of a complex system at 4 K with little available power due to stringent heat dissipation limits poses a significant obstacle. To keep power dissipation to a minimum, ABB had developed a novel stiffness compensated FTS scan mechanism [49, 50, 51, 52]. When performing measurements at 4 K after an accelerated lifetime testing, the FTSM did not work as expected and we were limited to obtaining data over half of its travel. However, it was still sufficient to prove the PDPFTS concept and we were able to obtain results for both intensity and spectral calibrations using the high resolution FTS to super-resolve the low resolution grating. Figure 6.1 presents the resolving power measurements from Chapter 5, highlighting the potential increase in FTS spectral resolution had we been able to collect data over the full travel of the FTSM.

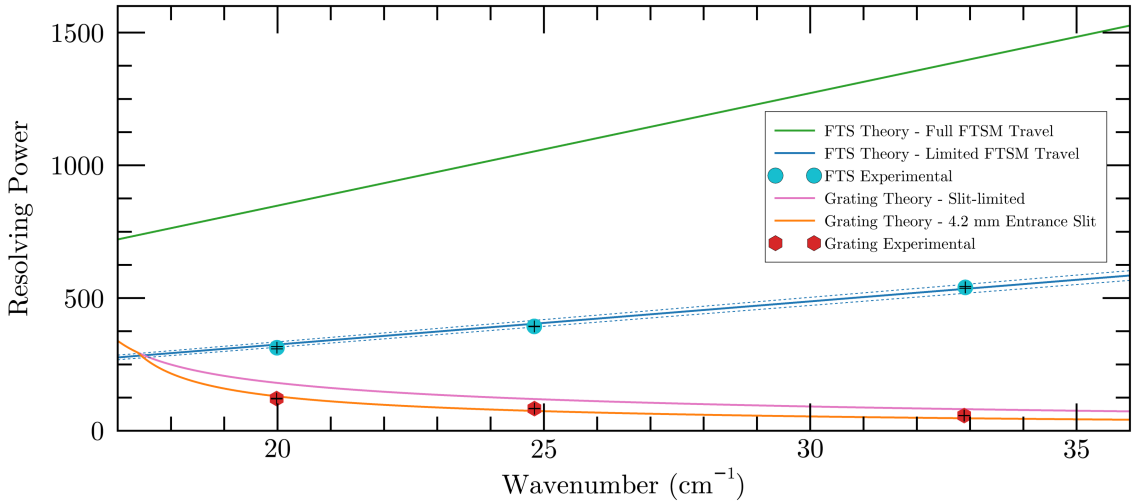

Figure 6.1: A comparison between the actual performance of the PDPFTS and the potential increase in the FTS spectral resolution with the full scan length of the FTSM.

The PDPFTS instrument concept presented in this thesis is widely considered by the European Space Agency (ESA), the Japan Aerospace Exploration Agency (JAXA), and the National Aeronautics and Space Administration (NASA) to be the leading candidate for a future far-infrared space astronomy mission. This instrument concept is fundamental to the advancement of high-priority science cases such as understanding the formation mechanism of exoplanets in protoplanetary disks [21], the evolution of high redshift galaxies over cosmic time scales [22], and a more diverse set of science cases presented in the PRobe far-Infrared Mission for Astrophysics (PRIMA) science book [23]. The PDPFTS instrument concept has been adopted for the PRIMA proposal [24, 25]. The PRIMA mission is currently under review by NASA, and we are hoping that it is selected so that the PDPFTS has a path-to-flight. If this is the case, it is expected that the work conducted in this thesis may refine and focus further research needs for the operation of a fully cryogenic far-infrared PDPFTS. The next steps will be to explore the performance of this hybrid instrument concept when using state-of-the-art microwave kinetic inductance detectors (MKIDs) with 4 orders of magnitude more sensitivity. However, it is not expected that the calibration strategy for the PRIMA PDPFTS will fundamentally change which speaks to the importance of the work presented in this thesis.

Bibliography

[1] I. S. Glass. *Handbook of Infrared Astronomy*. Cambridge Observing Handbooks for Research Astronomers. Cambridge: Cambridge University Press, 1999. ISBN: 978-0-521-63311-6. DOI: 10.1017/CBO9780511564949.

[2] *James Clerk Maxwell Telescope – Operated by East Asian Observatory*. Apr. 2024. URL: https://www.eaobservatory.org/jcmt/ (visited on 05/06/2024).

[3] *SMA Observer Center*. URL: http://sma1.sma.hawaii.edu/ (visited on 05/06/2024).

[4] University of Hawaii Institute for Astronomy. *Mauna kea Observatories*. URL: https://about.ifa.hawaii.edu/facility/mauna-kea-observatories/ (visited on 04/29/2024).

[5] *ALMA Observatory — ALMA*. URL: https://www.almaobservatory.org/en/home/ (visited on 05/06/2024).

[6] *CCAT-Prime*. URL: https://www.ccatobservatory.org/ (visited on 05/06/2024).

[7] *South Pole Telescope, Antarctica — Center for Astrophysics — Harvard & Smithsonian*. URL: https://www.cfa.harvard.edu/facilities-technology/telescopes-instruments/south-pole-telescope-antarctica (visited on 05/06/2024).

[8] NASA. *Atmospheric electromagnetic transmittance or opacity*. 2007. URL: https://commons.wikimedia.org/wiki/File:Atmospheric_electromagnetic_transmittance_or_opacity.jpg (visited on 01/22/2024).

[9] R. Hopwood et al. "Systematic characterization of the Herschel SPIRE Fourier Transform Spectrometer". In: *Monthly Notices of the Royal Astronomical Society* 449.3 (May 2015), pp. 2274–2303. ISSN: 0035-8711. DOI: 10.1093/mnras/stv353.

[10] G. Neugebauer et al. "The Infrared Astronomical Satellite (IRAS) mission." In: *The Astrophysical Journal* 278 (Mar. 1984), pp. L1–L6. ISSN: 0004-637X. DOI: 10.1086/184209.

[11] M. F. Kessler et al. "The Infrared Space Observatory (ISO) mission." In: *Astronomy and Astrophysics* 315 (Nov. 1996), pp. L27–L31. ISSN: 0004-6361.

[12] Hiroshi Murakami et al. "The Infrared Astronomical Mission AKARI". In: *Publications of the Astronomical Society of Japan* 59.sp2 (Oct. 2007), S369–S376. ISSN: 0004-6264. DOI: 10.1093/pasj/59.sp2.S369.

[13] Peter Hargrave, Tim Waskett, Tanya Lim, and Bruce Swinyard. "Performance of flight-model on-board calibration sources on Herschel-SPIRE". In: *Millimeter and Submillimeter Detectors and Instrumentation for Astronomy III*. Vol. 6275. SPIE, June 2006, pp. 353–364. DOI: 10.1117/12.673197.

[14] J. J. A. Baselmans, F. Facchin, A. Pascual Laguna, J. Bueno, D. J. Thoen, V. Murugesan, N. Llombart, and P. de Visser. "Ultra-sensitive Super-THz Microwave Kinetic Inductance Detectors for future space telescopes". In: *Astronomy & Astrophysics* 665 (Sept. 2022), A17. ISSN: 0004-6361, 1432-0746. DOI: 10.1051/0004-6361/202243840.

[15] Sumner P. Davis, Mark C. Abrams, and James W. Brault. *Fourier transform spectrometry*. Academic Press, Jan. 2001. ISBN: 978-0-12-042510-5.

[16] John C. Mather. "Bolometer noise: nonequilibrium theory". In: *Applied Optics* 21.6 (Mar. 1982). Publisher: Optica Publishing Group, pp. 1125–1129. ISSN: 2155-3165. DOI: 10.1364/AO.21.001125.

[17] D. H. Martin and E. Puplett. "Polarised interferometric spectrometry for the millimetre and submillimetre spectrum". In: *Infrared Physics* 10.2 (June 1970), pp. 105–109. ISSN: 0020-0891. DOI: 10.1016/0020-0891(70)90006-0.

[18] P. R. Roelfsema et al. "SPICA—A Large Cryogenic Infrared Space Telescope: Unveiling the Obscured Universe". In: *Publications of the Astronomical Society of Australia* 35 (Jan. 2018). Publisher: Cambridge University Press, e030. ISSN: 1323-3580, 1448-6083. DOI: 10.1017/pasa.2018.15.

[19] David Clements, Stephen Serjeant, and Shoko Jin. "Explain ESA's last-minute ditching of new space telescope". In: *Nature* 587.7835 (Nov. 2020). Publisher: Nature Publishing Group, pp. 548–548. DOI: 10.1038/d41586-020-03288-z.

[20] National Academies of Sciences, Engineering, and Medicine. *Pathways to Discovery in Astronomy and Astrophysics for the 2020s*. Washington, DC, 2021: The National Academies Press, 2021. URL: https://nap.nationalacademies.org/catalog/26141/pathways-to-discovery-in-astronomy-and-astrophysics-for-the-2020s (visited on 01/31/2024).

[21] I. Kamp et al. "The formation of planetary systems with SPICA". In: *Publications of the Astronomical Society of Australia* 38 (Jan. 2021). ISSN: 1323-3580, 1448-6083. DOI: 10.1017/pasa.2021.31.

[22] Luigi Spinoglio et al. "Mid-IR cosmological spectrophotometric surveys from space: Measuring AGN and star formation at the cosmic noon with a SPICA-like mission". In: *Publications of the Astronomical Society of Australia* 38 (Jan. 2021). ISSN: 1323-3580, 1448-6083. DOI: 10.1017/pasa.2021.13.

[23] A. Moullet, T. Kataria, D. Lis, S. Unwin, Y. Hasegawa, E. Mills, C. Battersby, A. Roc, and M. Meixner. *PRIMA General Observer Science Book*. Oct. 2023. DOI: 10.48550/arXiv.2310.20572.

[24] NASA Jet Propulsion Laboratory. *PRIMA The PRobe far-Infrared Mission for Astrophysics*. URL: https://prima.ipac.caltech.edu/ (visited on 04/24/2024).

[25] NASA Jet Propulsion Laboratory. *PRIMA Fact Sheet*. Jan. 2024. URL: https://prima.ipac.caltech.edu/page/fact-sheet (visited on 04/24/2024).

[26] Ian Veenendaal. “A Cryogenic test facility”. MA thesis. Lethbridge, Alta : University of Lethbridge, Dept. of Physics and Astronomy, 2016. URL: https://hdl.handle.net/10133/4420 (visited on 01/31/2024).

[27] Jack Ekin. *Experimental Techniques for Low-Temperature Measurements: Cryostat Design, Material Properties and Superconductor Critical-Current Testing*. Great Clarendon Street, Oxford OX2 6DP: Oxford University Press, Oct. 2006. ISBN: 978-0-19-171771-0. DOI: 10.1093/acprof:oso/9780198570547.001.0001.

[28] Astronomical Instrumentation Group. *Large Volume Cryogenic Test Facility (LFC) Specifications*. Tech. rep. University of Lethbridge, 2020.

[29] Bruce Swinyard and Takao Nakagawa. “The space infrared telescope for cosmology and astrophysics: SPICA A joint mission between JAXA and ESA”. In: *Experimental Astronomy* 23.1 (Mar. 2009), pp. 193–219. ISSN: 1572-9508. DOI: 10.1007/s10686-008-9090-0.

[30] MatWeb. *304 Stainless Steel*. URL: https://www.matweb.com/search/datasheet.aspx?MatGUID=abc4415b0f8b490387e3c922237098da&ckck=1 (visited on 09/12/2023).

[31] MatWeb. *Aluminum 6061-T6; 6061-T651*. URL: https://www.matweb.com/search/datasheet.aspx?matguid=b8d536e0b9b54bd7b69e4124d8f1d20a (visited on 09/12/2023).

[32] Clearwater Composites LLC. *1/2” X 0.570” Carbon Fiber Tube 72” Length*. URL: https://www.clearwatercomposites.com/product/1-2-x-0-570-carbon-fiber-tube-72-length-4/ (visited on 09/22/2023).

[33] Henkel. *LOCTITE® STYCAST 2850FT*. URL: https://www.henkel-adhesives.com/ca/en/product/potting-compounds/loctite_stycast_2850ft3.html (visited on 09/22/2023).

[34] Y. J. Chen, X. J. Ren, P. Zhang, T. Zhang, and A. B. Wu. “Measurement of Thermal Conductivity of CFRPs and Thermal Conductance of the Cold-to-Warm Joint at Low Temperatures”. In: *IEEE Transactions on Applied Superconductivity* 22.3 (June 2012), pp. 7700704–7700704. ISSN: 1558-2515. DOI: 10.1109/TASC.2011.2177231.

[35] William H. Press, Saul A. Teukolsky, William T. Vetterling, and Brian P. Flannery. *Numerical Recipes: The Art of Scientific Computing*. 3rd. Cambridge University Press, Sept. 2007. ISBN: 978-0-521-88068-8.

[36] R. L. Schmitt, G. Tatkowski, M. Ruschman, S. Golwala, N. Kellaris, M. Daal, J. Hall, and E. W. Hoppe. “Thermal conductance measurements of bolted copper joints for SuperCDMS”. In: *Cryogenics* 70 (Sept. 2015), pp. 41–46. ISSN: 0011-2275. DOI: 10.1016/j.cryogenics.2015.04.006.

[37] NIST. *Cryogenic Technology Resources*. URL: https://trc.nist.gov/cryogenics/ (visited on 09/29/2023).

[38] Cryomech. *PT415 Cryocoolers*. URL: https://www.cryomech.com/products/pt415/ (visited on 09/14/2023).

[39] Yunus A Çengel and Afshin J Ghajar. *Heat and Mass Transfer: Fundamentals and Applications*. McGraw-Hill Education, Mar. 2019. ISBN: 978-0-07-339819-8.

[40] Gold Plating Services. *24K Pure Gold Bath Plating Solution*. URL: https://www.goldplating.com/products/24k-pure-gold-solution (visited on 09/14/2023).

[41] Paul A. Kohl. "Electrodeposition of Gold". en. In: *Modern Electroplating*. Section: 4. John Wiley & Sons, Ltd, 2010, pp. 115–130. ISBN: 978-0-470-60263-8.

[42] Gold Plating Services. *Gold Replenisher for 24K, 18K, 14K Bright Gold & Pure Gold Solutions*. URL: https://www.goldplating.com/products/24k-bright-gold-replenisher (visited on 09/14/2023).

[43] Max Born and Emil Wolf. *Principles of Optics: Electromagnetic Theory of Propagation, Interference and Diffraction of Light*. 7th ed. Cambridge: Cambridge University Press, 1999. DOI: 10.1017/CBO9781139644181.

[44] Michelle Froese. *What is lap shear strength in an epoxy?* Nov. 2020. URL: https://fastenerengineering.com/what-is-lap-shear-strength-in-an-epoxy/ (visited on 10/03/2023).

[45] Lake Shore. *NRC-2 Superinsulation*. URL: https://www.lakeshore.com/docs/default-source/product-downloads/installation-instructions/f069-00-00.pdf?sfvrsn=751757f9_4 (visited on 10/02/2023).

[46] Amphenol Industrial. *PT / 26482 Series 1*. URL: https://amphenol-industrial.com/products/pt-26482-series-1/ (visited on 06/14/2024).

[47] ITT Cannon. *Micro Series*. URL: https://www.ittcannon.com/micro (visited on 06/14/2024).

[48] Edwards Ltd. *XDS35i DRY SCROLL PUMPS*. Mar. 2024. URL: https://www.edwardsvacuum.com/content/dam/brands/edwards-vacuum/edwards-website-assets/scientific-vacuum/documents/datasheets/Edwards-XDS35i-Dry-Scroll-Pump-PD-3601-0458-01.pdf (visited on 03/27/2024).

[49] Alain Cournoyer et al. "Design of a novel cryogenic stiffness-compensated reactionless scan mechanism for the Fourier transform spectrometer of SPICA SAFARI instrument". In: *Millimeter, Submillimeter, and Far-Infrared Detectors and Instrumentation for Astronomy X*. Vol. 11453. SPIE, Dec. 2020, pp. 526–545. DOI: 10.1117/12.2560530.

[50] Alain Cournoyer et al. "A Novel Cryogenic Scan Mechanism Design for the Post-Dispersed Polarizing FTS of the SPICA SAFARI Instrument". In: *OSA Optical Sensors and Sensing Congress 2021 (AIS, FTS, HISE, SENSORS, ES)*. Optica Publishing Group, July 2021, FM5C.6. DOI: 10.1364/FTS.2021.FM5C.6.

[51] Alain Cournoyer et al. "Cryogenic testing towards TRL-5 demonstration of a novel stiffness-compensated, reactionless scan mechanism for the Fourier transform spectrometer of SPICA SAFARI instrument". In: *Millimeter, Submillimeter, and Far-Infrared Detectors and Instrumentation for Astronomy XI*. Vol. 12190. SPIE, Aug. 2022, pp. 1015–1030. DOI: 10.1117/12.2627861.

[52] Alain Cournoyer et al. “Cryogenic Testing and Performance Characterization of a Novel Stiffness-compensated, Reactionless Scan Mechanism for a Far-infrared Post-dispersed Polarizing Fourier Transform Spectrometer”. In: *Optica Sensing Congress 2023 (AIS, FTS, HISE, Sensors, ES)*. Optica Publishing Group, July 2023, FM4B.5. DOI: 10.1364/FTS.2023.FM4B.5.

[53] Alicia May Anderson. “Development of the dispersing component for a cryogenic post-dispersed polarizing Fourier transform spectrometer”. MA thesis. Lethbridge, Alta. : University of Lethbridge, Dept. of Physics and Astonomy, 2022. URL: https://hdl.handle.net/10133/6214 (visited on 01/31/2024).

[54] Alicia M. Anderson, David A. Naylor, Brad G. Gom, Ian T. Veenendaal, Adam J. Christiansen, Willem Jellema, and Peter A. R. Ade. “Determining the efficiency of a cryogenic far-infrared diffraction grating spectrometer used as a post-dispersing module for a high-resolution spectrometer”. In: *Millimeter, Submillimeter, and Far-Infrared Detectors and Instrumentation for Astronomy XI*. Vol. 12190. SPIE, Aug. 2022, pp. 995–1006. DOI: 10.1117/12.2628259.

[55] Alicia M. Anderson, David A. Naylor, Brad G. Gom, Matthew A. Buchan, Adam J. Christiansen, and Ian T. Veenendaal. “Development and validation of a cryogenic far-infrared diffraction grating spectrometer used to post-disperse the output from a Fourier transform spectrometer”. In: *Review of Scientific Instruments* 95.1 (Jan. 2024), p. 015116. ISSN: 0034-6748, 1089-7623. DOI: 10.1063/5.0177603.

[56] Bradley Gustav Gom. “A cryogenic detector for submillimetre astronomy”. MA thesis. Lethbridge, Alta. : University of Lethbridge, Faculty of Arts and Science, 1999, 1999. URL: https://hdl.handle.net/10133/102 (visited on 01/31/2024).

[57] D. A. Naylor, B. G. Gom, P. A. R. Ade, and J. E. Davis. “Design and performance of a dual polarizing detector system for broadband astronomical spectroscopy at submillimeter wavelengths”. In: *Review of Scientific Instruments* 70.10 (Oct. 1999). Publisher: AIP Publishing, pp. 4097–4109. ISSN: 0034-6748. DOI: 10.1063/1.1149304.

[58] M. J. Griffin et al. “The Herschel-SPIRE instrument and its in-flight performance”. In: *Astronomy and Astrophysics* 518 (July 2010), p. L3. ISSN: 0004-6361, 1432-0746. DOI: 10.1051/0004-6361/201014519.

[59] QMC Instruments. *QMC Instruments Ltd - The Home of Terahertz Optics & Detectors*. URL: https://www.qmcinstruments.co.uk (visited on 01/31/2024).

[60] Anthony Irving Huber. “Exploring the challenges of a far-infrared post-dispersed polarising Fourier transform spectrometer”. MA thesis. Lethbridge, Alta. : University of Lethbridge, Dept. of Physics and Astronomy, 2021. URL: https://hdl.handle.net/10133/6068 (visited on 05/14/2024).

[61] Lake Shore. *Cernox®*. URL: https://www.lakeshore.com/products/categories/overview/temperature-products/cryogenic-temperature-sensors/cernox (visited on 04/07/2024).

[62] Vishay. *High Precision Wraparound - Wide Ohmic Value Range Thin Film Chip Resistors, Sulfur Resistant*. Oct. 2022. URL: https://www.vishay.com/docs/53017/p.pdf (visited on 04/07/2024).

[63] Photodigm. *PH780DBR Series High-Power Single-Frequency Laser Diode*. Mar. 2023. URL: https://www.photodigm.com/products/780-nm-laser-diode (visited on 03/22/2023).

[64] Emilien Peytavit, Guillaume Ducournau, and Jean-Francois Lampin. "THz Photomixers". In: *Fundamentals of terahertz devices and applications*. Ed. by Dimitris Pavlidis. Wiley, Aug. 2021. URL: https://hal.science/hal-03282222 (visited on 01/31/2024).

[65] Backman Technologies. *PB1319 Photomixers*. URL: https://www.bakmantechnologies.com/PB1319-photomixer.php (visited on 01/31/2024).

[66] MatWeb. *Polyplastics TOPAS® 5013 Cyclic Olefin Copolymer (COC) (Asia/Pacific Grade)*. URL: https://www.matweb.com/search/datasheet.aspx?matguid=036e6bd32666489ab367a44a7852da5d&ckck=1 (visited on 01/29/2024).

[67] Kristian Nielsen, Henrik K. Rasmussen, Aurèle J. L. Adam, Paul C. M. Planken, Ole Bang, and Peter Uhd Jepsen. "Bendable, low-loss Topas fibers for the terahertz frequency range". In: *Optics Express* 17.10 (May 2009). Publisher: Optica Publishing Group, pp. 8592–8601. ISSN: 1094-4087. DOI: 10.1364/OE.17.008592.

[68] B-Con Engineering Inc. *Optics - Aspheric, Diamond Turned, Freeform, Plastic - B-Con Engineering*. URL: http://www.bconeng.com/ (visited on 01/17/2024).

[69] David A. Naylor and Arvid A. Schultz. "A Simple Technique for Accurately Measuring the Dihedral Angle of a Roof-Top Mirror". In: *Applied Optics* 39.34 (Dec. 2000). Publisher: Optica Publishing Group, pp. 6533–6534. ISSN: 2155-3165. DOI: 10.1364/AO.39.006533.

[70] Newport Corporation. *AJS254-0.5H-NL Adjustment Screw*. URL: https://www.newport.com/p/AJS254-0.5H-NL (visited on 01/18/2024).

[71] Eblana Photonics. *EP1550 Narrow-Linewidth — Eblana Photonics*. URL: https://eblanaphotonics.com/products/1550-nlw/ (visited on 04/09/2024).

[72] New Imaging Technologies. *SWIR Cameras — InGaAs — HDR Cameras — High Sensitivity SWIR*. URL: https://new-imaging-technologies.com/swir-cameras/ (visited on 04/09/2024).

[73] Lifeng Li, Jean Chandezon, Gérard Granet, and Jean-Pierre Plumey. "Rigorous and efficient grating-analysis method made easy for optical engineers". In: *Applied Optics* 38.2 (Jan. 1999). Publisher: Optica Publishing Group, pp. 304–313. ISSN: 2155-3165. DOI: 10.1364/AO.38.000304.

[74] Melanie R. Leclerc, Brad Gom, and David Naylor. "Optical design of the SCUBA-2 IFTS". In: *Ground-based and Airborne Instrumentation for Astronomy II*. Ed. by Ian S. McLean and Mark M. Casali. Marseille, France, July 2008, p. 70147I. DOI: 10.1117/12.787606.

[75] George M. Voellmer, Christine A. Allen, Schidananda R. Babu, Arlin E. Bartels, C. Darren Dowell, Jessie Dotson, D. Al Harper, Harvey Moseley, and Timothy Rennick. *A Two-Dimensional, Semiconducting Bolometer Array for HAWC*. Jan. 2004. URL: https://ntrs.nasa.gov/citations/20040191379 (visited on 04/07/2024).

[76] Virginia Diodes. *Custom Transmitters*. URL: https://www.vadiodes.com/en/products/custom-sources-and-receivers (visited on 02/01/2024).

[77] M. Czerny and A. F. Turner. "Über den Astigmatismus bei Spiegelspektrometern". de. In: *Zeitschrift für Physik* 61.11 (Nov. 1930), pp. 792–797. ISSN: 0044-3328. DOI: 10.1007/BF01340206.

[78] David A. Naylor, Brad G. Gom, Scott C. Jones, and Locke D. Spencer. "Non-linear Behaviour of Bolometric Detectors in Fourier Spectroscopy". In: *Advances in Imaging (2009), paper JTuB15*. Optica Publishing Group, Apr. 2009, JTuB15. DOI: 10.1364/FTS.2009.JTuB15.

[79] Adam J. Christiansen. "A cryogenic multiaxis range-resolved laser interferometer". PhD thesis. Lethbridge, Alta. : University of Lethbridge, Dept. of Physics and Astronomy, 2023. URL: https://hdl.handle.net/10133/6671 (visited on 05/09/2024).

Appendix A LFC Part Drawings

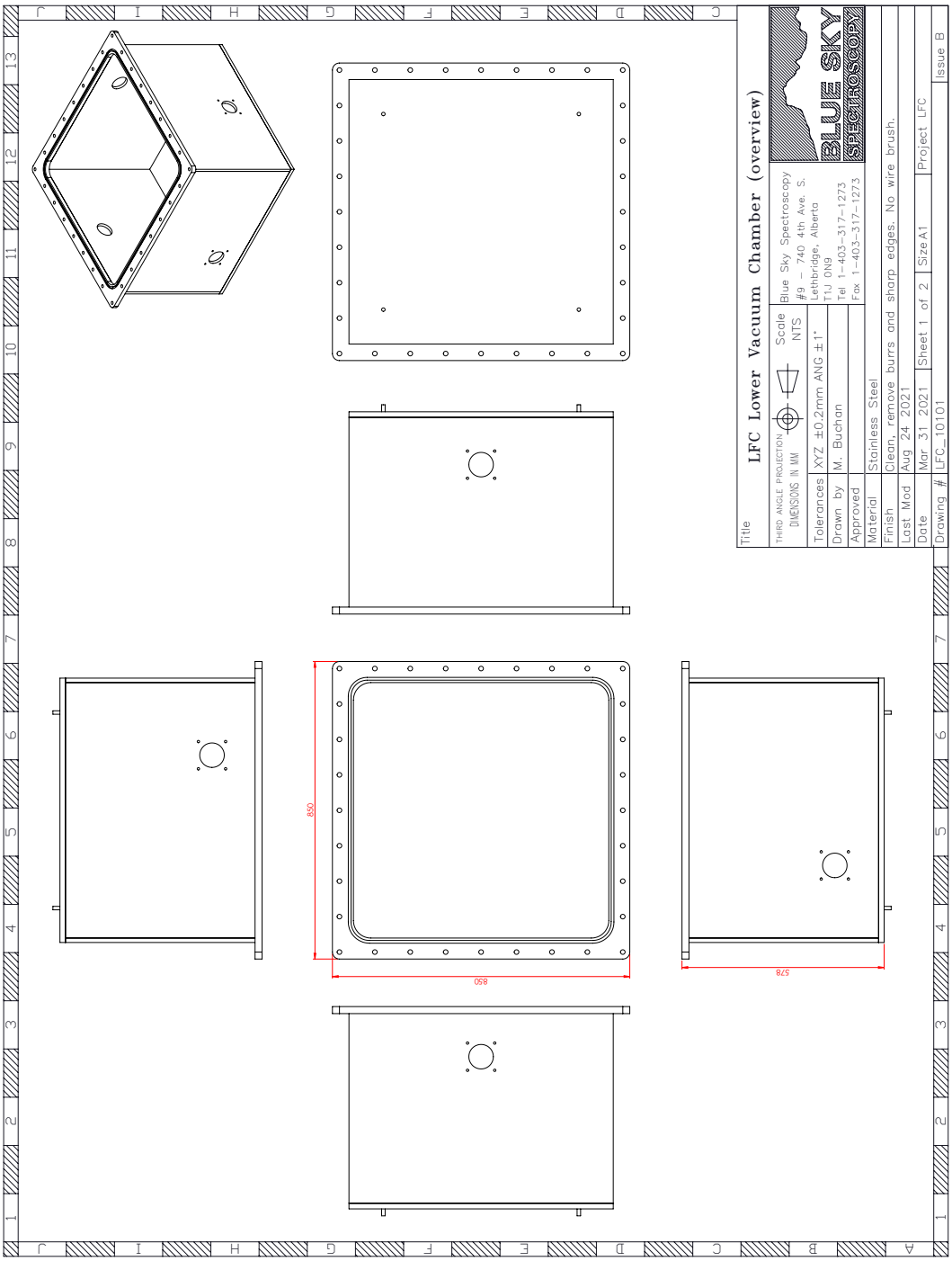

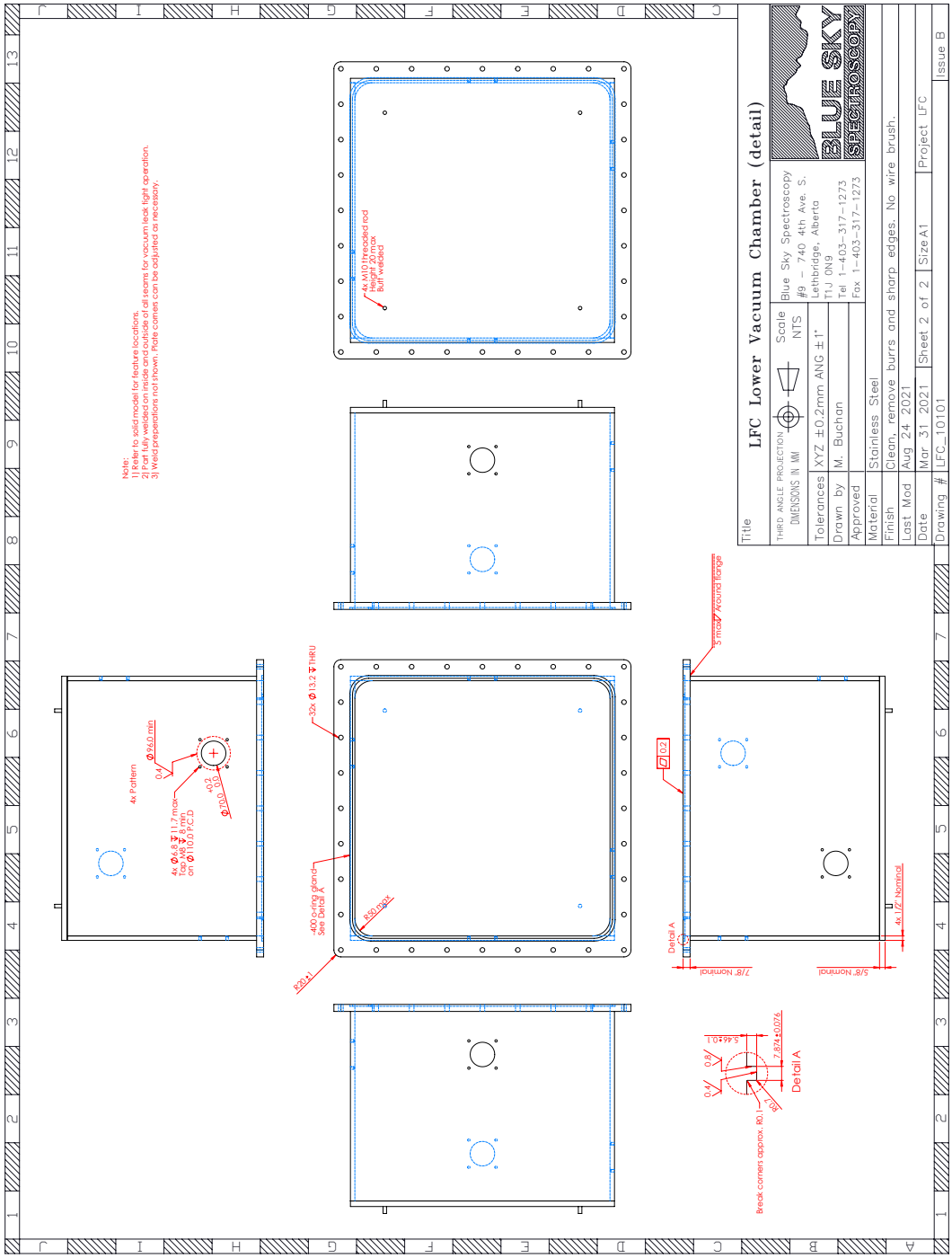
LFC Lower Vacuum Chamber (detail)
BLUE SKY SPECTROSCOPY
Blue Sky Spectroscopy
#9 – 740 4th Ave. S.
Lethbridge, Alberta
T1J 0N9
Tel 1-403-317-1273
Fax 1-403-317-1273
THIRD ANGLE PROJECTION
DIMENSIONS IN MM
Scale NTS
Tolerances XYZ ±0.2mm ANG ±1°
Drawn by M. Buchan
Approved
Material Stainless Steel
Finish Clean, remove burrs and sharp edges. No wire brush.
Last Mod Aug 24 2021
Date Mar 31 2021
Sheet 2 of 2
Size A1
Project LFC
Drawing # LFC_10101
Issue B
Note:
1) Refer to solid model for feature locations.
2) Part fully welded on inside and outside of all seams for vacuum leak tight operation.
3) Weld preperations not shown. Plate corners can be adjusted as necessary.
4x M10 threaded rod
Height 20 max
Butt welded
4x Pattern
Ø96.0 min
4x Ø6.8 ↧11.7 max
Tap M8 ↧8 min
on Ø110.0 P.C.D
Ø70.0 +0.2 -0.0
32x Ø13.2 THRU
-400 o-ring gland
See Detail A
R30 min
320±1
5 max Around flange
0.2
Detail A
7/8" Nominal
5/8" Nominal
46 1/2" Nominal
5.44±0.1
7.82±0.076
Break corners approx. R0.1
Detail A

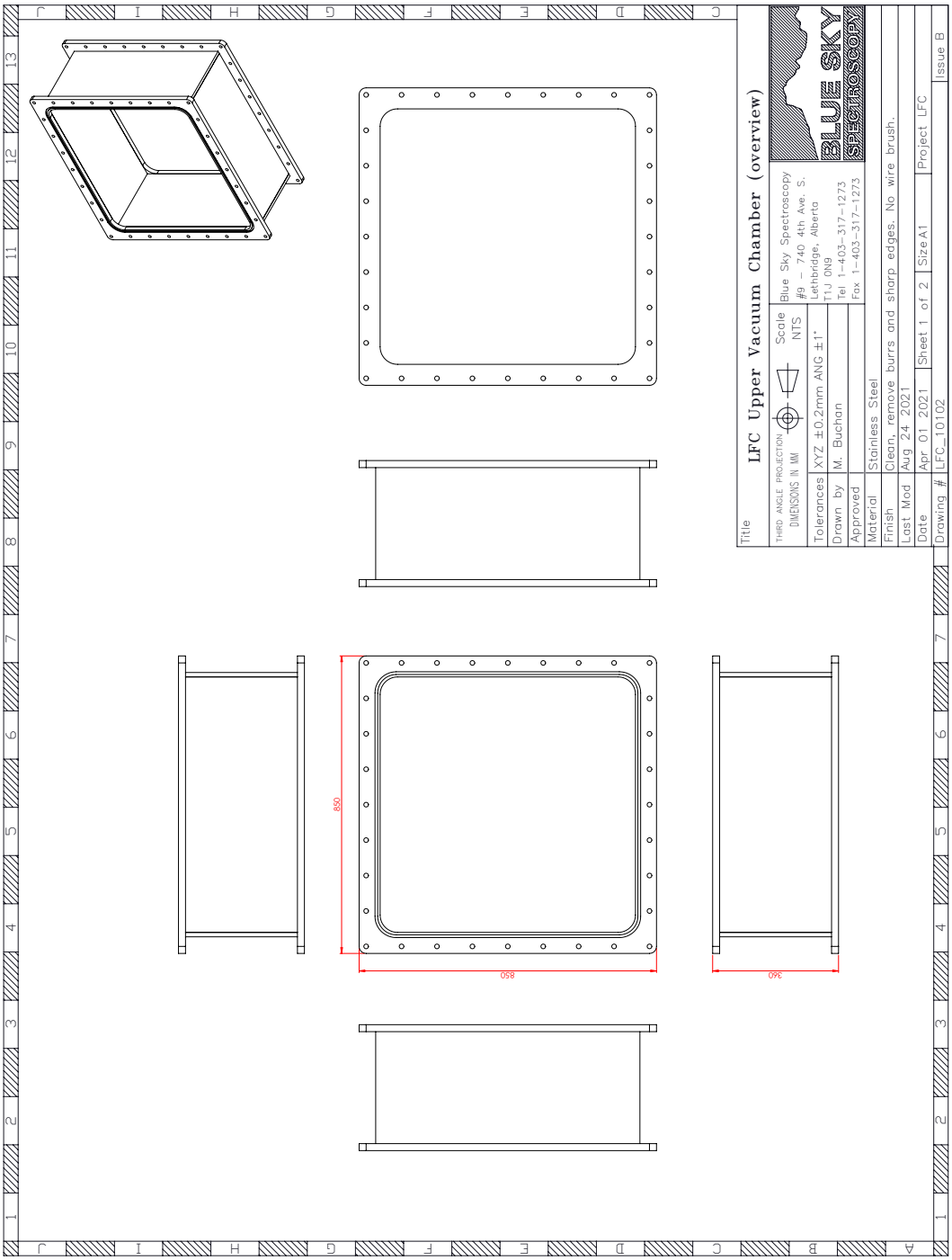
LFC Upper Vacuum Chamber (overview)
THIRD ANGLE PROJECTION
DIMENSIONS IN MM
Scale NTS
Tolerances XYZ ±0.2mm ANG ±1°
Drawn by M. Buchan
Approved
Material Stainless Steel
Finish Clean, remove burrs and sharp edges. No wire brush.
Last Mod Aug 24 2021
Date Apr 01 2021
Drawing # LFC_10102
Sheet 1 of 2
Size A1
Project LFC
Issue B
Blue Sky Spectroscopy
#9 – 740 4th Ave. S.
Lethbridge, Alberta
T1J 0N9
Tel 1-403-317-1273
Fax 1-403-317-1273
BLUE SKY SPECTROSCOPY
850
850
360

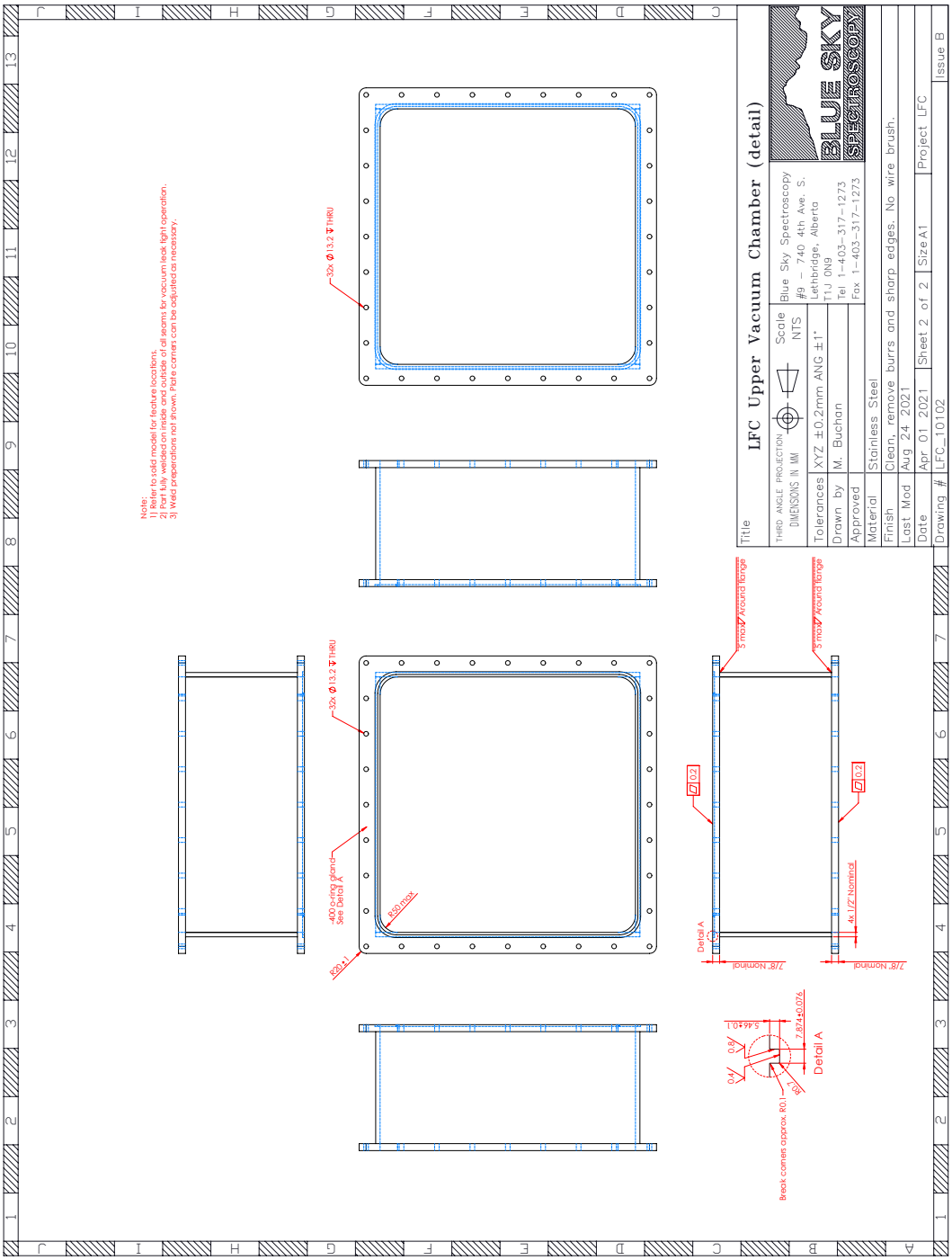
LFC Upper Vacuum Chamber (detail)
Title
THIRD ANGLE PROJECTION
DIMENSIONS IN MM
Scale NTS
Blue Sky Spectroscopy
#9 – 740 4th Ave. S.
Lethbridge, Alberta
T1J 0N9
Tel 1-403-317-1273
Fax 1-403-317-1273
Tolerances XYZ ±0.2mm ANG ±1°
Drawn by M. Buchan
Approved
Material Stainless Steel
Finish Clean, remove burrs and sharp edges. No wire brush.
Last Mod Aug 24 2021
Date Apr 01 2021
Sheet 2 of 2
Size A1
Project LFC
Drawing # LFC_10102
Issue B
BLUE SKY SPECTROSCOPY
Note:
1) Refer to solid model for feature locations.
2) Part is welded on inside and outside of all seams for vacuum leak tight operation.
3) Weld preparation not shown, Parts corners can be adjusted as necessary.
32x Ø 13.2 THRU
400 o-ring gland See Detail A
Ø60 max
Ø20.1
3 mm Around flange
4x 1/2" Nominal
7/8" Nominal
Detail A
Break corners approx. R0.1

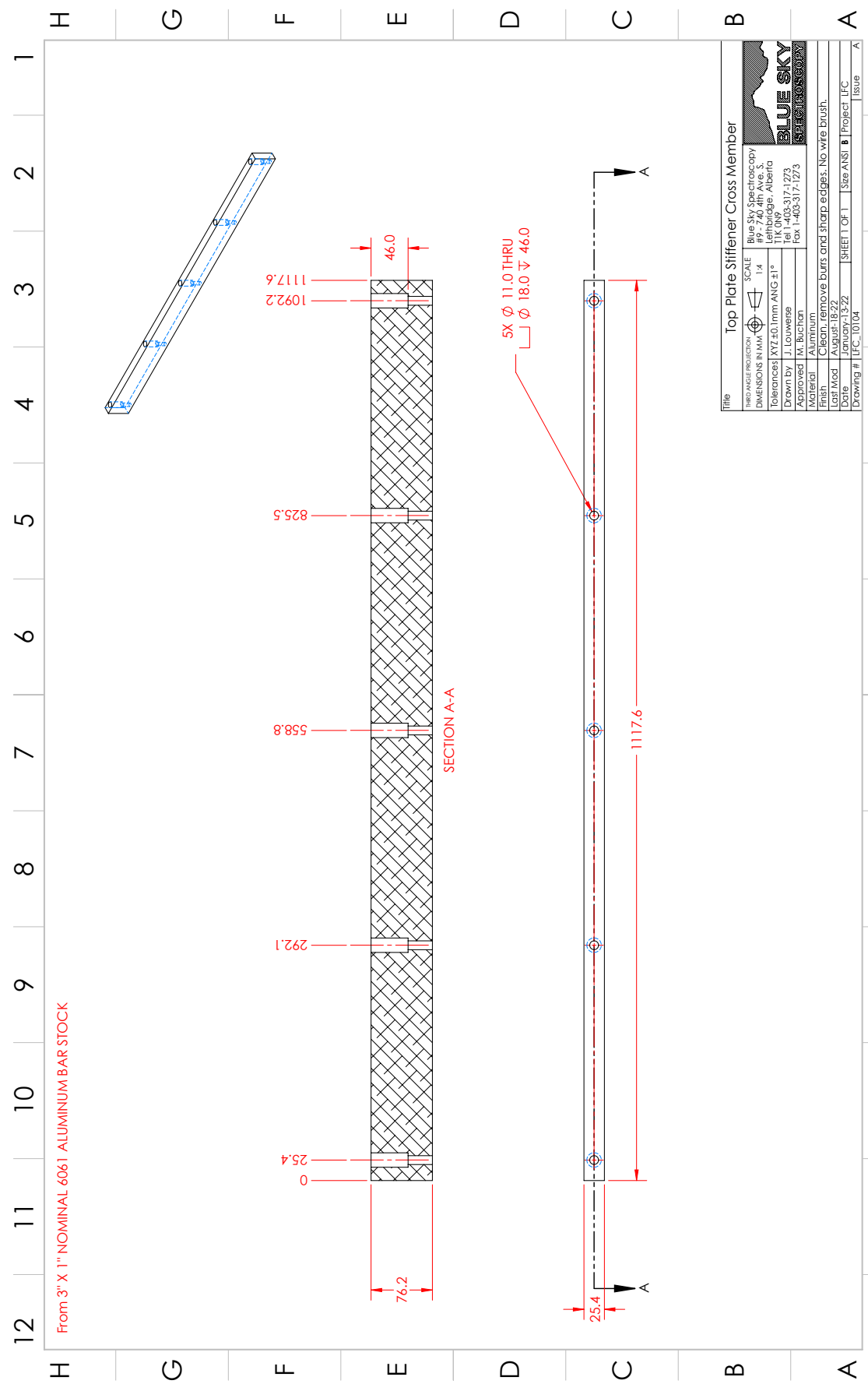
Top Plate Stiffener Cross Member
Blue Sky Spectroscopy
#8 2702 Aldo Rd S.
Lethbridge, Alberta
T1K 0N9
Tel 1-403-317-1273
Fax 1-403-317-1273
BLUE SKY SPECTROSCOPY
SCALE 1:4
THIRD ANGLE PROJECTION
DIMENSIONS IN MM
Tolerances XYZ ±0.1mm ANG ±1°
Drawn by J. Louwerse
Approved M. Buchan
Material Aluminum
Finish Clean, remove burs and sharp edges. No wire brush.
Last Mod August-18-22
Date January-13-22
Drawing # LFC_10104
SHEET 1 OF 1
Size ANSI B
Project LFC
Issue A
From 3" X 1" NOMINAL 6061 ALUMINUM BAR STOCK
SECTION A-A
46.0
1117.6
1092.2
825.5
558.8
292.1
25.4
0
76.2
5X Ø 11.0 THRU
Ø 18.0 ▽ 46.0
1117.6
25.4
A
A

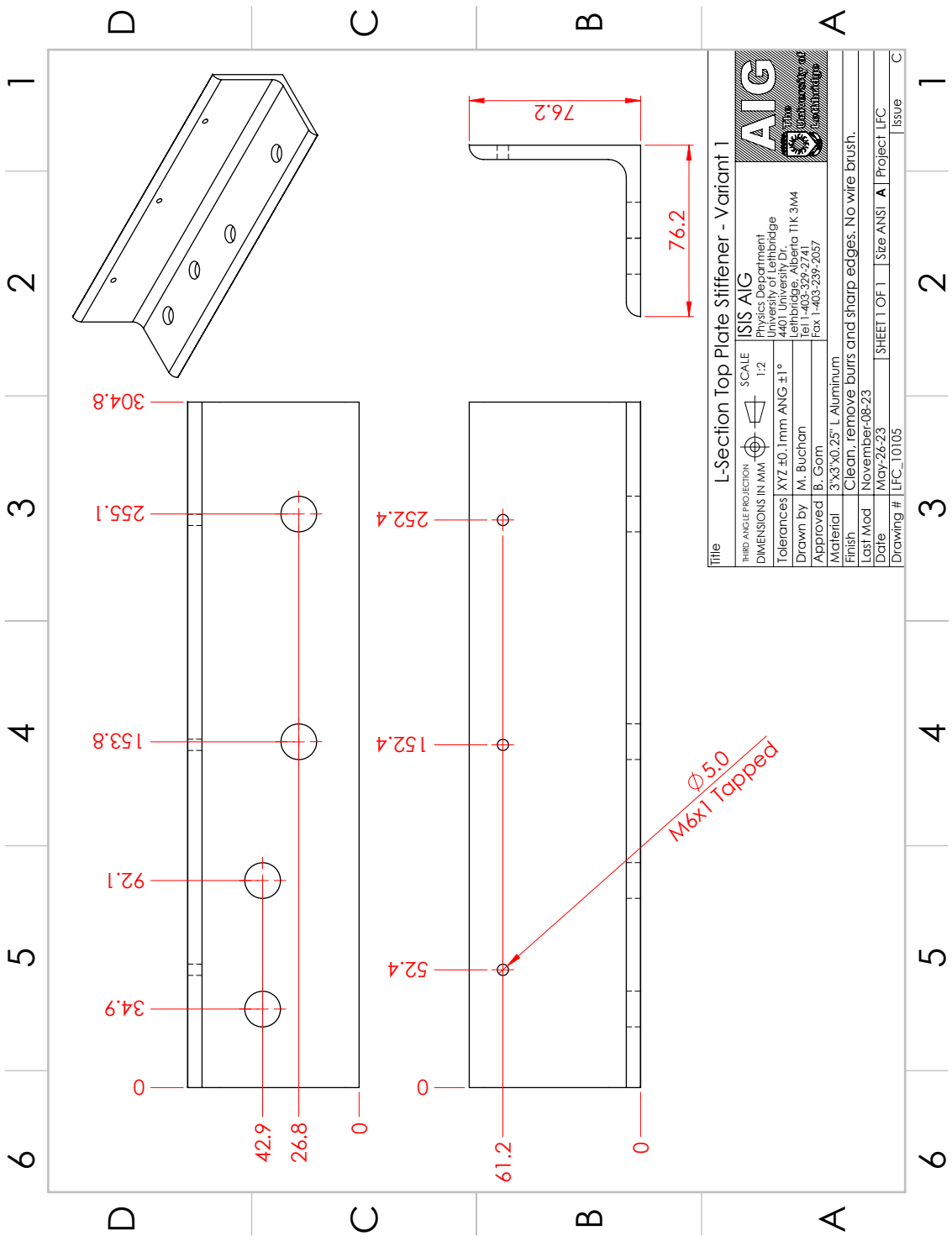
Title
L-Section Top Plate Stiffener - Variant 1
THIRD ANGLE PROJECTION
DIMENSIONS IN MM
SCALE 1:2
ISIS AIG
Physics Department
University of Lethbridge
4401 University Dr.
Lethbridge, Alberta T1K 3M4
Tel 1-403-329-2741
Fax 1-403-239-2057
Tolerances
XYZ ±0.1mm ANG ±1°
Drawn by
M. Buchan
Approved
B. Gom
Material
3"x3"x0.25" L Aluminum
Finish
Clean, remove burrs and sharp edges. No wire brush.
Last Mod
November-08-23
Date
May-26-23
Drawing #
LFC_10105
SHEET 1 OF 1
Size ANSI A
Project LFC
Issue C
76.2
76.2
304.8
255.1
153.8
92.1
34.9
0
42.9
26.8
0
252.4
152.4
52.4
0
61.2
0
Ø5.0
M6x1 Tapped

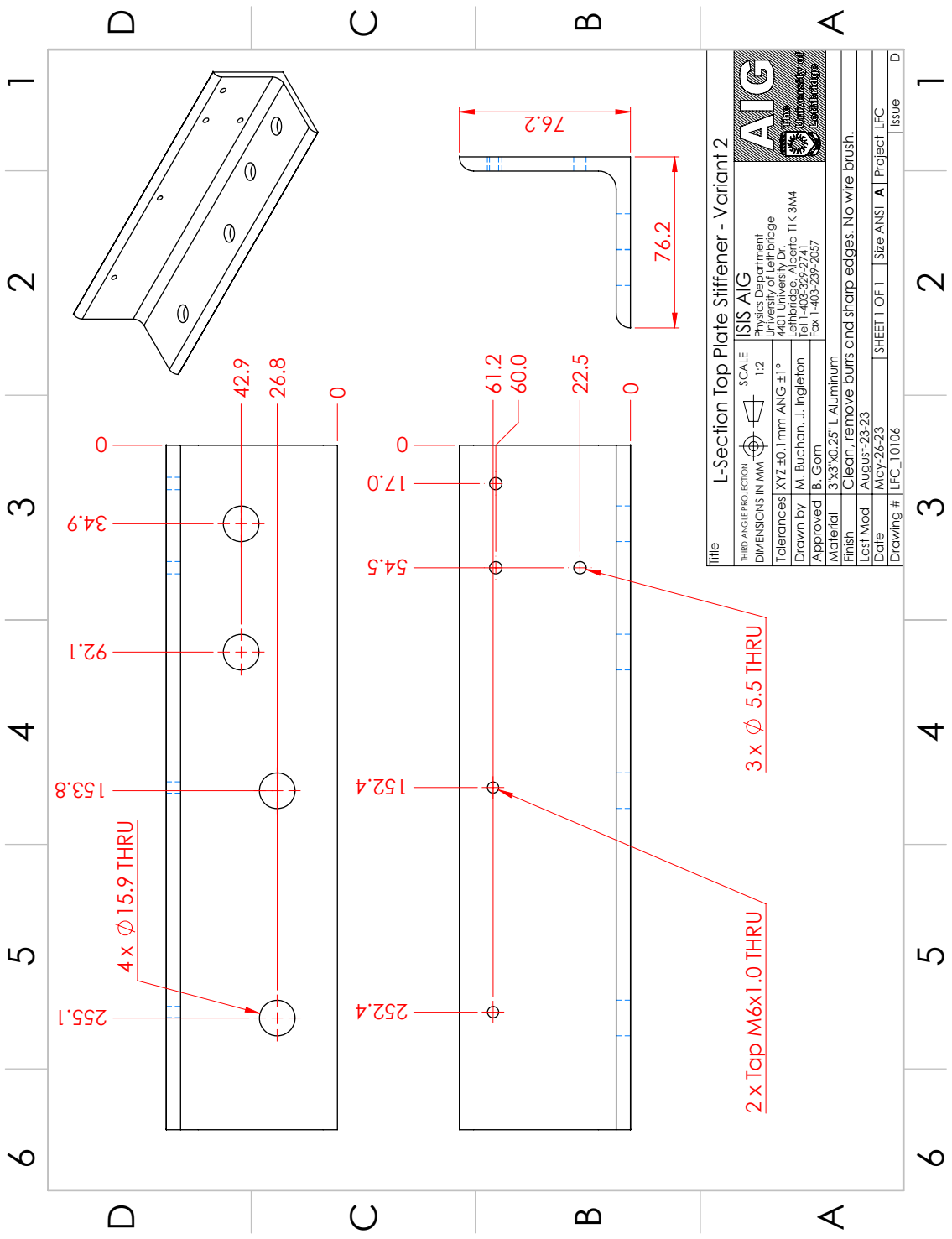
76.2
76.2
0
42.9
26.8
0
34.9
92.1
153.8
255.1
4 x ∅15.9 THRU
0
61.2
60.0
22.5
0
17.0
54.5
152.4
252.4
3 x ∅ 5.5 THRU
2 x Tap M6x1.0 THRU
Title
L-Section Top Plate Stiffener - Variant 2
THIRD ANGLE PROJECTION
DIMENSIONS IN MM
SCALE 1:2
ISIS AIG
Physics Department
University of Lethbridge
4401 University Dr.
Lethbridge, Alberta T1K 3M4
Tel 1-403-329-2741
Fax 1-403-239-2057
Tolerances XYZ ±0.1mm ANG ±1°
Drawn by M. Buchan, J. Ingleton
Approved B. Gom
Material 3"x3"x0.25" L Aluminum
Finish Clean, remove burrs and sharp edges. No wire brush.
Last Mod August-23-23
Date May-26-23
Drawing # LFC_10106
SHEET 1 OF 1
Size ANSI A
Project LFC
Issue D

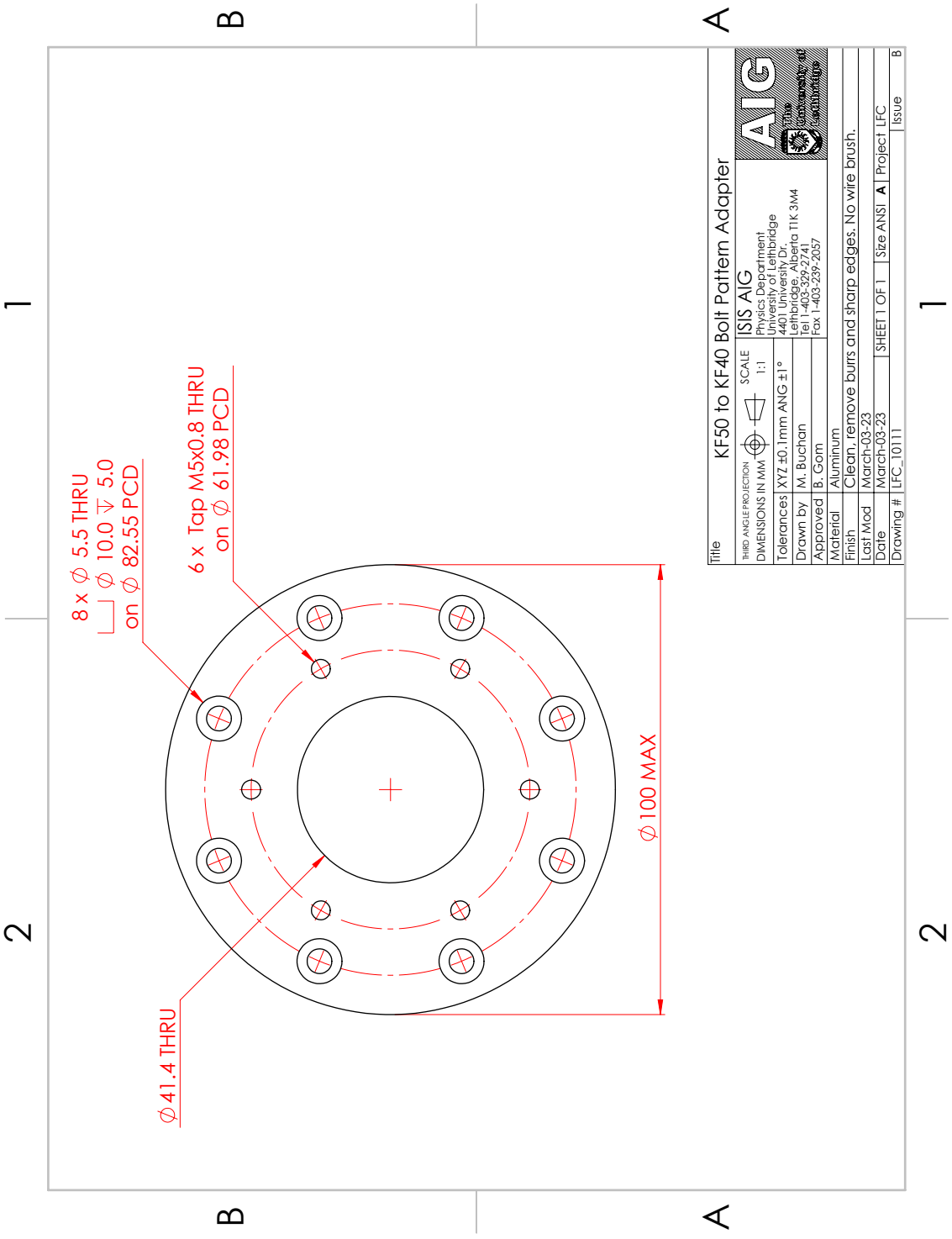
8 x ⌀ 5.5 THRU
⌴ ⌀ 10.0 ▽ 5.0
on ⌀ 82.55 PCD
6 x Tap M5x0.8 THRU
on ⌀ 61.98 PCD
⌀41.4 THRU
⌀100 MAX
Title
KF50 to KF40 Bolt Pattern Adapter
THIRD ANGLE PROJECTION
DIMENSIONS IN MM
SCALE 1:1
ISIS AIG
Physics Department
University of Lethbridge
4401 University Dr.
Lethbridge, Alberta T1K 3M4
Tel 1-403-329-2741
Fax 1-403-239-2057
Tolerances XYZ ±0.1mm ANG ±1°
Drawn by M. Buchan
Approved B. Gom
Material Aluminum
Finish Clean, remove burrs and sharp edges. No wire brush.
Last Mod March-03-23
Date March-03-23
Drawing # LFC_10111
SHEET 1 OF 1
Size ANSI A
Project LFC
Issue B
AIG
The University of Lethbridge
A
B
1
2

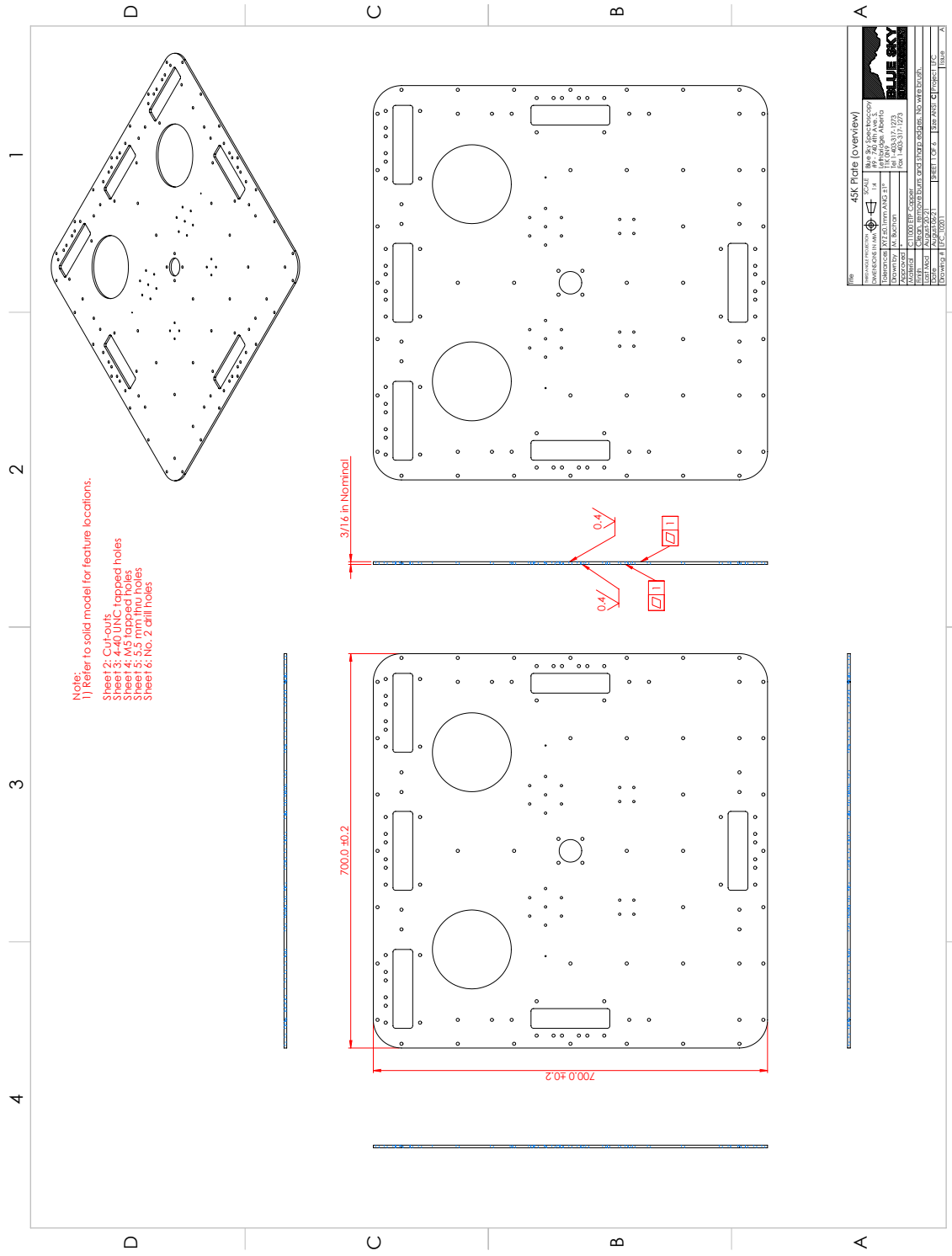
Note:
1) Refer to solid model for feature locations.
Sheet 2: Cut-outs
Sheet 3: 4-40 UNC tapped holes
Sheet 4: M5 tapped holes
Sheet 5: 5.5 mm thru holes
Sheet 6: No. 2 drill holes
3/16 in Nominal
0.4
0.4
700.0 ±0.2
700.0 ±0.2
45K Plate (overview)
Material: c1100 EP Copper
Finish: Clean, remove burn and sharp edges. No weld brush.
Date: August 2021
Drawing #: LFC-1000
Sheet 1 of 6
Size ANSI B
Project: LFC
Issue: A
Blue Sky Spaceships
Tel: 1.403.317.1223
Fax: 1.403.317.1223

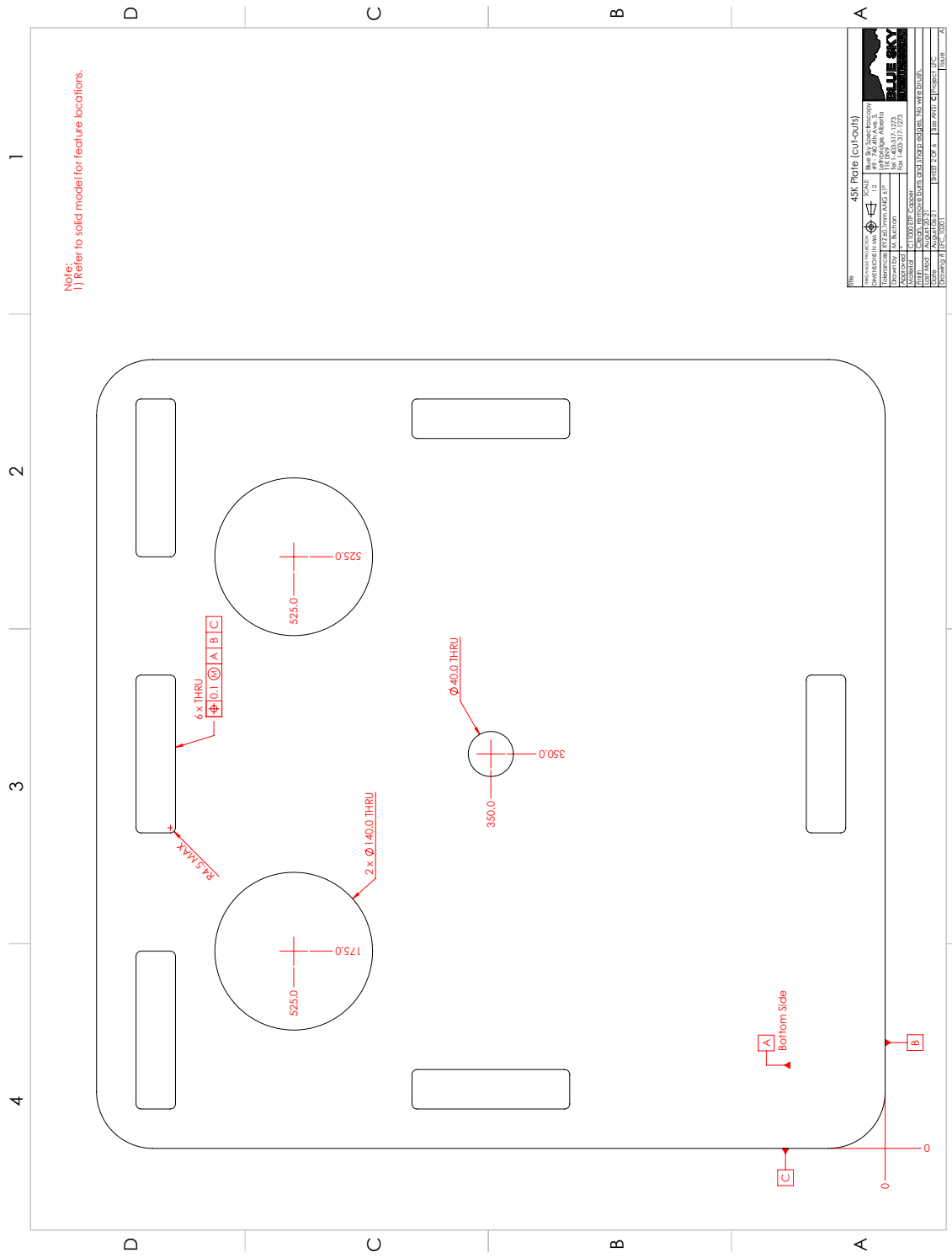
Note:
1) Refer to solid model for feature locations.
45K Plate (cut-outs)
Blue Sky Robotics
Project LFC
Bottom Side
6 x THRU
0.1 M A B C
R4.5 MAX
2 x Ø140.0 THRU
Ø40.0 THRU
525.0
525.0
175.0
525.0
350.0
350.0
0
0
A
B
C

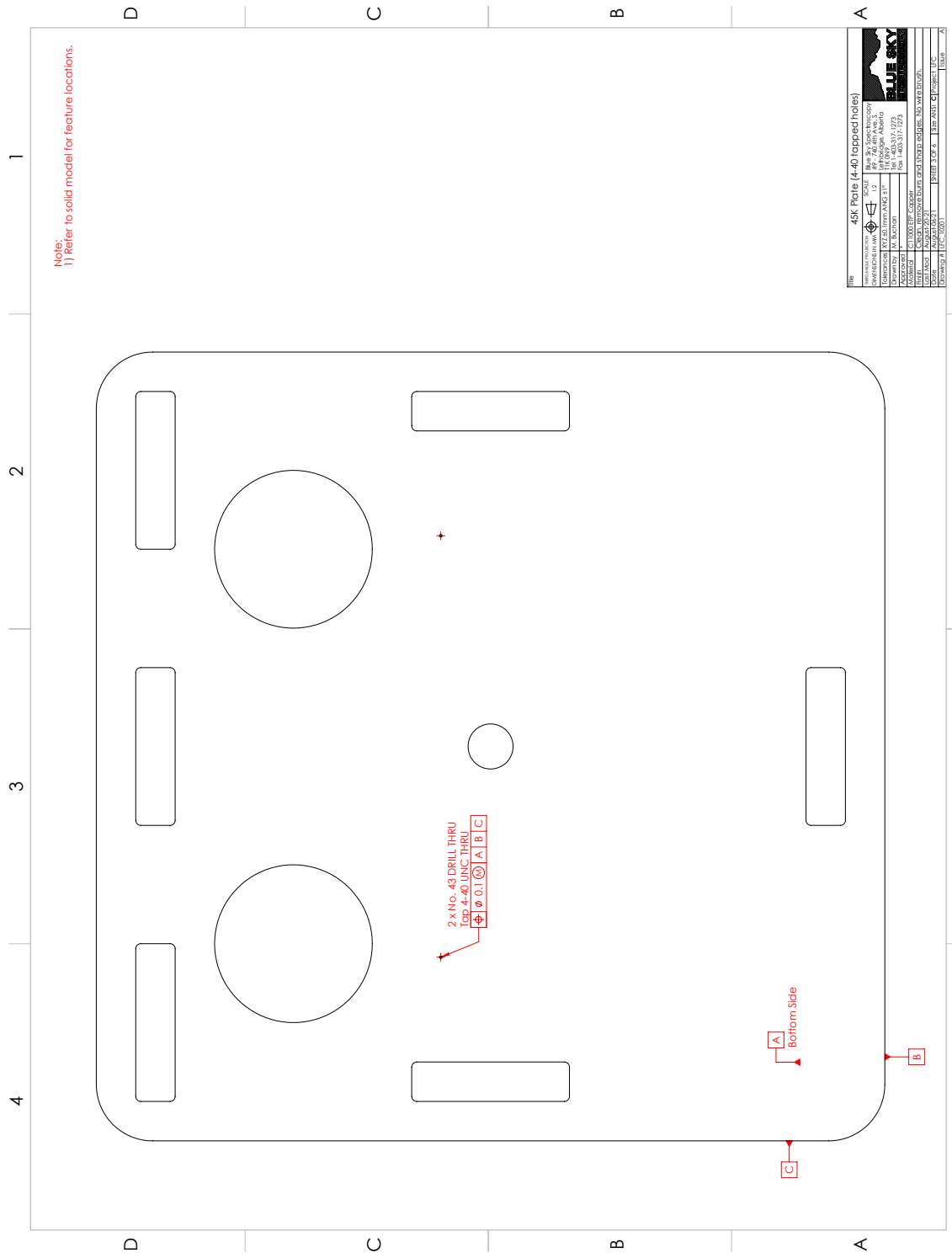
Note:
1) Refer to solid model for feature locations.
45K Plate (4-40 tapped holes)
2 x No. 43 DRILL THRU
Tap 4-40 UNC THRU
Bottom Side
BLUE SKY

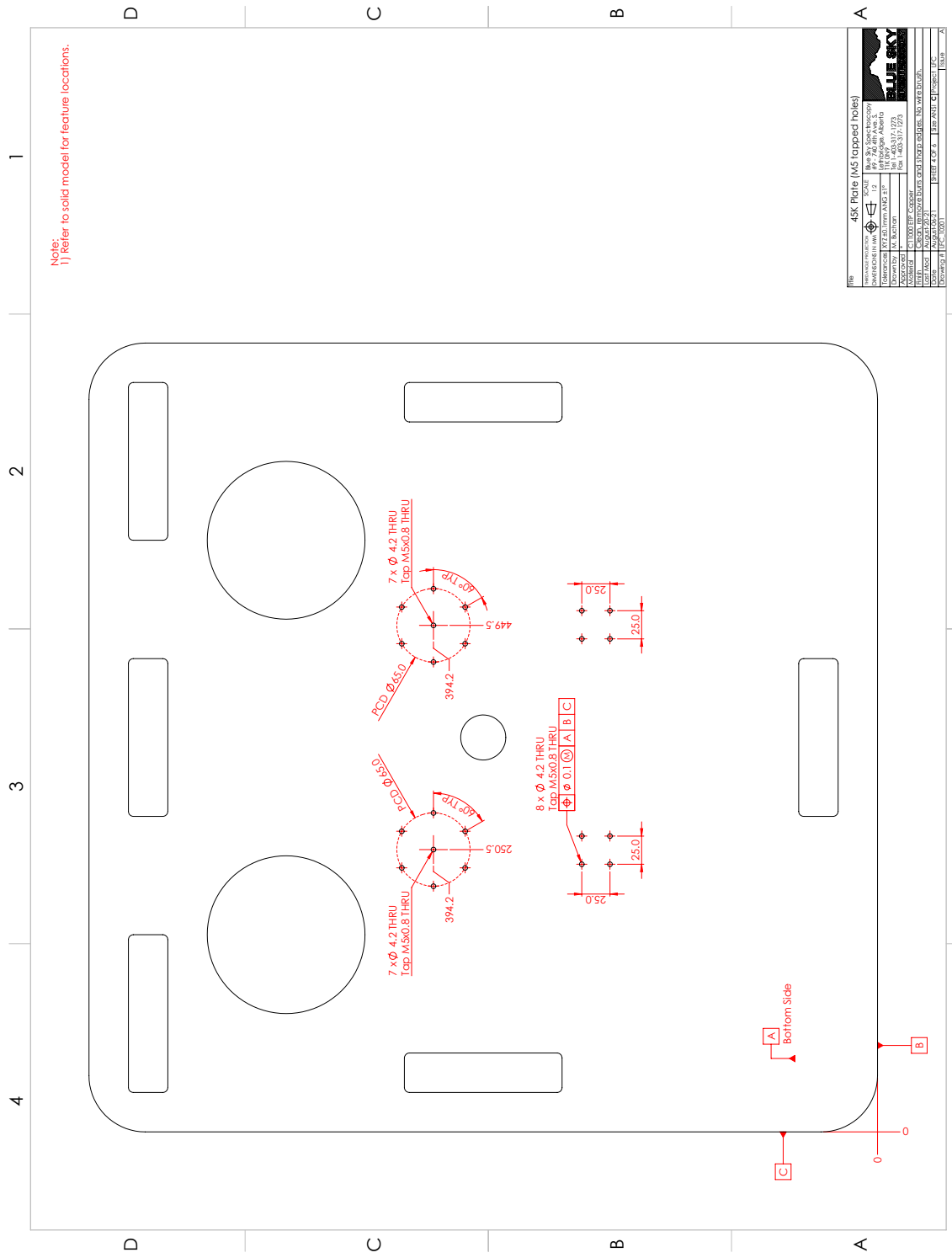
Note:
1) Refer to solid model for feature locations.
45K Plate (M5 tapped holes)
BLUE SKY
7 x Ø 4.2 THRU
Tap M5x0.8 THRU
PCD Ø65.0
449.5
394.2
8 x Ø 4.2 THRU
Tap M5x0.8 THRU
Ø 0.1 M A B C
25.0
Bottom Side
A
B
C
0
0

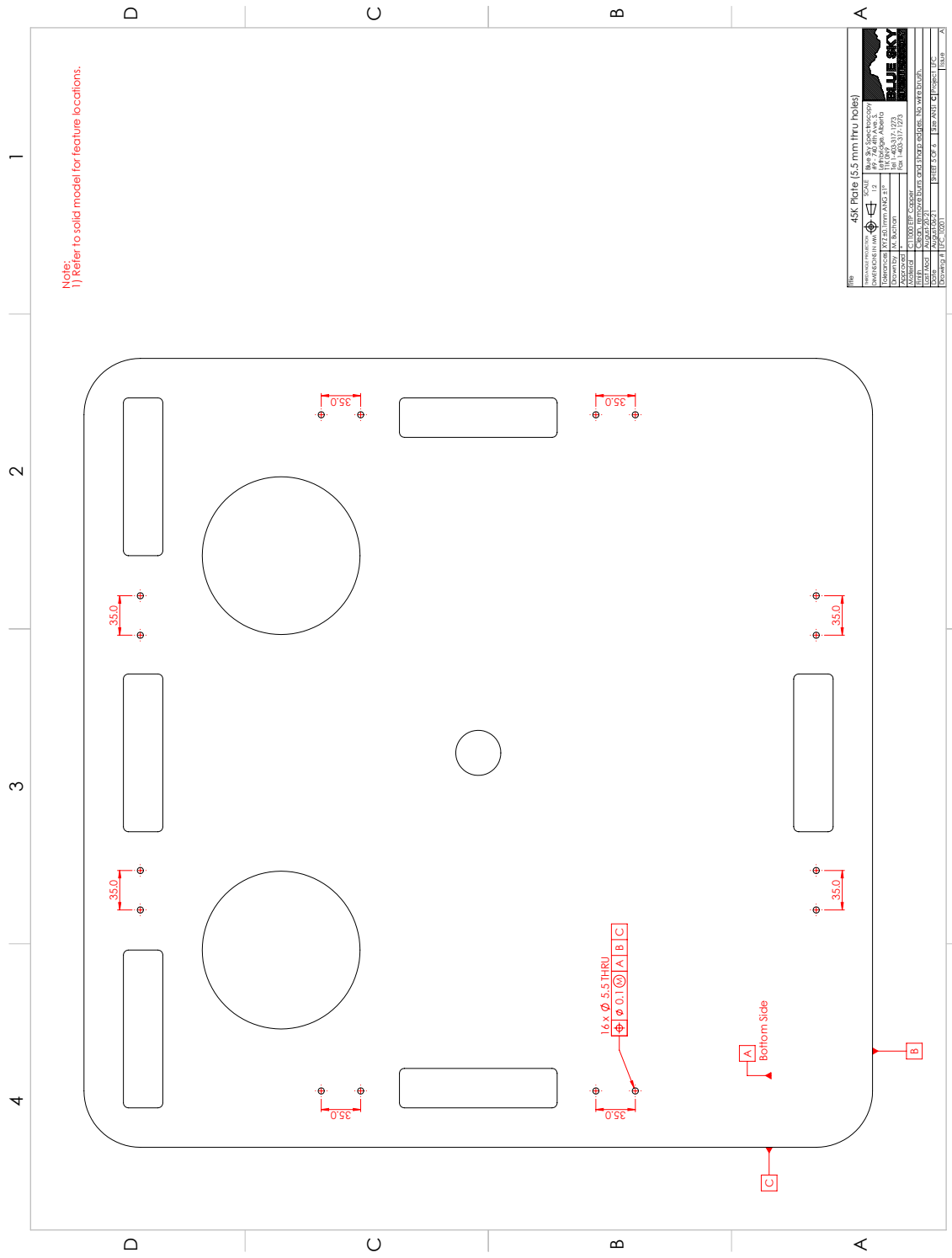
Note:
1) Refer to solid model for feature locations.
45K Plate (5.5 mm thru holes)
Blue Sky Robotics
FP - 740 4th Ave. S
Lethbridge, Alberta
T1J 0N9
tel: 1.403.317.1223
fax: 1.403.317.1223
Tolerances: XY ±0.1mm ANG ±1°
Drawn by: M. Bichan
Approved:
Material: c1100 ETP Copper
Finish: Clean, remove burn and sharp edges. No weld brush.
Last Mod: Aug 21 2012
Date: Aug 21 2012
Drawing #: LFC - 10001
Size: ANSI B
Project: LFC
Issue: A
35.0
1.6 x Ø 5.5 THRU
Ø 0.1 M A B C
Bottom Side
A
B
C

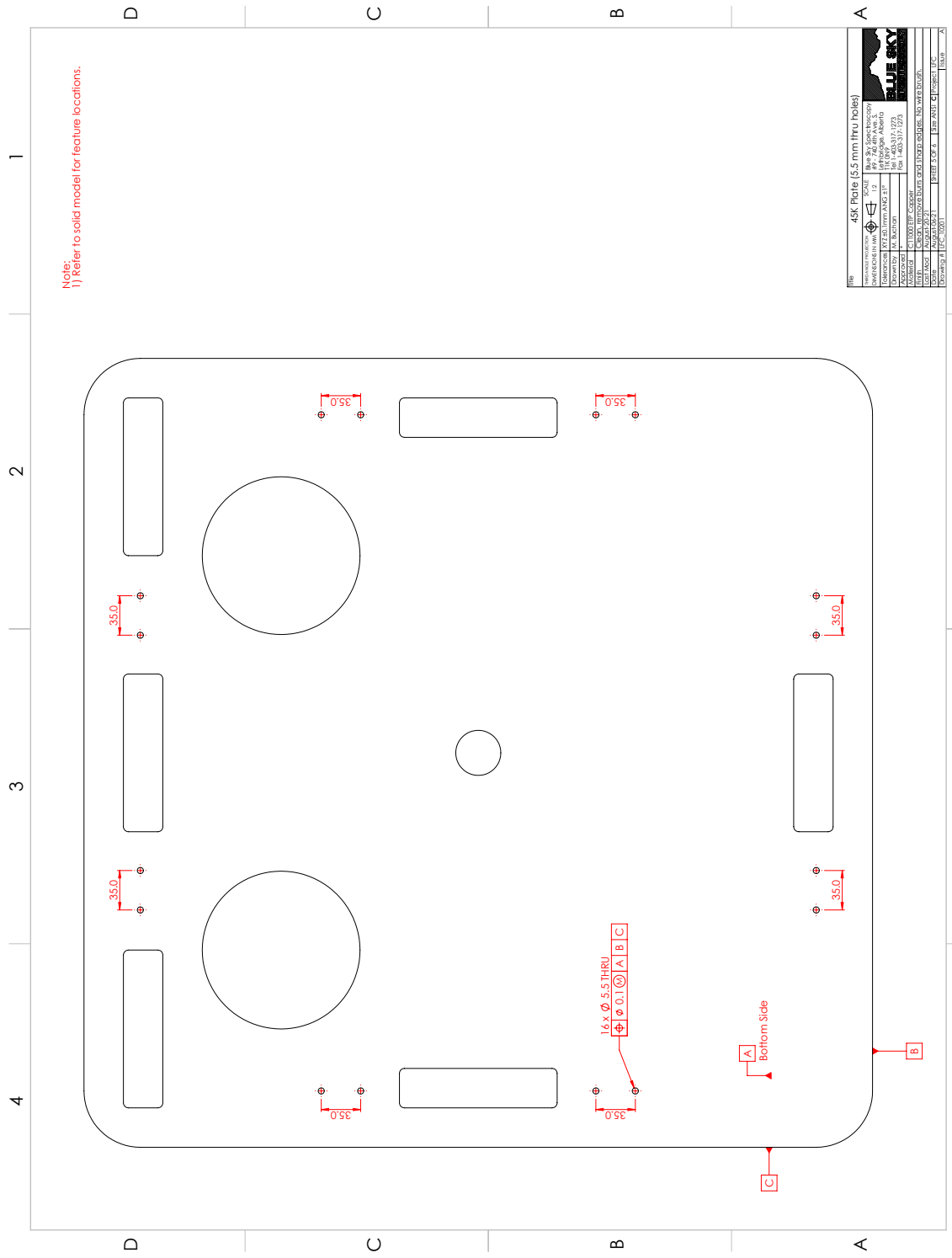
Note:
1) Refer to solid model for feature locations.
45K Plate (5.5 mm thru holes)
Bay 9, 3304 Hospital Dr NW
Calgary, Alberta, Canada T2N 4N1
Ph: 403-317-1223
Fax: 403-317-1273
BLUE SKY ROBOTICS
Tolerances: XY ±0.1mm ANG ±1°
Drawn by: M. Bichan
Approved:
Material: C1100 ETP Copper
Finish: Clean, remove burn and sharp edges. No weld brush.
Qty / Sheet: 1 / 1
Date: August 10, 2021
Drawing #: LFC-10001
Size: ANSI B
Project: LFC
Issue: A
35.0
1.6 x Ø 5.5 THRU
Ø 0.1 M A B C
Bottom Side
A
B
C

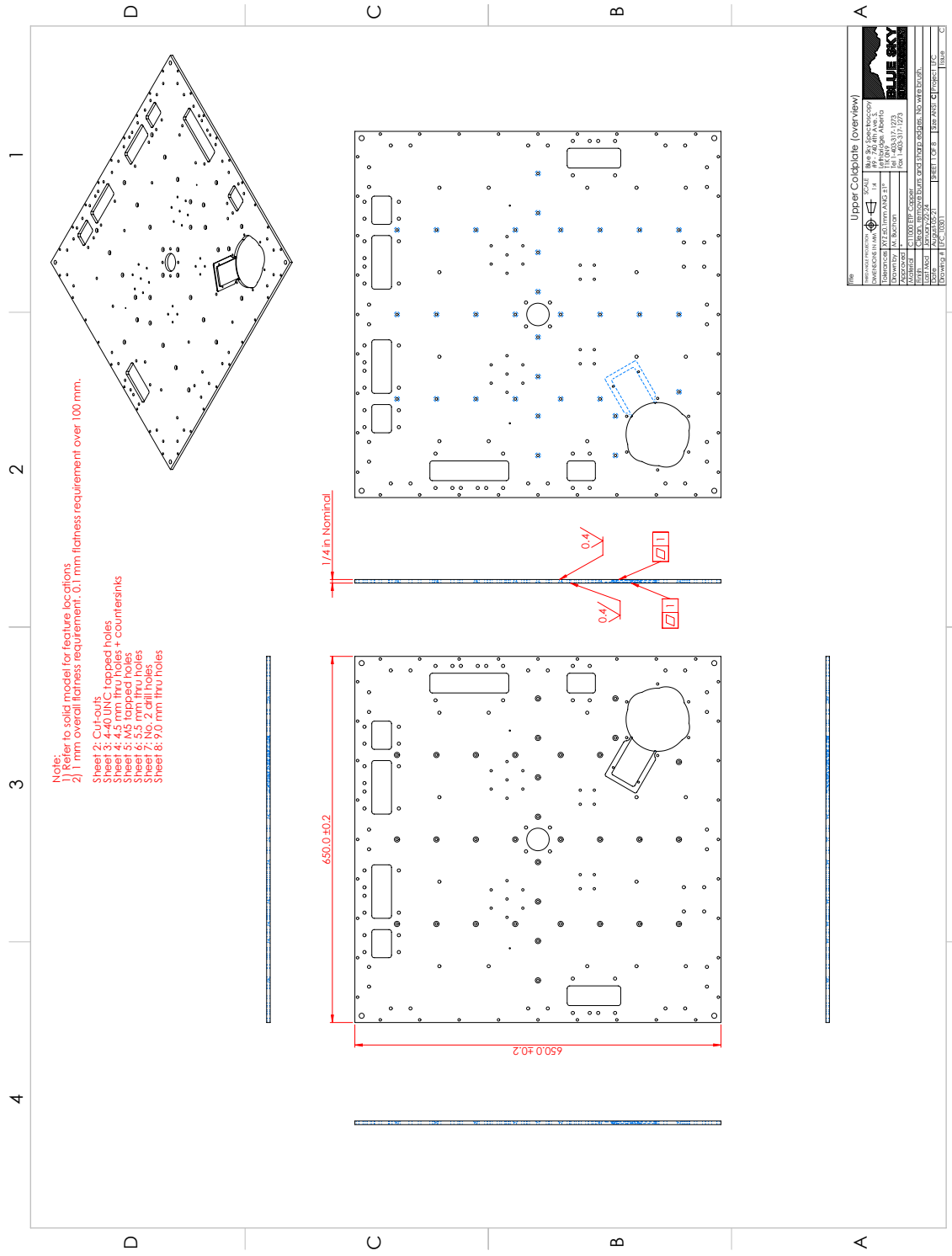
Upper Coldplate (overview)
Blue Sky Rocketry
Tolerances: XX ±0.1mm ANG ±1°
Material: c1100 EP Copper
Finish: Clean, remove burn and sharp edges. No weld brush.
Qty: 1
Sheet 1 of 8
Size ANSI B
Project: LFC
Drawing #: LFC-11001
Issue: C
Notes:
1) Refer to solid model for feature locations
2) 1 mm overall flatness requirement. 0.1 mm flatness requirement over 100 mm.
Sheet 2: Cut-outs
Sheet 3: 4-40 UNC tapped holes
Sheet 4: 4.5 mm thru holes + countersinks
Sheet 5: M5 tapped holes
Sheet 6: 5.5 mm thru holes
Sheet 7: No drill holes
Sheet 8: 9.0 mm thru holes
1/4 in Nominal
650.0 ±0.2
650.0 +0.2
0.4
0.4
1
1

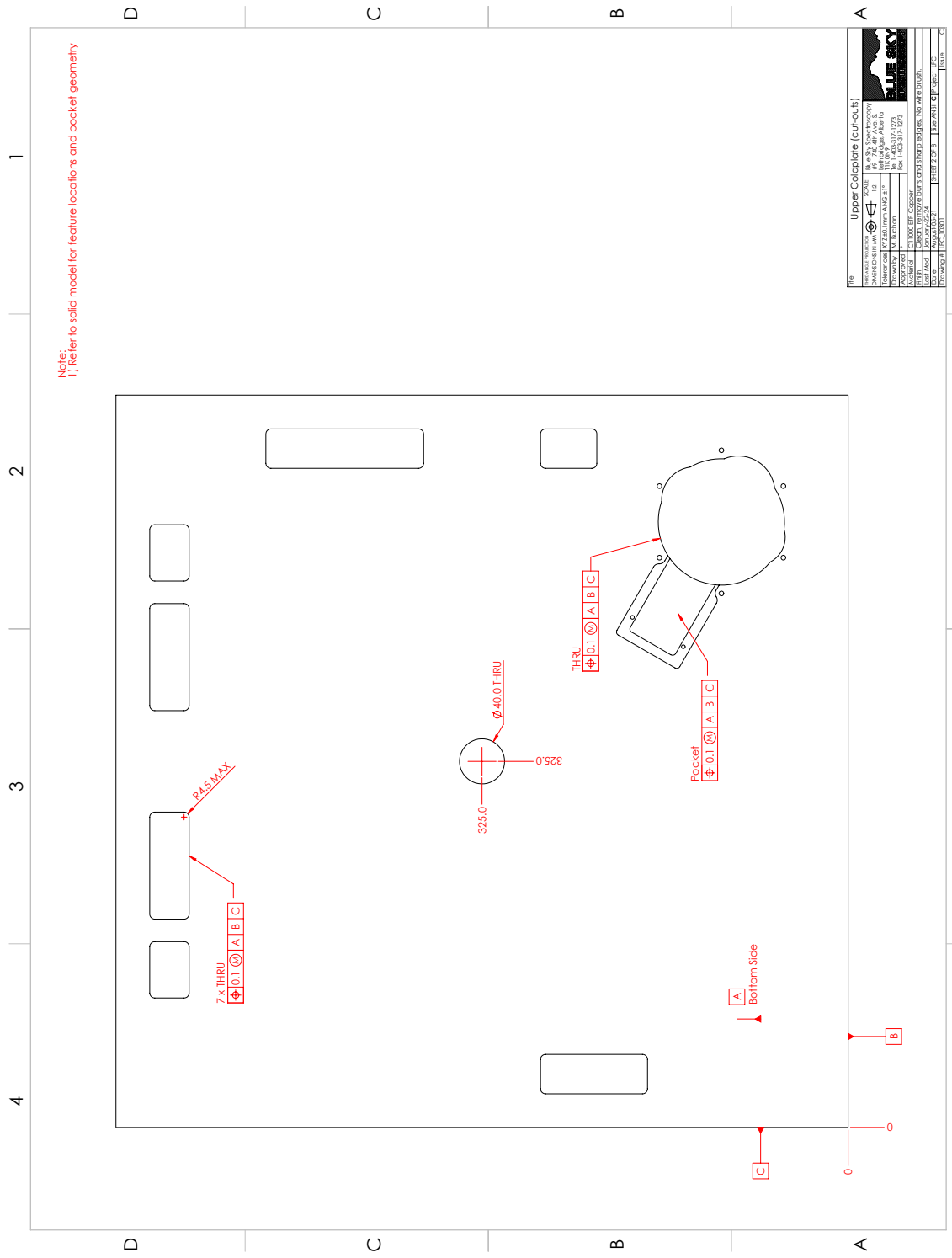
Note:
1) Refer to solid model for feature locations and pocket geometry
Upper Coldplate (cut-outs)
BLUE SKY
R4.5 MAX
7 x THRU
0.1 M A B C
Ø40.0 THRU
325.0
325.0
THRU
Pocket
A
Bottom Side
B
C
0
0

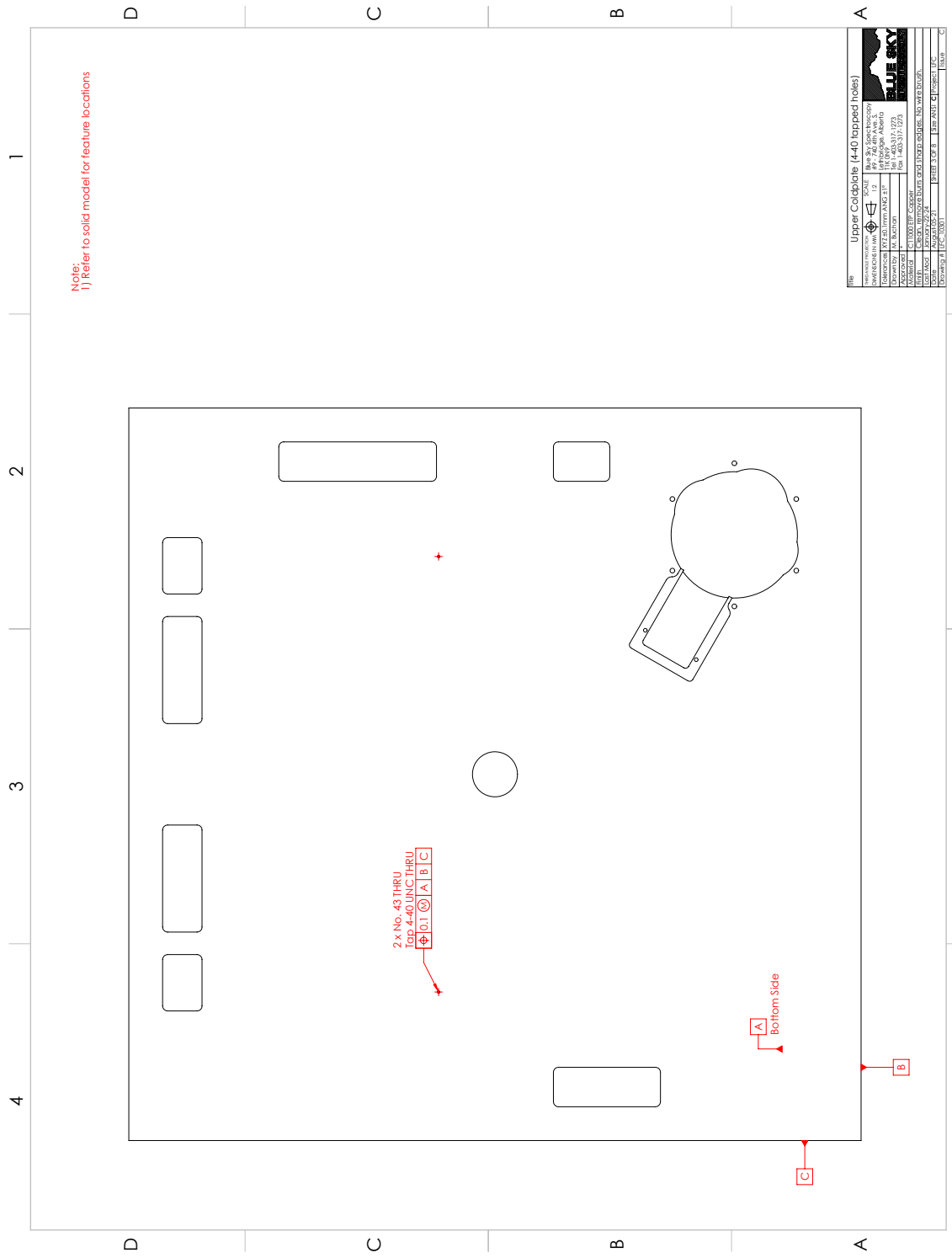
Note:
1) Refer to solid model for feature locations
2 x No. 43 THRU
Tap 4-40 UNC THRU
⌖ 0.1 Ⓜ A B C
A
Bottom Side
B
C
Upper Coldplate (4-40 tapped holes)
BLUE SKY
Project LFC
Issue C

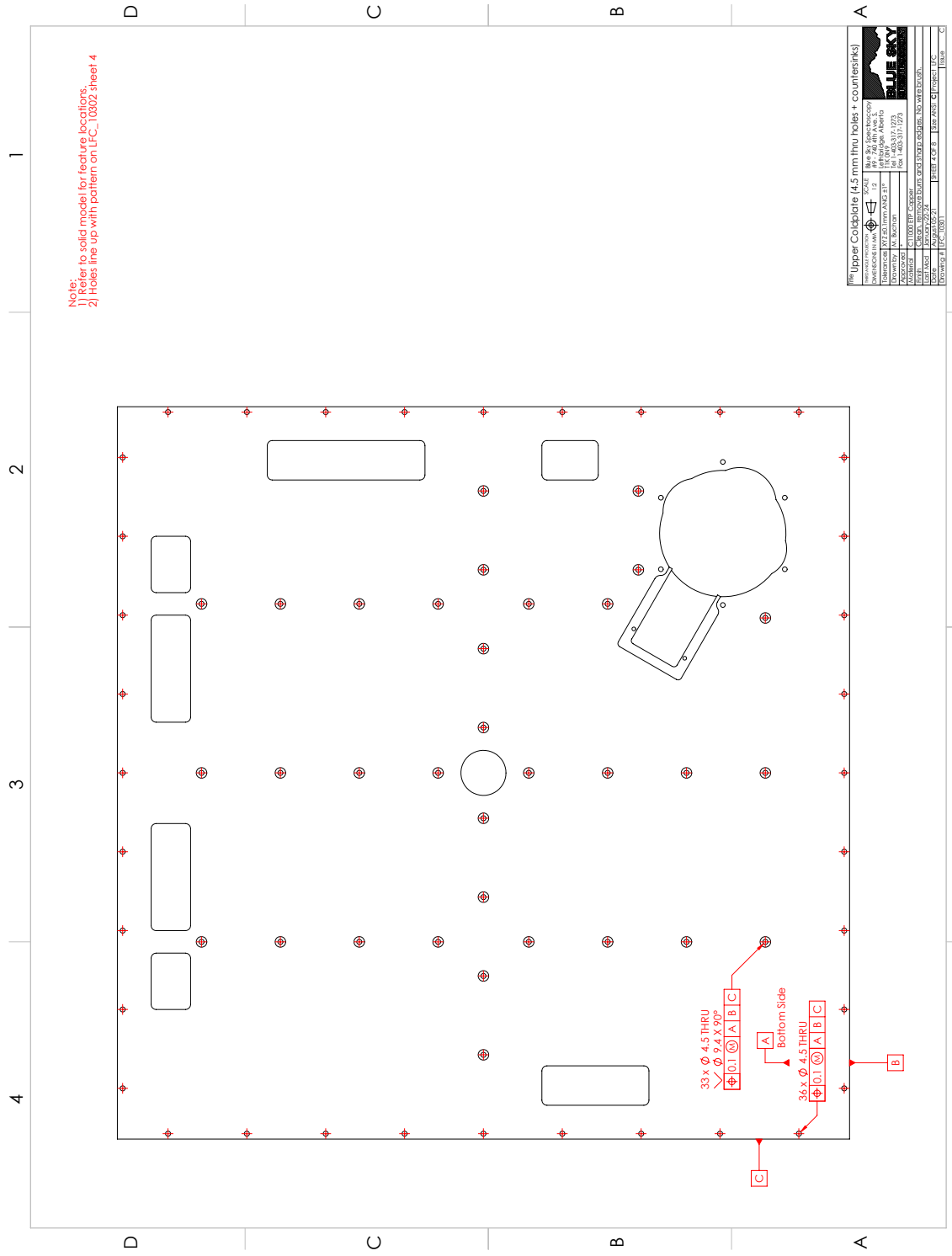
Note:
1) Refer to solid model for feature locations.
2) Holes line up with pattern on LFC_10302 sheet 4
Upper Coldplate (4.5 mm thru holes + countersinks)
DIMENSIONS IN MM
SCALE 1/2
Tolerances X/1.0 mm ANG ±1°
Drawn by M. Bolton
Approved
Material c1100 ETP Copper
Finish Clean, remove burn and sharp edges. No wire brush.
Qty of Sheets 1
Date August 15, 2014
Drawing # LFC_10301
Bay 3 Technology
#P - 740 4th Ave S.
Hinton, Alberta
Tel: 1.403.817.1223
Fax: 1.403.817.1223
BLUE SKY
BOREALIS
Size ANSI C
Sheet 4 of 8
Project LFC
Issue C
33 x Ø 4.5 THRU
Ø 9.4 X 90°
0.1 M A B C
36 x Ø 4.5 THRU
0.1 M A B C
A
Bottom Side
B
C
1
2
3
4
A
B
C
D

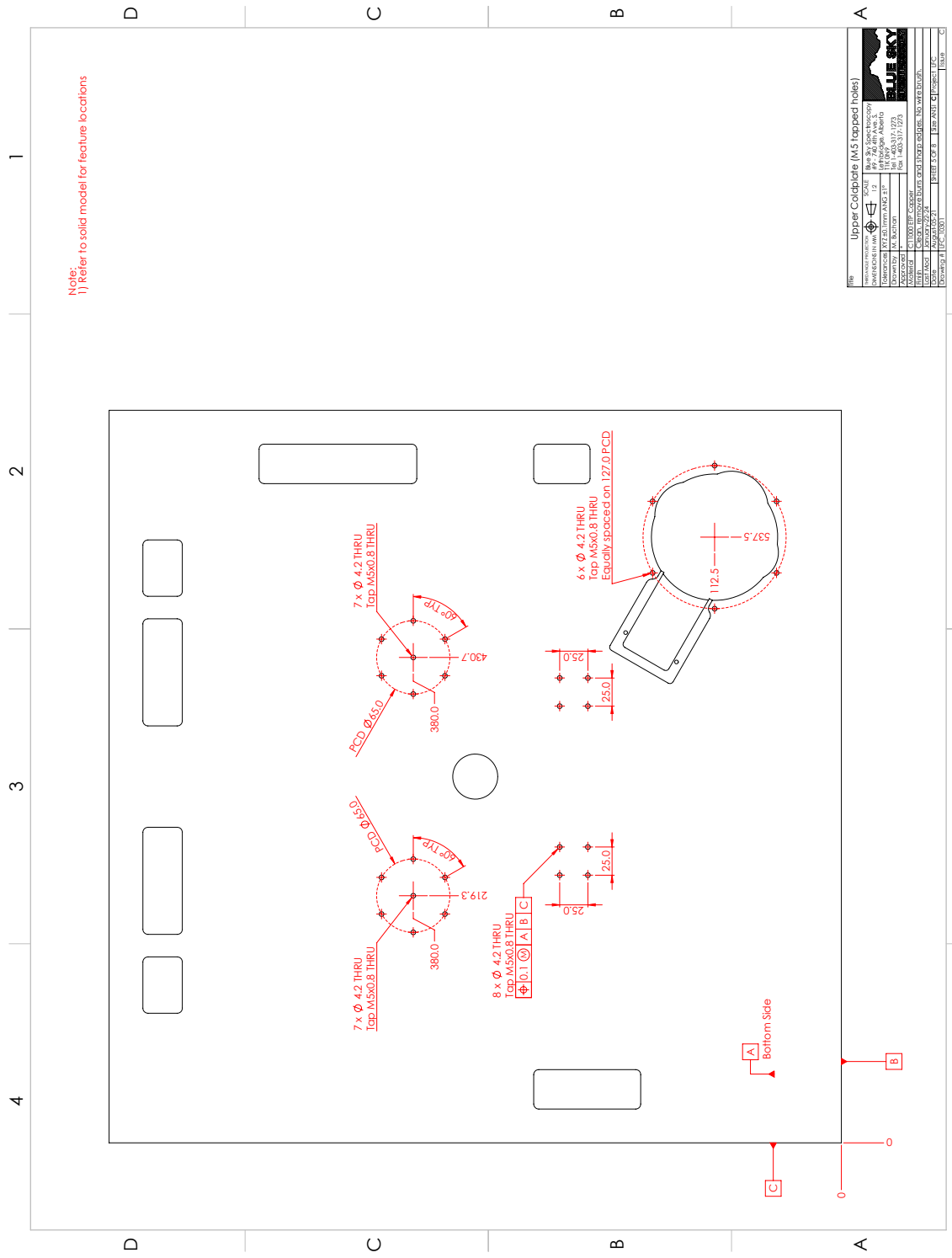
Note:
1) Refer to solid model for feature locations
Upper Coldplate (M5 tapped holes)
Bottom Side
7 x Ø 4.2 THRU
Tap M5x0.8 THRU
60° TYP
PCD Ø450
380.0
430.7
6 x Ø 4.2 THRU
Tap M5x0.8 THRU
Equally spaced on 127.0 PCD
537.5
112.5
25.0
8 x Ø 4.2 THRU
Tap M5x0.8 THRU
0.1 M A B C
219.3
Blue Sky Thermal
Dimensions in mm
Tolerances: XY ±0.1mm ANG ±1°
Drawn by: M. Bichan
Material: c1100 EP Copper
Finish: Clean, remove burn and sharp edges. No weak brush.
Date: August 2024
Drawing #: LFC-11001
Project: LFC
Issue: C

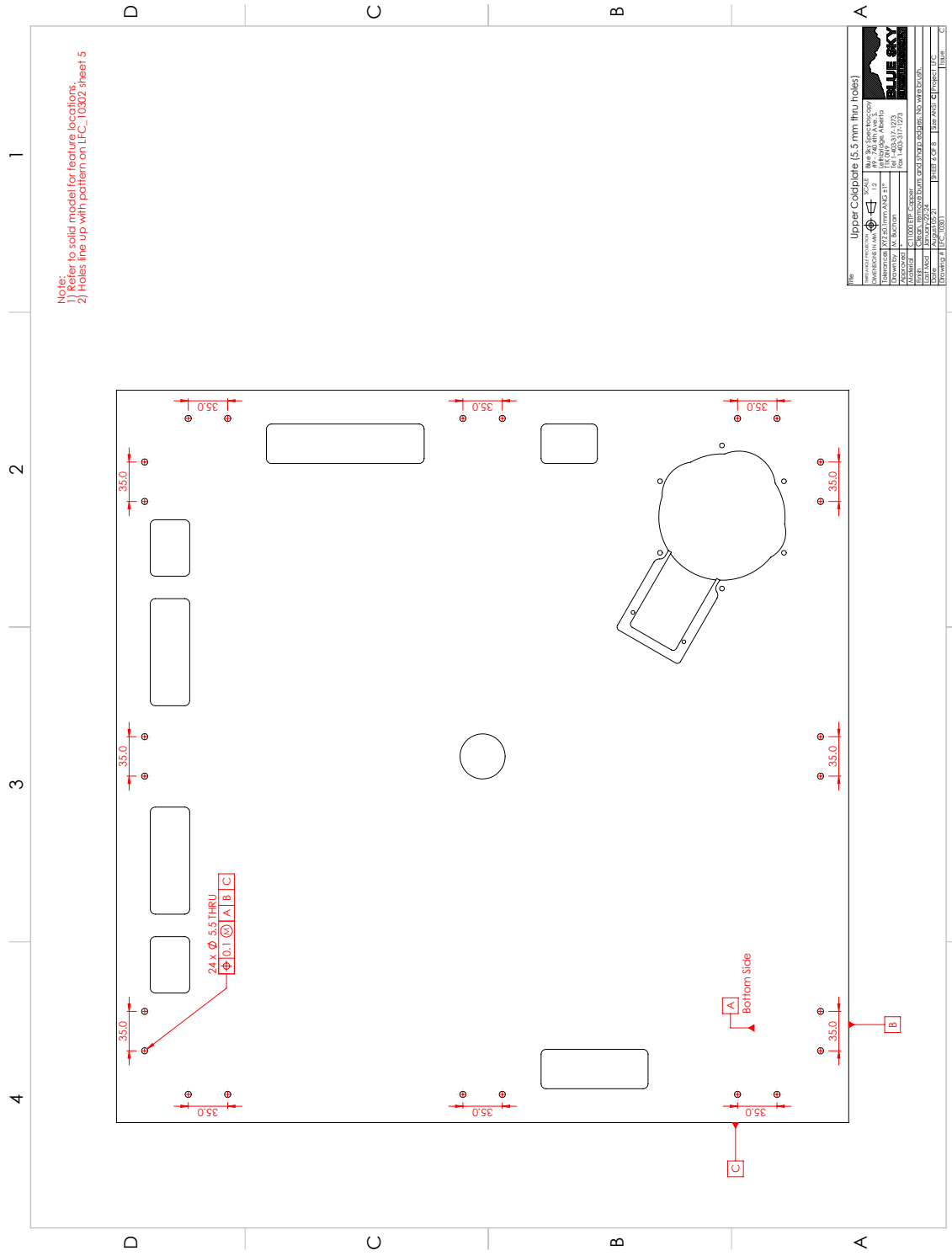
Note:
1) Refer to solid model for feature locations.
2) Holes line up with pattern on LFC_10302 sheet 5
Upper Coldplate (5.5 mm thru holes)
24 x Ø 5.5 THRU
Bottom Side
35.0

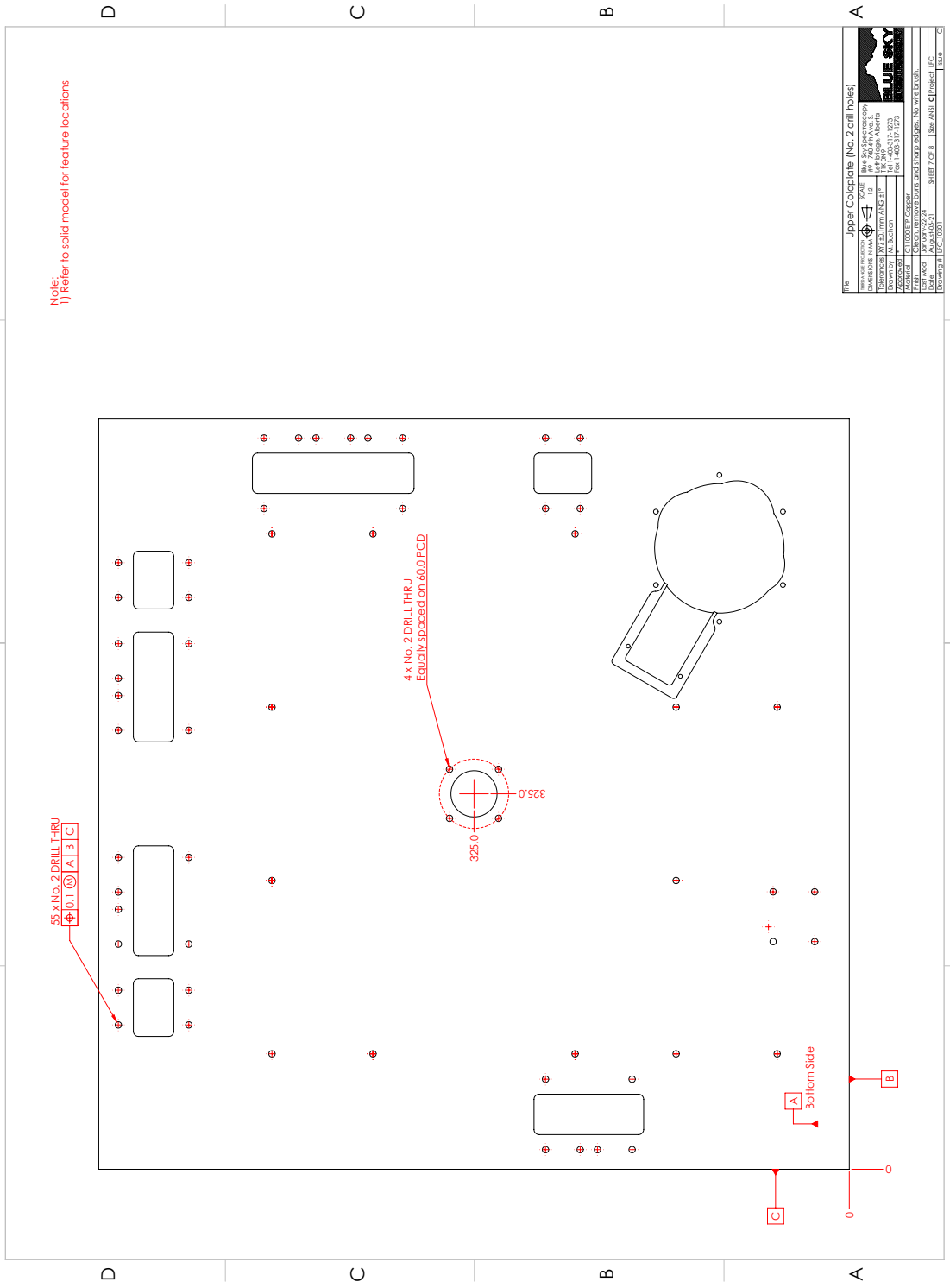
Note:
1) Refer to solid model for feature locations
4 x No. 2 DRILL THRU
Equally spaced on 60.0 PCD
325.0
325.0
55 x No. 2 DRILL THRU
0.1 M A B C
Bottom Side
A
B
C
0
0
Upper Coldplate (No. 2 drill holes)
SCALE 1:2
Dr. Kevin Hanson
PP - 740, 4th Ave. S.W.
Tel: 1.403.317.1223
Fax: 1.403.317.1223
C1100 ETP Copper
Deburr, remove burn and sharp edges. No weld brush.
Argon No. 2.4
Drawing # LFC - 11001
Project: LFC
Issue
C

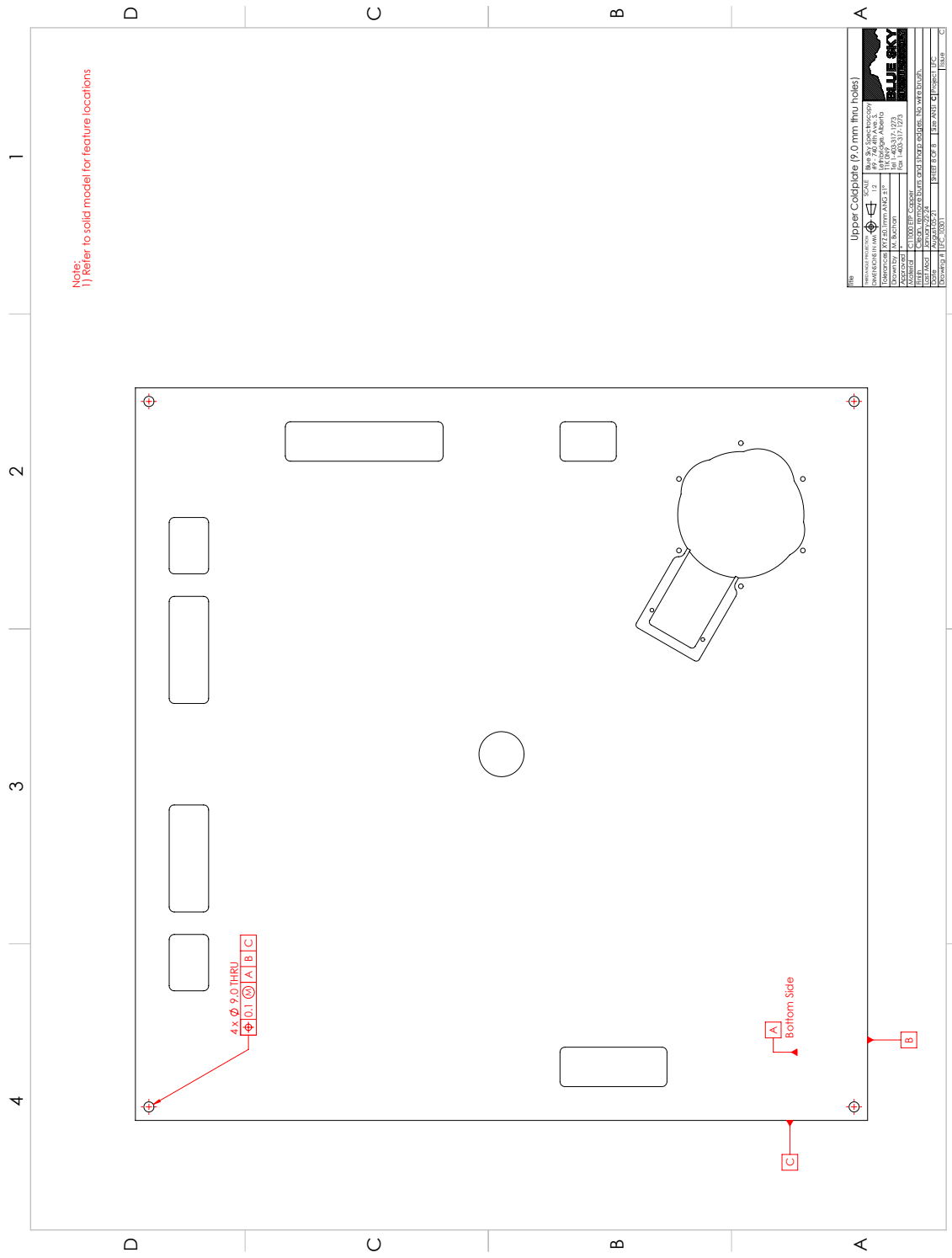
Note:
1) Refer to solid model for feature locations
4 x Ø 9.0 THRU
0.1 M A B C
A
Bottom Side
B
C
Upper Coldplate (9.0 mm thru holes)
BLUE SKY
Project LFC
Issue C
Sheet 1 of 1
Size ANSI B
Drawing # LFC-11001
Material C11000 ETP Copper
Finish Clean, remove burrs and sharp edges. No weld brush.
Surface Finish 32 µ
Qty Required 1
Drawn by M. Bichan
Tolerances .X/1.X±0.1mm ANG ±1°
Scale 1:2
Date August 15, 2014

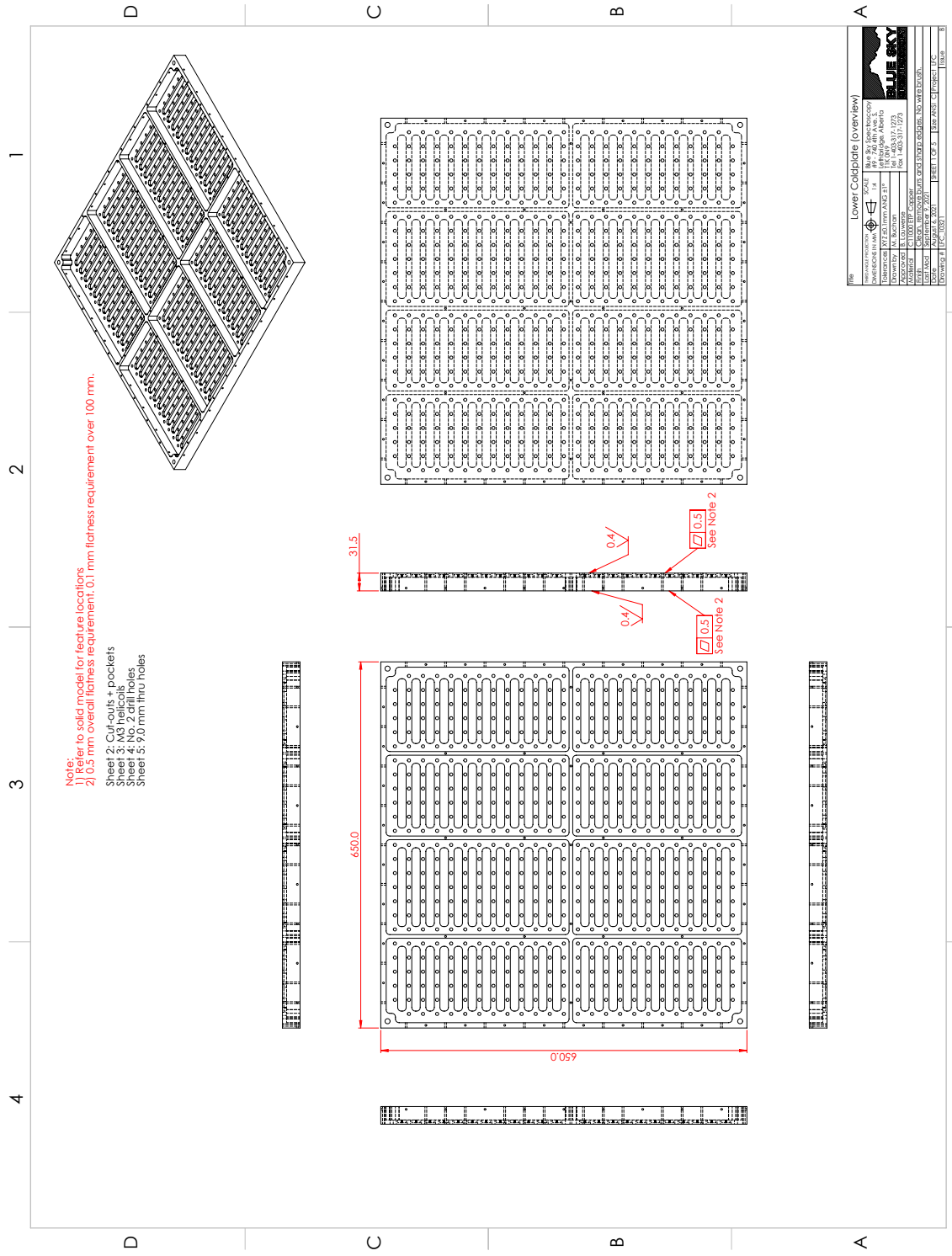
Note:
1) Refer to solid model for feature locations
2) 0.3 mm overall flatness requirement, 0.1 mm flatness requirement over 100 mm.
Sheet 2: Cut-outs + pockets
Sheet 3: M3 helicoils
Sheet 4: No. 2 drill holes
Sheet 5: 9.0 mm thru holes
31.5
0.4
0.4
0.5
See Note 2
0.5
See Note 2
650.0
650.0
Lower Coldplate (overview)
Blue Sky Detectors
Tolerances: XX ±0.1mm ANG ±1°
Drawn by: M. Buchan
Material: C1100 EP Copper
Finish: Clean, remove burn and sharp edges. No weld brush.
Date: August X, 2021
Drawing #: LFC-1002
Sheet 1 of 5
Size ANSI C
Project: LFC
Issue: B

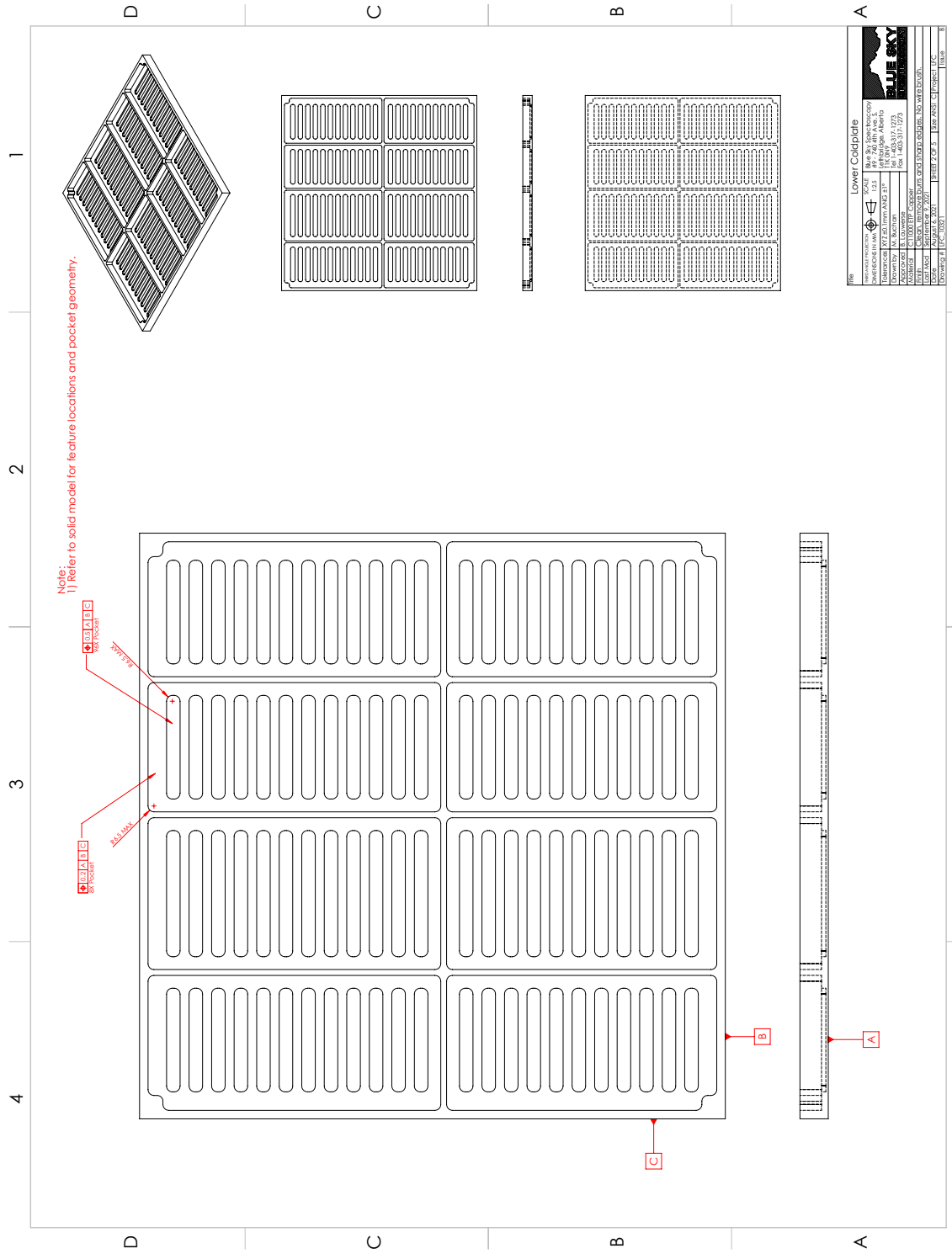
Note:
1) Refer to solid model for feature locations and pocket geometry.
Lower Coldplate
BLUE SKY
R2.5 MAX
R2.5 MAX
SX Pocket
MAX Pocket

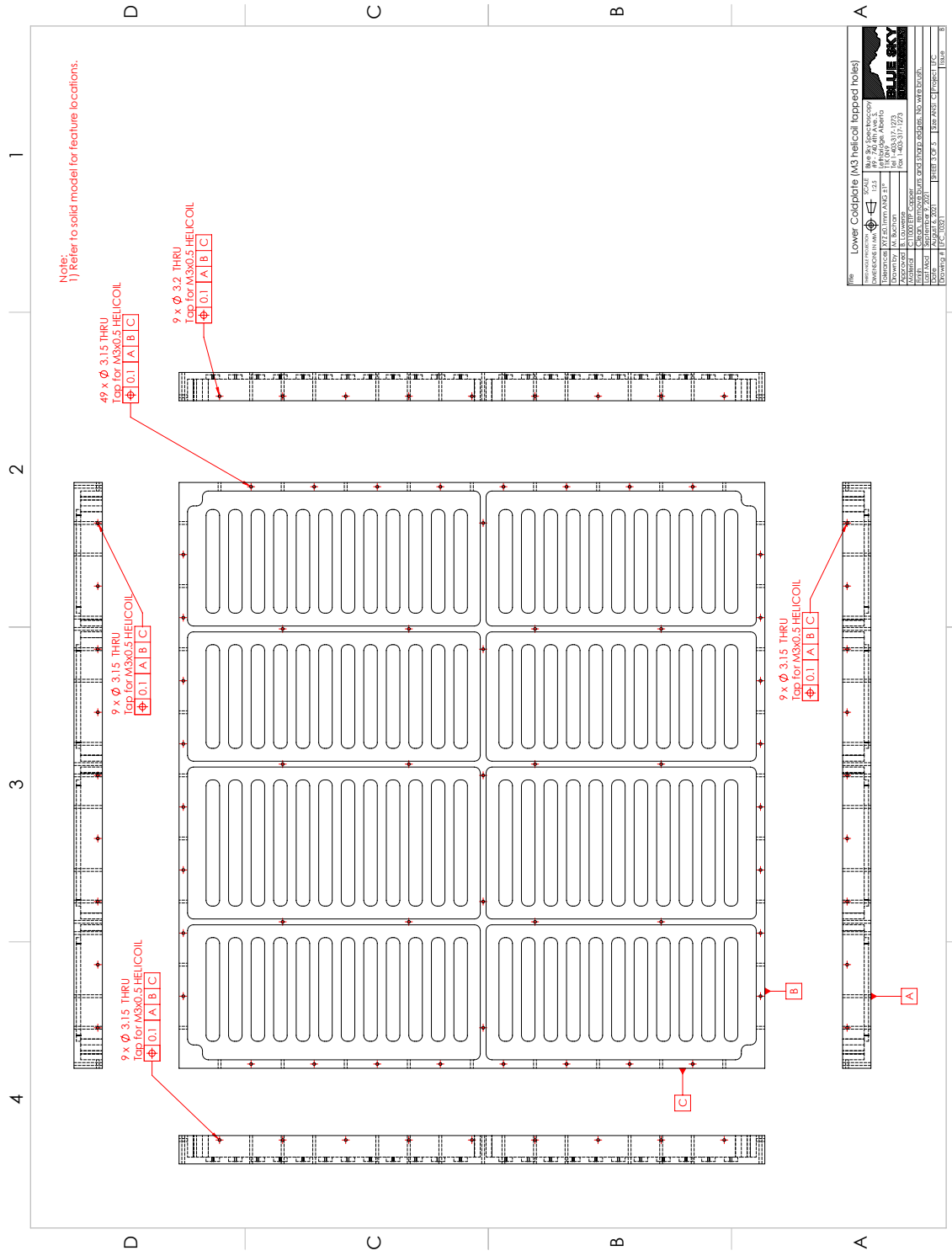
Note:
1) Refer to solid model for feature locations.
49 x Ø 3.15 THRU
Tap for M3x0.5 HELICOIL
0.1 A B C
9 x Ø 3.2 THRU
Tap for M3x0.5 HELICOIL
0.1 A B C
9 x Ø 3.15 THRU
Tap for M3x0.5 HELICOIL
0.1 A B C
9 x Ø 3.15 THRU
Tap for M3x0.5 HELICOIL
0.1 A B C
9 x Ø 3.15 THRU
Tap for M3x0.5 HELICOIL
0.1 A B C
A
B
C
D
1
2
3
4
Lower Coldplate (M3 helicoil tapped holes)
BLUE SKY

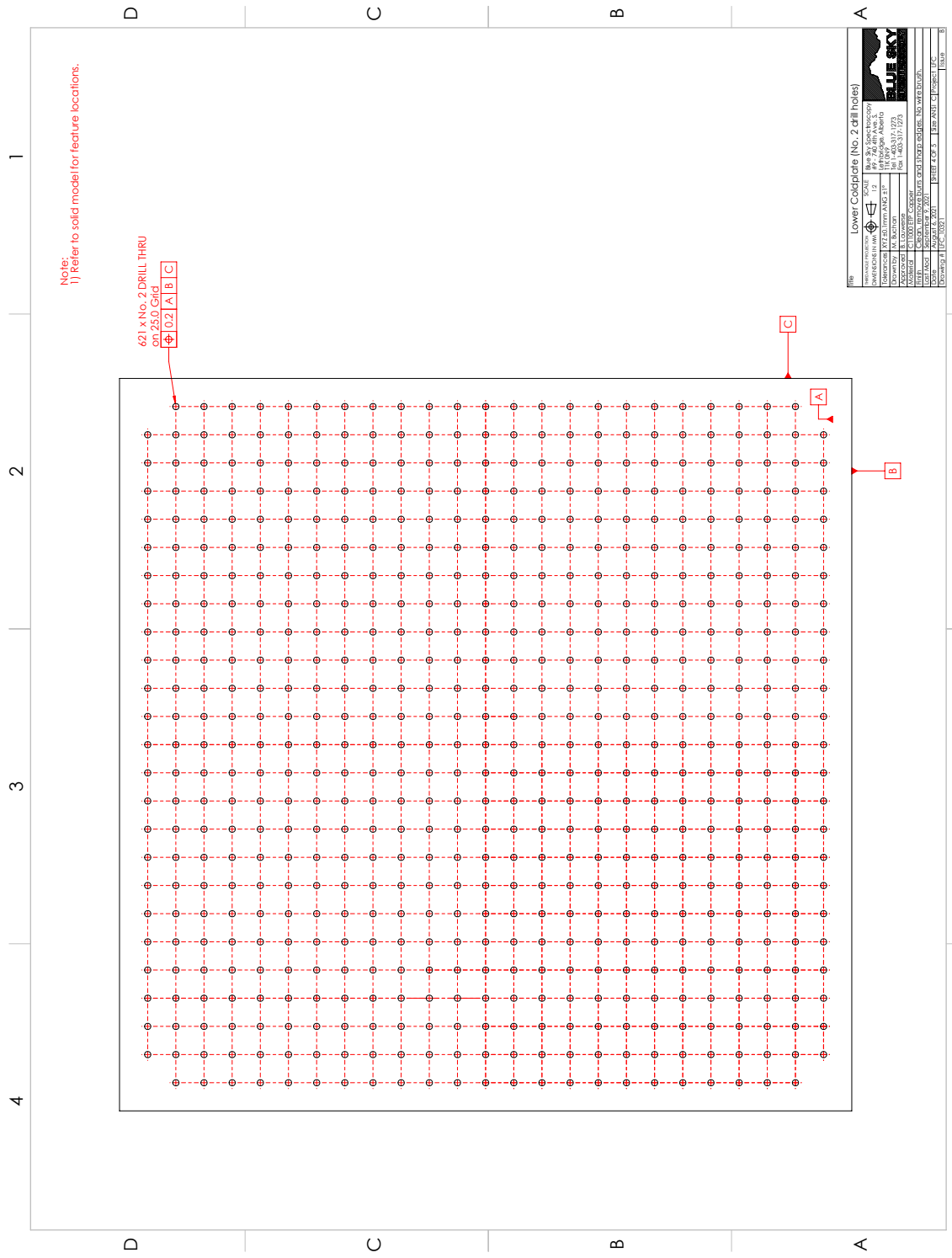
Note:
1) Refer to solid model for feature locations.
621 x No. 2 DRILL THRU
on 25.0 Grid
0.2 A B C
A
B
C
Lower Coldplate (No. 2 drill holes)
SCALE 1:2
Tolerances: XY ±0.1mm ANG ±1°
Drawn by: M. Bochon
Approved by: D. Howlett
Material: C1100 EFP Copper
Finish: Deburr and break sharp edges. No weld brush.
Qty / sheet: 1
Date: August 4, 2021
Drawing #: LFC-1052
Size: ANSI - C
Project: LFC
Issue: B

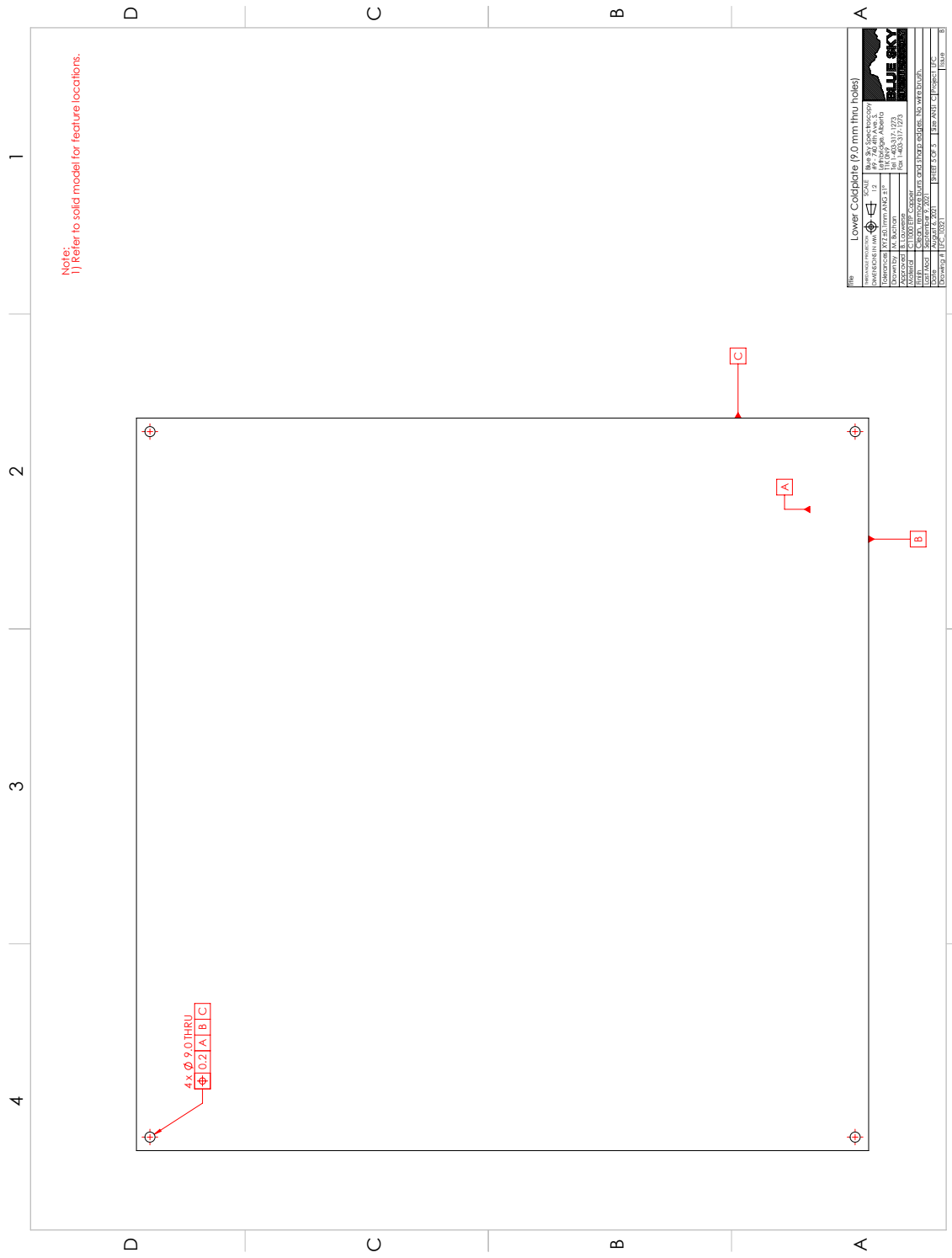
Note:
1) Refer to solid model for feature locations.
Title: Lower Coldplate (9.0 mm thru holes)
Dimensions in mm
DIMENSIONS IN MM
SCALE: 1/2
Tolerances: X±0.1mm ANG ±1°
Drawn by: M. Bachan
Approved: B. Livingstone
Material: C1100 RIP Copper
Finish: Deburr, remove burn and sharp edges. No weld brush.
Surface: Ra 3.2 unless otherwise specified
Date: August 4, 2021
Drawing #: LFC-1002
Blue Sky Thermal
#9 - 740 4th Ave. S.W.
Medicine Hat, Alberta
Tel: 1.403.317.1223
Fax: 1.403.317.1273
BLUE SKY
THERMAL
Sheet 1 of 1
Size ANSI - C
Project: LFC
Issue: B
4 x Ø 9.0 THRU
Ø 0.2 A B C
A
B
C

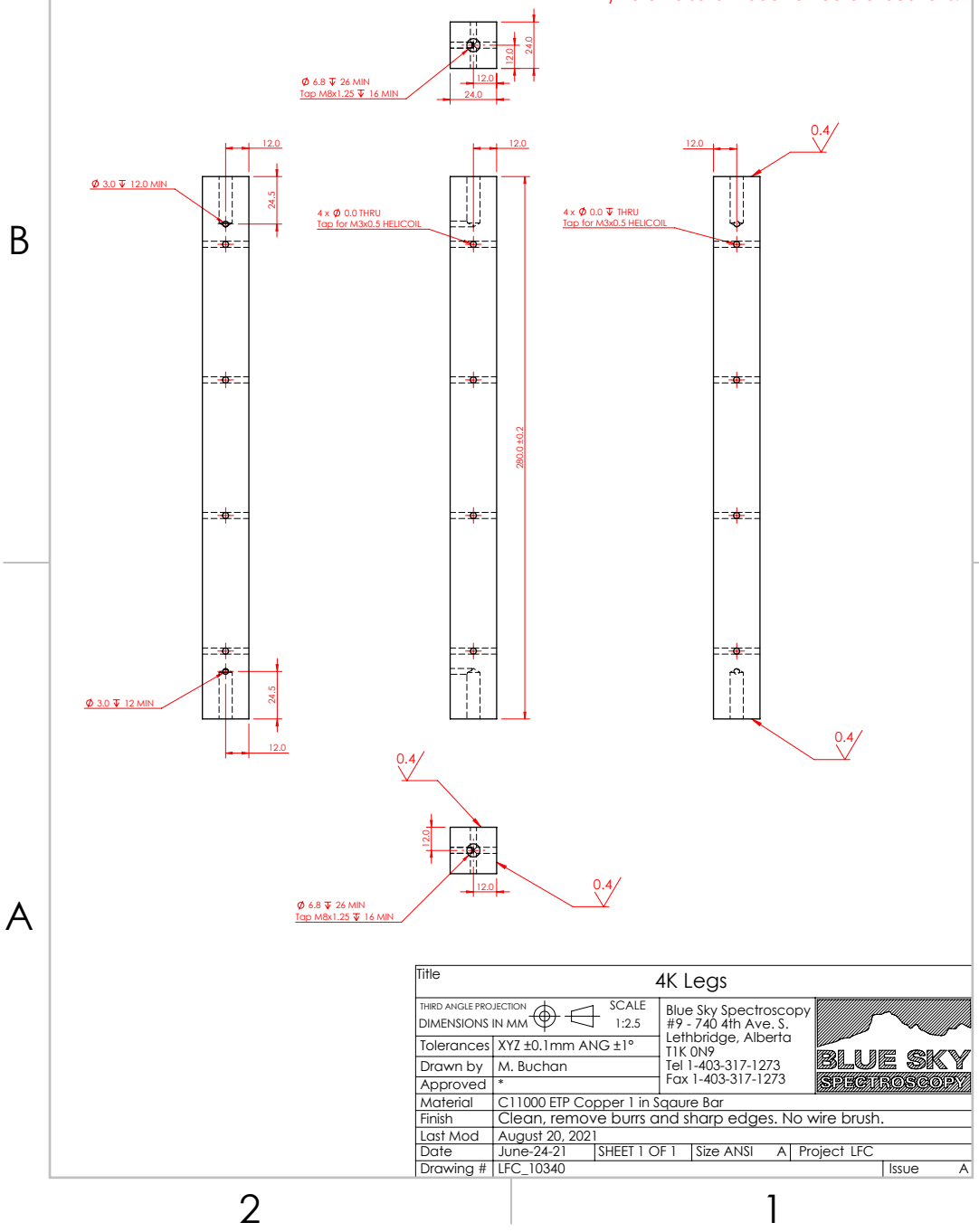

Title	4K Legs			
THIRD ANGLE PROJECTION DIMENSIONS IN MM	SCALE 1:2.5	Blue Sky Spectroscopy #9 - 740 4th Ave. S. Lethbridge, Alberta T1K 0N9 Tel 1-403-317-1273 Fax 1-403-317-1273		
Tolerances	XYZ ±0.1mm ANG ±1°			
Drawn by	M. Buchan			
Approved	*			
Material	C11000 ETP Copper 1 in Sqaure Bar			
Finish	Clean, remove burrs and sharp edges. No wire brush.			
Last Mod	August 20, 2021			
Date	June-24-21	SHEET 1 OF 1	Size ANSI A	Project LFC
Drawing #	LFC_10340			Issue A

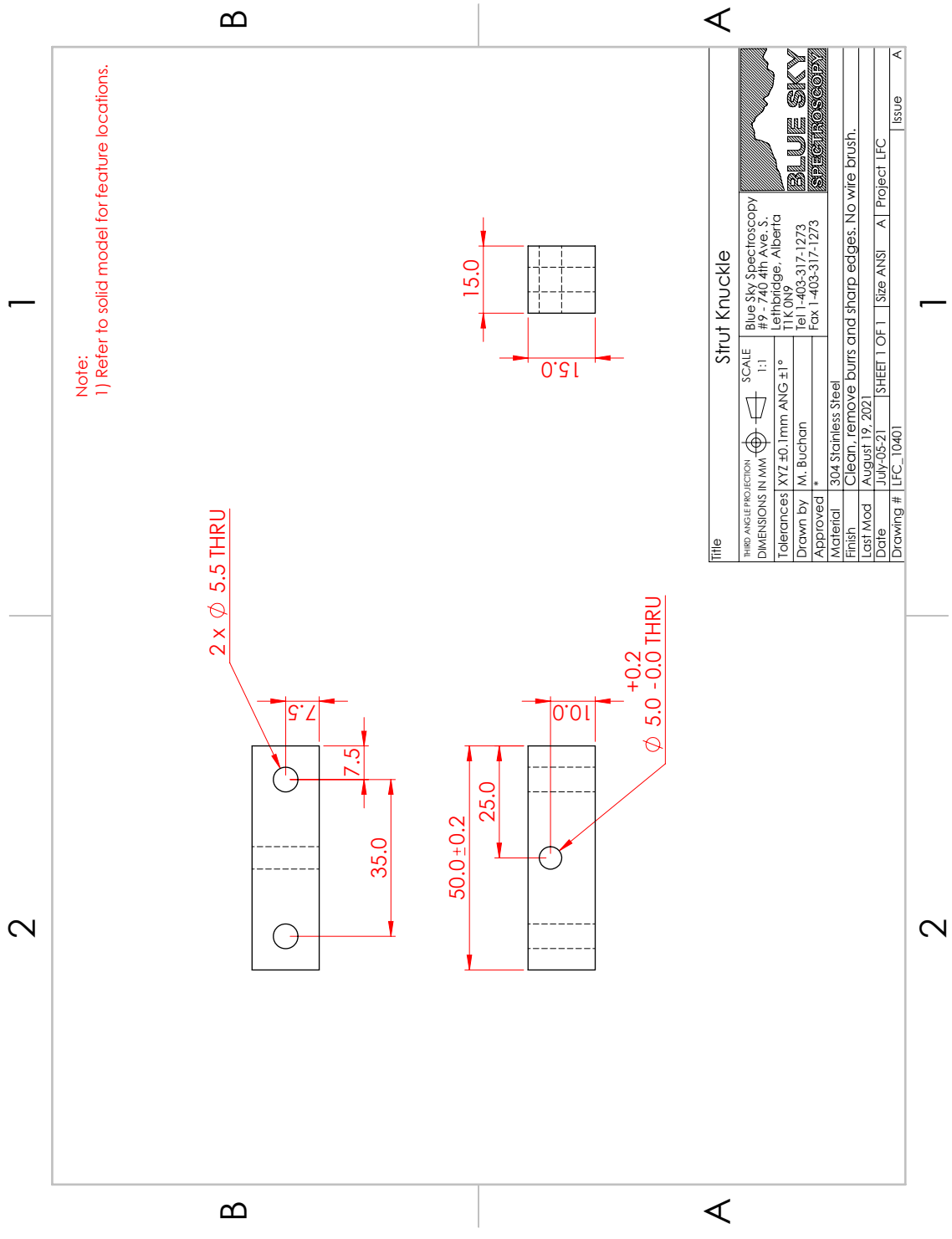
Note:
1) Refer to solid model for feature locations.
2 x ∅ 5.5 THRU
7.5
7.5
35.0
50.0±0.2
25.0
10.0
+0.2
∅ 5.0 -0.0 THRU
15.0
15.0
Title
Strut Knuckle
THIRD ANGLE PROJECTION
DIMENSIONS IN MM
SCALE 1:1
Blue Sky Spectroscopy
#9 - 740 4th Ave. S.
Lethbridge, Alberta
T1K 0N9
Tel 1-403-317-1273
Fax 1-403-317-1273
BLUE SKY SPECTROSCOPY
Tolerances XYZ ±0.1mm ANG ±1°
Drawn by M. Buchan
Approved *
Material 304 Stainless Steel
Finish Clean, remove burrs and sharp edges. No wire brush.
Last Mod August 19, 2021
Date July-05-21
SHEET 1 OF 1
Size ANSI A
Project LFC
Drawing # LFC_1040
Issue A

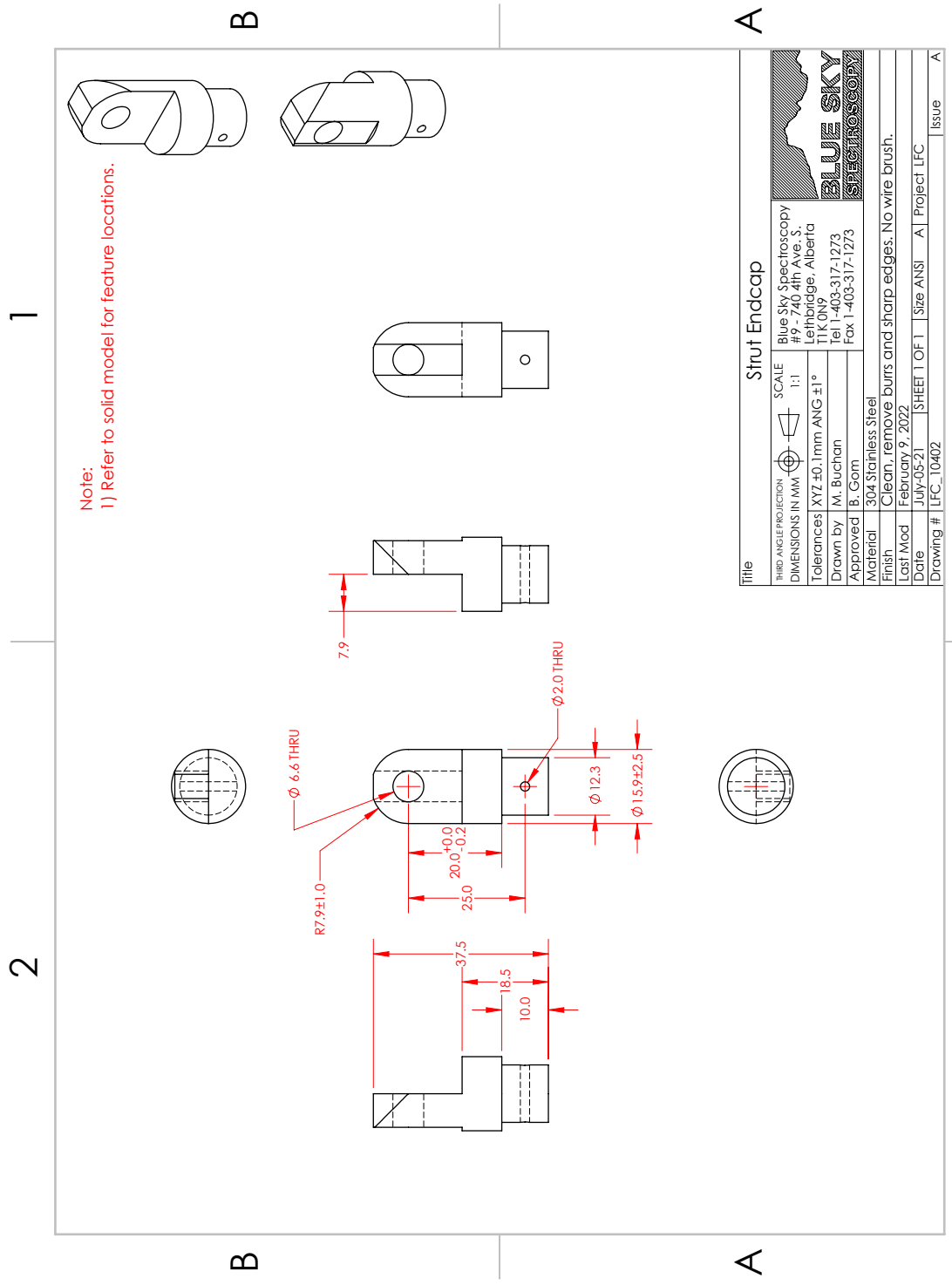
Note:
1) Refer to solid model for feature locations.
7.9
Ø 6.6 THRU
Ø 2.0 THRU
Ø 12.3
Ø 15.9±2.5
R7.9±1.0
20.0 +0.0 -0.2
25.0
37.5
18.5
10.0
Title
Strut Endcap
THIRD ANGLE PROJECTION
DIMENSIONS IN MM
SCALE 1:1
Tolerances XYZ ±0.1mm ANG ±1°
Drawn by M. Buchan
Approved B. Gom
Material 304 Stainless Steel
Finish Clean, remove burrs and sharp edges. No wire brush.
Last Mod February 9, 2022
Date July-05-21
SHEET 1 OF 1
Size ANSI A
Project LFC
Drawing # LFC_10402
Issue A
Blue Sky Spectroscopy
#9 - 740 4th Ave. S.
Lethbridge, Alberta
T1K 0N9
Tel 1-403-317-1273
Fax 1-403-317-1273
BLUE SKY
SPECTROSCOPY

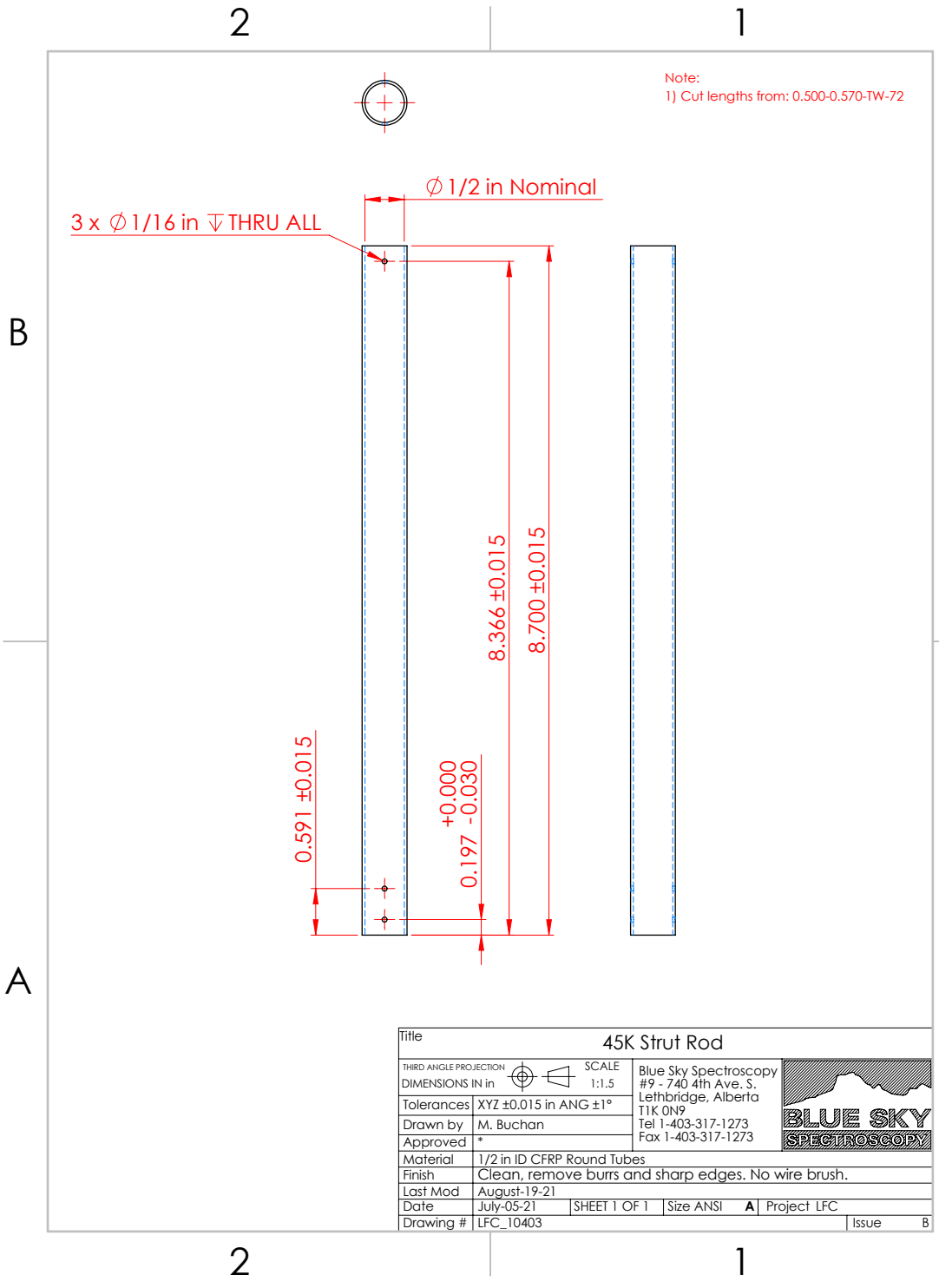
2
1
B
A
Note:
1) Cut lengths from: 0.500-0.570-TW-72
∅ 1/2 in Nominal
3 x ∅ 1/16 in ↧ THRU ALL
8.366 ±0.015
8.700 ±0.015
0.591 ±0.015
+0.000
0.197 -0.030
Title
45K Strut Rod
THIRD ANGLE PROJECTION
DIMENSIONS IN in
SCALE
1:1.5
Blue Sky Spectroscopy
#9 - 740 4th Ave. S.
Lethbridge, Alberta
T1K 0N9
Tel 1-403-317-1273
Fax 1-403-317-1273
BLUE SKY SPECTROSCOPY
Tolerances
XYZ ±0.015 in ANG ±1°
Drawn by
M. Buchan
Approved
*
Material
1/2 in ID CFRP Round Tubes
Finish
Clean, remove burrs and sharp edges. No wire brush.
Last Mod
August-19-21
Date
July-05-21
SHEET 1 OF 1
Size ANSI A
Project LFC
Drawing #
LFC_10403
Issue
B

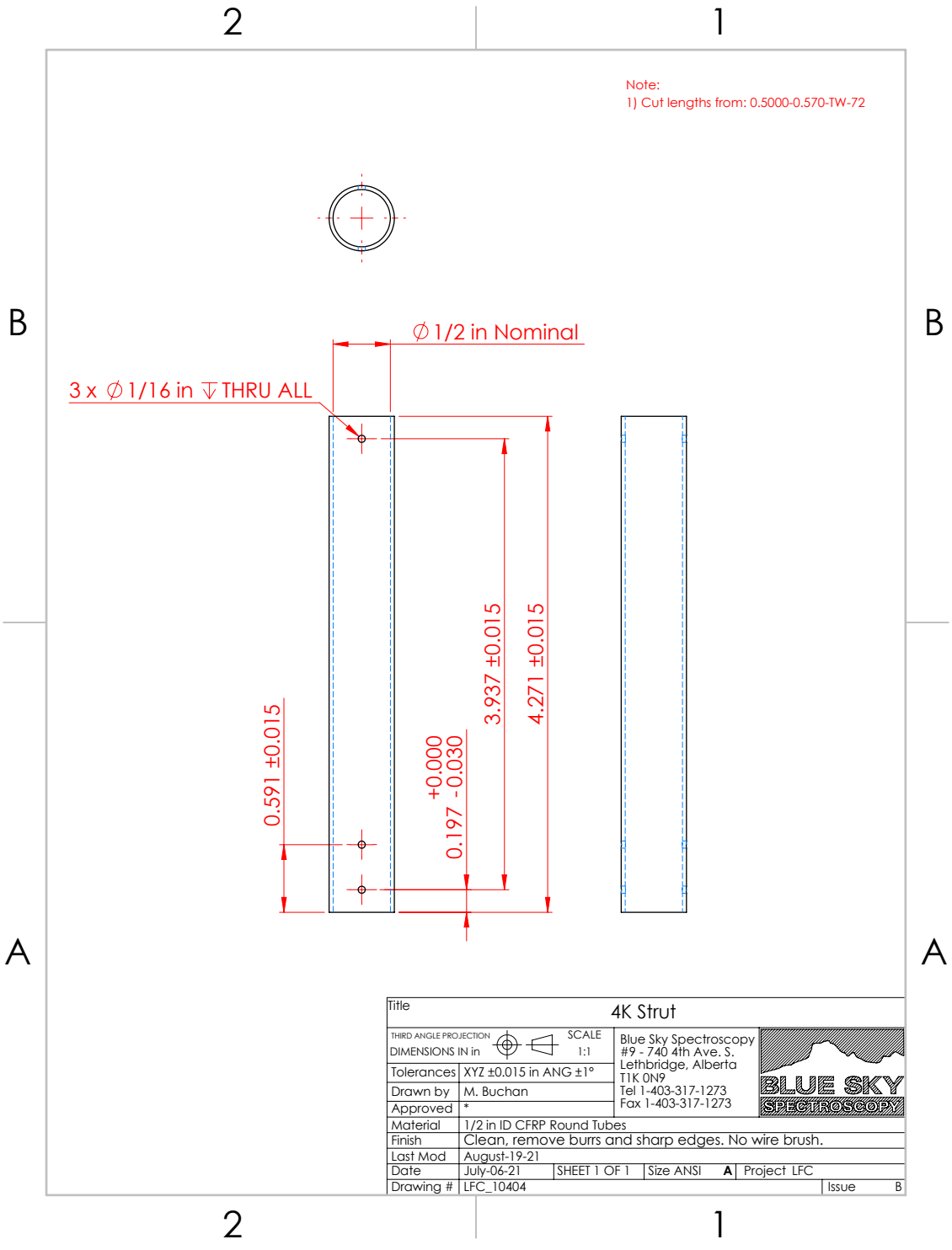

Title	4K Strut			
THIRD ANGLE PROJECTION DIMENSIONS IN in	SCALE 1:1	Blue Sky Spectroscopy #9 - 740 4th Ave. S. Lethbridge, Alberta T1K 0N9 Tel 1-403-317-1273 Fax 1-403-317-1273		
Tolerances	XYZ ±0.015 in ANG ±1°			
Drawn by	M. Buchan			
Approved	*			
Material	1/2 in ID CFRP Round Tubes			
Finish	Clean, remove burrs and sharp edges. No wire brush.			
Last Mod	August-19-21			
Date	July-06-21	SHEET 1 OF 1	Size ANSI A	Project LFC
Drawing #	LFC_10404			Issue B

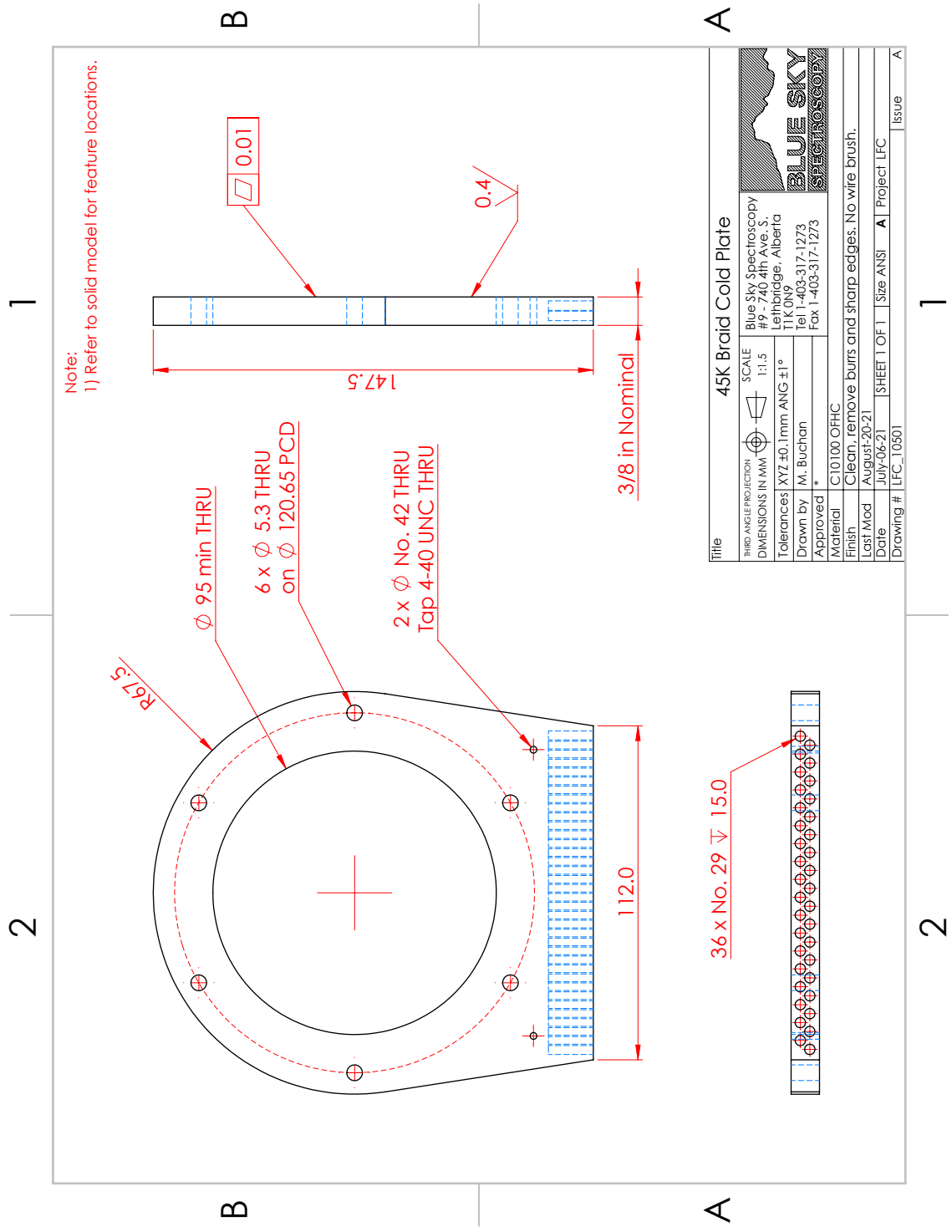
Note:
1) Refer to solid model for feature locations.
0.01
0.4
147.5
3/8 in Nominal
Ø 95 min THRU
6 x Ø 5.3 THRU
on Ø 120.65 PCD
2 x Ø No. 42 THRU
Tap 4-40 UNC THRU
R7.5
112.0
36 x No. 29 ↧ 15.0
Title
45K Braid Cold Plate
THIRD ANGLE PROJECTION
DIMENSIONS IN MM
SCALE 1:1.5
Tolerances XYZ ±0.1mm ANG ±1°
Drawn by M. Buchan
Approved *
Material C10100 OFHC
Finish Clean, remove burrs and sharp edges. No wire brush.
Last Mod August-20-21
Date July-06-21
Drawing # LFC_10501
SHEET 1 OF 1
Size ANSI A
Project LFC
Issue A
Blue Sky Spectroscopy
#9 - 740 4th Ave. S.
Lethbridge, Alberta
T1K 0N9
Tel 1-403-317-1273
Fax 1-403-317-1273
BLUE SKY SPECTROSCOPY

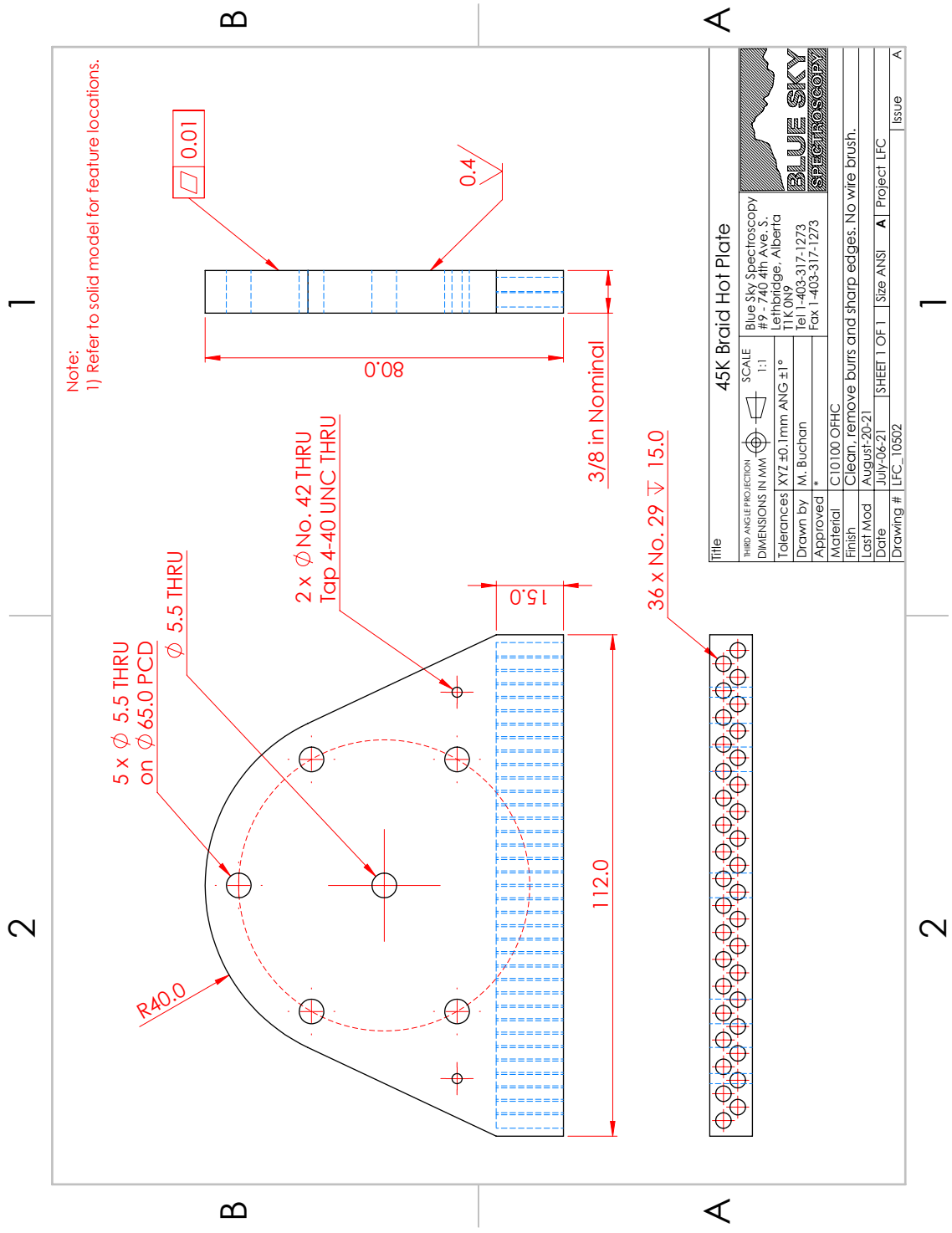
Note:
1) Refer to solid model for feature locations.
0.01
0.4
80.0
3/8 in Nominal
2 x ⌀ No. 42 THRU
Tap 4-40 UNC THRU
⌀ 5.5 THRU
5 x ⌀ 5.5 THRU
on ⌀ 65.0 PCD
R40.0
15.0
112.0
36 x No. 29 ↧ 15.0
Title
45K Braid Hot Plate
THIRD ANGLE PROJECTION
DIMENSIONS IN MM
SCALE 1:1
Tolerances XYZ ±0.1mm ANG ±1°
Drawn by M. Buchan
Approved *
Material C10100 OFHC
Finish Clean, remove burrs and sharp edges. No wire brush.
Last Mod August-20-21
Date July-06-21
Drawing # LFC_10502
SHEET 1 OF 1
Size ANSI A
Project LFC
Issue A
Blue Sky Spectroscopy
#9 - 740 4th Ave. S.
Lethbridge, Alberta
T1K 0N9
Tel 1-403-317-1273
Fax 1-403-317-1273
BLUE SKY
SPECTROSCOPY

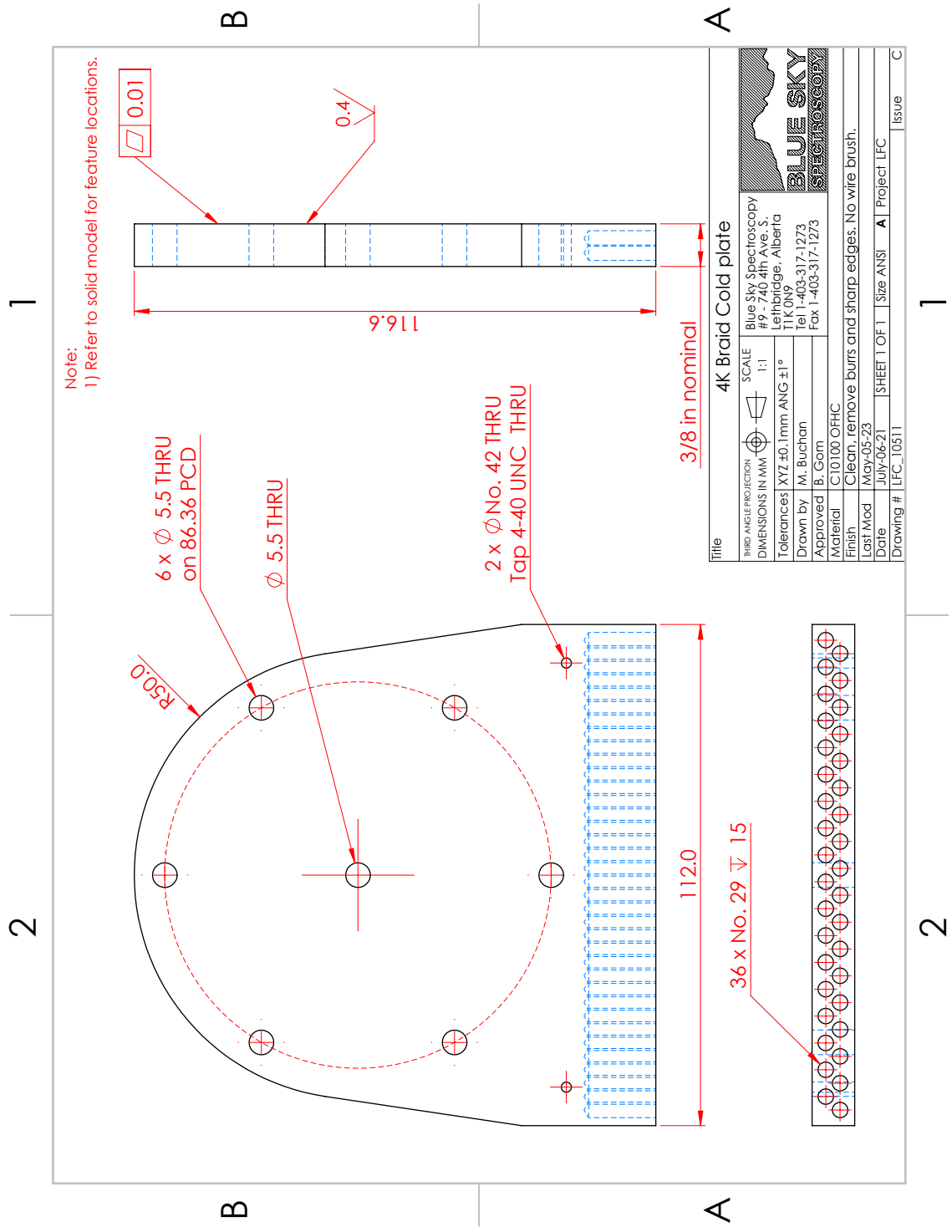
Note:
1) Refer to solid model for feature locations.
0.01
0.4
116.6
3/8 in nominal
6 x ∅ 5.5 THRU
on 86.36 PCD
∅ 5.5 THRU
2 x ∅No. 42 THRU
Tap 4-40 UNC THRU
R50.0
112.0
36 x No. 29 ↧ 15
Title
4K Braid Cold plate
THIRD ANGLE PROJECTION
DIMENSIONS IN MM
SCALE 1:1
Tolerances XYZ ±0.1mm ANG ±1°
Drawn by M. Buchan
Approved B. Gom
Material C10100 OFHC
Finish Clean, remove burrs and sharp edges. No wire brush.
Last Mod May-05-23
Date July-06-21
Drawing # LFC_10511
SHEET 1 OF 1
Size ANSI A
Project LFC
Issue C
Blue Sky Spectroscopy
#9 - 740 4th Ave. S.
Lethbridge, Alberta
T1K 0N9
Tel 1-403-317-1273
Fax 1-403-317-1273
BLUE SKY
SPECTROSCOPY

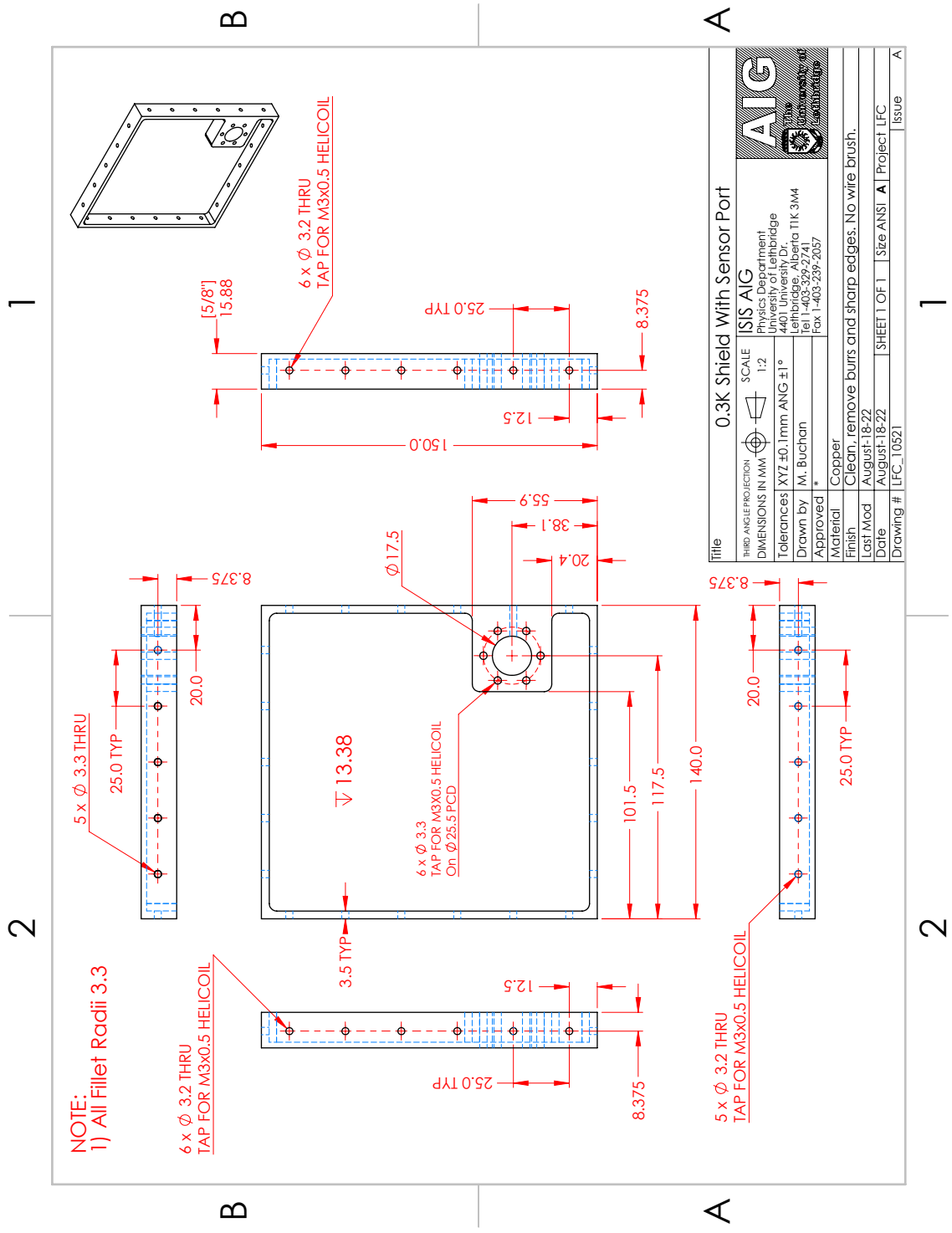
NOTE:
1) All Fillet Radii 3.3
6 x Ø 3.2 THRU
TAP FOR M3x0.5 HELICOIL
[5/8"]
15.88
25.0 TYP
8.375
12.5
150.0
55.9
38.1
20.4
Ø17.5
8.375
20.0
5 x Ø 3.3 THRU
25.0 TYP
13.38
6 x Ø 3.3
TAP FOR M3X0.5 HELICOIL
On Ø25.5 PCD
101.5
117.5
140.0
3.5 TYP
5 x Ø 3.2 THRU
TAP FOR M3x0.5 HELICOIL
Title
0.3K Shield With Sensor Port
THIRD ANGLE PROJECTION
DIMENSIONS IN MM
SCALE 1:2
ISIS AIG
Physics Department
University of Lethbridge
4401 University Dr.
Lethbridge, Alberta T1K 3M4
Tel 1-403-329-2741
Fax 1-403-239-2057
Tolerances XYZ ±0.1mm ANG ±1°
Drawn by M. Buchan
Approved *
Material Copper
Finish Clean, remove burrs and sharp edges. No wire brush.
Last Mod August-18-22
Date August-18-22
Drawing # LFC_10521
SHEET 1 OF 1
Size ANSI A
Project LFC
Issue A

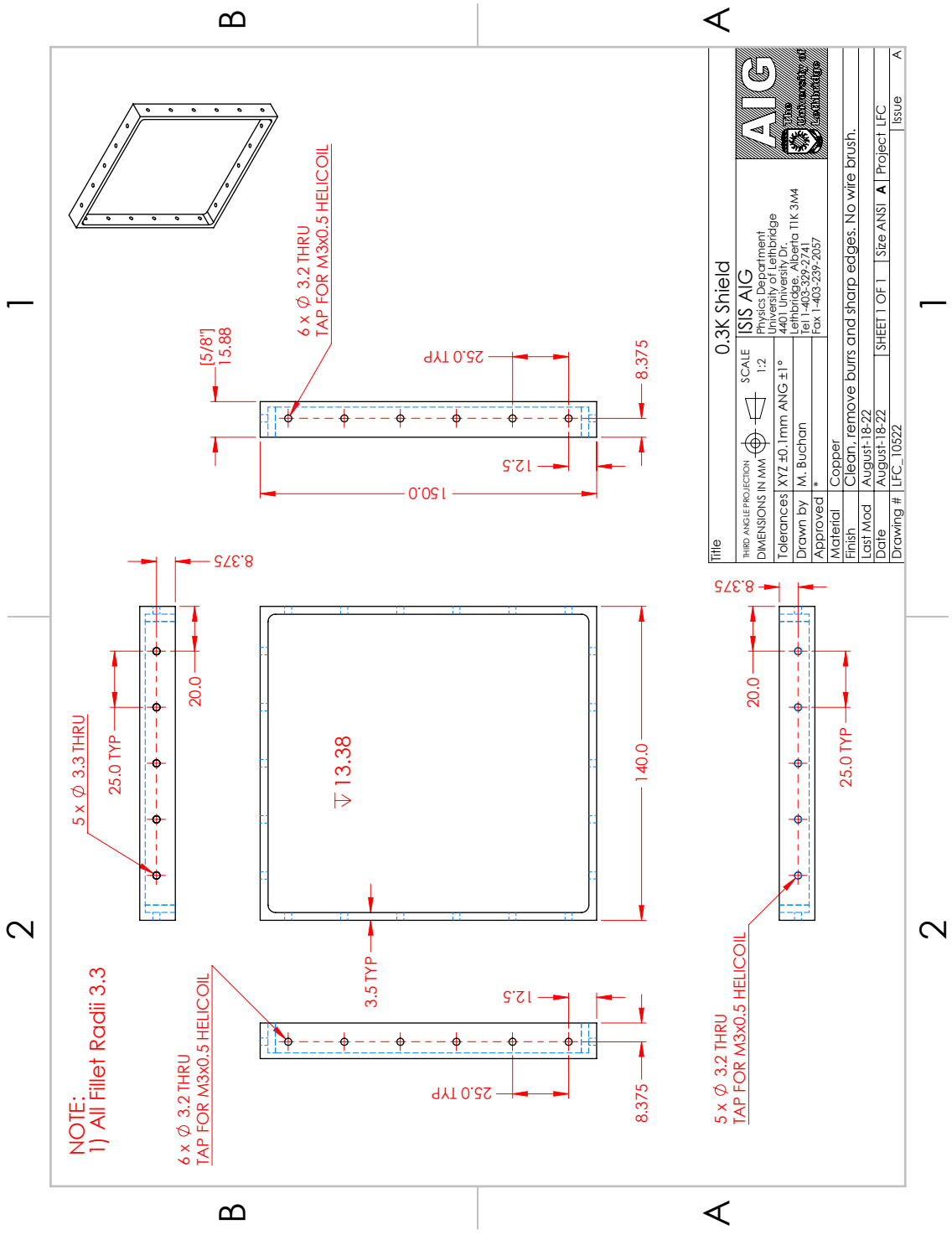
NOTE:
1) All Fillet Radii 3.3
6 x Ø 3.2 THRU
TAP FOR M3x0.5 HELICOIL
5 x Ø 3.3 THRU
25.0 TYP
20.0
8.375
13.38
140.0
3.5 TYP
12.5
25.0 TYP
8.375
[5/8"]
15.88
150.0
5 x Ø 3.2 THRU
TAP FOR M3x0.5 HELICOIL
Title
0.3K Shield
SCALE 1:2
THIRD ANGLE PROJECTION
DIMENSIONS IN MM
Tolerances XYZ ±0.1mm ANG ±1°
Drawn by M. Buchan
Approved *
Material Copper
Finish Clean, remove burrs and sharp edges. No wire brush.
Last Mod August-18-22
Date August-18-22
Drawing # LFC_10522
ISIS AIG
Physics Department
University of Lethbridge
4401 University Dr.
Lethbridge, Alberta T1K 3M4
Tel 1-403-329-2741
Fax 1-403-239-2057
The University of Lethbridge
SHEET 1 OF 1
Size ANSI A
Project LFC
Issue A

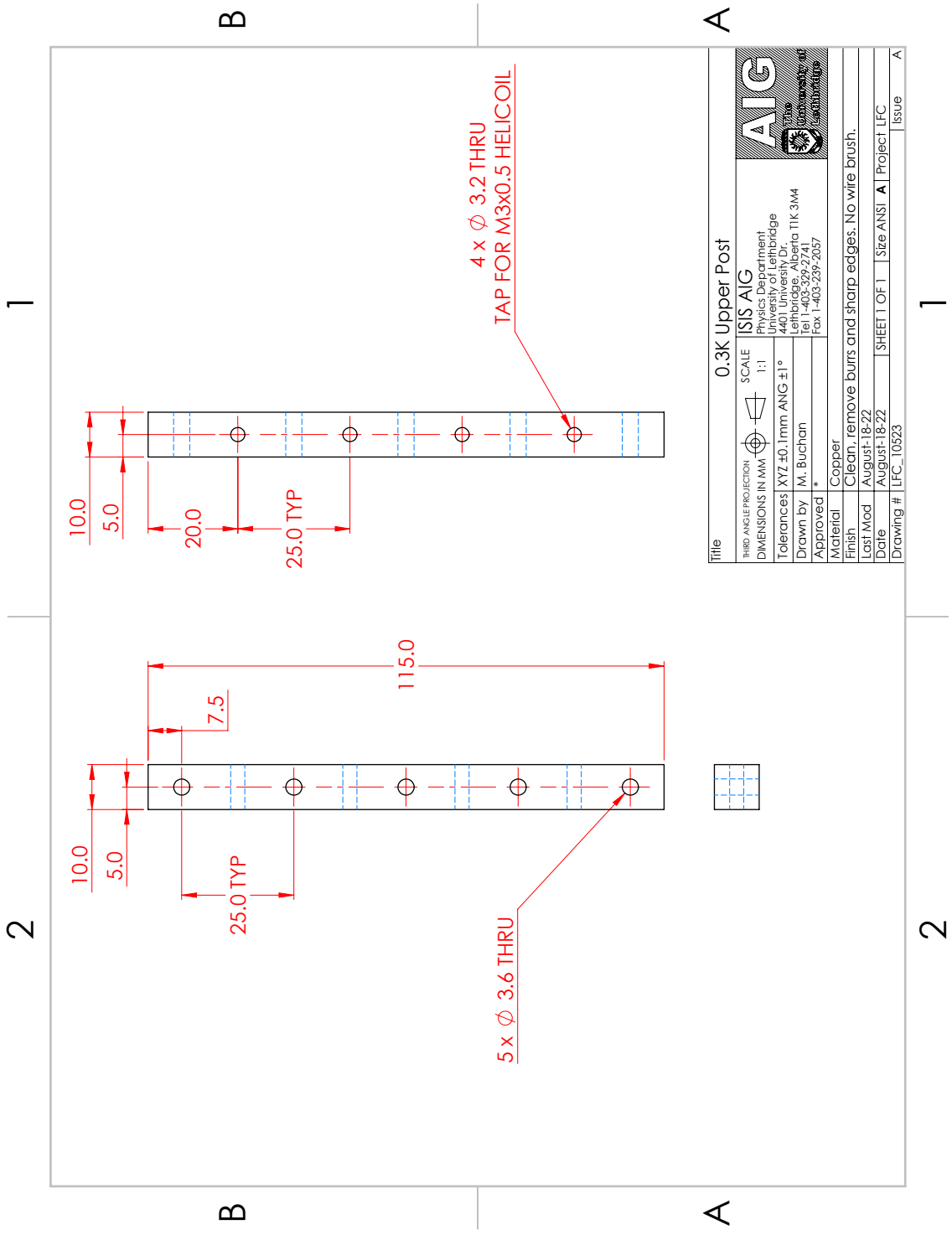
4 x ∅ 3.2 THRU
TAP FOR M3x0.5 HELICOIL
10.0
5.0
20.0
25.0 TYP
115.0
7.5
10.0
5.0
25.0 TYP
5 x ∅ 3.6 THRU
Title
0.3K Upper Post
THIRD ANGLE PROJECTION
DIMENSIONS IN MM
SCALE 1:1
ISIS AIG
Physics Department
University of Lethbridge
4401 University Dr.
Lethbridge, Alberta T1K 3M4
Tel 1-403-329-2741
Fax 1-403-239-2057
Tolerances XYZ ±0.1mm ANG ±1°
Drawn by M. Buchan
Approved *
Material Copper
Finish Clean, remove burrs and sharp edges. No wire brush.
Last Mod August-18-22
Date August-18-22
Drawing # LFC_10523
SHEET 1 OF 1
Size ANSI A
Project LFC
Issue A

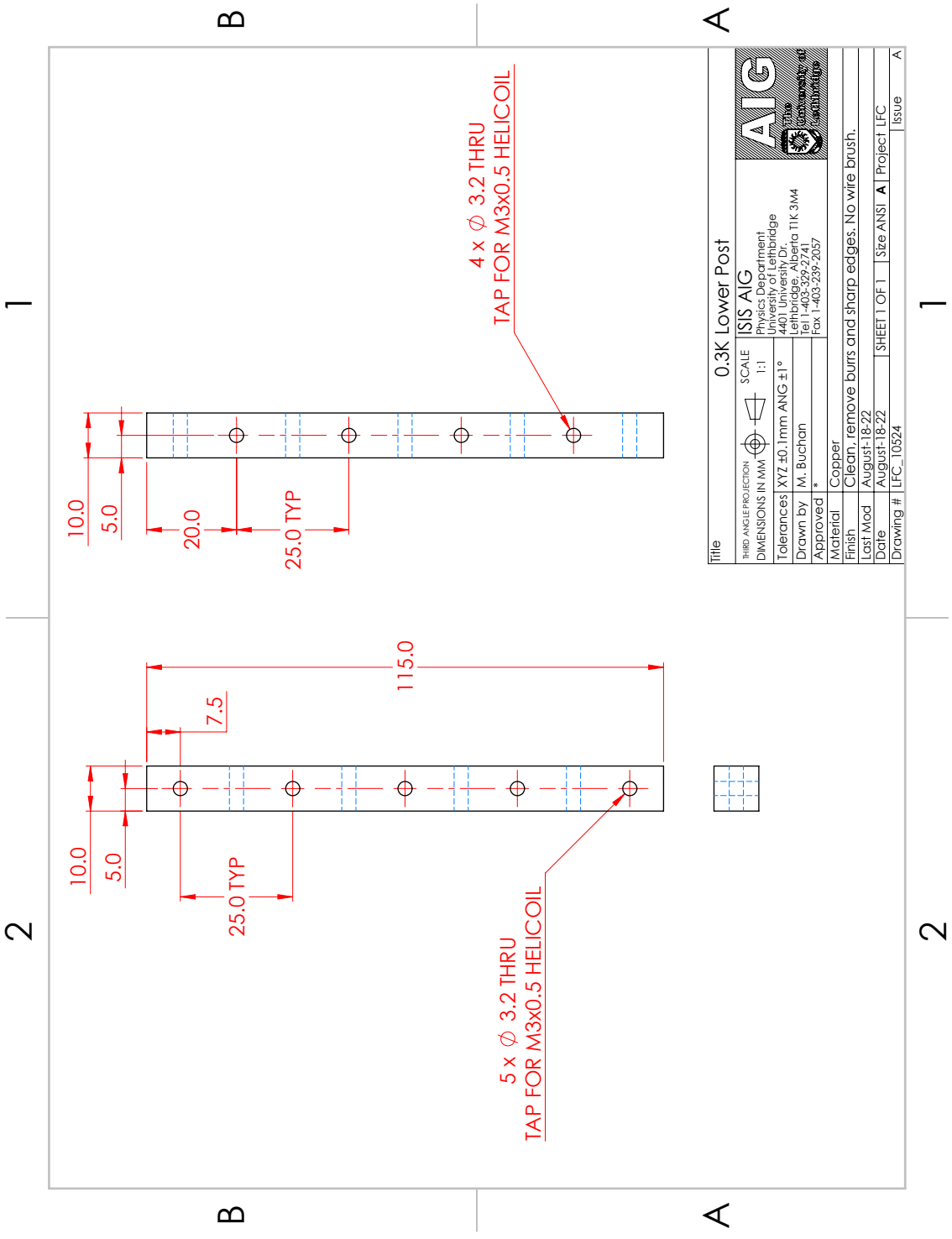
4 x ∅ 3.2 THRU
TAP FOR M3x0.5 HELICOIL
10.0
5.0
20.0
25.0 TYP
115.0
7.5
10.0
5.0
25.0 TYP
5 x ∅ 3.2 THRU
TAP FOR M3x0.5 HELICOIL
Title
0.3K Lower Post
THIRD ANGLE PROJECTION
DIMENSIONS IN MM
SCALE 1:1
ISIS AIG
Physics Department
University of Lethbridge
4401 University Dr.
Lethbridge, Alberta T1K 3M4
Tel 1-403-329-2741
Fax 1-403-239-2057
Tolerances XYZ ±0.1mm ANG ±1°
Drawn by M. Buchan
Approved *
Material Copper
Finish Clean, remove burrs and sharp edges. No wire brush.
Last Mod August-18-22
Date August-18-22
Drawing # LFC_10524
SHEET 1 OF 1
Size ANSI A
Project LFC
Issue A

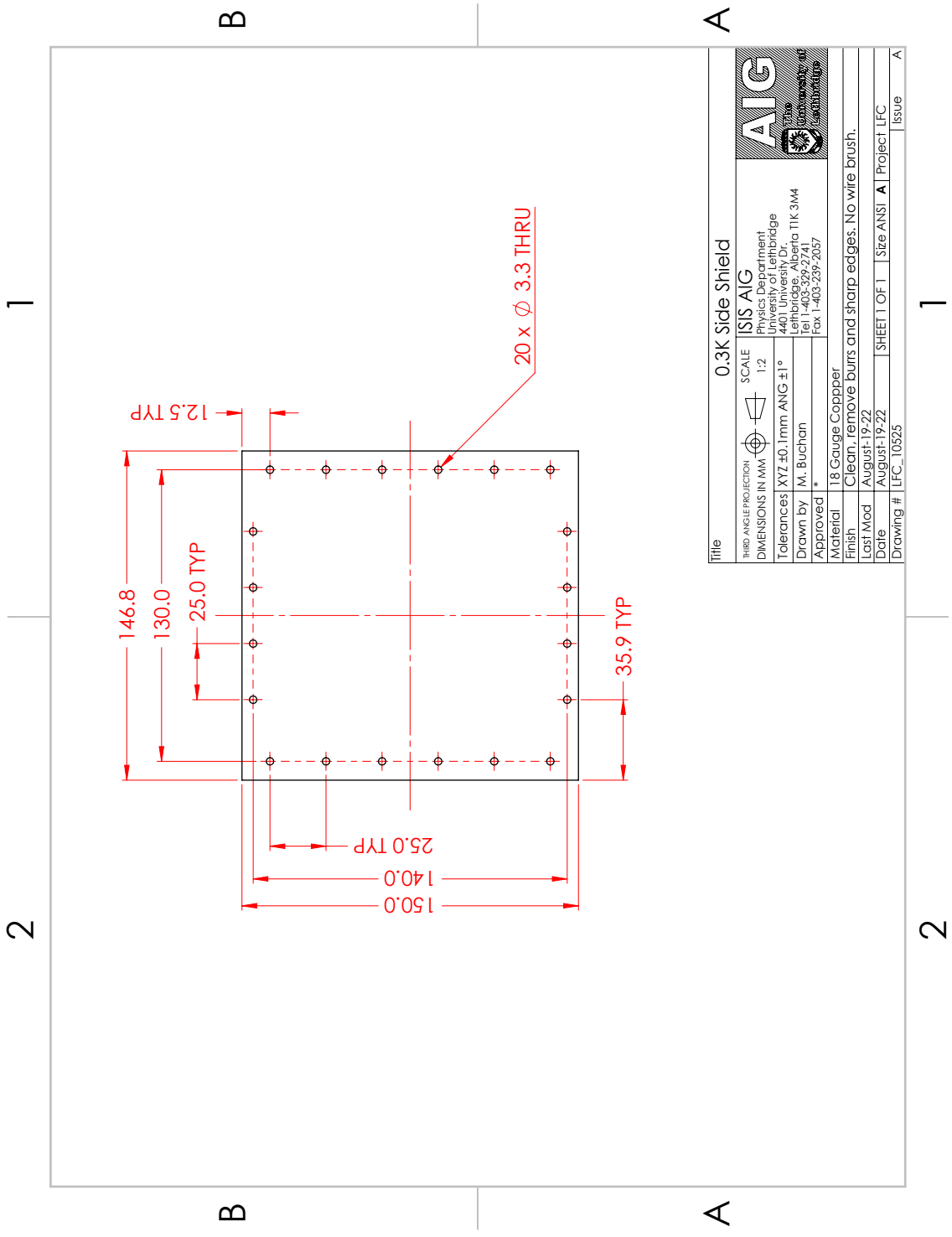
B
A
1
2
20 x ∅ 3.3 THRU
12.5 TYP
146.8
130.0
25.0 TYP
35.9 TYP
25.0 TYP
140.0
150.0
Title
0.3K Side Shield
THIRD ANGLE PROJECTION
DIMENSIONS IN MM
SCALE 1:2
ISIS AIG
Physics Department
University of Lethbridge
4401 University Dr.
Lethbridge, Alberta T1K 3M4
Tel 1-403-329-2741
Fax 1-403-239-2057
Tolerances XYZ ±0.1mm ANG ±1°
Drawn by M. Buchan
Approved *
Material 18 Gauge Coppper
Finish Clean, remove burrs and sharp edges. No wire brush.
Last Mod August-19-22
Date August-19-22
Drawing # LFC_10525
SHEET 1 OF 1
Size ANSI A
Project LFC
Issue A

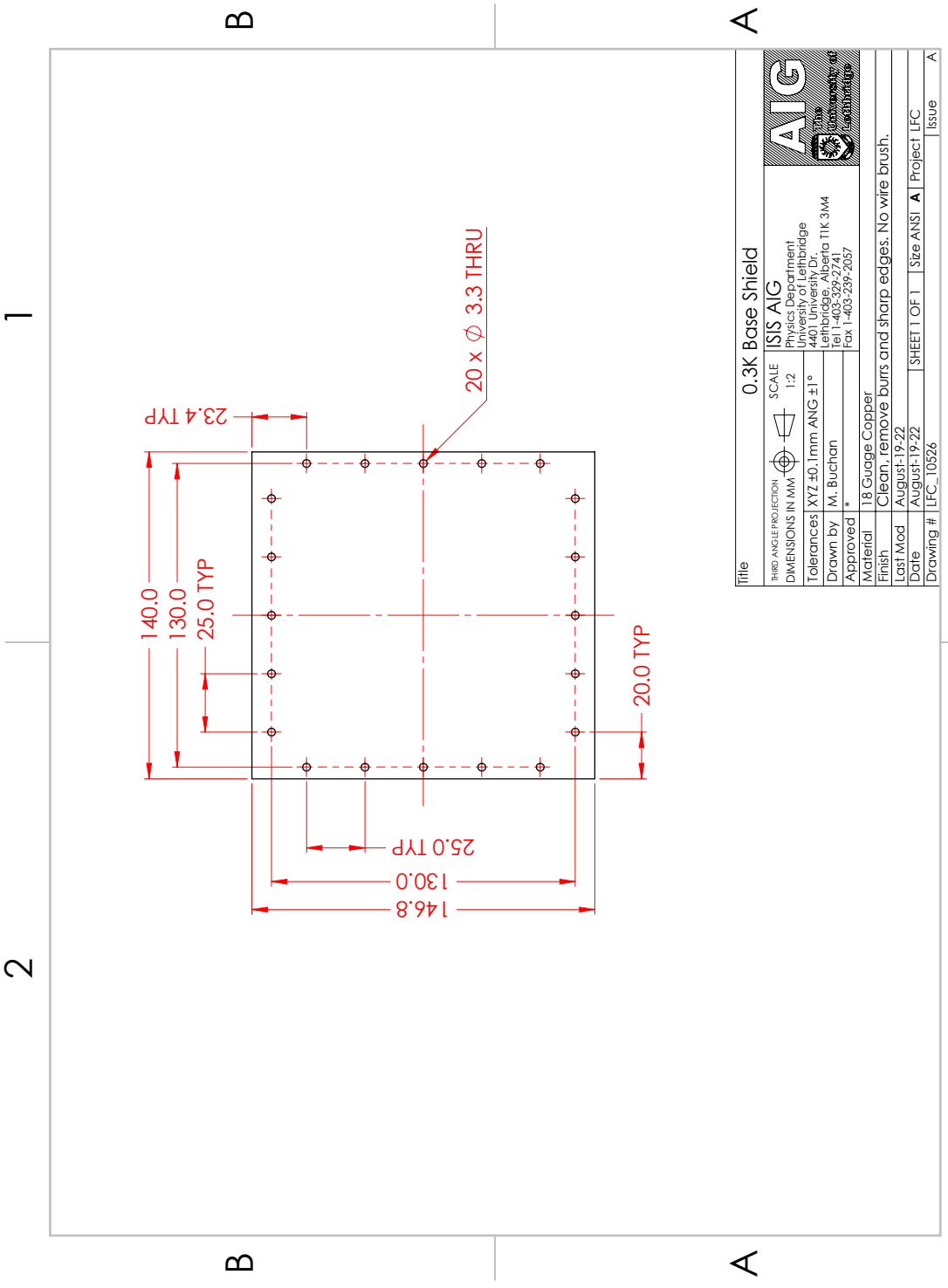
B
A
1
2
20 x ∅ 3.3 THRU
23.4 TYP
140.0
130.0
25.0 TYP
20.0 TYP
25.0 TYP
130.0
146.8
Title
0.3K Base Shield
THIRD ANGLE PROJECTION
DIMENSIONS IN MM
SCALE 1:2
ISIS AIG
Physics Department
University of Lethbridge
4401 University Dr.
Lethbridge, Alberta T1K 3M4
Tel 1-403-329-2741
Fax 1-403-239-2057
Tolerances XYZ ±0.1mm ANG ±1°
Drawn by M. Buchan
Approved *
Material 18 Guage Copper
Finish Clean, remove burrs and sharp edges. No wire brush.
Last Mod August-19-22
Date August-19-22
Drawing # LFC_10526
SHEET 1 OF 1
Size ANSI A
Project LFC
Issue A

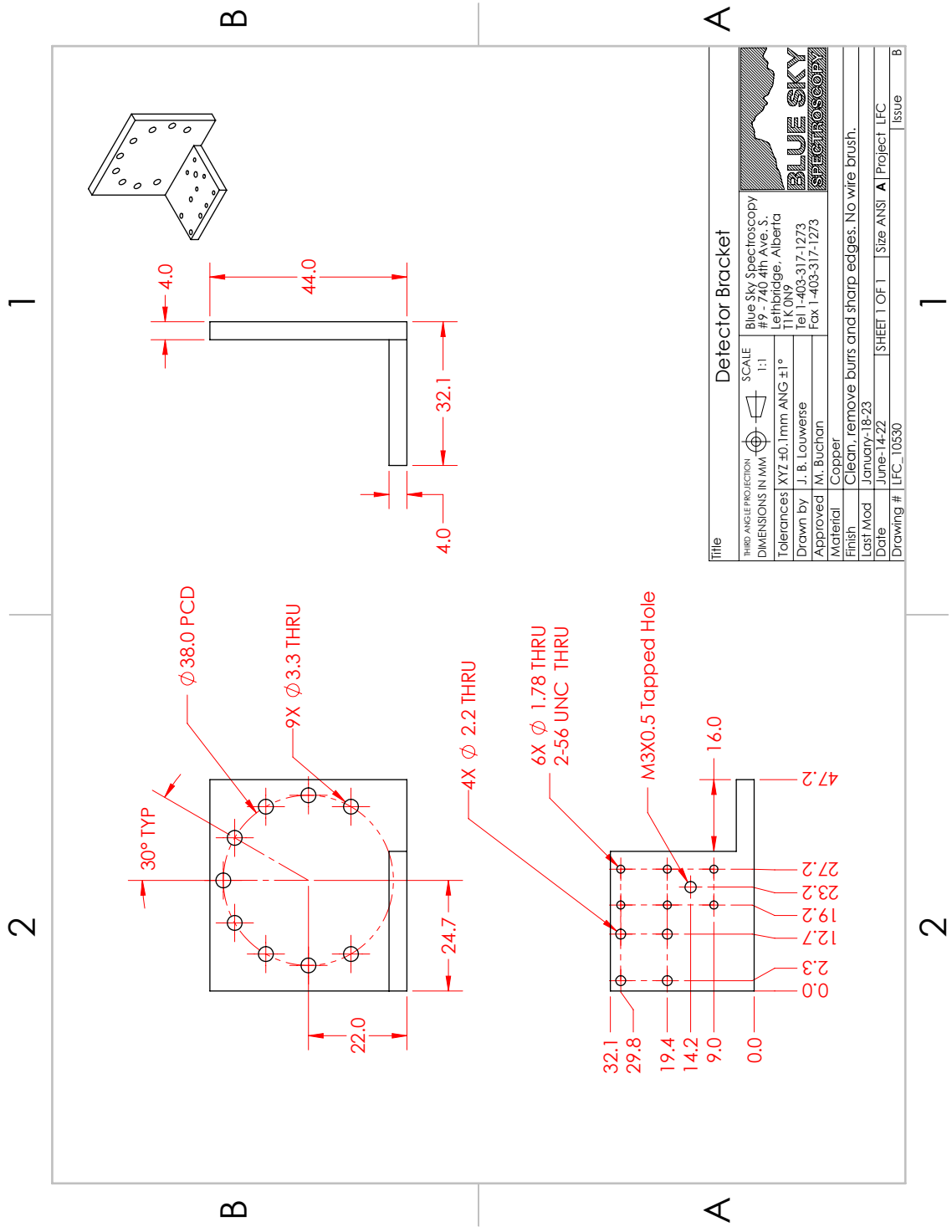
Detector Bracket
Blue Sky Spectroscopy
#9 - 740 4th Ave. S.
Lethbridge, Alberta
T1K 0N9
Tel 1-403-317-1273
Fax 1-403-317-1273
BLUE SKY
SPECTROSCOPY
THIRD ANGLE PROJECTION
DIMENSIONS IN MM
SCALE 1:1
Tolerances XYZ ±0.1mm ANG ±1°
Drawn by J. B. Louwerse
Approved M. Buchan
Material Copper
Finish Clean, remove burrs and sharp edges. No wire brush.
Last Mod January-18-23
Date June-14-22
Drawing # LFC_10530
SHEET 1 OF 1
Size ANSI A
Project LFC
Issue B
4.0
44.0
32.1
4.0
Ø38.0 PCD
9X Ø3.3 THRU
30° TYP
24.7
22.0
4X Ø 2.2 THRU
6X Ø 1.78 THRU
2-56 UNC THRU
M3X0.5 Tapped Hole
16.0
47.2
27.2
23.2
19.2
12.7
2.3
0.0
32.1
29.8
19.4
14.2
9.0
0.0

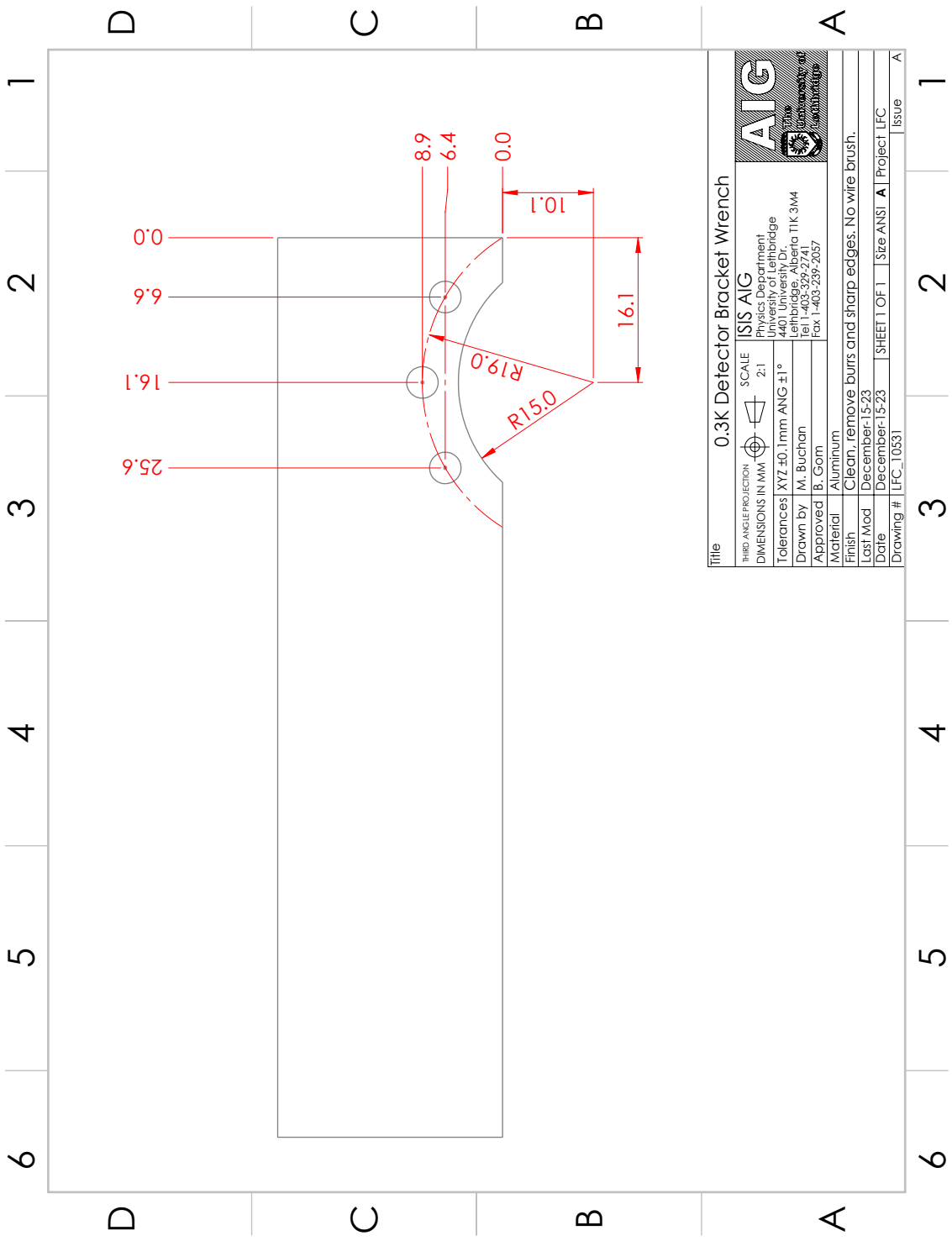
D
C
B
A
1
2
3
4
5
6
8.9
6.4
0.0
10.1
0.0
6.6
16.1
25.6
16.1
R19.0
R15.0
Title
0.3K Detector Bracket Wrench
THIRD ANGLE PROJECTION
DIMENSIONS IN MM
SCALE
2:1
ISIS AIG
Physics Department
University of Lethbridge
4401 University Dr.
Lethbridge, Alberta T1K 3M4
Tel 1-403-329-2741
Fax 1-403-239-2057
AIG
The University of Lethbridge
Tolerances
XYZ ±0.1mm ANG ±1°
Drawn by
M. Buchan
Approved
B. Gom
Material
Aluminum
Finish
Clean, remove burrs and sharp edges. No wire brush.
Last Mod
December-15-23
Date
December-15-23
SHEET 1 OF 1
Size ANSI A
Project LFC
Drawing #
LFC_10531
Issue
A

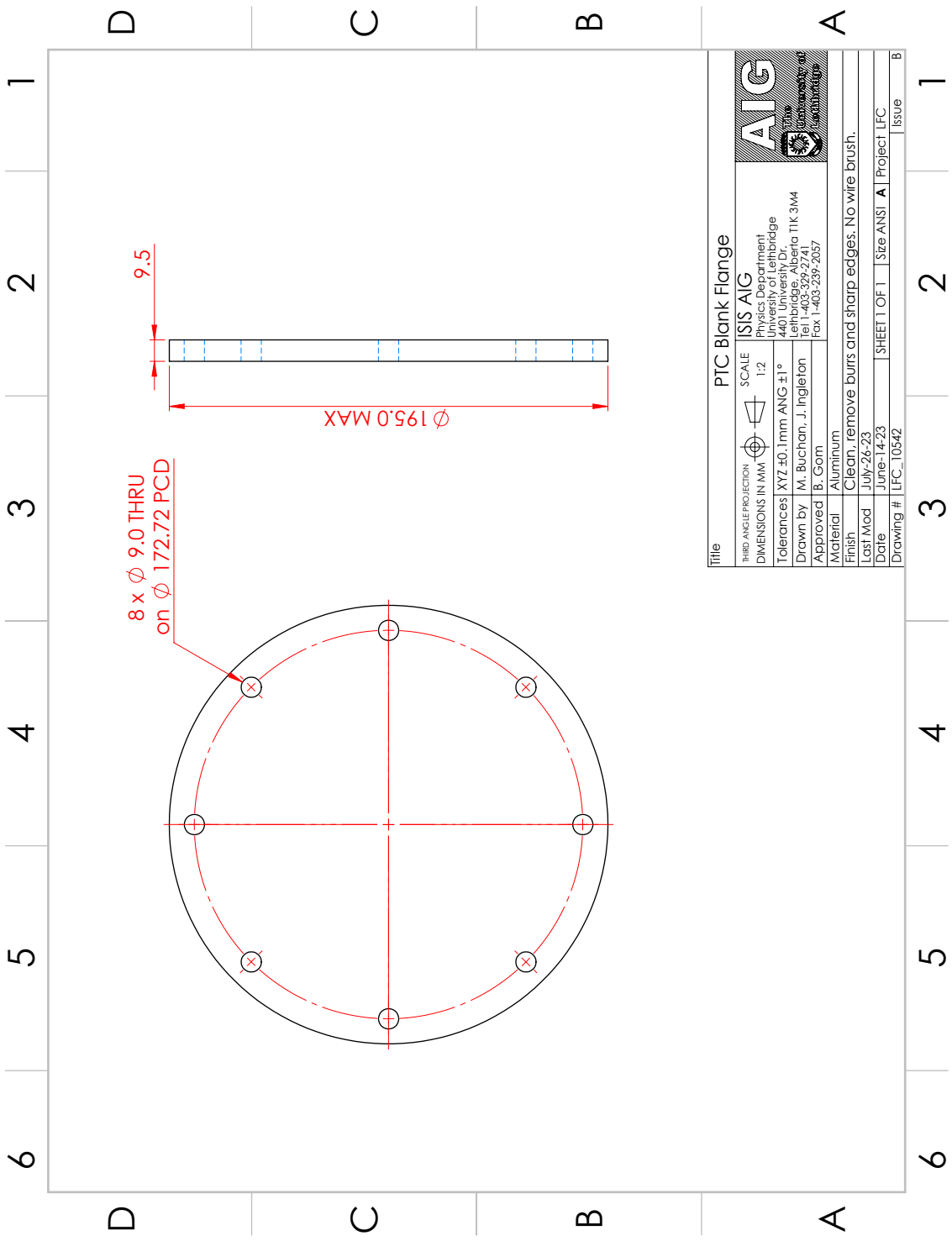
9.5
Ø 195.0 MAX
8 x Ø 9.0 THRU
on Ø 172.72 PCD
Title
PTC Blank Flange
THIRD ANGLE PROJECTION
DIMENSIONS IN MM
SCALE 1:2
ISIS AIG
Physics Department
University of Lethbridge
4401 University Dr.
Lethbridge, Alberta T1K 3M4
Tel 1-403-329-2741
Fax 1-403-239-2057
Tolerances XYZ ±0.1mm ANG ±1°
Drawn by M. Buchan, J. Ingleton
Approved B. Gom
Material Aluminum
Finish Clean, remove burrs and sharp edges. No wire brush.
Last Mod July-26-23
Date June-14-23
Drawing # LFC_10542
SHEET 1 OF 1
Size ANSI A
Project LFC
Issue B

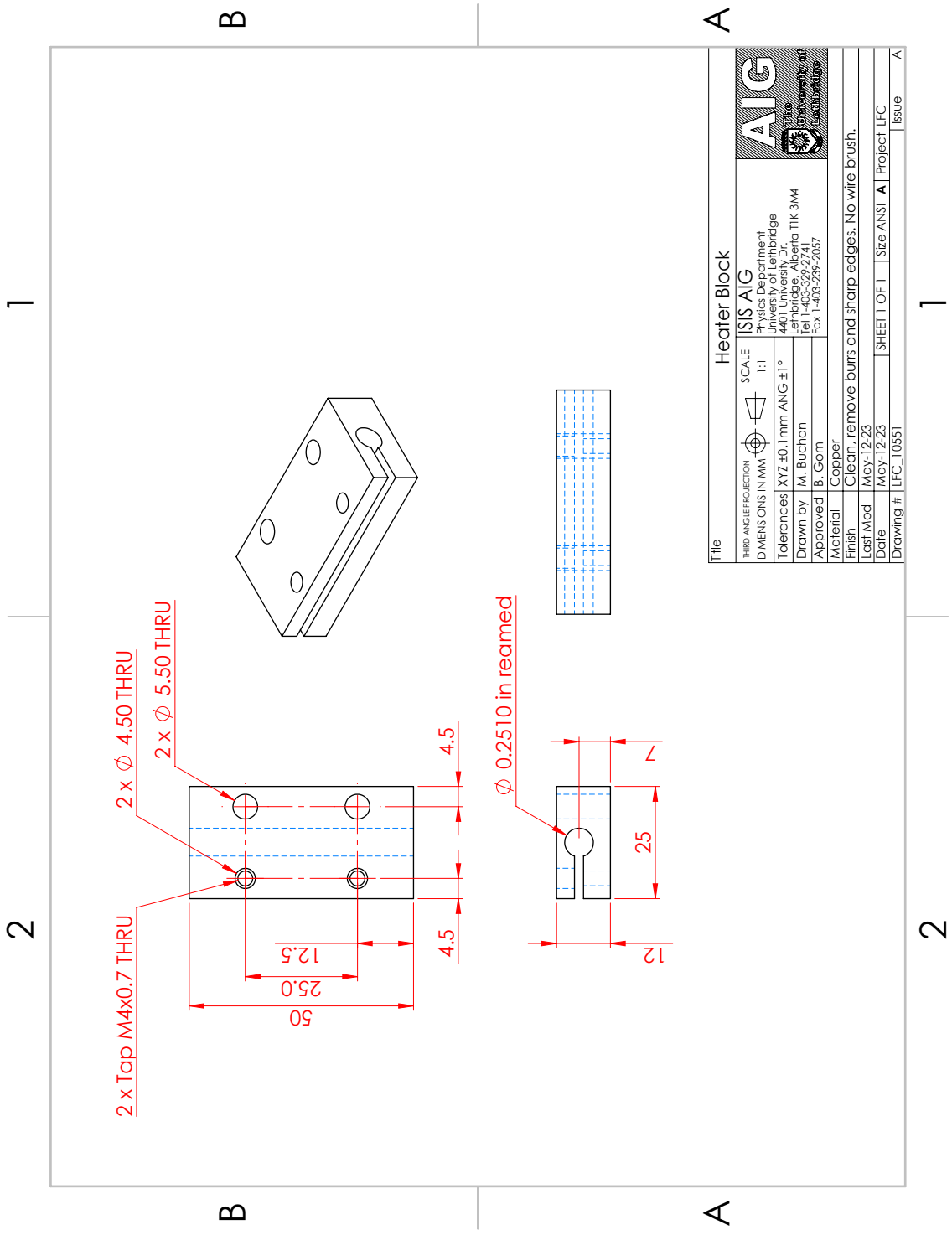
2 x ∅ 4.50 THRU
2 x ∅ 5.50 THRU
2 x Tap M4x0.7 THRU
∅ 0.2510 in reamed
4.5
4.5
12.5
25.0
50
7
25
12
Heater Block
SCALE 1:1
THIRD ANGLE PROJECTION
DIMENSIONS IN MM
ISIS AIG
Physics Department
University of Lethbridge
4401 University Dr.
Lethbridge, Alberta T1K 3M4
Tel 1-403-329-2741
Fax 1-403-239-2057
Tolerances XYZ ±0.1mm ANG ±1°
Drawn by M. Buchan
Approved B. Gom
Material Copper
Finish Clean, remove burrs and sharp edges. No wire brush.
Last Mod May-12-23
Date May-12-23
Drawing # LFC_10551
SHEET 1 OF 1
Size ANSI A
Project LFC
Issue A

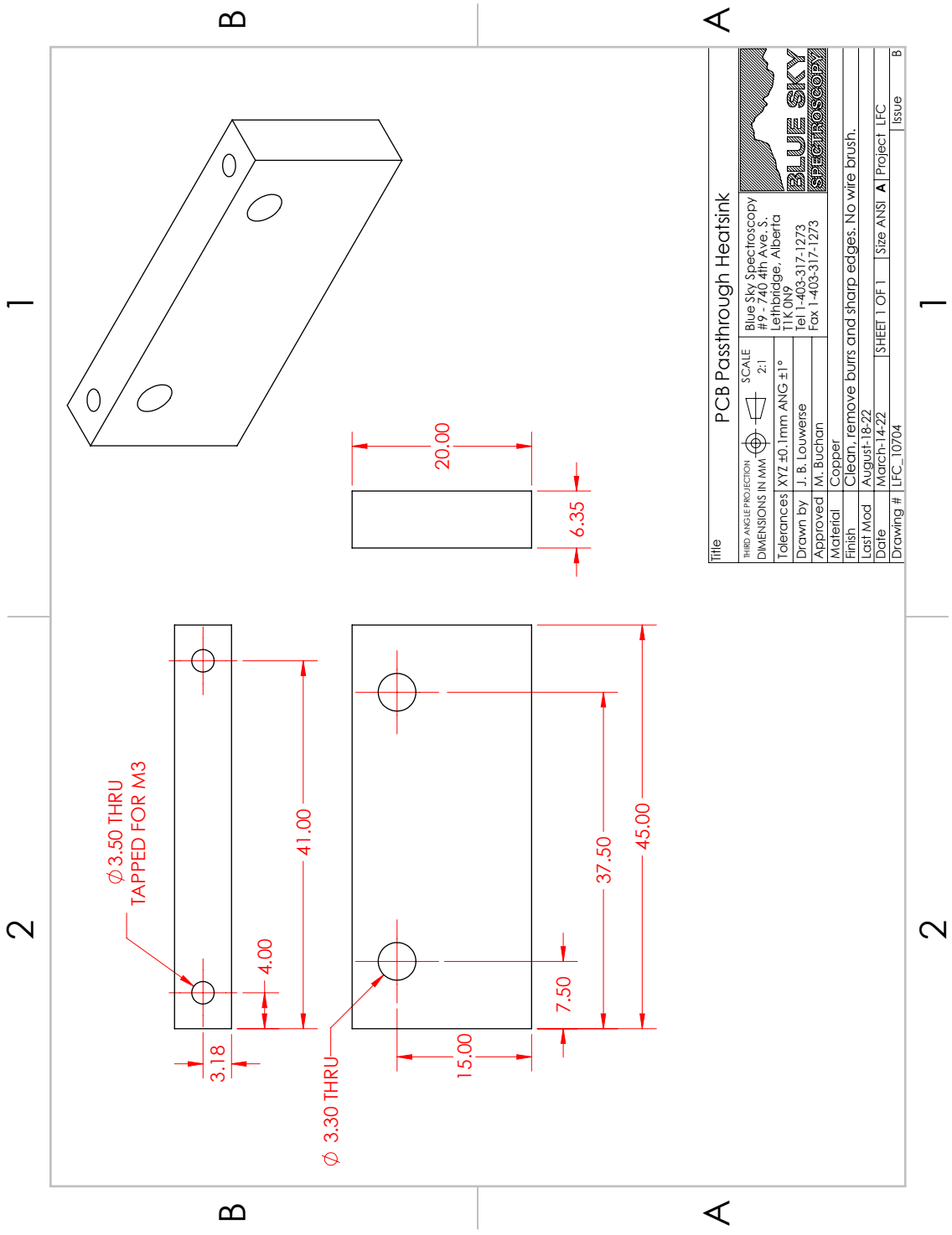
PCB Passthrough Heatsink
Blue Sky Spectroscopy
#9 - 740 4th Ave. S.
Lethbridge, Alberta
T1K 0N9
Tel 1-403-317-1273
Fax 1-403-317-1273
BLUE SKY
SPECTROSCOPY
THIRD ANGLE PROJECTION
DIMENSIONS IN MM
SCALE 2:1
Tolerances XYZ ±0.1mm ANG ±1°
Drawn by J. B. Louwerse
Approved M. Buchan
Material Copper
Finish Clean, remove burrs and sharp edges. No wire brush.
Last Mod August-18-22
Date March-14-22
Drawing # LFC_10704
SHEET 1 OF 1
Size ANSI A
Project LFC
Issue B
20.00
6.35
Ø3.50 THRU
TAPPED FOR M3
41.00
4.00
3.18
Ø 3.30 THRU
37.50
45.00
7.50
15.00
1
2
A
B

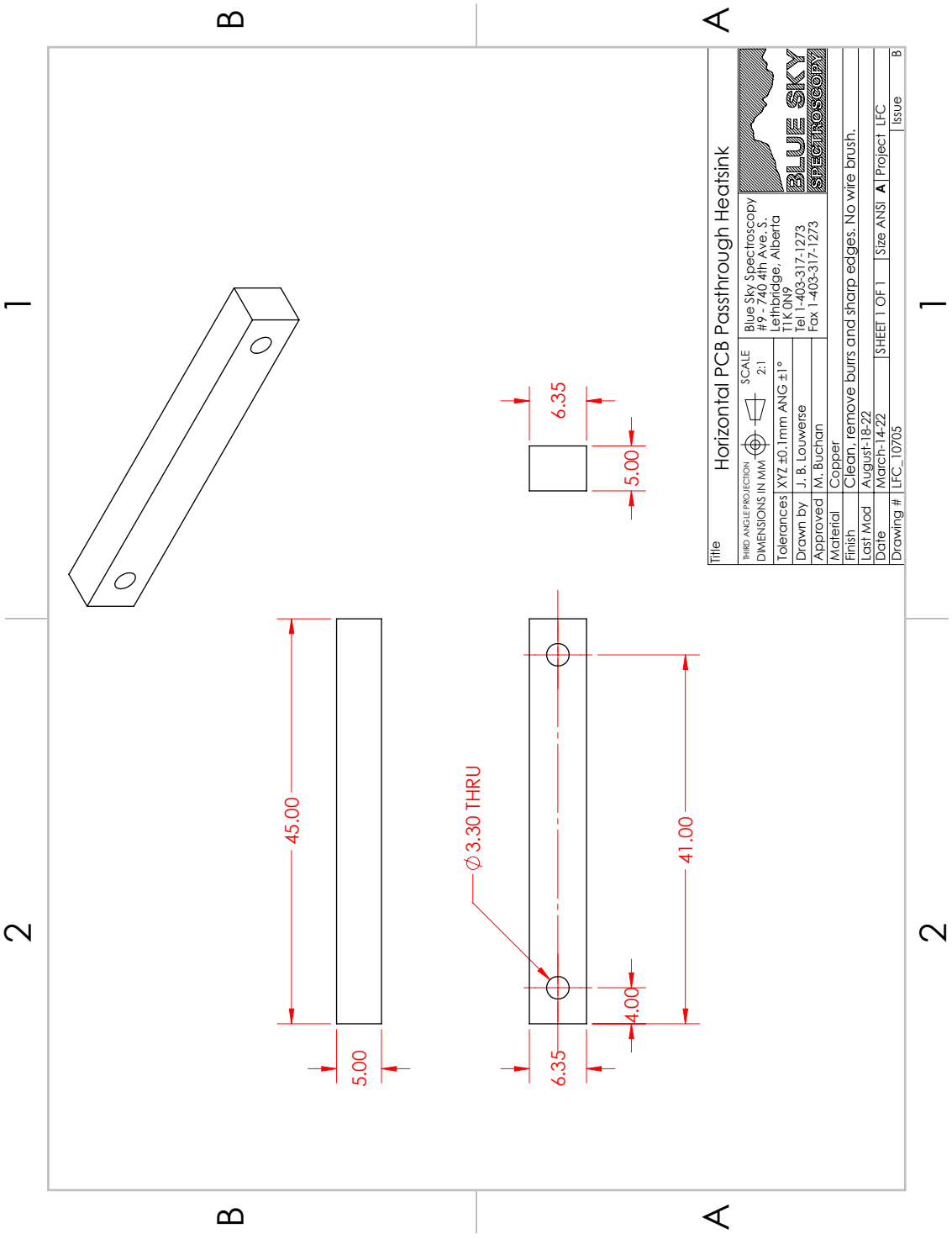
B
A
1
2
45.00
5.00
Ø3.30 THRU
41.00
4.00
6.35
5.00
6.35
Title
Horizontal PCB Passthrough Heatsink
THIRD ANGLE PROJECTION
DIMENSIONS IN MM
SCALE 2:1
Tolerances XYZ ±0.1mm ANG ±1°
Drawn by J. B. Louwerse
Approved M. Buchan
Material Copper
Finish Clean, remove burrs and sharp edges. No wire brush.
Last Mod August-18-22
Date March-14-22
Drawing # LFC_10705
Blue Sky Spectroscopy
#9 - 740 4th Ave. S.
Lethbridge, Alberta
T1K 0N9
Tel 1-403-317-1273
Fax 1-403-317-1273
BLUE SKY
SPECTROSCOPY
SHEET 1 OF 1
Size ANSI A
Project LFC
Issue B

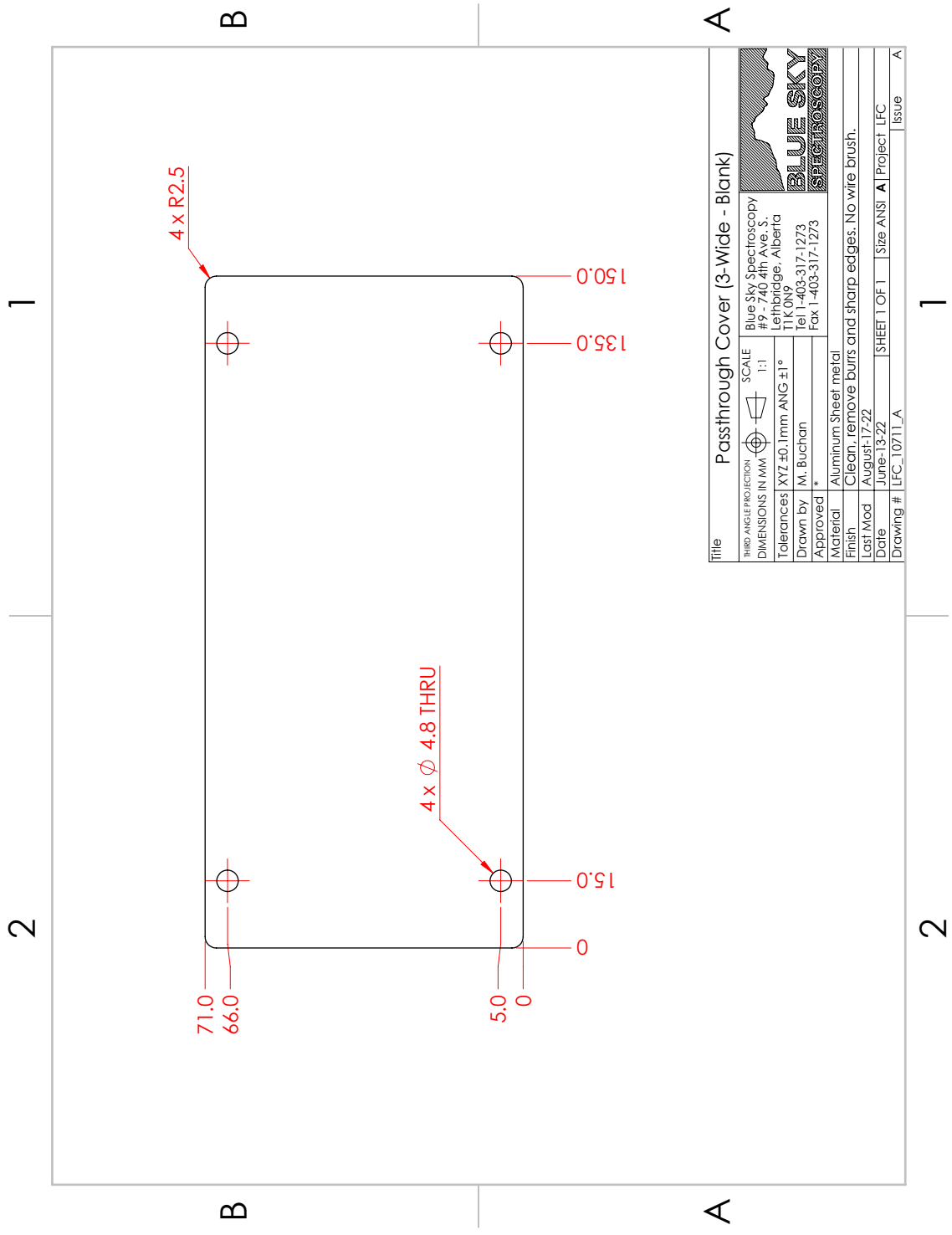
4 x R2.5
150.0
135.0
4 x ∅ 4.8 THRU
15.0
0
71.0
66.0
5.0
0
Title
Passthrough Cover (3-Wide - Blank)
THIRD ANGLE PROJECTION
DIMENSIONS IN MM
SCALE 1:1
Tolerances
XYZ ±0.1mm ANG ±1°
Drawn by
M. Buchan
Approved
*
Blue Sky Spectroscopy
#9 - 740 4th Ave. S.
Lethbridge, Alberta
T1K 0N9
Tel 1-403-317-1273
Fax 1-403-317-1273
BLUE SKY
SPECTROSCOPY
Material
Aluminum Sheet metal
Finish
Clean, remove burrs and sharp edges. No wire brush.
Last Mod
August-17-22
Date
June-13-22
SHEET 1 OF 1
Size ANSI A
Project LFC
Drawing #
LFC_10711_A
Issue A

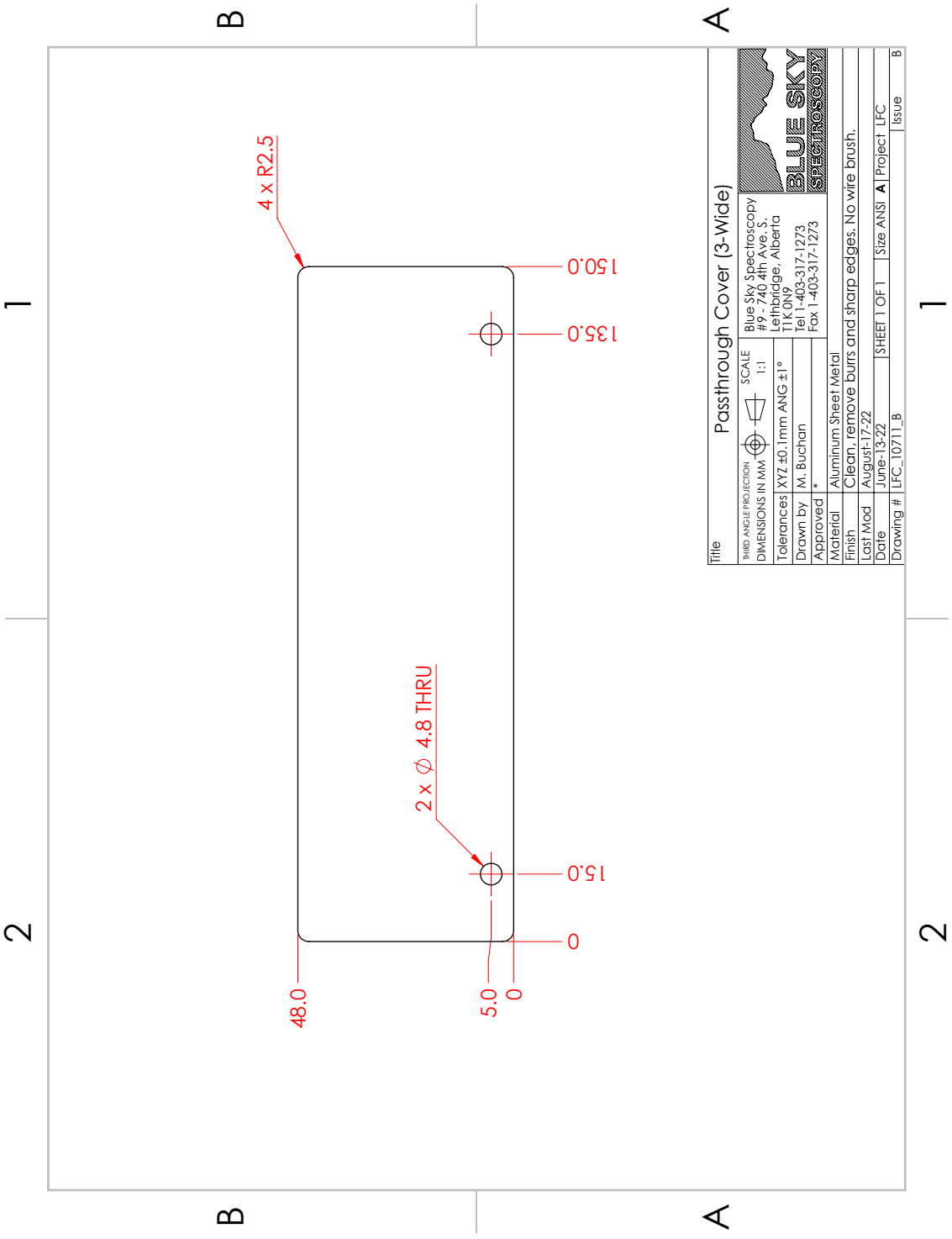
B
A
1
2
4 x R2.5
150.0
135.0
2 x ∅ 4.8 THRU
15.0
0
48.0
5.0
0
Title
Passthrough Cover (3-Wide)
THIRD ANGLE PROJECTION
DIMENSIONS IN MM
SCALE 1:1
Blue Sky Spectroscopy
#9 - 740 4th Ave. S.
Lethbridge, Alberta
T1K 0N9
Tel 1-403-317-1273
Fax 1-403-317-1273
BLUE SKY SPECTROSCOPY
Tolerances XYZ ±0.1mm ANG ±1°
Drawn by M. Buchan
Approved *
Material Aluminum Sheet Metal
Finish Clean, remove burrs and sharp edges. No wire brush.
Last Mod August-17-22
Date June-13-22
Drawing # LFC_10711_B
SHEET 1 OF 1
Size ANSI A
Project LFC
Issue B

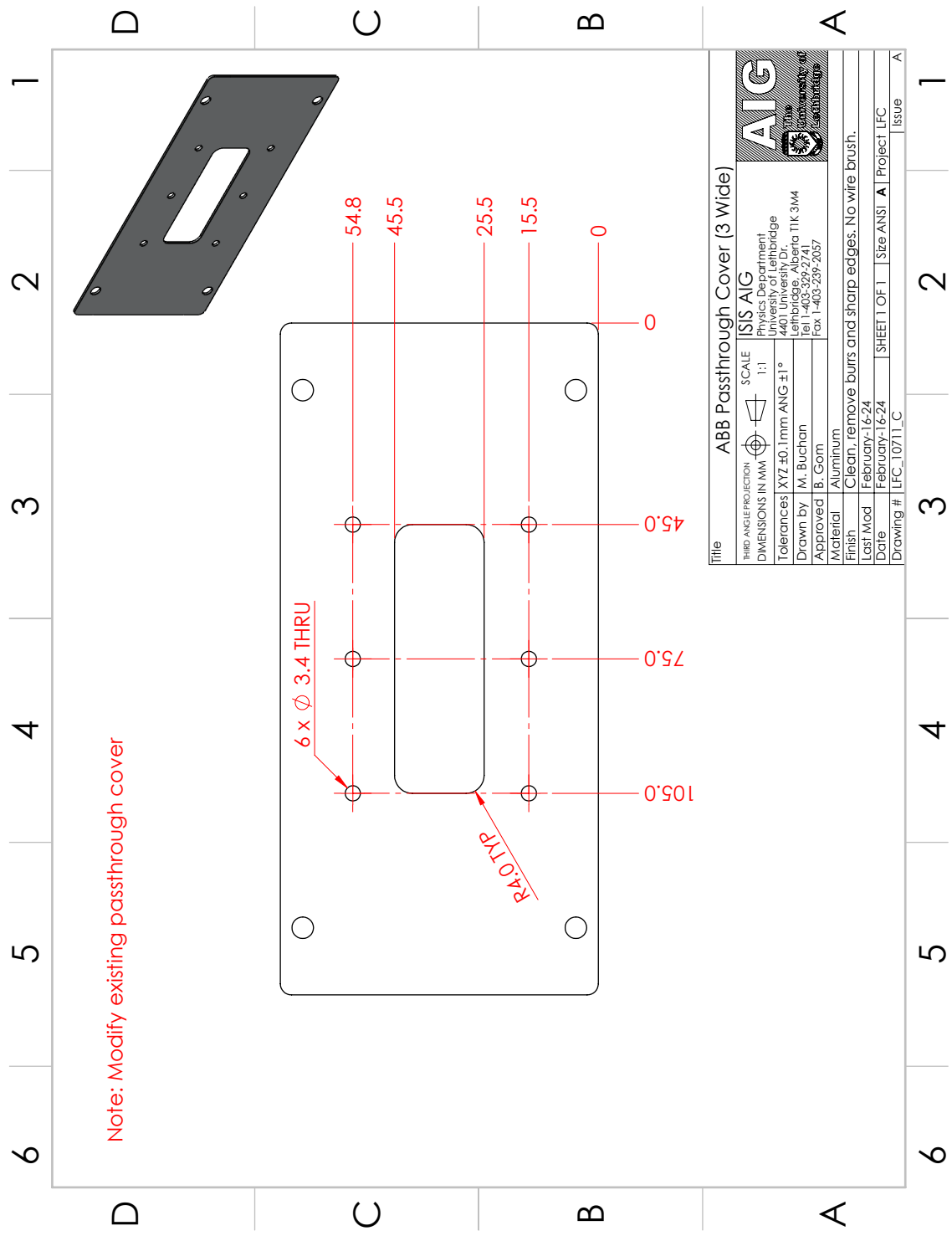
Note: Modify existing passthrough cover
6 x ∅ 3.4 THRU
R4.0 TYP
54.8
45.5
25.5
15.5
0
0
45.0
75.0
105.0
Title
ABB Passthrough Cover (3 Wide)
THIRD ANGLE PROJECTION
DIMENSIONS IN MM
SCALE 1:1
ISIS AIG
Physics Department
University of Lethbridge
4401 University Dr.
Lethbridge, Alberta T1K 3M4
Tel 1-403-329-2741
Fax 1-403-239-2057
Tolerances XYZ ±0.1mm ANG ±1°
Drawn by M. Buchan
Approved B. Gom
Material Aluminum
Finish Clean, remove burrs and sharp edges. No wire brush.
Last Mod February-16-24
Date February-16-24
SHEET 1 OF 1
Size ANSI A
Project LFC
Drawing # LFC_10711_C
Issue A

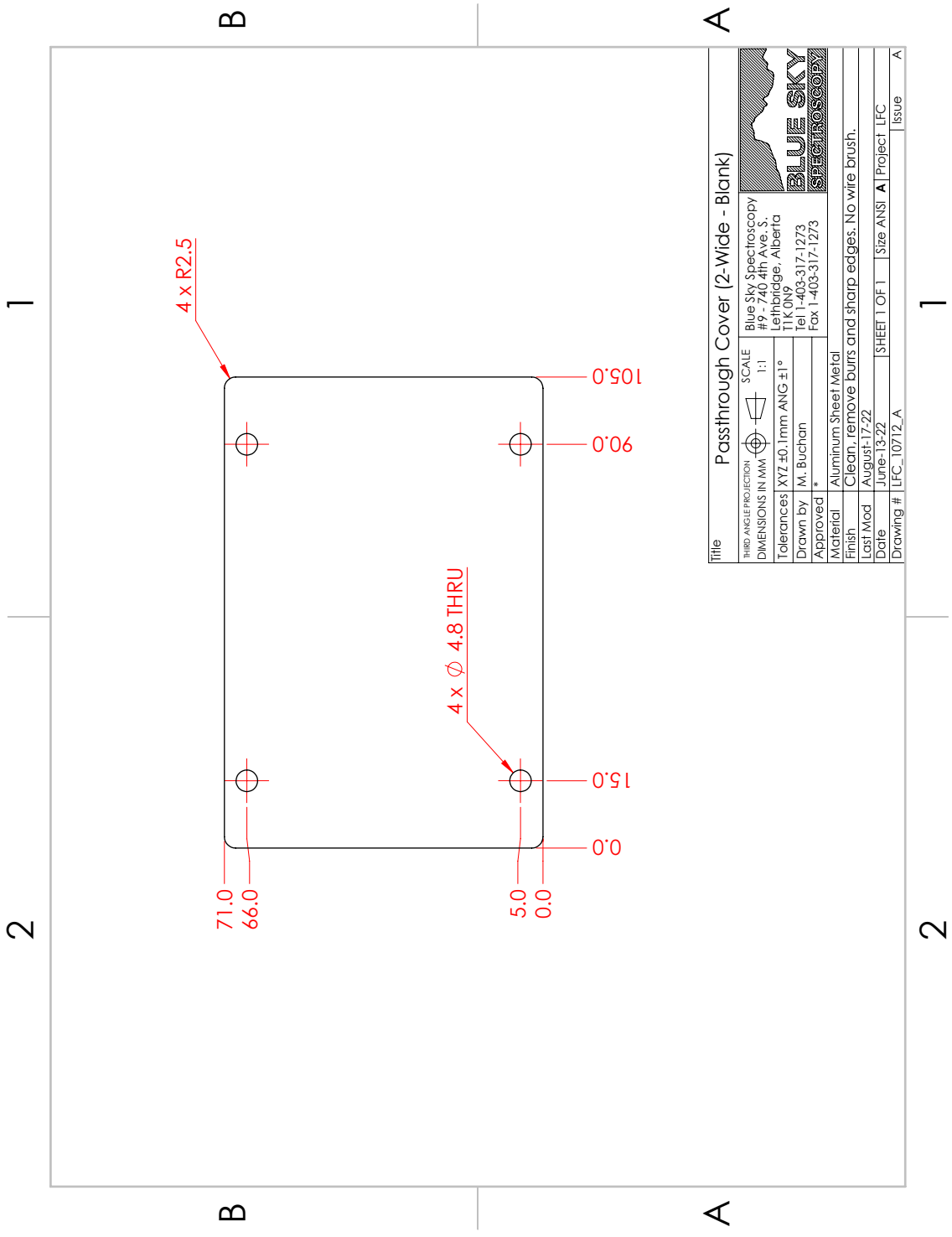
4 x R2.5
105.0
90.0
4 x ∅ 4.8 THRU
15.0
0.0
71.0
66.0
5.0
0.0
Title
Passthrough Cover (2-Wide - Blank)
THIRD ANGLE PROJECTION
DIMENSIONS IN MM
SCALE 1:1
Tolerances XYZ ±0.1mm ANG ±1°
Drawn by M. Buchan
Approved *
Blue Sky Spectroscopy
#9 - 740 4th Ave. S.
Lethbridge, Alberta
T1K 0N9
Tel 1-403-317-1273
Fax 1-403-317-1273
BLUE SKY SPECTROSCOPY
Material Aluminum Sheet Metal
Finish Clean, remove burrs and sharp edges. No wire brush.
Last Mod August-17-22
Date June-13-22
SHEET 1 OF 1
Size ANSI A
Project LFC
Drawing # LFC_10712_A
Issue A

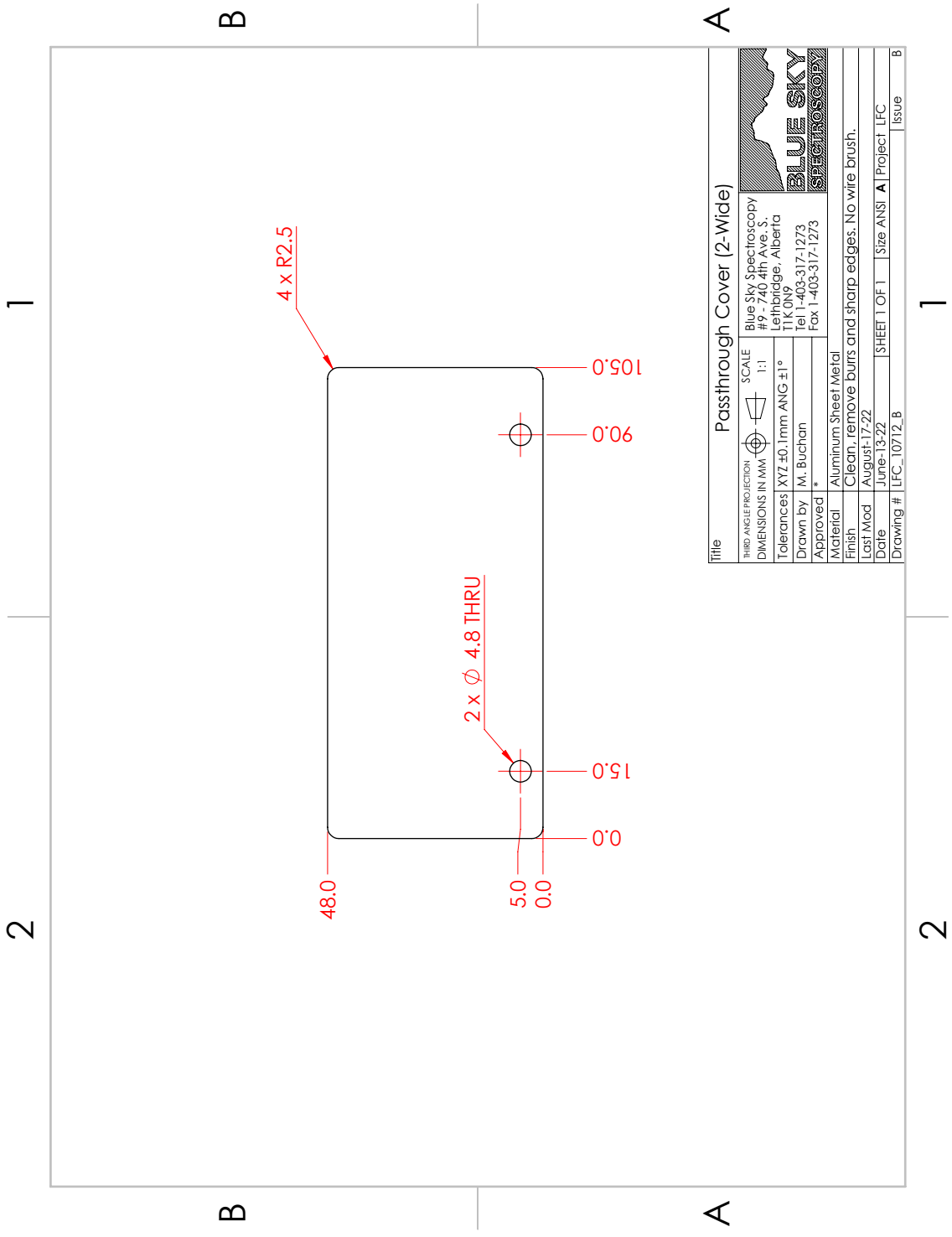
B
A
1
2
4 x R2.5
105.0
90.0
2 x ∅ 4.8 THRU
15.0
0.0
48.0
5.0
0.0
Title
Passthrough Cover (2-Wide)
THIRD ANGLE PROJECTION
DIMENSIONS IN MM
SCALE 1:1
Blue Sky Spectroscopy
#9 - 740 4th Ave. S.
Lethbridge, Alberta
T1K 0N9
Tel 1-403-317-1273
Fax 1-403-317-1273
BLUE SKY SPECTROSCOPY
Tolerances XYZ ±0.1mm ANG ±1°
Drawn by M. Buchan
Approved *
Material Aluminum Sheet Metal
Finish Clean, remove burrs and sharp edges. No wire brush.
Last Mod August-17-22
Date June-13-22
Drawing # LFC_10712_B
SHEET 1 OF 1
Size ANSI A
Project LFC
Issue B

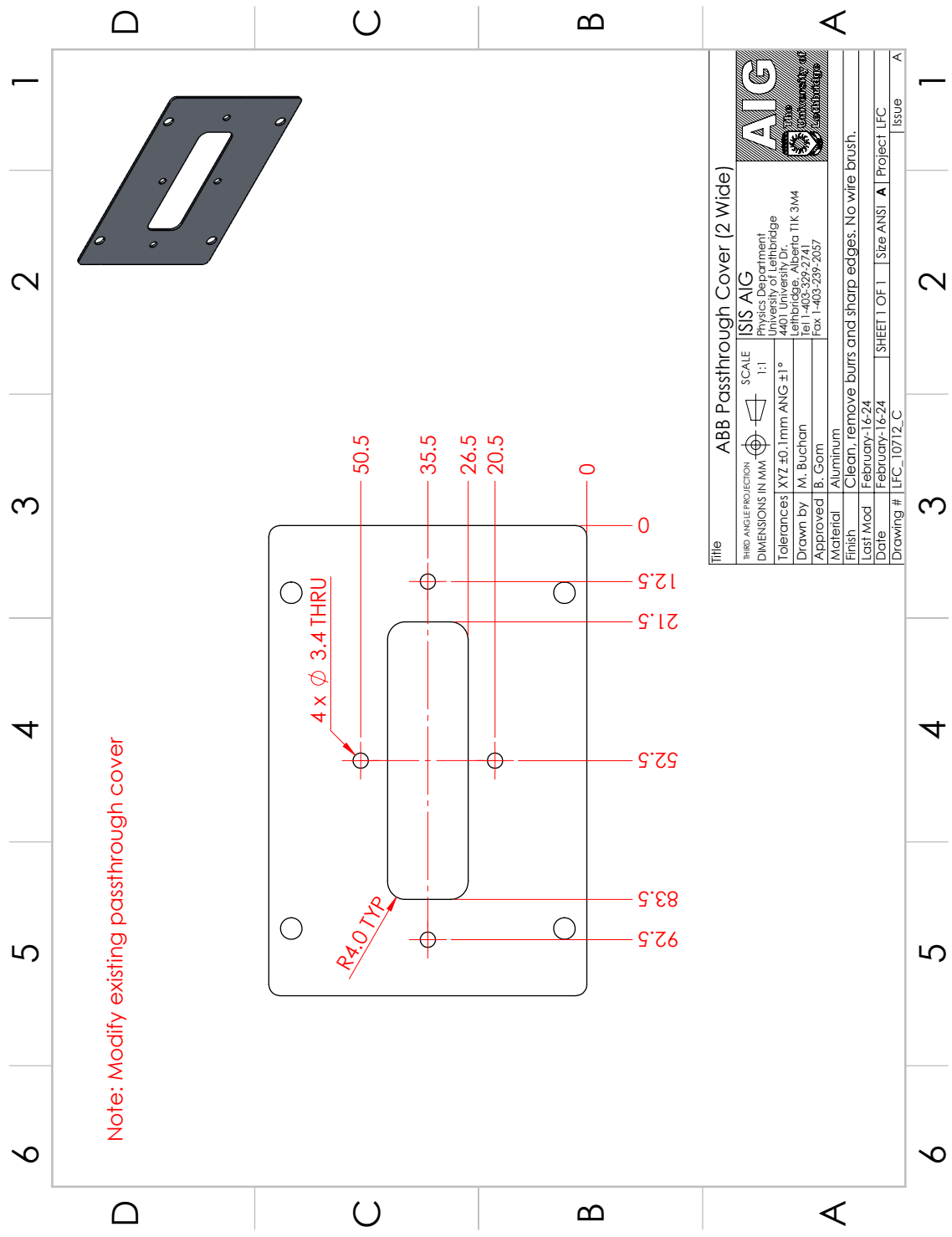
Note: Modify existing passthrough cover
4 x ∅ 3.4 THRU
R4.0 TYP
50.5
35.5
26.5
20.5
0
0
12.5
21.5
52.5
83.5
92.5
Title
ABB Passthrough Cover (2 Wide)
THIRD ANGLE PROJECTION
DIMENSIONS IN MM
SCALE 1:1
ISIS AIG
Physics Department
University of Lethbridge
4401 University Dr.
Lethbridge, Alberta T1K 3M4
Tel 1-403-329-2741
Fax 1-403-239-2057
Tolerances XYZ ±0.1mm ANG ±1°
Drawn by M. Buchan
Approved B. Gorn
Material Aluminum
Finish Clean, remove burrs and sharp edges. No wire brush.
Last Mod February-16-24
Date February-16-24
SHEET 1 OF 1
Size ANSI A
Project LFC
Drawing # LFC_10712_C
Issue A

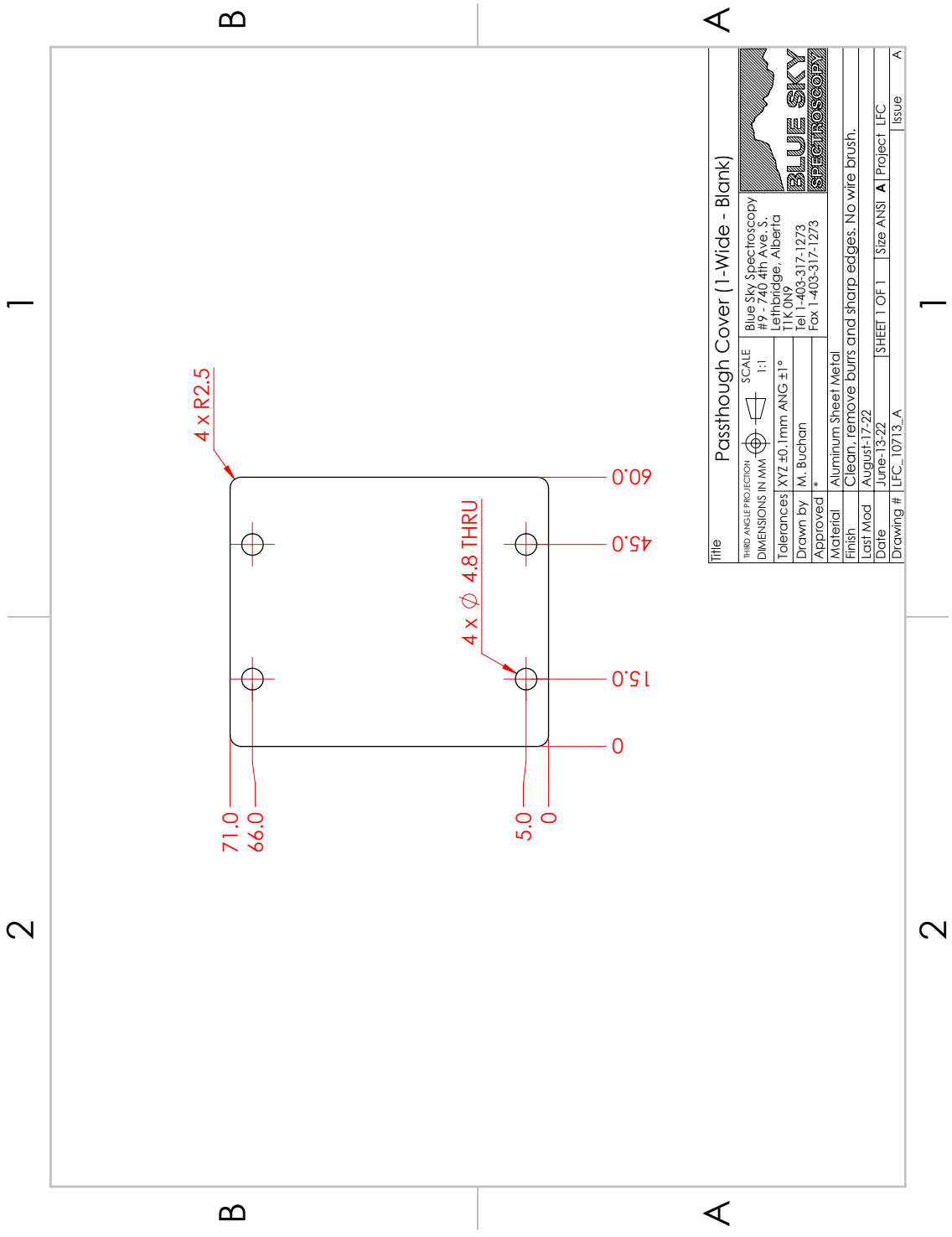
B
A
1
2
4 x R2.5
4 x ∅ 4.8 THRU
60.0
45.0
15.0
0
71.0
66.0
5.0
0
Title
Passthough Cover (1-Wide - Blank)
THIRD ANGLE PROJECTION
DIMENSIONS IN MM
SCALE 1:1
Tolerances XYZ ±0.1mm ANG ±1°
Drawn by M. Buchan
Approved *
Material Aluminum Sheet Metal
Finish Clean, remove burrs and sharp edges. No wire brush.
Last Mod August-17-22
Date June-13-22
Drawing # LFC_10713_A
Blue Sky Spectroscopy
#9 - 740 4th Ave. S.
Lethbridge, Alberta
T1K 0N9
Tel 1-403-317-1273
Fax 1-403-317-1273
BLUE SKY SPECTROSCOPY
SHEET 1 OF 1
Size ANSI A
Project LFC
Issue A

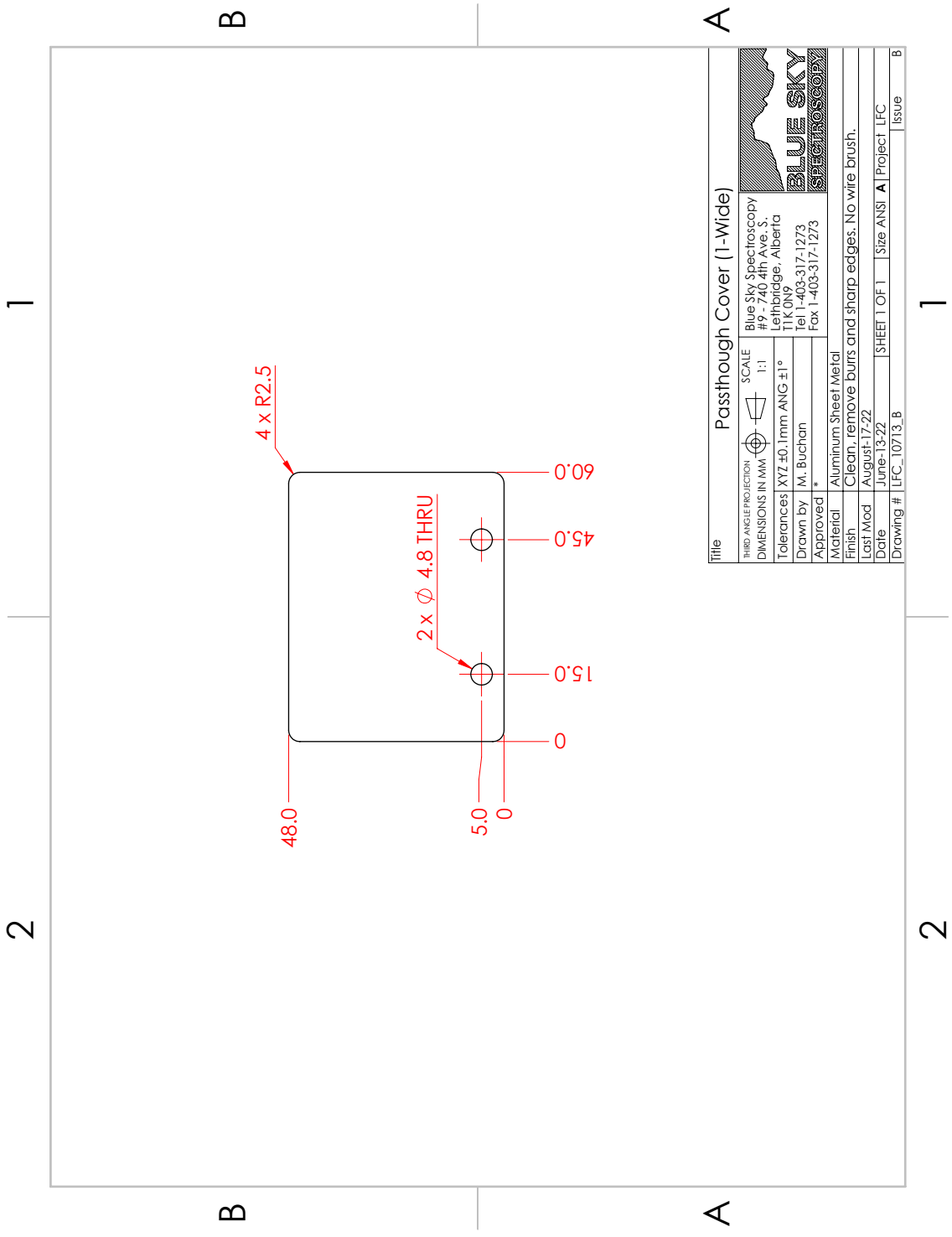
B
A
1
2
4 x R2.5
2 x ∅ 4.8 THRU
60.0
45.0
15.0
0
48.0
5.0
0
Title
Passthough Cover (1-Wide)
THIRD ANGLE PROJECTION
DIMENSIONS IN MM
SCALE 1:1
Tolerances XYZ ±0.1mm ANG ±1°
Drawn by M. Buchan
Approved *
Blue Sky Spectroscopy
#9 - 740 4th Ave. S.
Lethbridge, Alberta
T1K 0N9
Tel 1-403-317-1273
Fax 1-403-317-1273
BLUE SKY SPECTROSCOPY
Material Aluminum Sheet Metal
Finish Clean, remove burrs and sharp edges. No wire brush.
Last Mod August-17-22
Date June-13-22
Drawing # LFC_10713_B
SHEET 1 OF 1
Size ANSI A
Project LFC
Issue B

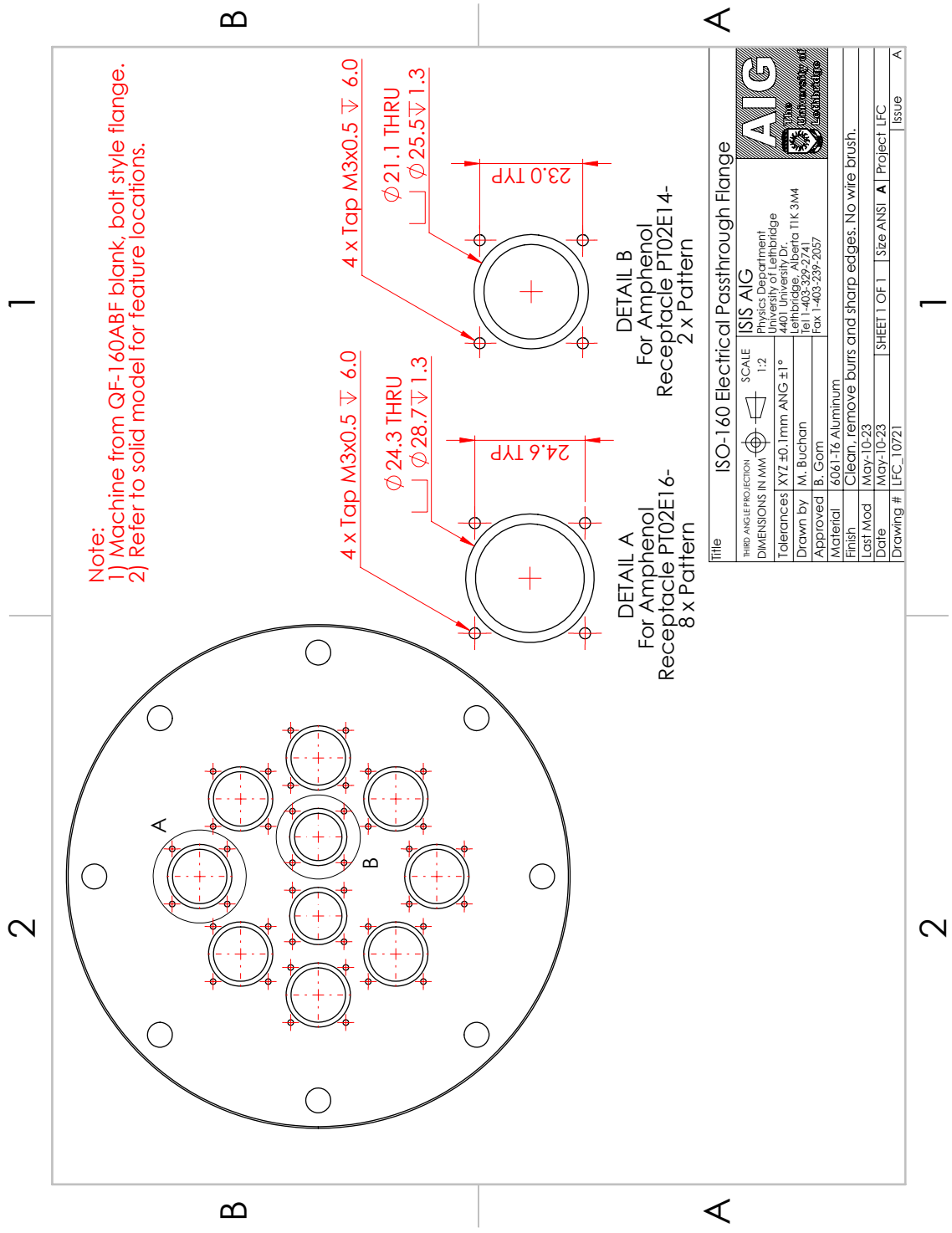
Note:
1) Machine from QF-160ABF blank, bolt style flange.
2) Refer to solid model for feature locations.
4 x Tap M3x0.5 ↧ 6.0
⌀24.3 THRU
⌴ ⌀28.7↧1.3
24.6 TYP
DETAIL A
For Amphenol
Receptacle PT02E16-
8 x Pattern
4 x Tap M3x0.5 ↧ 6.0
⌀21.1 THRU
⌴ ⌀25.5↧1.3
23.0 TYP
DETAIL B
For Amphenol
Receptacle PT02E14-
2 x Pattern
A
B
Title
ISO-160 Electrical Passthrough Flange
THIRD ANGLE PROJECTION
DIMENSIONS IN MM
SCALE 1:2
ISIS AIG
Physics Department
University of Lethbridge
4401 University Dr.
Lethbridge, Alberta T1K 3M4
Tel 1-403-329-2741
Fax 1-403-239-2057
Tolerances XYZ ±0.1mm ANG ±1°
Drawn by M. Buchan
Approved B. Gom
Material 6061-T6 Aluminum
Finish Clean, remove burrs and sharp edges. No wire brush.
Last Mod May-10-23
Date May-10-23
Drawing # LFC_10721
SHEET 1 OF 1
Size ANSI A
Project LFC
Issue A

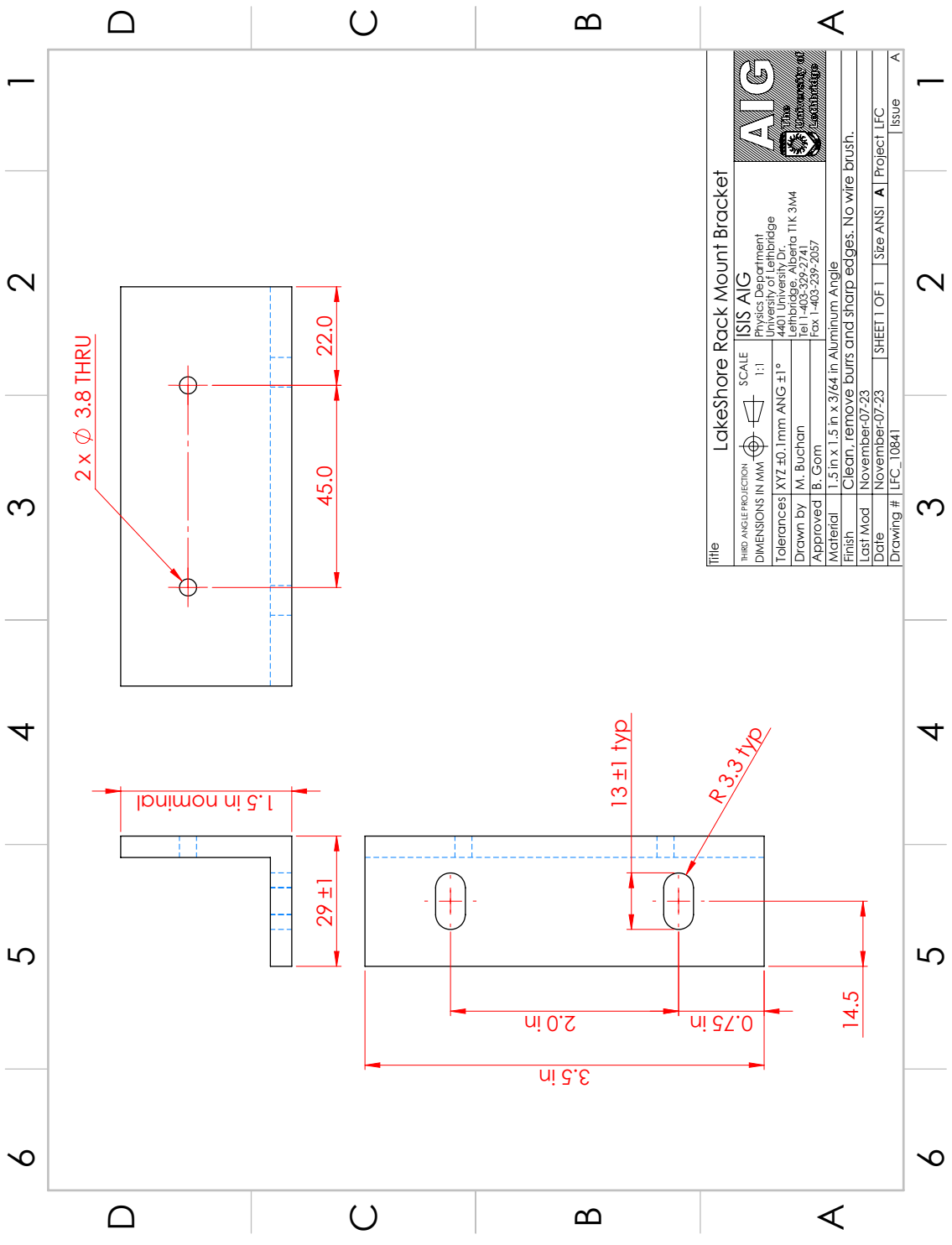
2 x ∅ 3.8 THRU
22.0
45.0
1.5 in nominal
29 ±1
13 ±1 typ
R 3.3 typ
2.0 in
0.75 in
3.5 in
14.5
Title
LakeShore Rack Mount Bracket
THIRD ANGLE PROJECTION
DIMENSIONS IN MM
SCALE 1:1
ISIS AIG
Physics Department
University of Lethbridge
4401 University Dr.
Lethbridge, Alberta T1K 3M4
Tel 1-403-329-2741
Fax 1-403-239-2057
Tolerances XYZ ±0.1mm ANG ±1°
Drawn by M. Buchan
Approved B. Gom
Material 1.5 in x 1.5 in x 3/64 in Aluminum Angle
Finish Clean, remove burrs and sharp edges. No wire brush.
Last Mod November-07-23
Date November-07-23
Drawing # LFC_10841
SHEET 1 OF 1
Size ANSI A
Project LFC
Issue A

Appendix B LFC Wiring Diagram

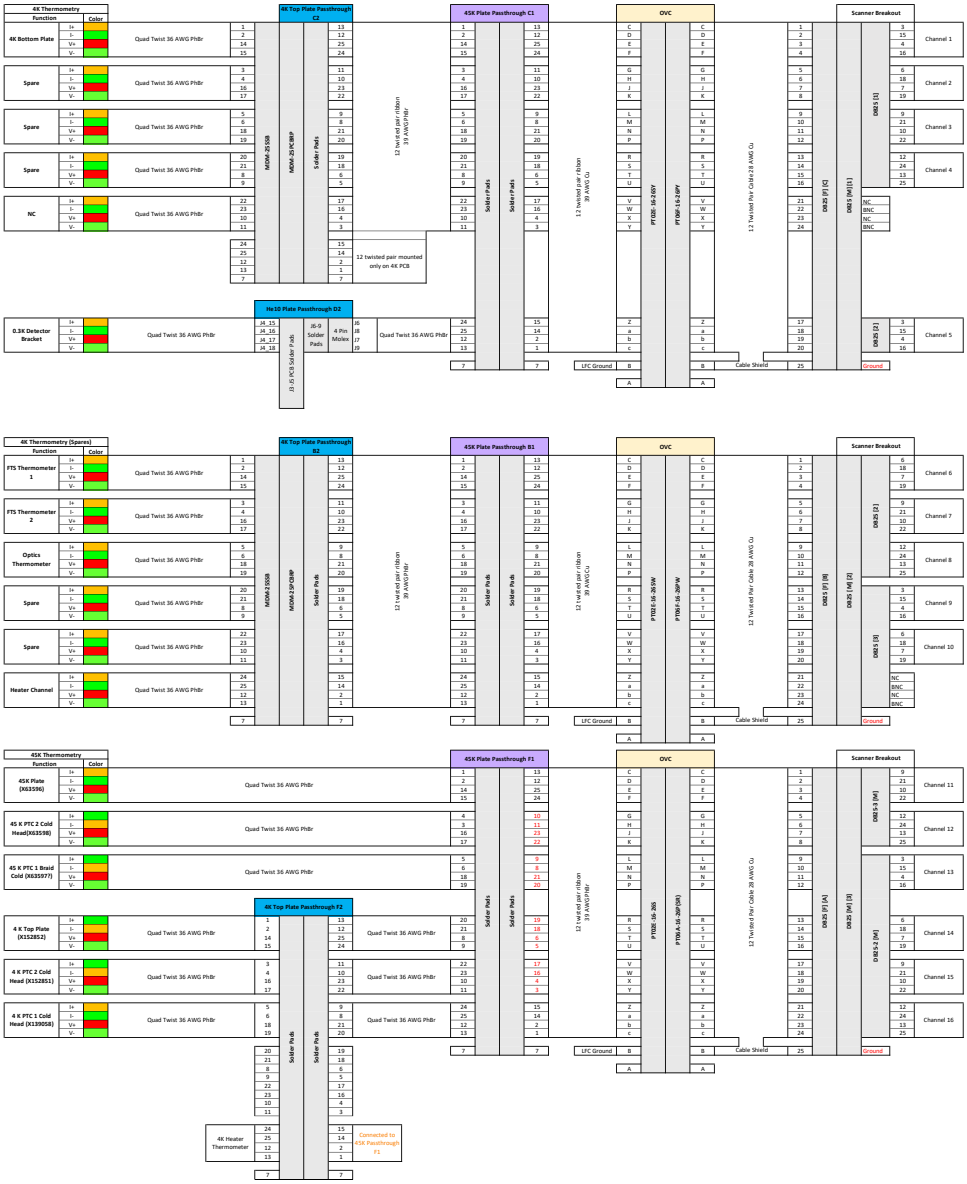


He10 Fridge Thermometry Ru02
Function
Original MDM37 Wiring Resoldered to J3-J5 Solder Pads
He10 Plate Passthrough D2
45K Plate Passthrough D1
OVC
Cycle Box
Ultra-Cold Head
V+
V-
I+
I-
Existing Fridge Wiring
3He Head
4He HEAD
He10 Fridge Thermometry Diode
4He FILM
4He PUMP
3He PUMP
ULTRA-COLD
4He HEAT
3He HEAT
ULTRA-COLD
J1 MDM-25PBSP
J1 MDM-25SSB
12 twisted pair ribbon 39 AWG PhBr
Solder Pads
12 twisted pair ribbon 39 AWG PhBr
PTO2E-15-3S2
PTO6F-9-2SP2
12 Twisted Pair Cable 28 AWG Cu
DB25 [M] (Room Temp)
DB25 [F]
Ultrahead
InterHead
BufferHead
Buffer Film
4- Pump
I-Pump Sensor
U- Pump
High Temperature Thermometry
Low-Temperature Thermometry
LFC Ground
Cable Shield and
Ground
Pin 21 shared as common ground within cyclebox.
PCB on board connections
Spare
He10 Fridge Heaters
Function
4He HEAT
3He HEAT
ULTRA-COLD
4He PUMP
3He PUMP
ULTRA-COLD
J3-J5 PCB Solder Pads
J2 MDM-25PBSP
J2 MDM-25SSB
12 twisted pair ribbon 39 AWG Cu
45K Plate Passthrough E1
Solder Pads
12 twisted pair ribbon 39 AWG Cu
PTO2E-14-12P
PTO5A-14-12PSR
12x AWG21 Cu
DB25 [F] (Room Temp)
DB25 [M] (Cycle Box)
Wires
Heat Switches
I-Pump Heat
U- Pump
4- Pump
Pump Heater
I-Pump Heater
NC
0.3K Detector
Function
Bias
Bias High 1
Bias Low 1
Bias High 2
Bias Low 2
36 AWG Manganin
Not Connected
DET
DET High 1
DET Low 1
DET High 2
DET Low 2
Dual Twist 36 AWG PhBr
JFET Module
VDD_1
VSS_1
VDD_2
VSS_2
PTO6F-14-18P
PTO2E-14-18S
Preamp Box
12 Twisted Pair Cable 28 AWG Cu
He Shield Connected to Amphenol S

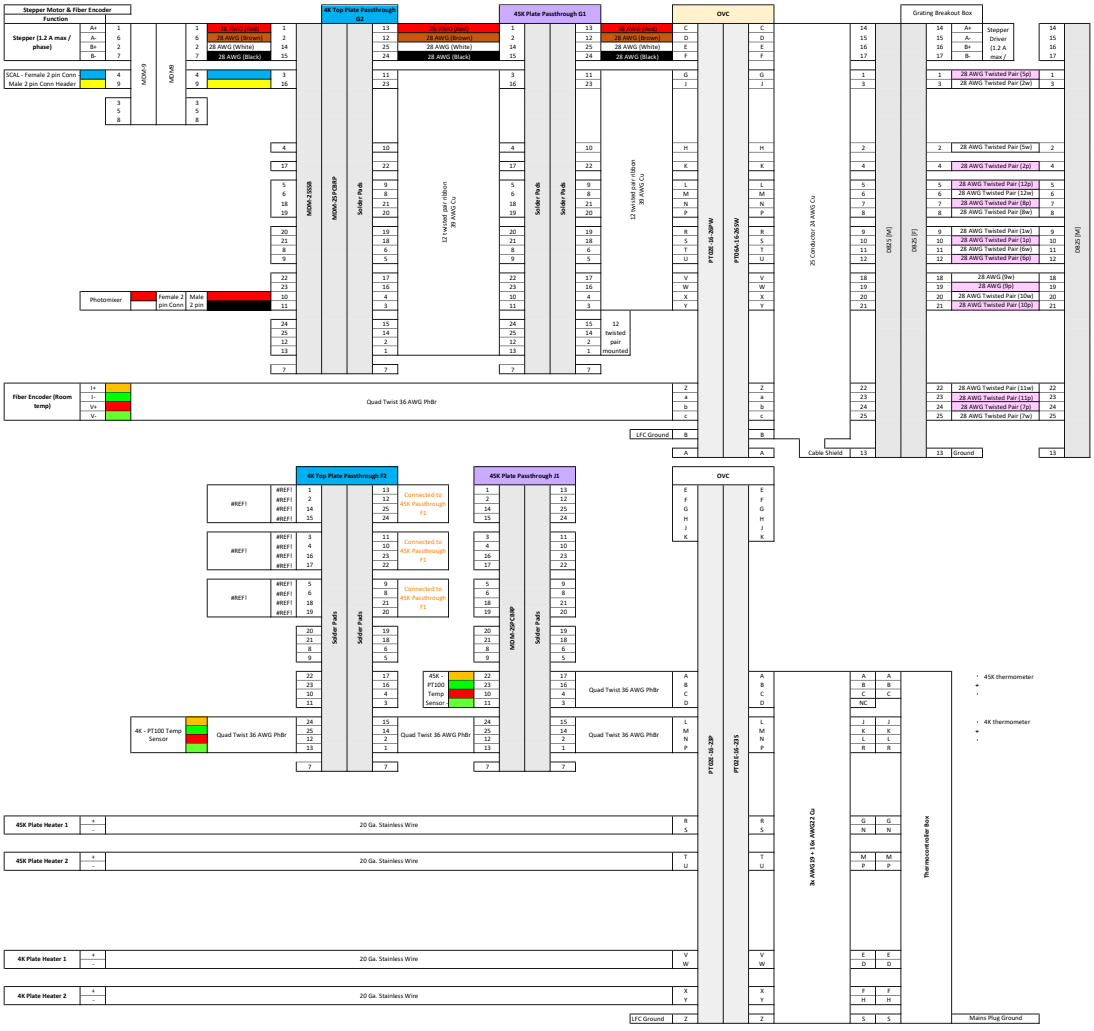
Stepper Motor & Fiber Encoder
Function
Stepper (1.2 A max / phase)
A+
A-
B+
B-
SCAL - Female 2 pin Conn
Male 2 pin Conn Header
MDM-9
MD-9
28 AWG (Red)
28 AWG (Brown)
28 AWG (White)
28 AWG (Black)
4K Top Plate Passthrough G2
MDM-25PCBRP
Solder Pads
12 twisted pair ribbon 30 AWG Cu
45K Plate Passthrough G1
12 twisted pair ribbon 30 AWG Cu
12 twisted pair mounted
OVC
PTDE-16-26PW
PTDEA-16-26SW
25 Conductor 24 AWG Cu
DB25 (M)
DB25 (F)
Grating Breakout Box
Stepper Driver (1.2 A max /
28 AWG Twisted Pair (5p)
28 AWG Twisted Pair (2w)
28 AWG Twisted Pair (5w)
28 AWG Twisted Pair (2p)
28 AWG Twisted Pair (12p)
28 AWG Twisted Pair (12w)
28 AWG Twisted Pair (8p)
28 AWG Twisted Pair (8w)
28 AWG Twisted Pair (1w)
28 AWG Twisted Pair (1p)
28 AWG Twisted Pair (6w)
28 AWG Twisted Pair (6p)
28 AWG (9w)
28 AWG (9p)
28 AWG Twisted Pair (10w)
28 AWG Twisted Pair (10p)
Photomixer
Female 2 pin Conn
Male 2 pin
Fiber Encoder (Room temp)
I+
I-
V+
V-
Quad Twist 36 AWG PhBr
28 AWG Twisted Pair (11w)
28 AWG Twisted Pair (11p)
28 AWG Twisted Pair (7p)
28 AWG Twisted Pair (7w)
LFC Ground
Cable Shield
Ground
4K Top Plate Passthrough F2
45K Plate Passthrough J1
#REF!
Connected to 45K Passthrough F1
MDM-50PCBRP
45K - PT100 Temp Sensor
4K - PT100 Temp Sensor
Quad Twist 36 AWG PhBr
45K thermometer
4K thermometer
PTDE-16-2SP
PTDEE-16-25S
3x AWG 19 + 16x AWG22 Cu
Thermocontroller Box
45K Plate Heater 1
45K Plate Heater 2
4K Plate Heater 1
4K Plate Heater 2
20 Ga. Stainless Wire
Mains Plug Ground


4K Top Plate Passthrough
45K Plate Passthrough A1
OVC
I+
I-
V+
V-
12 twisted pair ribbon
39 AWG Cu
12 twisted pair
mounted only
on 45K PCB
LFC
Ground
MDM-25P/CBRP
Solder Pads
PTIDE-16-325
PTMA-16-2SP
This board left unpopulated.
Will populate and install if we need more wires @ 4K.
4K Top Plate Passthrough H2
45K Plate Passthrough H1
Spare Wiring
MDM-25SSB
MDM-25PCBRP
Solder Pads
12 twisted pair ribbon
39 AWG Cu
13 twisted pair ribbon
39 AWG Cu
PTIDE-16-3KBW
PTIDF-16-2SEPW
TBD
DR25 (PT)
NFG
LFC Ground
Cable Shield

Appendix C PDPFTS Part Drawings

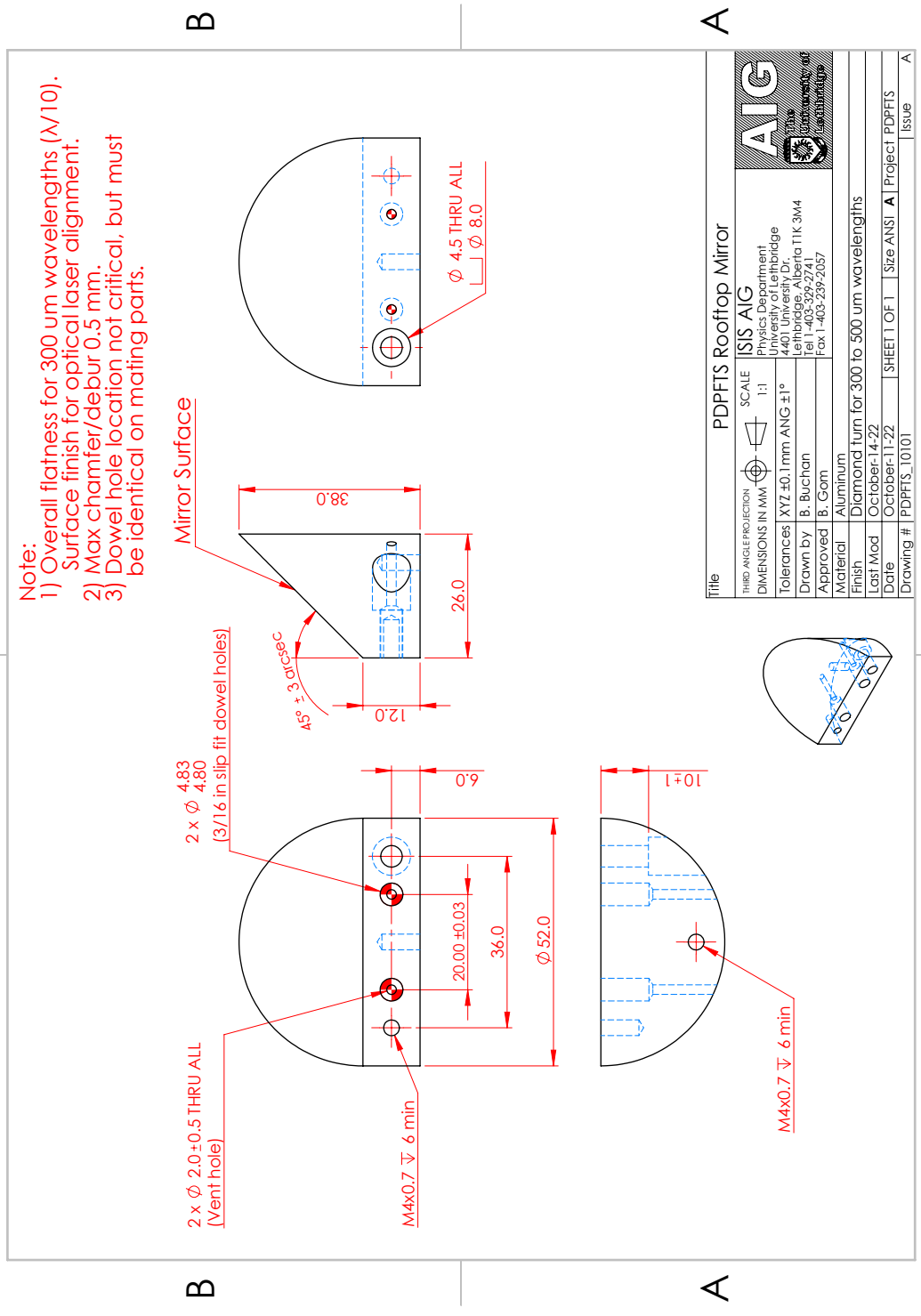

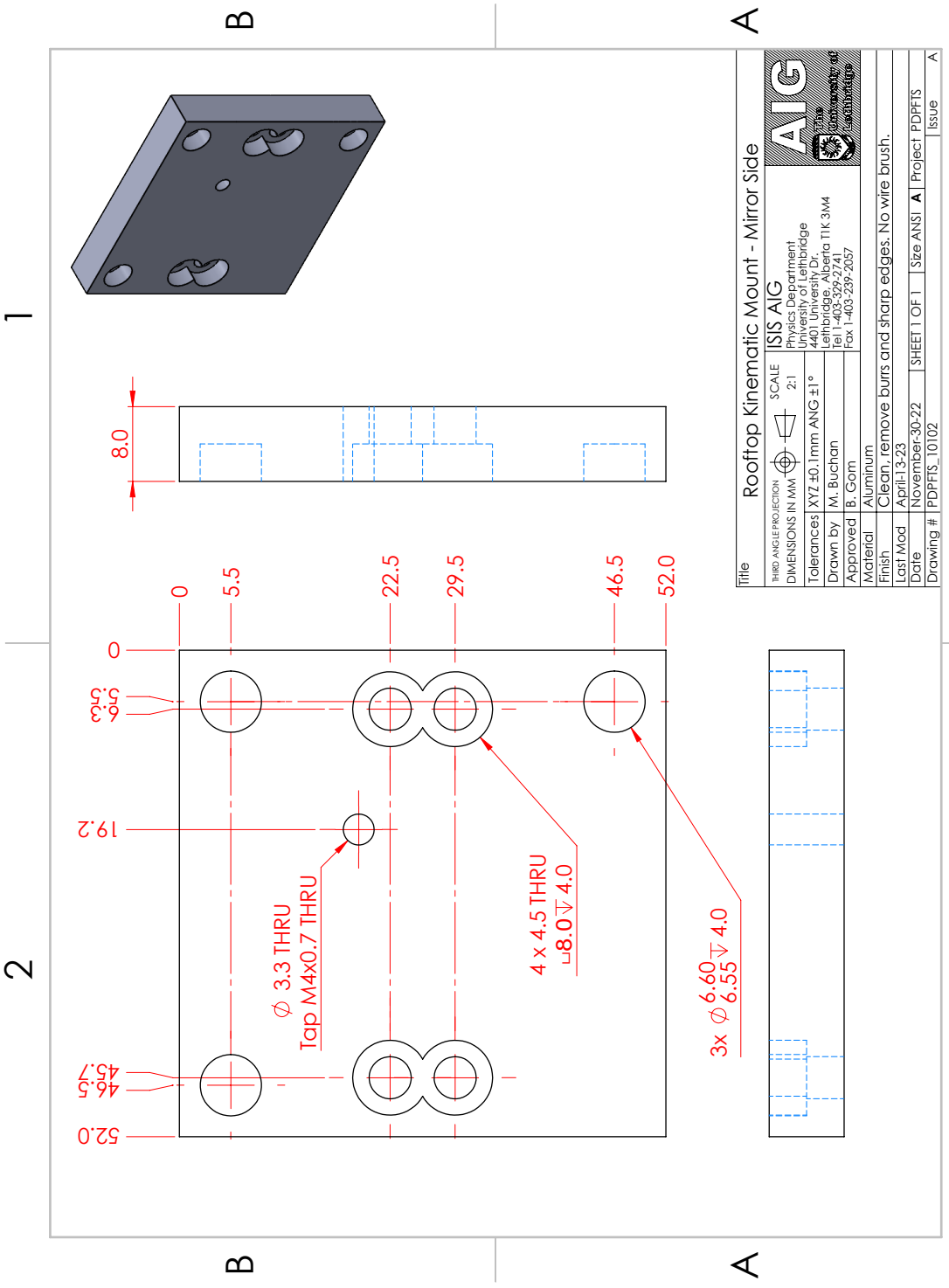
Rooftop Kinematic Mount - Mirror Side
ISIS AIG
Physics Department
University of Lethbridge
4401 University Dr.
Lethbridge, Alberta T1K 3M4
Tel 1-403-329-2741
Fax 1-403-239-2057
THIRD ANGLE PROJECTION
DIMENSIONS IN MM
SCALE 2:1
Tolerances XYZ ±0.1mm ANG ±1°
Drawn by M. Buchan
Approved B. Gom
Material Aluminum
Finish Clean, remove burrs and sharp edges. No wire brush.
Last Mod April-13-23
Date November-30-22
SHEET 1 OF 1
Size ANSI A
Project PDPFTS
Drawing # PDPFTS_10102
Issue A
8.0
0
5.5
22.5
29.5
46.5
52.0
0
6.5
19.2
45.7
52.0
∅ 3.3 THRU
Tap M4x0.7 THRU
4 x 4.5 THRU
⌴8.0↧4.0
3x ∅6.60
∅6.55↧4.0

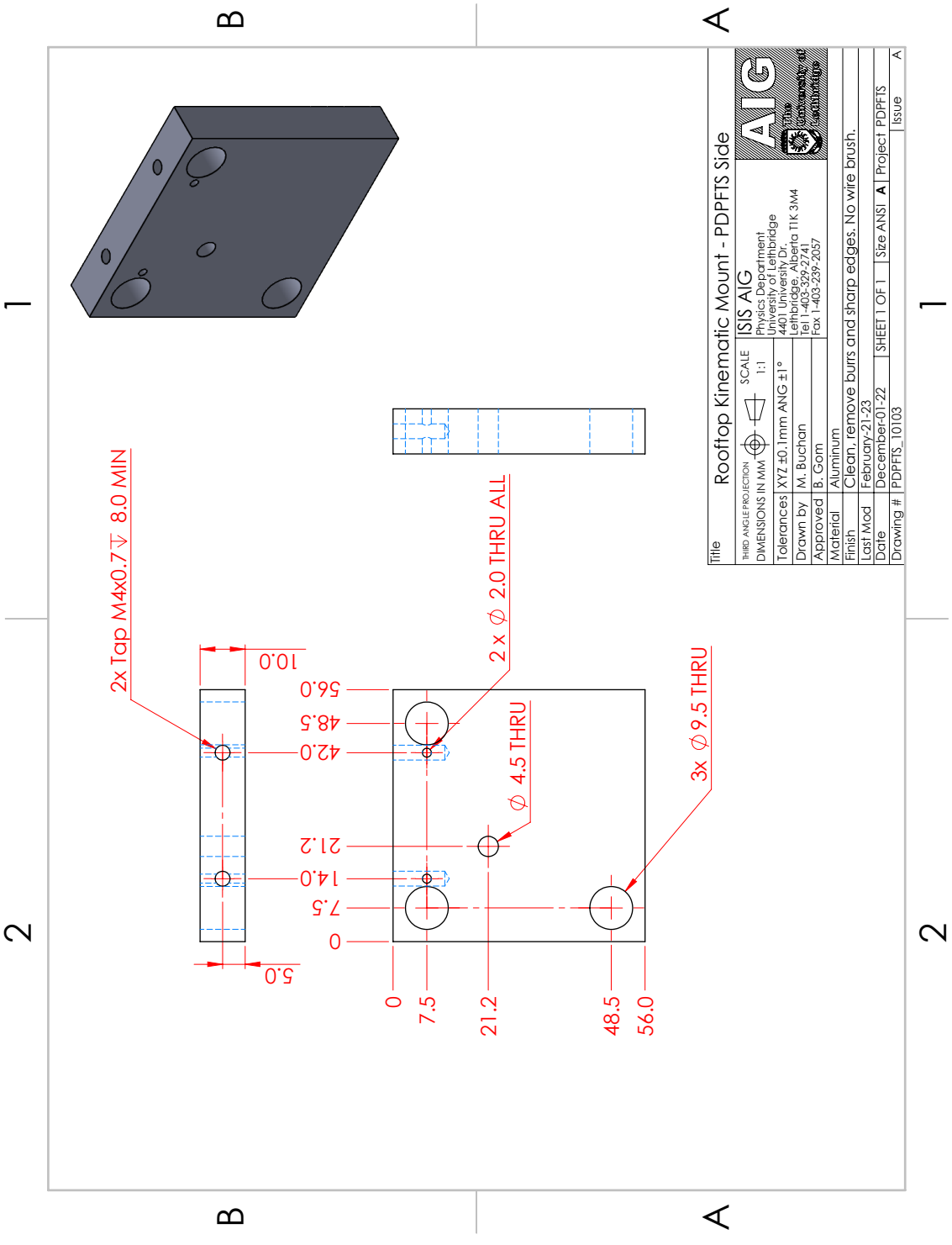
Rooftop Kinematic Mount - PDPFTS Side
SCALE 1:1
THIRD ANGLE PROJECTION
DIMENSIONS IN MM
Tolerances XYZ ±0.1mm ANG ±1°
Drawn by M. Buchan
Approved B. Gorn
Material Aluminum
Finish Clean, remove burrs and sharp edges. No wire brush.
Last Mod February-21-23
Date December-01-22
Drawing # PDPFTS_10103
SHEET 1 OF 1
Size ANSI A
Project PDPFTS
Issue A
ISIS AIG
Physics Department
University of Lethbridge
4401 University Dr.
Lethbridge, Alberta T1K 3M4
Tel 1-403-329-2741
Fax 1-403-239-2057
2x Tap M4x0.7↧ 8.0 MIN
2 x ∅ 2.0 THRU ALL
∅ 4.5 THRU
3x ∅9.5 THRU
10.0
5.0
56.0
48.5
42.0
21.2
14.0
7.5
0
0
7.5
21.2
48.5
56.0

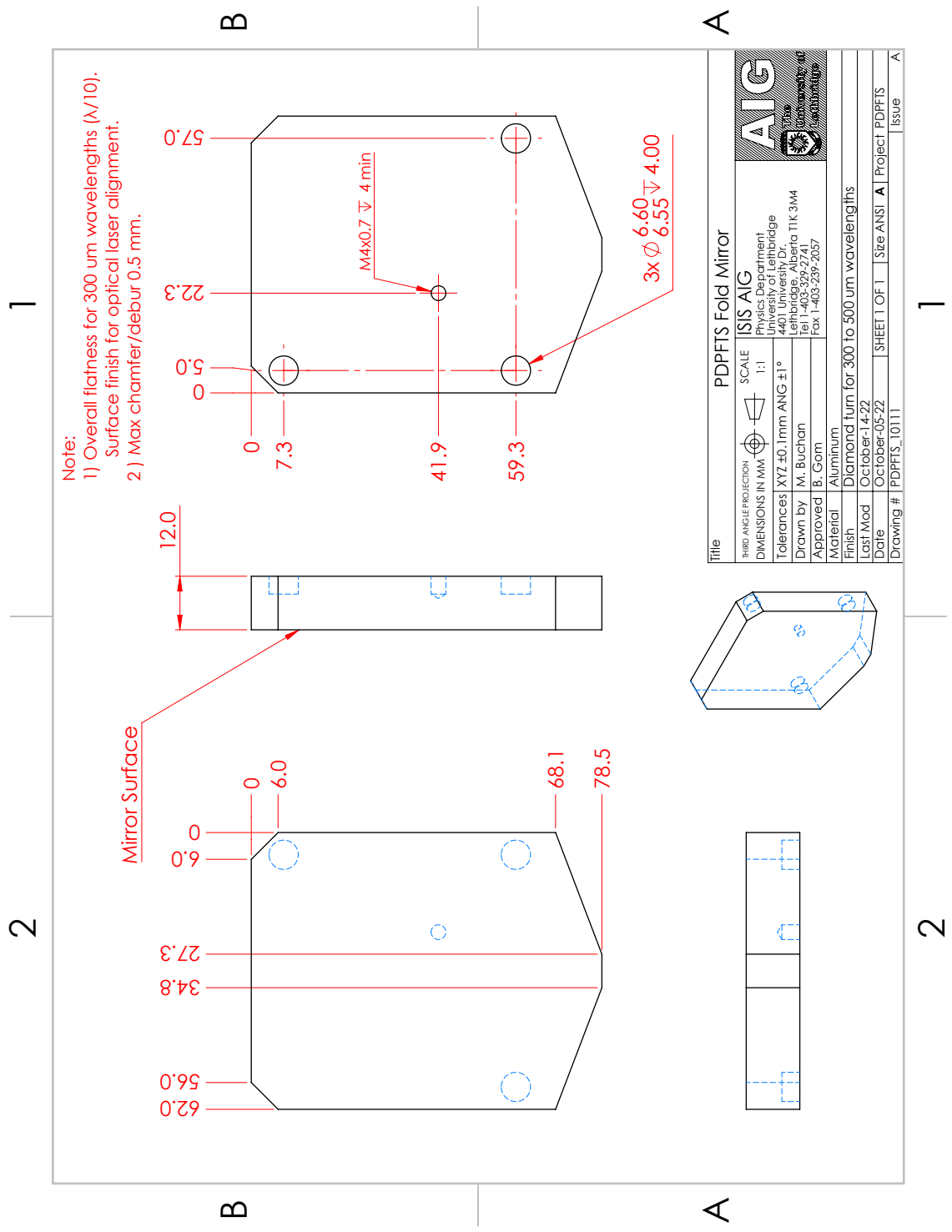
Note:
1) Overall flatness for 300 um wavelengths (λ/10).
Surface finish for optical laser alignment.
2) Max chamfer/debur 0.5 mm.
Mirror Surface
12.0
57.0
22.3
5.0
0
M4x0.7 ↧ 4 min
3x ⌀ 6.60 6.55 ↧ 4.00
0
7.3
41.9
59.3
0
6.0
6.0
0
68.1
78.5
27.3
34.8
56.0
62.0
Title
PDPFTS Fold Mirror
THIRD ANGLE PROJECTION
DIMENSIONS IN MM
SCALE 1:1
ISIS AIG
Physics Department
University of Lethbridge
4401 University Dr.
Lethbridge, Alberta T1K 3M4
Tel 1-403-329-2741
Fax 1-403-239-2057
AIG
The University of Lethbridge
Tolerances XYZ ±0.1mm ANG ±1°
Drawn by M. Buchan
Approved B. Gorn
Material Aluminum
Finish Diamond turn for 300 to 500 um wavelengths
Last Mod October-14-22
Date October-05-22
Drawing # PDPFTS_10111
SHEET 1 OF 1
Size ANSI A
Project PDPFTS
Issue A
A
B
1
2

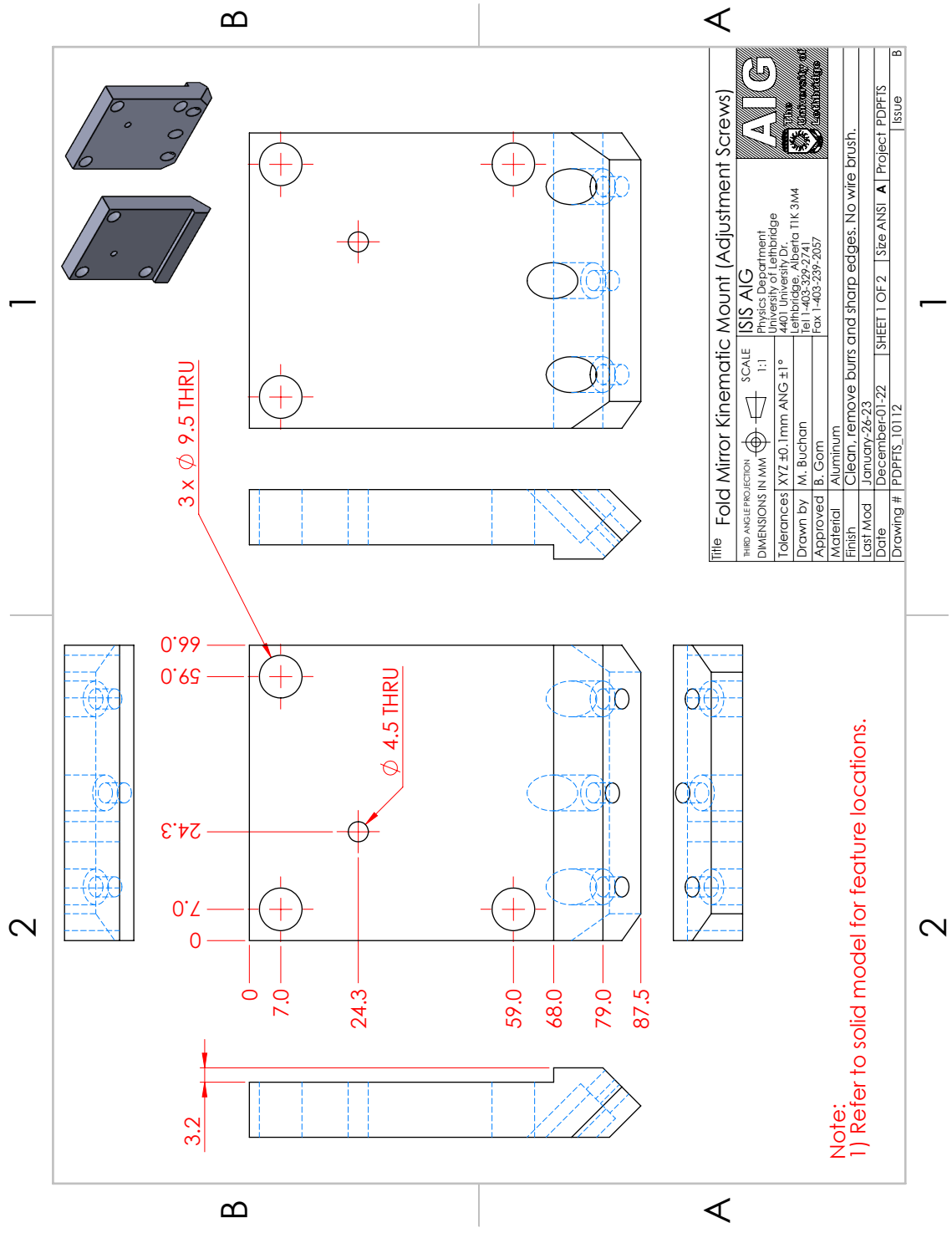
Title Fold Mirror Kinematic Mount (Adjustment Screws)
THIRD ANGLE PROJECTION
DIMENSIONS IN MM
SCALE 1:1
ISIS AIG
Physics Department
University of Lethbridge
4401 University Dr.
Lethbridge, Alberta T1K 3M4
Tel 1-403-329-2741
Fax 1-403-239-2057
Tolerances XYZ ±0.1mm ANG ±1°
Drawn by M. Buchan
Approved B. Gorn
Material Aluminum
Finish Clean, remove burrs and sharp edges. No wire brush.
Last Mod January-26-23
Date December-01-22
SHEET 1 OF 2
Size ANSI A
Project PDPFTS
Drawing # PDPFTS_10112
Issue B
3 x ∅ 9.5 THRU
∅ 4.5 THRU
66.0
59.0
24.3
7.0
0
0
7.0
24.3
59.0
68.0
79.0
87.5
3.2
Note:
1) Refer to solid model for feature locations.

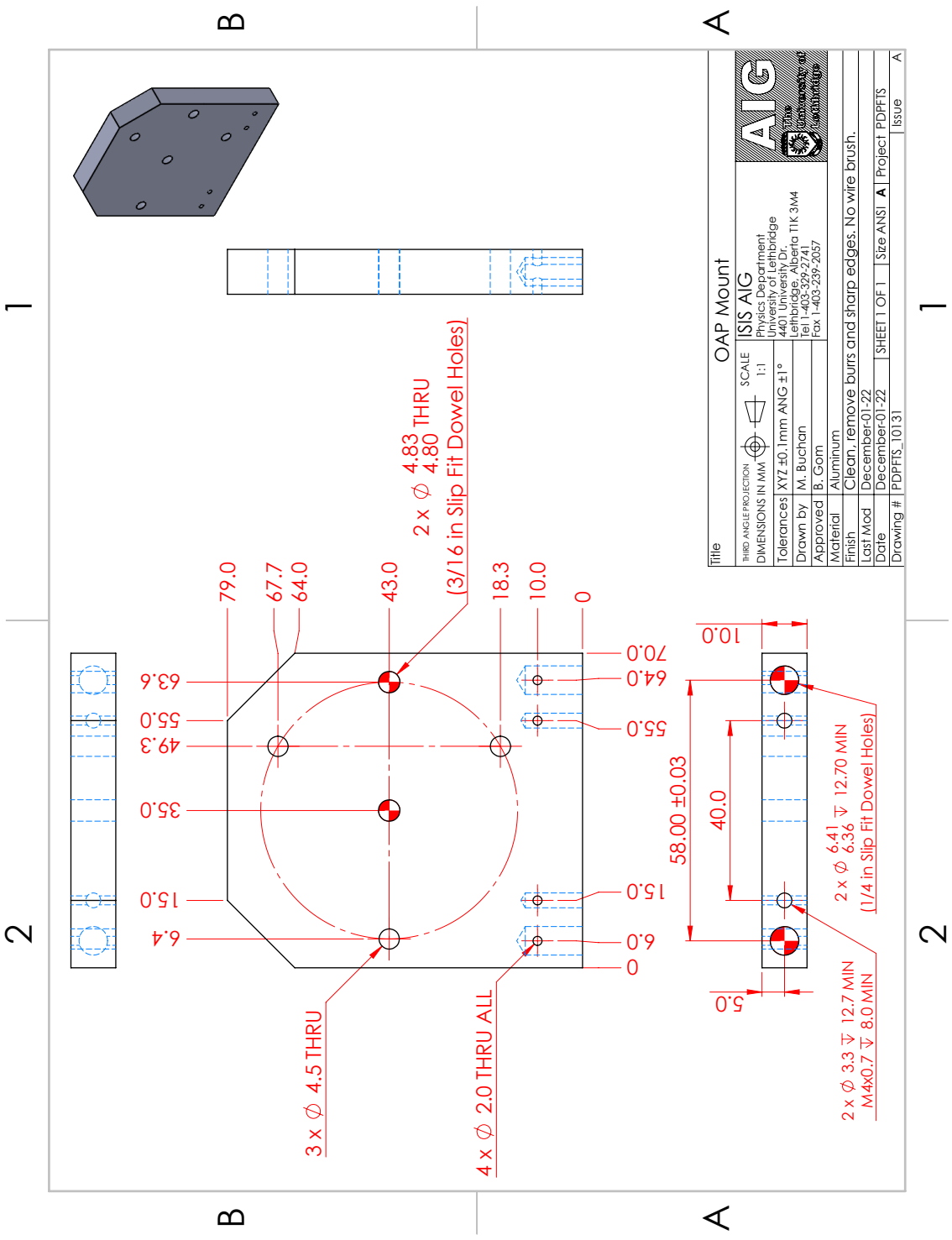
OAP Mount
ISIS AIG
Physics Department
University of Lethbridge
4401 University Dr.
Lethbridge, Alberta T1K 3M4
Tel 1-403-329-2741
Fax 1-403-239-2057
SCALE 1:1
THIRD ANGLE PROJECTION
DIMENSIONS IN MM
Tolerances XYZ ±0.1mm ANG ±1°
Drawn by M. Buchan
Approved B. Gom
Material Aluminum
Finish Clean, remove burrs and sharp edges. No wire brush.
Last Mod December-01-22
Date December-01-22
Drawing # PDPFTS_10131
SHEET 1 OF 1
Size ANSI A
Project PDPFTS
Issue A
2 x ∅ 4.83 4.80 THRU
(3/16 in Slip Fit Dowel Holes)
79.0
67.7
64.0
43.0
18.3
10.0
0
70.0
64.0
55.0
15.0
6.0
0
63.6
55.0
49.3
35.0
15.0
6.4
3 x ∅ 4.5 THRU
4 x ∅ 2.0 THRU ALL
10.0
58.00 ±0.03
40.0
5.0
2 x ∅ 6.41 6.36 ↧ 12.70 MIN
(1/4 in Slip Fit Dowel Holes)
2 x ∅ 3.3 ↧ 12.7 MIN
M4x0.7 ↧ 8.0 MIN

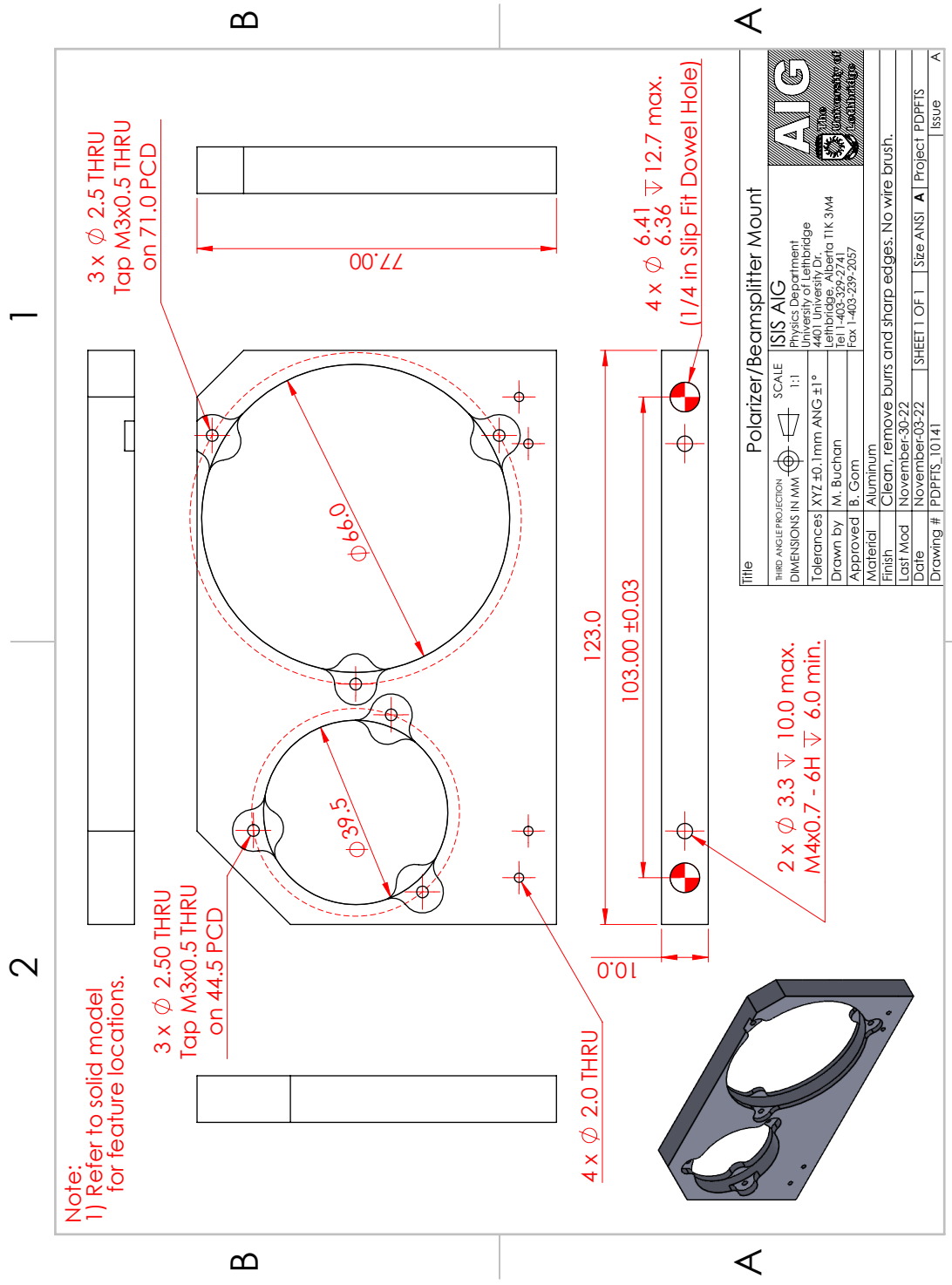
Note:
1) Refer to solid model
for feature locations.
3 x ∅ 2.5 THRU
Tap M3x0.5 THRU
on 71.0 PCD
3 x ∅ 2.50 THRU
Tap M3x0.5 THRU
on 44.5 PCD
4 x ∅ 2.0 THRU
4 x ∅ 6.41
6.36 ↧ 12.7 max.
(1/4 in Slip Fit Dowel Hole)
2 x ∅ 3.3 ↧ 10.0 max.
M4x0.7 - 6H ↧ 6.0 min.
77.00
ϕ66.0
ϕ39.5
123.0
103.00 ±0.03
10.0
Polarizer/Beamsplitter Mount
ISIS AIG
Physics Department
University of Lethbridge
4401 University Dr.
Lethbridge, Alberta T1K 3M4
Tel 1-403-329-2741
Fax 1-403-239-2057
THIRD ANGLE PROJECTION
DIMENSIONS IN MM
SCALE 1:1
Tolerances XYZ ±0.1mm ANG ±1°
Drawn by M. Buchan
Approved B. Gorn
Material Aluminum
Finish Clean, remove burrs and sharp edges. No wire brush.
Last Mod November-30-22
Date November-03-22
Drawing # PDPFTS_10141
SHEET 1 OF 1
Size ANSI A
Project PDPFTS
Issue A

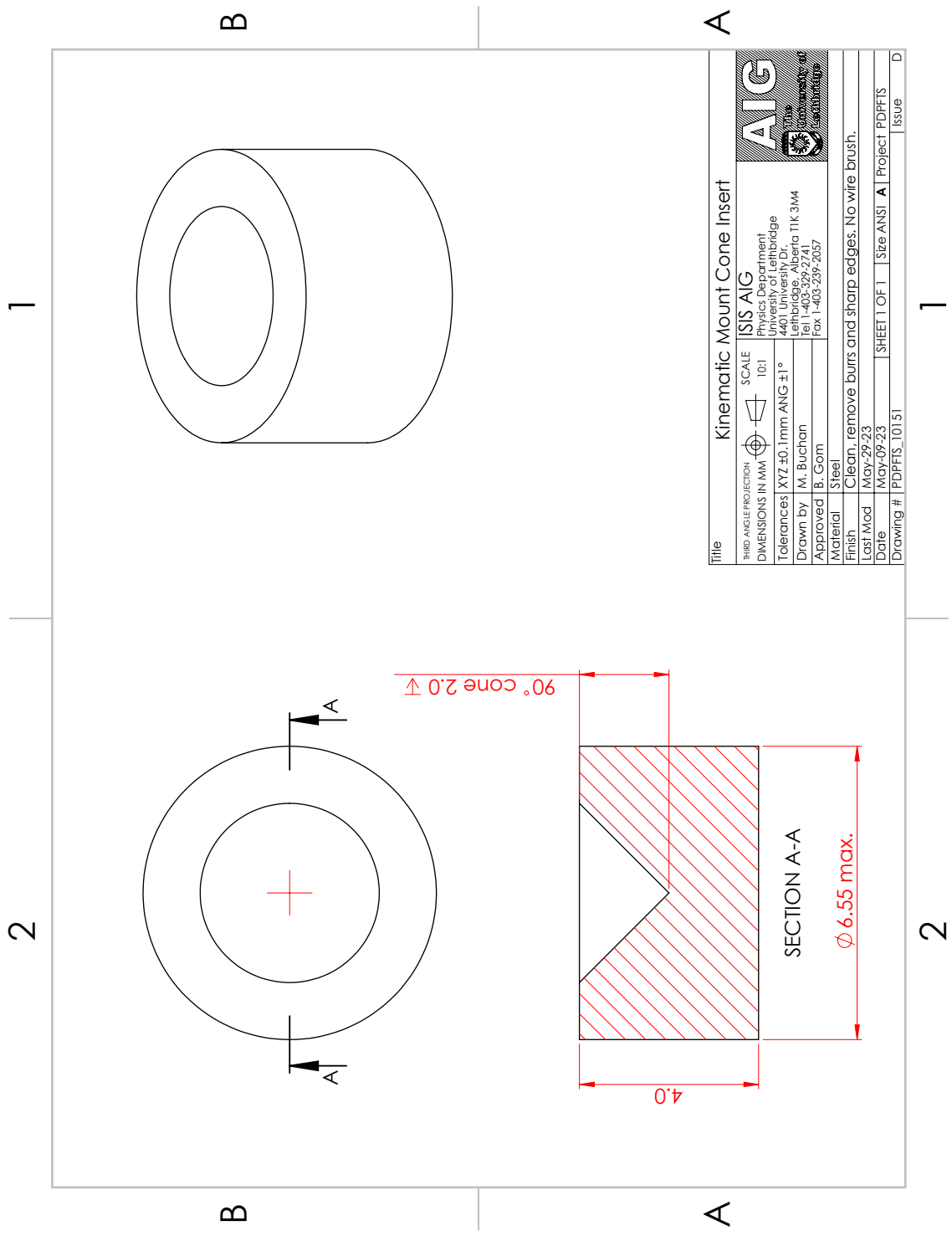
1
2
A
B
A
B
A
A
90° cone 2.0
4.0
SECTION A-A
Ø 6.55 max.
Title
Kinematic Mount Cone Insert
THIRD ANGLE PROJECTION
DIMENSIONS IN MM
SCALE 10:1
ISIS AIG
Physics Department
University of Lethbridge
4401 University Dr.
Lethbridge, Alberta T1K 3M4
Tel 1-403-329-2741
Fax 1-403-239-2057
The University of Lethbridge
Tolerances
XYZ ±0.1mm ANG ±1°
Drawn by
M. Buchan
Approved
B. Gom
Material
Steel
Finish
Clean, remove burrs and sharp edges. No wire brush.
Last Mod
May-29-23
Date
May-09-23
SHEET 1 OF 1
Size ANSI A
Project PDPFTS
Drawing #
PDPFTS_10151
Issue
D

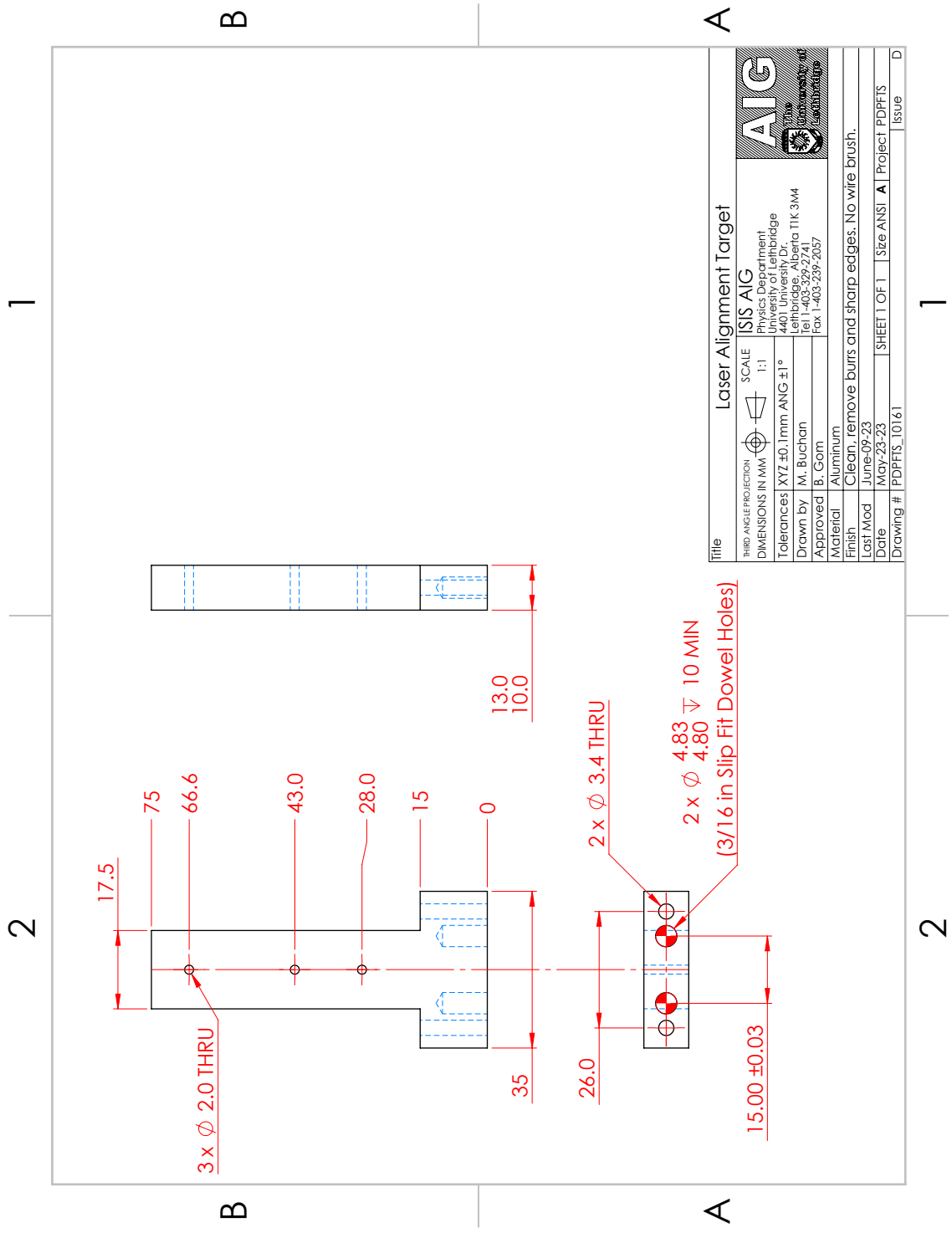
Laser Alignment Target
ISIS AIG
Physics Department
University of Lethbridge
4401 University Dr.
Lethbridge, Alberta T1K 3M4
Tel 1-403-329-2741
Fax 1-403-239-2057
THIRD ANGLE PROJECTION
DIMENSIONS IN MM
SCALE 1:1
Tolerances XYZ ±0.1mm ANG ±1°
Drawn by M. Buchan
Approved B. Gorn
Material Aluminum
Finish Clean, remove burrs and sharp edges. No wire brush.
Last Mod June-09-23
Date May-23-23
Drawing # PDPFTS_10161
SHEET 1 OF 1
Size ANSI A
Project PDPFTS
Issue D
17.5
75
66.6
43.0
28.0
15
0
13.0
10.0
3 x ∅ 2.0 THRU
35
2 x ∅ 3.4 THRU
26.0
2 x ∅ 4.83 ⌅ 4.80 ⌅ 10 MIN
(3/16 in Slip Fit Dowel Holes)
15.00 ±0.03

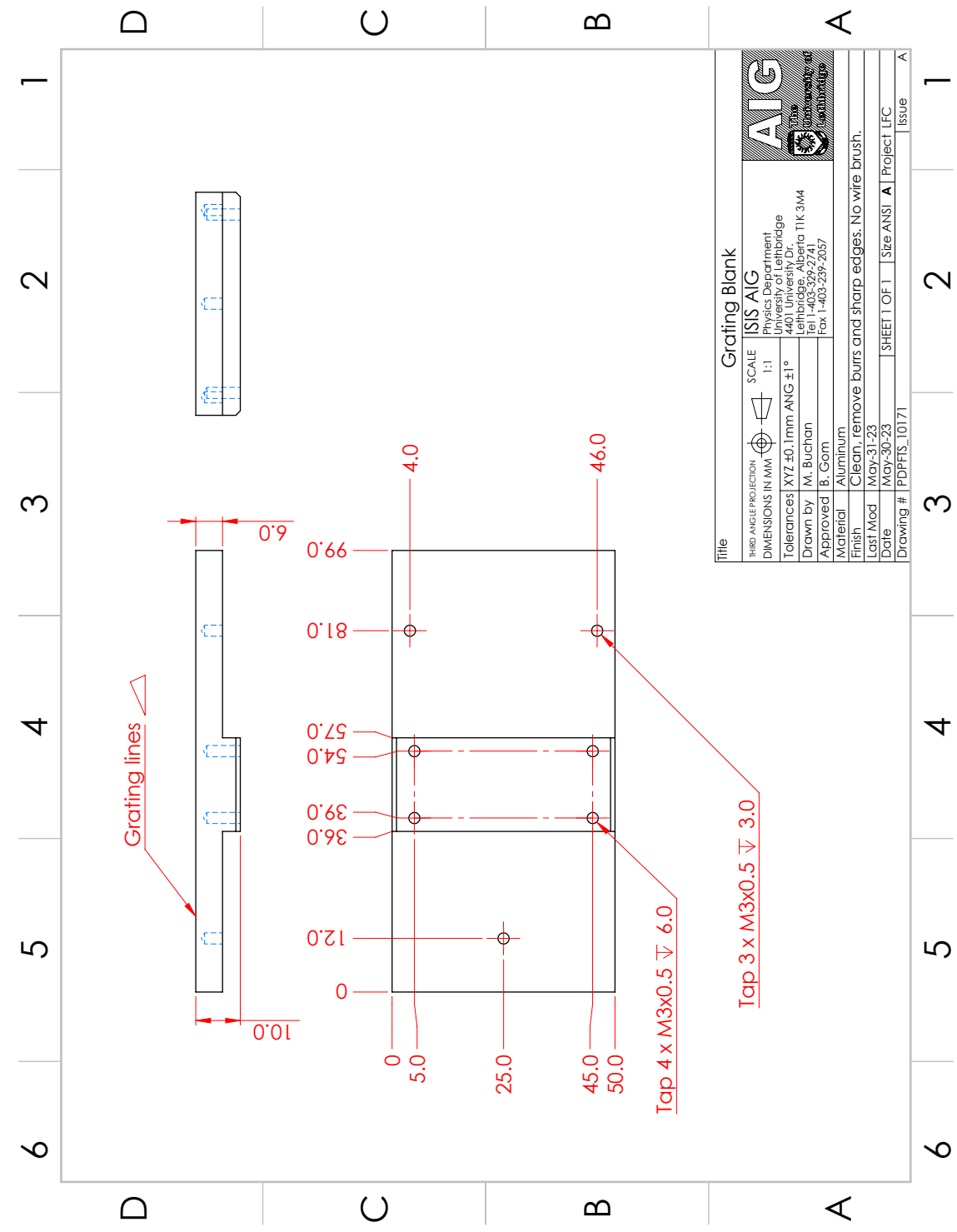
Grating lines
6.0
10.0
4.0
46.0
99.0
81.0
57.0
54.0
39.0
36.0
12.0
0
0
5.0
25.0
45.0
50.0
Tap 4 x M3x0.5 ↧ 6.0
Tap 3 x M3x0.5 ↧ 3.0
Title
Grating Blank
THIRD ANGLE PROJECTION
DIMENSIONS IN MM
SCALE 1:1
ISIS AIG
Physics Department
University of Lethbridge
4401 University Dr.
Lethbridge, Alberta T1K 3M4
Tel 1-403-329-2741
Fax 1-403-239-2057
Tolerances XYZ ±0.1mm ANG ±1°
Drawn by M. Buchan
Approved B. Gom
Material Aluminum
Finish Clean, remove burrs and sharp edges. No wire brush.
Last Mod May-31-23
Date May-30-23
SHEET 1 OF 1
Size ANSI A
Project LFC
Drawing # PDPFTS_10171
Issue A

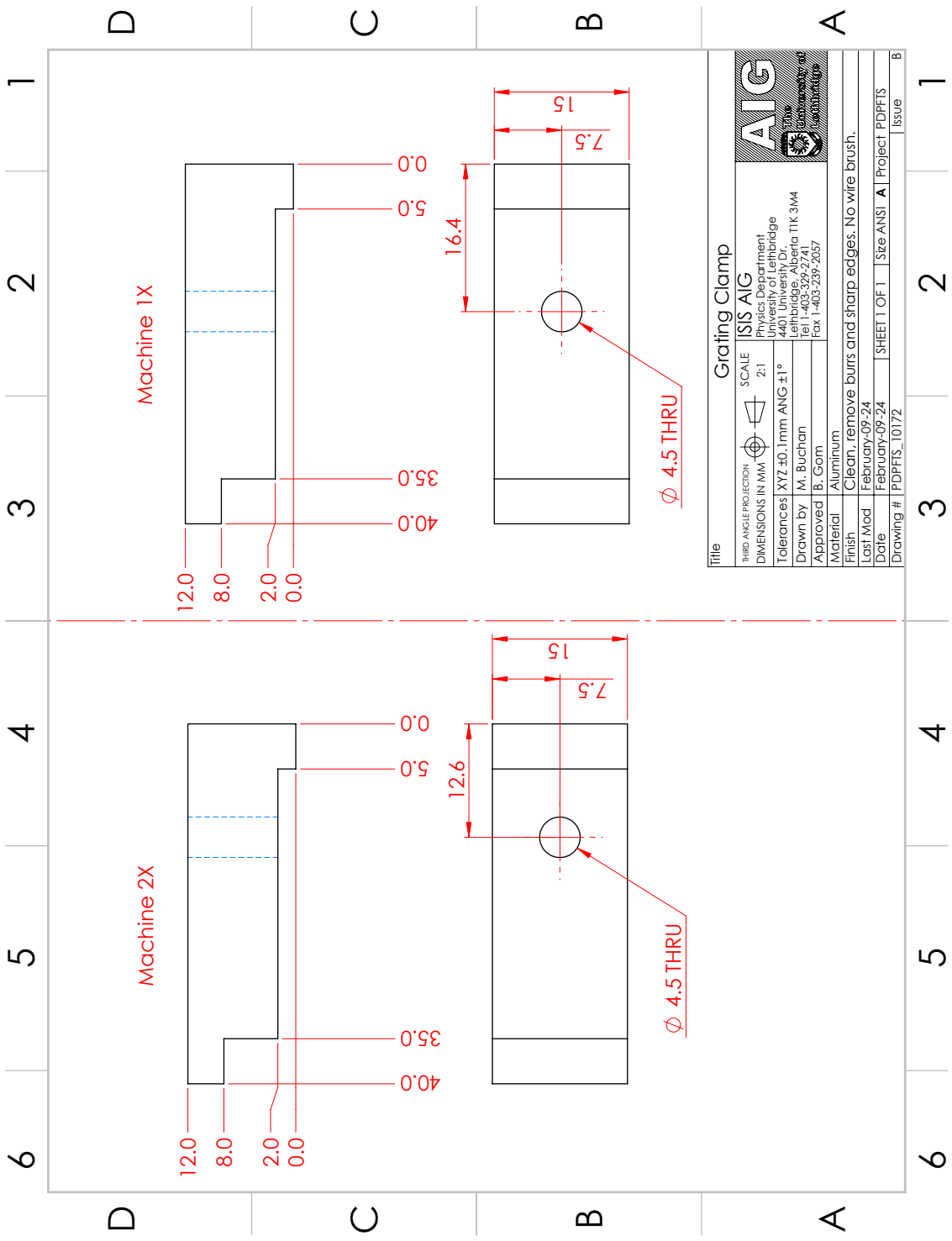
Machine 1X
Machine 2X
0.0
5.0
35.0
40.0
12.0
8.0
2.0
0.0
16.4
12.6
15
7.5
Ø 4.5 THRU
Title
Grating Clamp
THIRD ANGLE PROJECTION
DIMENSIONS IN MM
SCALE 2:1
ISIS AIG
Physics Department
University of Lethbridge
4401 University Dr.
Lethbridge, Alberta T1K 3M4
Tel 1-403-329-2741
Fax 1-403-239-2057
Tolerances XYZ ±0.1mm ANG ±1°
Drawn by M. Buchan
Approved B. Gorn
Material Aluminum
Finish Clean, remove burrs and sharp edges. No wire brush.
Last Mod February-09-24
Date February-09-24
Drawing # PDPFTS_10172
SHEET 1 OF 1
Size ANSI A
Project PDPFTS
Issue B

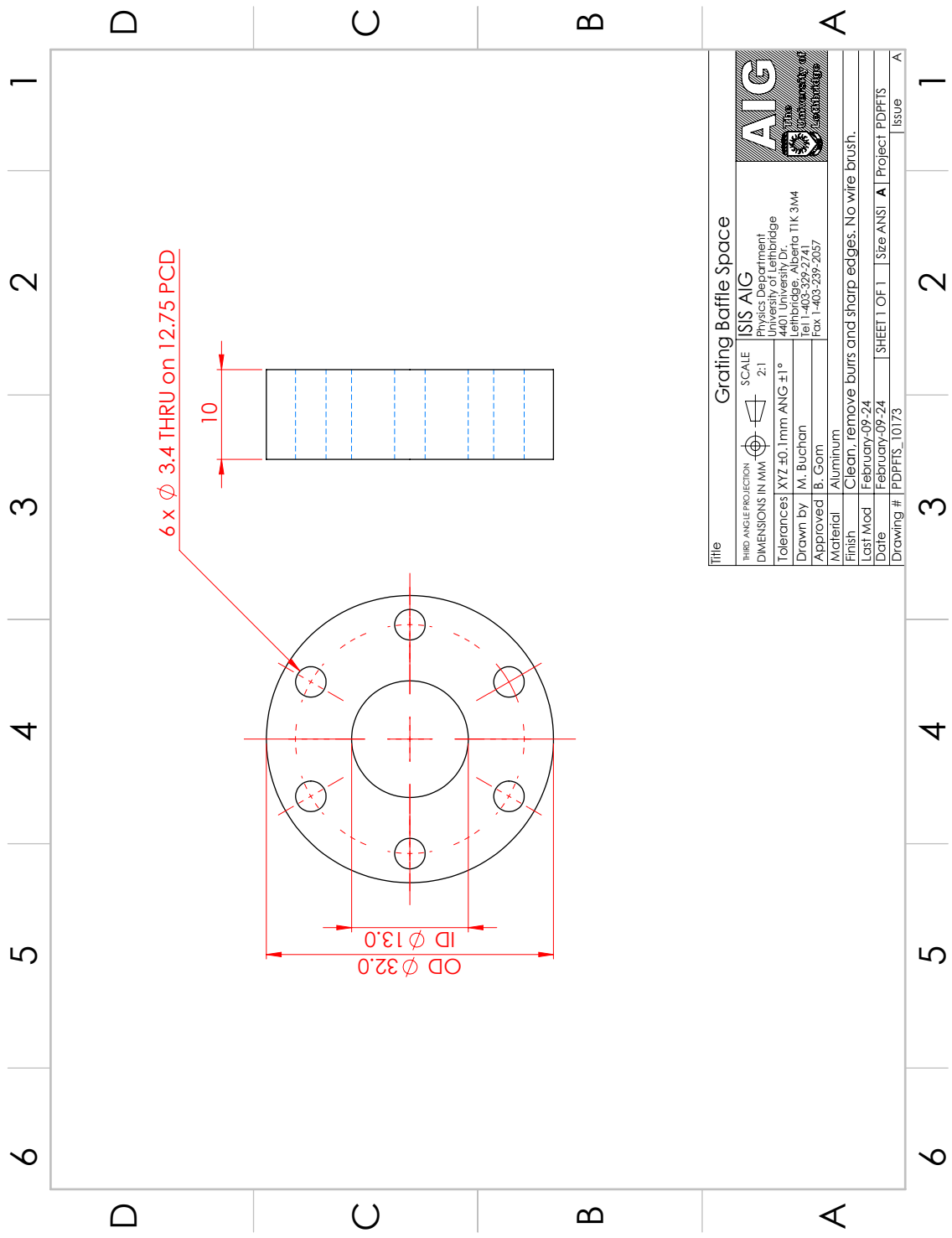
6 x ∅ 3.4 THRU on 12.75 PCD
10
OD ∅ 32.0
ID ∅ 13.0
Title
Grating Baffle Space
THIRD ANGLE PROJECTION
DIMENSIONS IN MM
SCALE 2:1
ISIS AIG
Physics Department
University of Lethbridge
4401 University Dr.
Lethbridge, Alberta T1K 3M4
Tel 1-403-329-2741
Fax 1-403-239-2057
AIG
The University of Lethbridge
Tolerances XYZ ±0.1mm ANG ±1°
Drawn by M. Buchan
Approved B. Gom
Material Aluminum
Finish Clean, remove burrs and sharp edges. No wire brush.
Last Mod February-09-24
Date February-09-24
SHEET 1 OF 1
Size ANSI A
Project PDPFTS
Drawing # PDPFTS_10173
Issue A

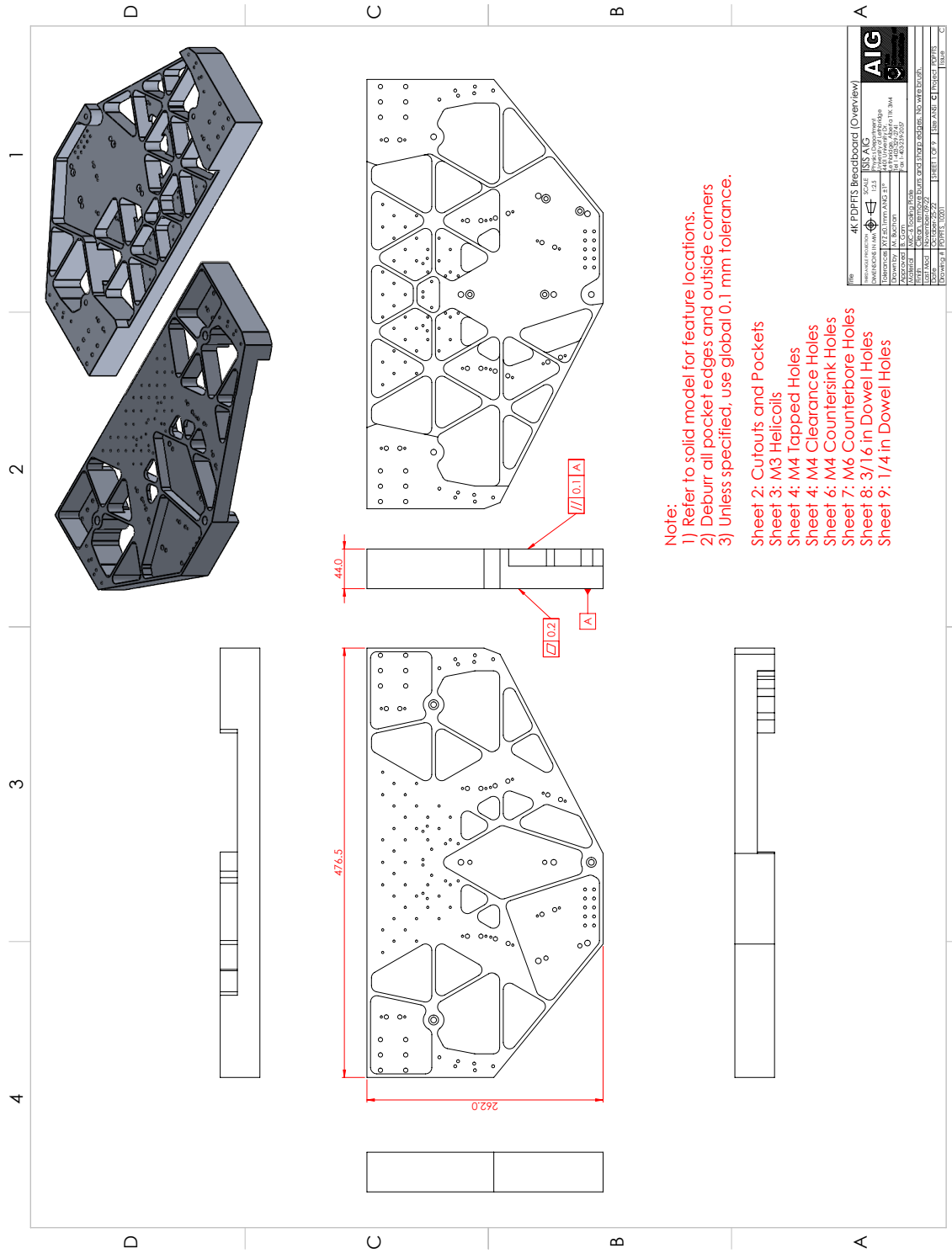
Note:
1) Refer to solid model for feature locations.
2) Deburr all pocket edges and outside corners
3) Unless specified, use global 0.1 mm tolerance.
Sheet 2: Cutouts and Pockets
Sheet 3: M3 Helicoils
Sheet 4: M4 Tapped Holes
Sheet 4: M4 Clearance Holes
Sheet 6: M4 Countersink Holes
Sheet 7: M6 Counterbore Holes
Sheet 8: 3/16 in Dowel Holes
Sheet 9: 1/4 in Dowel Holes
476.5
262.0
44.0
0.1 A
0.2 A
4K PDPFTS Breadboard (Overview)
AIG

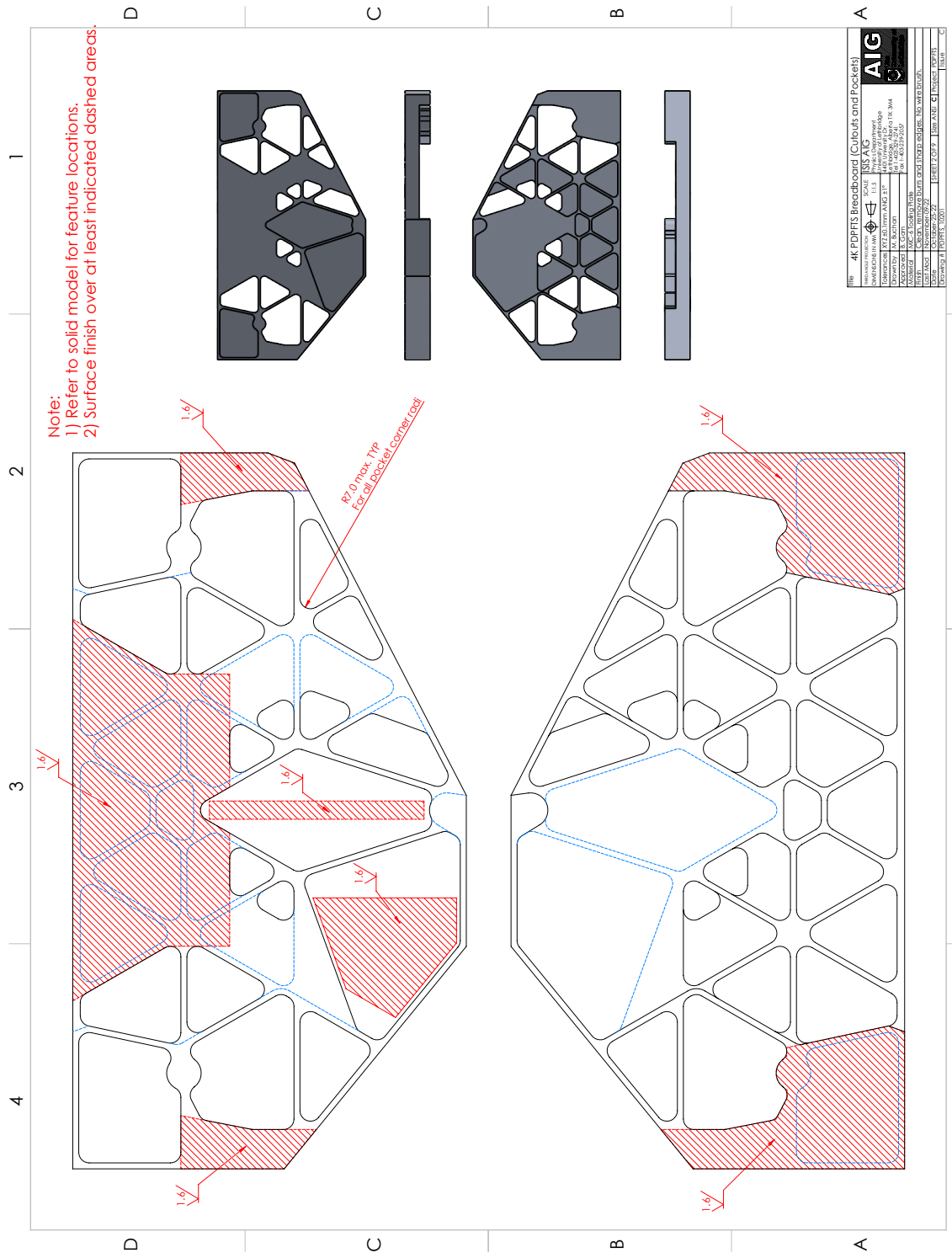
Note:
1) Refer to solid model for feature locations.
2) Surface finish over at least indicated dashed areas.
R7.0 max. TYP
For all pocket corner radii
1.6
Title 4K PDPFTS Breadboard (Cutouts and Pockets)
AIG
Material
Finish
Drawing # PDPFTS_10001
Issue C

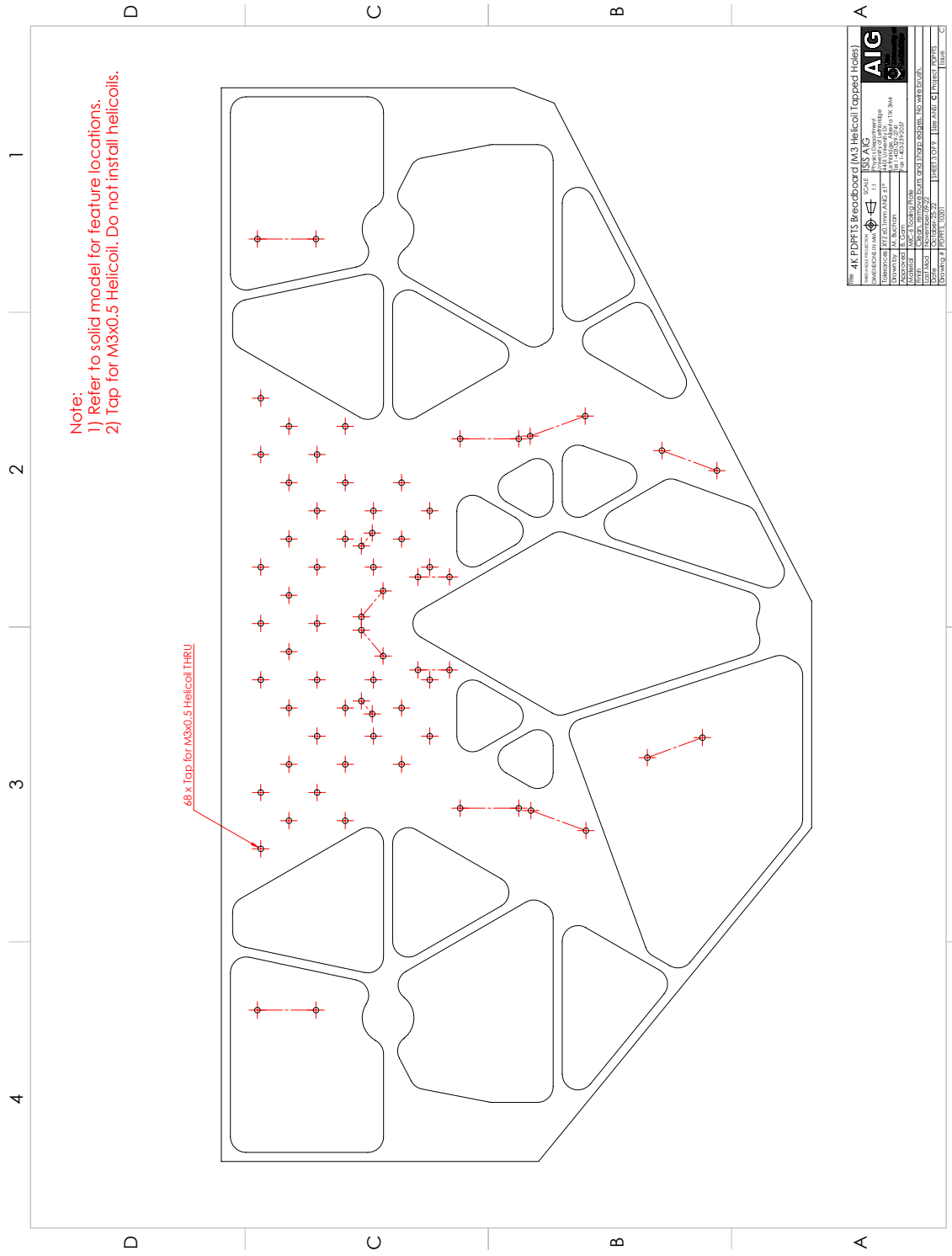
Note:
1) Refer to solid model for feature locations.
2) Tap for M3x0.5 Helicoil. Do not install helicoils.
68 x Tap for M3x0.5 Helicoil THRU
Title 4K PDPFTS Breadboard (M3 Helicoil Tapped Holes)
AIG
ISIS AIG
Material
Finish
Drawing #
Issue
A
B
C
D
1
2
3
4

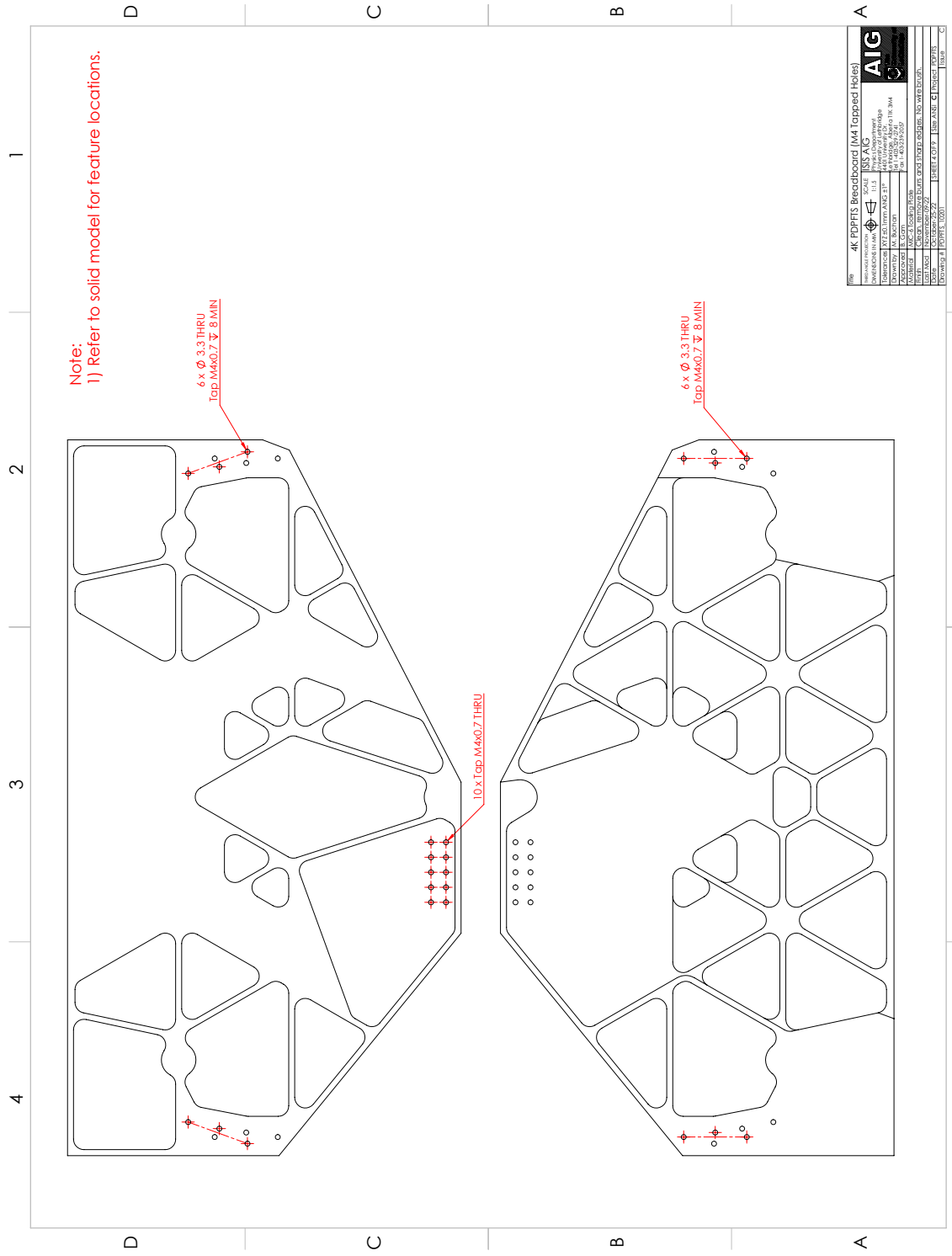
Note:
1) Refer to solid model for feature locations.
6 x Ø 3.3 THRU
Tap M4x0.7 ↧ 8 MIN
10 x Tap M4x0.7 THRU
6 x Ø 3.3 THRU
Tap M4x0.7 ↧ 8 MIN
File 4K PDPFTS Breadboard (M4 Tapped Holes)
AIG
Tolerances X±0.4mm ANG ±1°
Drawn by K. Bochan
Material AlMg3
Finish Clean, remove burn and sharp edges. No weld brush.
Date 04 Dec '25
Drawing # PDPFTS_10001
SCALE 1:1.5
SHEET 4 OF 9
Size ANSI - C
Project PDPFTS
Issue C

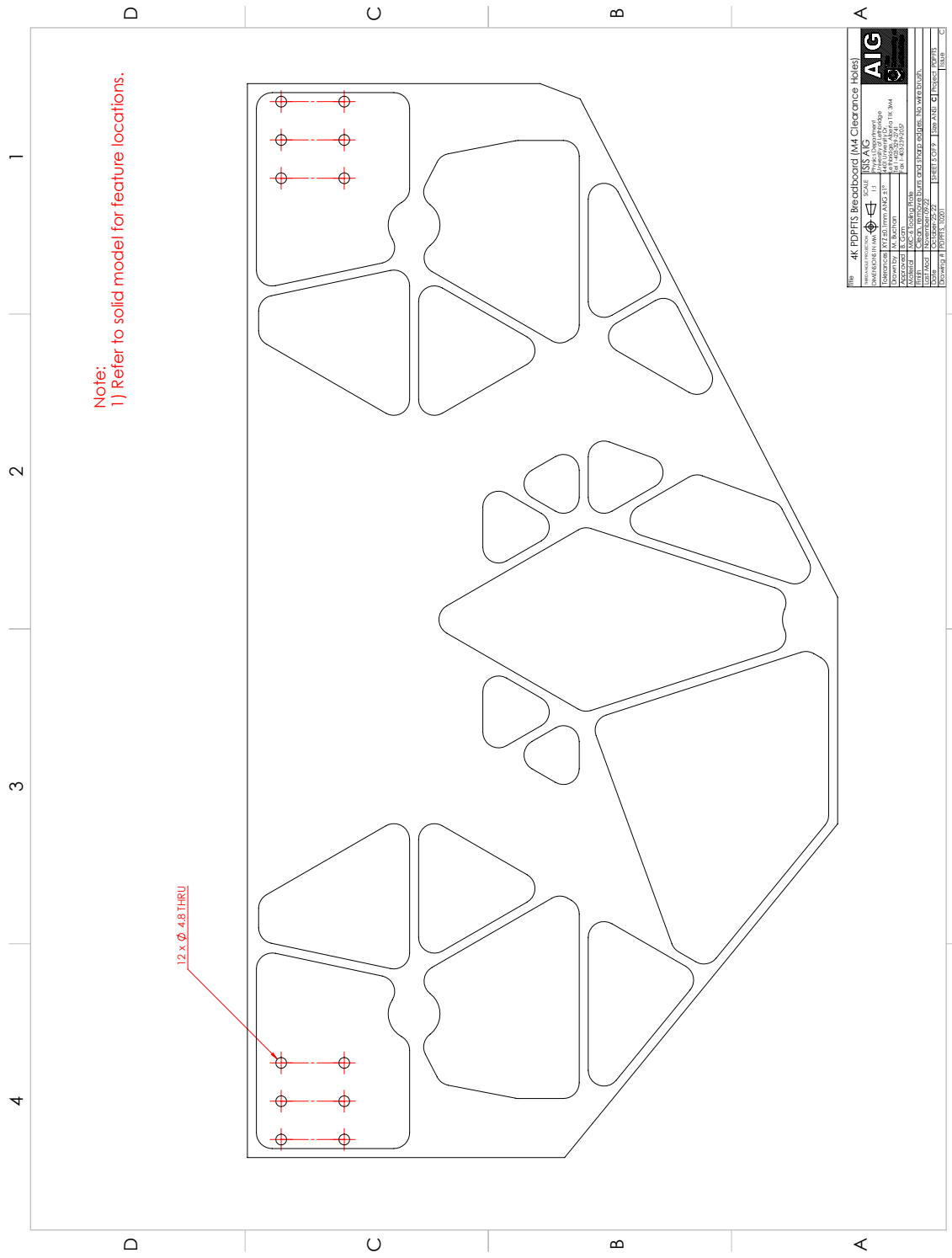
Note:
1) Refer to solid model for feature locations.
12 x Ø 4.8 THRU
4K PDPFTS Breadboard (M4 Clearance Holes)
AIG
ISIS AIG
Physics Department
Imperial College London
Prince Consort Road
London SW7 2BW
Tel +44(0)20 7594 7744
Fax +44(0)20 7594 7707
SCALE 1:1
Tolerances X/Y ±0.1mm ANG ±1°
Drawn by M. Buchan
Approved S. Green
Material FR4 - 1.6 clad, Polyimide
Finish Clean, remove burrs and sharp edges. No wire brush.
Surface treatment ENIG
Date 24 Sept 2012
SHEET 1 OF 1
Size A3(L)
Project PDPFTS
Drawing # PDPFTS_10001
Issue C
A
B
C
D
1
2
3
4

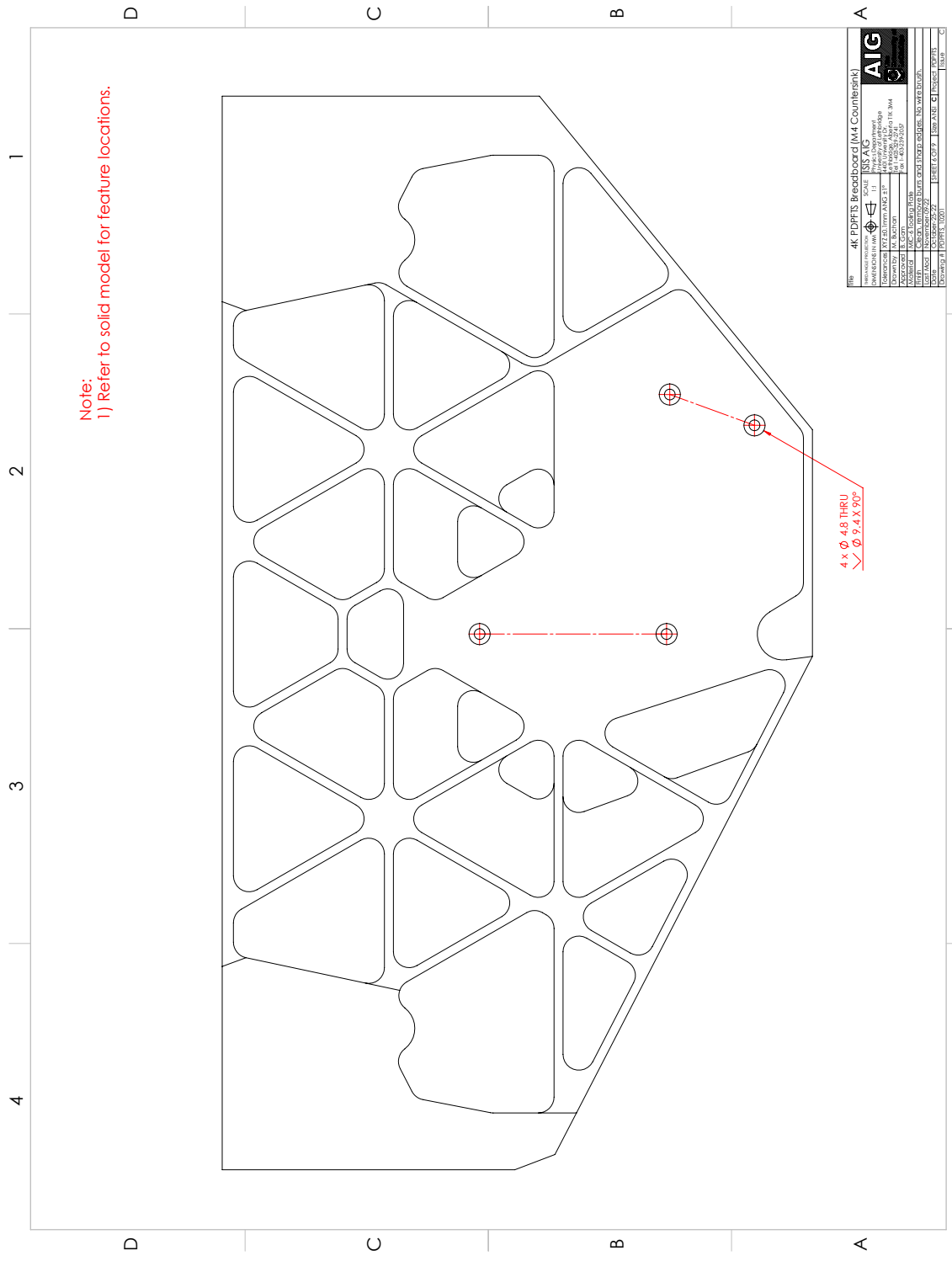
Note:
1) Refer to solid model for feature locations.
4 x Ø 4.8 THRU
Ø 9.4 X 90°
4K PDPFTS Breadboard (M4 Countersink)
AIG
ISIS AIG
Physics Department
University of Liverpool
Oliver Lodge Laboratory
Oxford Road
Liverpool L69 7ZE
tel +44(0)151 794 3644
fax +44(0)151 794 3555
Drawn by: M. Bochen
Approved: K.V. Grimm
Material: 10C-1 Locking Plate
Finish: Clean, remove burrs and sharp edges. No weld brush.
Date: 04 Dec 2012
Drawing #: PDPFTS_10001
Issue: C

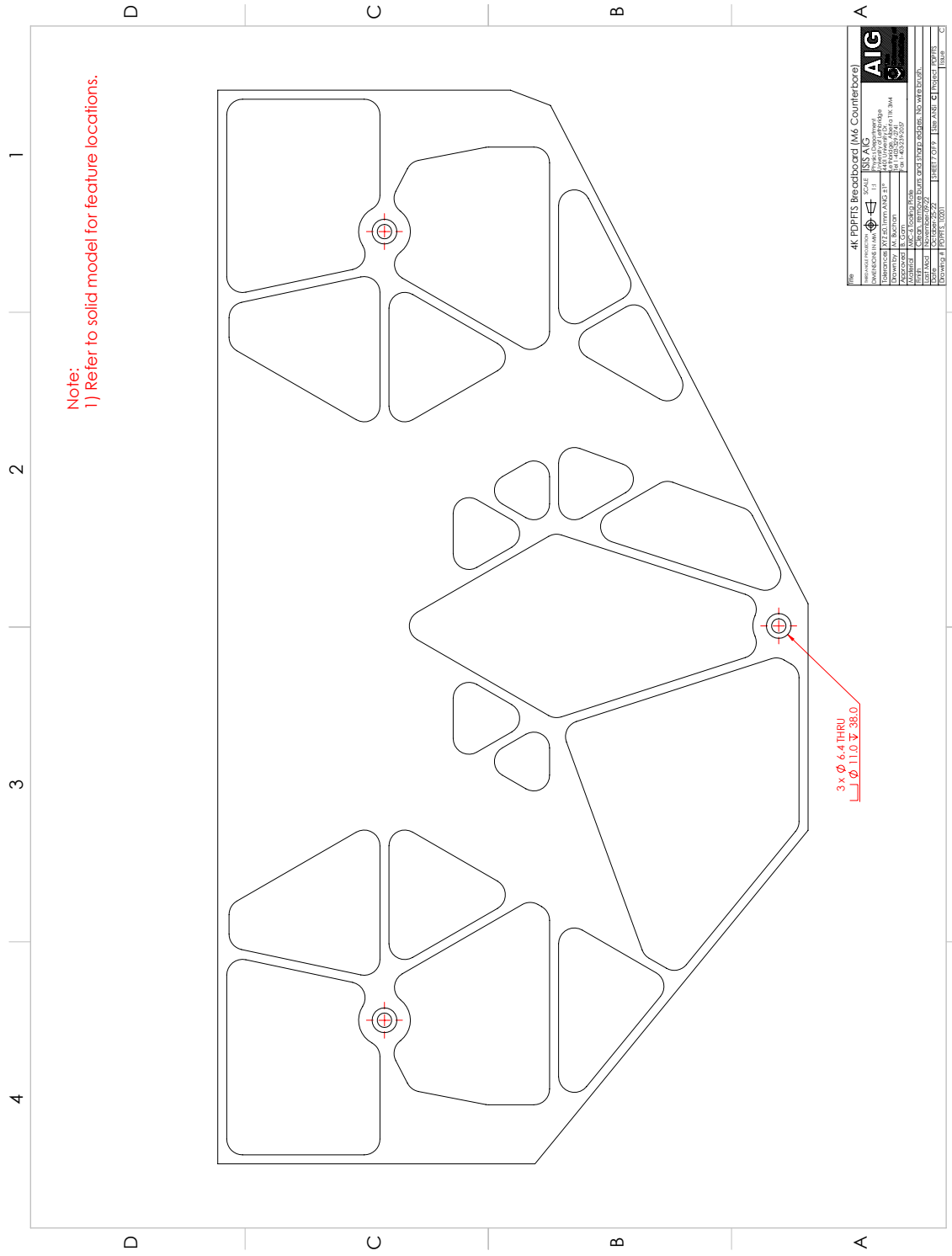
Note:
1) Refer to solid model for feature locations.
3 x Ø 6.4 THRU
⌴ Ø 11.0 ↧ 38.0
4K PDPFTS Breadboard (M6 Counterbore)
AIG
ISIS AIG
Physics Department
University of Liverpool
Oliver Lodge Laboratory
Oxford Road
Liverpool L69 7ZE
tel +44(0)151 794 3644
fax +44(0)151 794 3434
SCALE 1:1
Tolerances X±1.0, mm ANG ±1°
Drawn by M. Bochen
Approved by S. Cox
Material HDPE
Finish Clean, remove burn and sharp edges. No weak brush.
Surface texture 3.2
Date 04 Dec 2020
Drawing # PDPFTS_10001
SHEET 1 OF 1
Title ANSI - C Project PDPFTS
Issue C

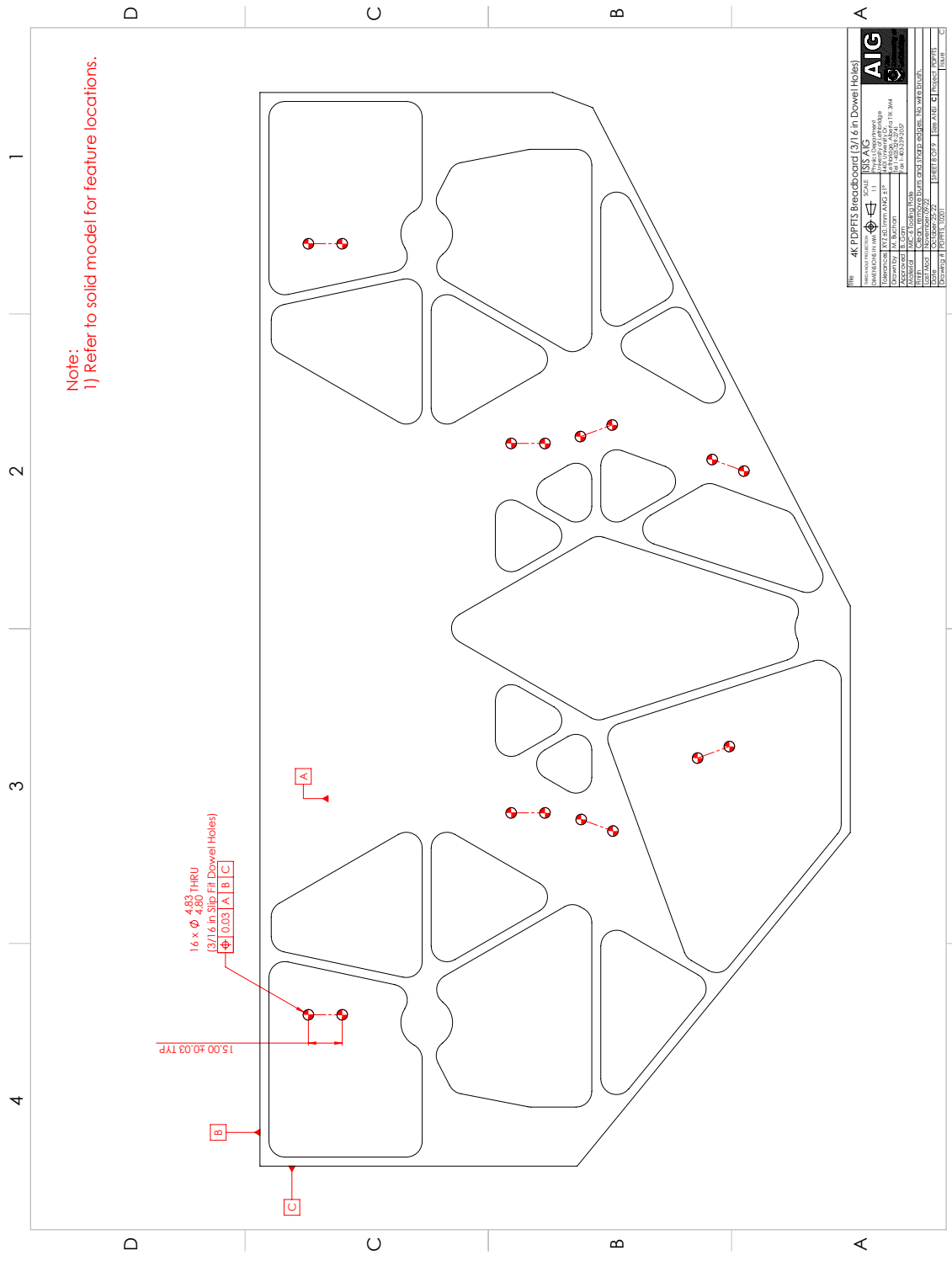
Note:
1) Refer to solid model for feature locations.
16 x Ø 4.83
4.80 THRU
(3/16 in Slip Fit Dowel Holes)
0.03 A B C
15.00 ±0.03 TYP
A
B
C
D
C
B
A
1
2
3
4
AIG
4K PDPFTS Breadboard (3/16 in Dowel Holes)
ISIS AIG
Physics Department
University of Waterloo
Tolerances: X/7.62, .mm, ANG. ±1°
Drawn by: M. Buchan
Approved by: S. Cook
Material: 1/8" G-10 Fiberglass
Finish: Clean, remove burn and sharp edges. No wire brush.
Date: 04 Sept 2012
Drawing #: PDPFTS_1000
SCALE: 1:1
SHEET 1 OF 1
Size: ANSI - C
Project: PDPFTS
Issue: C

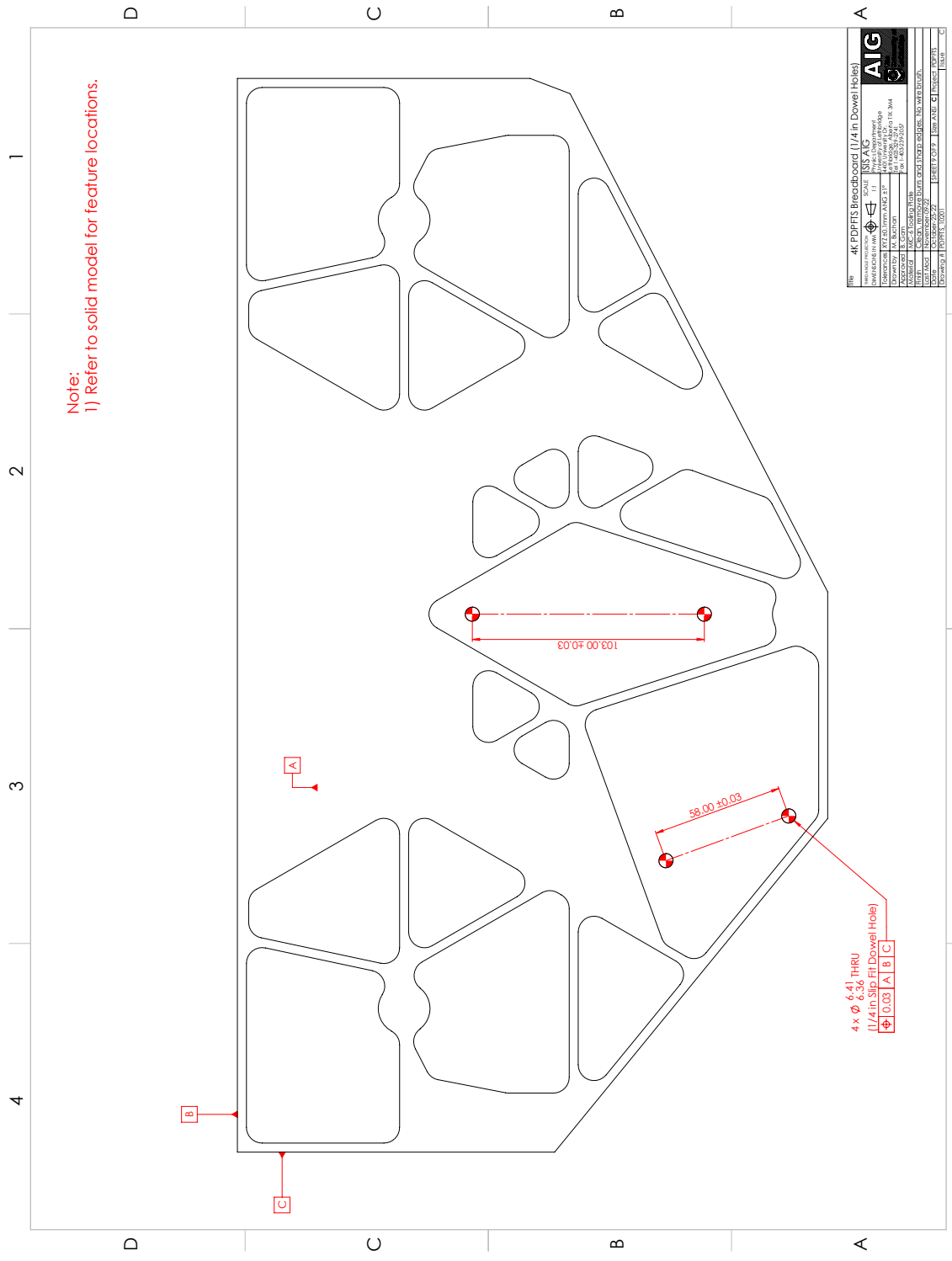
Note:
1) Refer to solid model for feature locations.
103.00 ±0.03
58.00 ±0.03
4 x Ø 6.41
6.36 THRU
(1/4 in Slip Fit Dowel Hole)
0.03 A B C
A
B
C
4K PDPFTS Breadboard (1/4 in Dowel Holes)
AIG

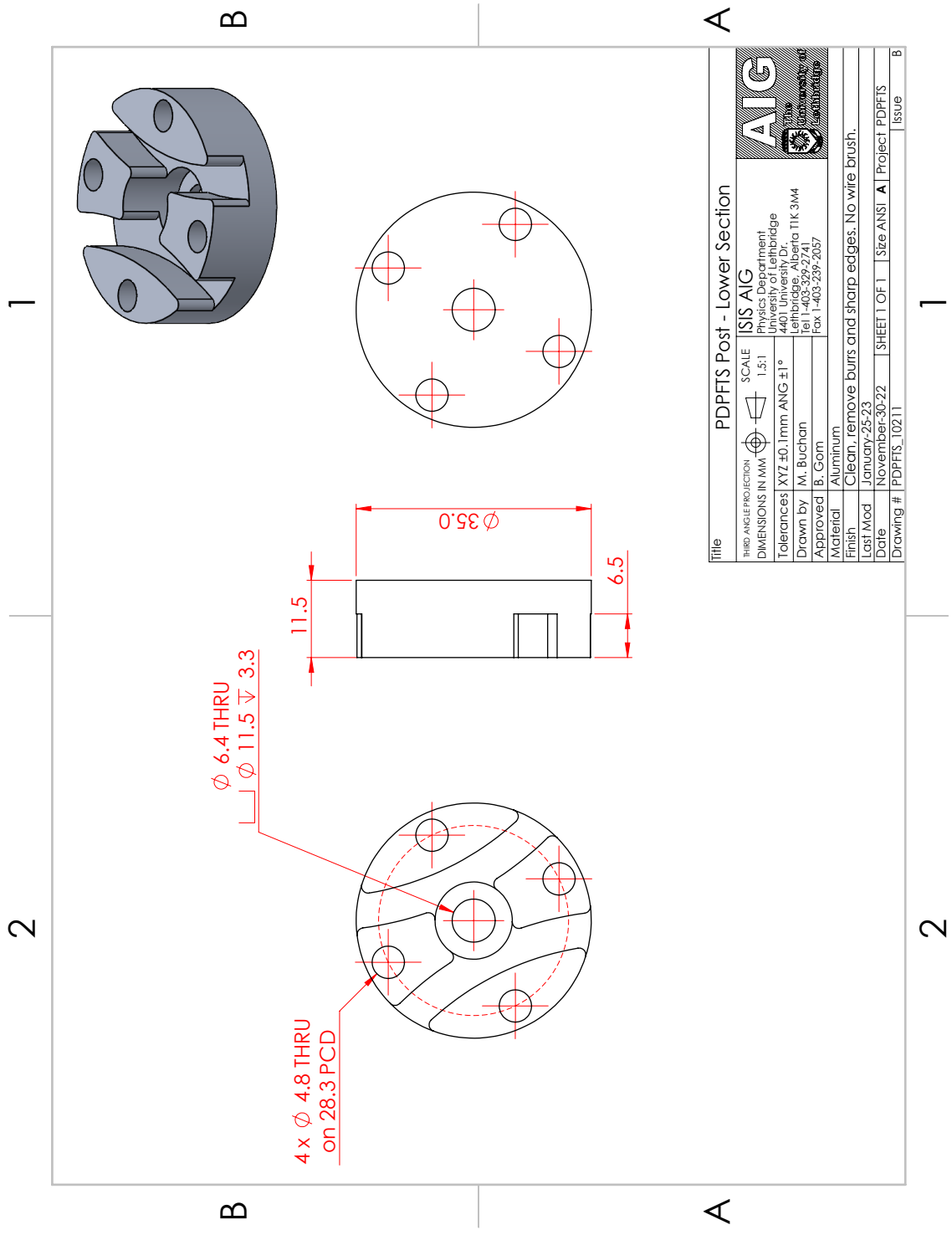
Ø 35.0
11.5
6.5
Ø 6.4 THRU
⌴ Ø 11.5 ↧ 3.3
4 x Ø 4.8 THRU
on 28.3 PCD
Title
PDPFTS Post - Lower Section
THIRD ANGLE PROJECTION
DIMENSIONS IN MM
SCALE 1.5:1
ISIS AIG
Physics Department
University of Lethbridge
4401 University Dr.
Lethbridge, Alberta T1K 3M4
Tel 1-403-329-2741
Fax 1-403-239-2057
Tolerances XYZ ±0.1mm ANG ±1°
Drawn by M. Buchan
Approved B. Gorn
Material Aluminum
Finish Clean, remove burrs and sharp edges. No wire brush.
Last Mod January-25-23
Date November-30-22
SHEET 1 OF 1
Size ANSI A
Project PDPFTS
Drawing # PDPFTS_10211
Issue B

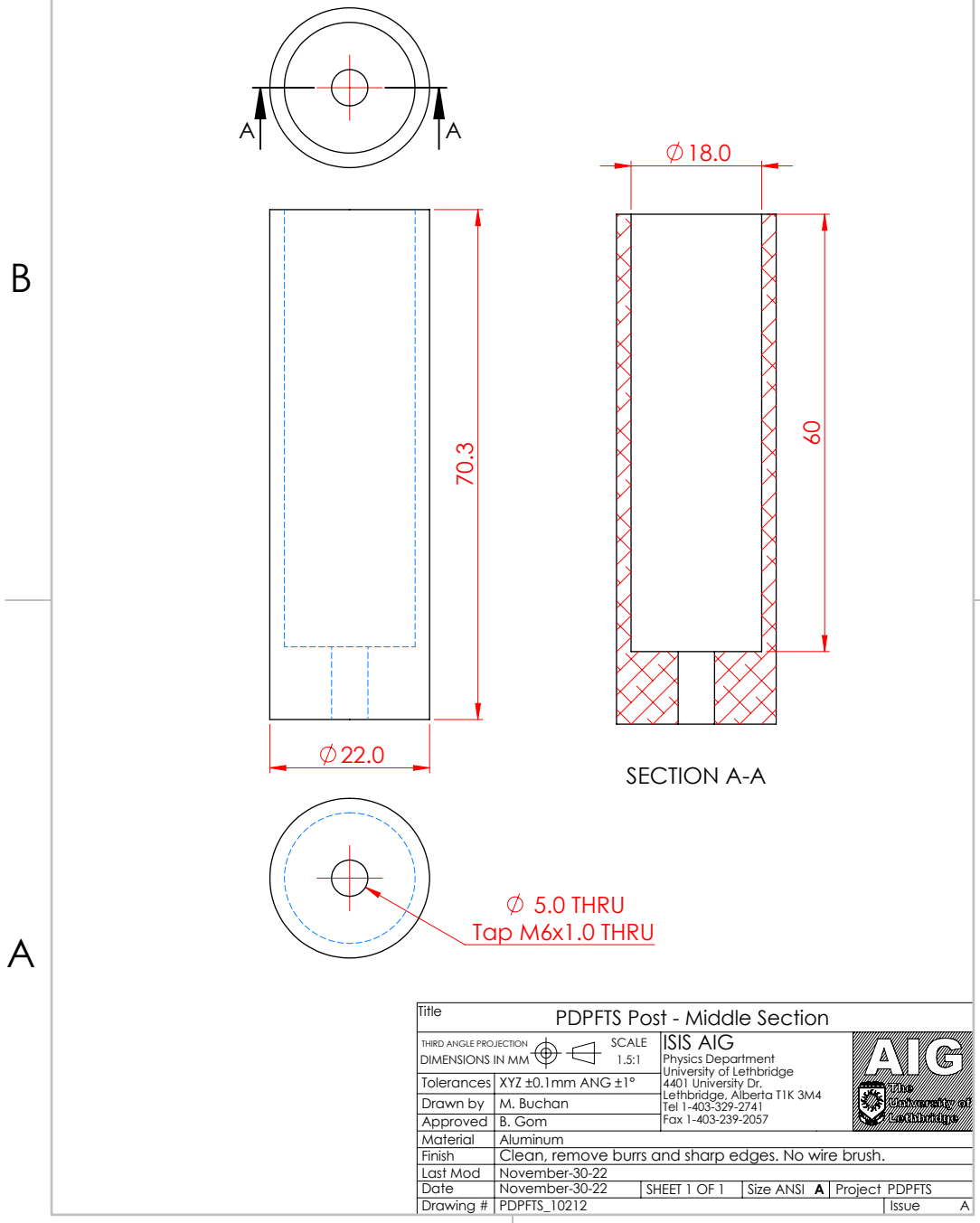

Title	PDPFTS Post - Middle Section			
THIRD ANGLE PROJECTION DIMENSIONS IN MM	SCALE 1.5:1	ISIS AIG Physics Department University of Lethbridge 4401 University Dr. Lethbridge, Alberta T1K 3M4 Tel 1-403-329-2741 Fax 1-403-239-2057		
Tolerances	XYZ ±0.1mm ANG ±1°			
Drawn by	M. Buchan			
Approved	B. Gom			
Material	Aluminum			
Finish	Clean, remove burrs and sharp edges. No wire brush.			
Last Mod	November-30-22			
Date	November-30-22	SHEET 1 OF 1	Size ANSI **A**	Project PDPFTS
Drawing #	PDPFTS_10212			Issue A

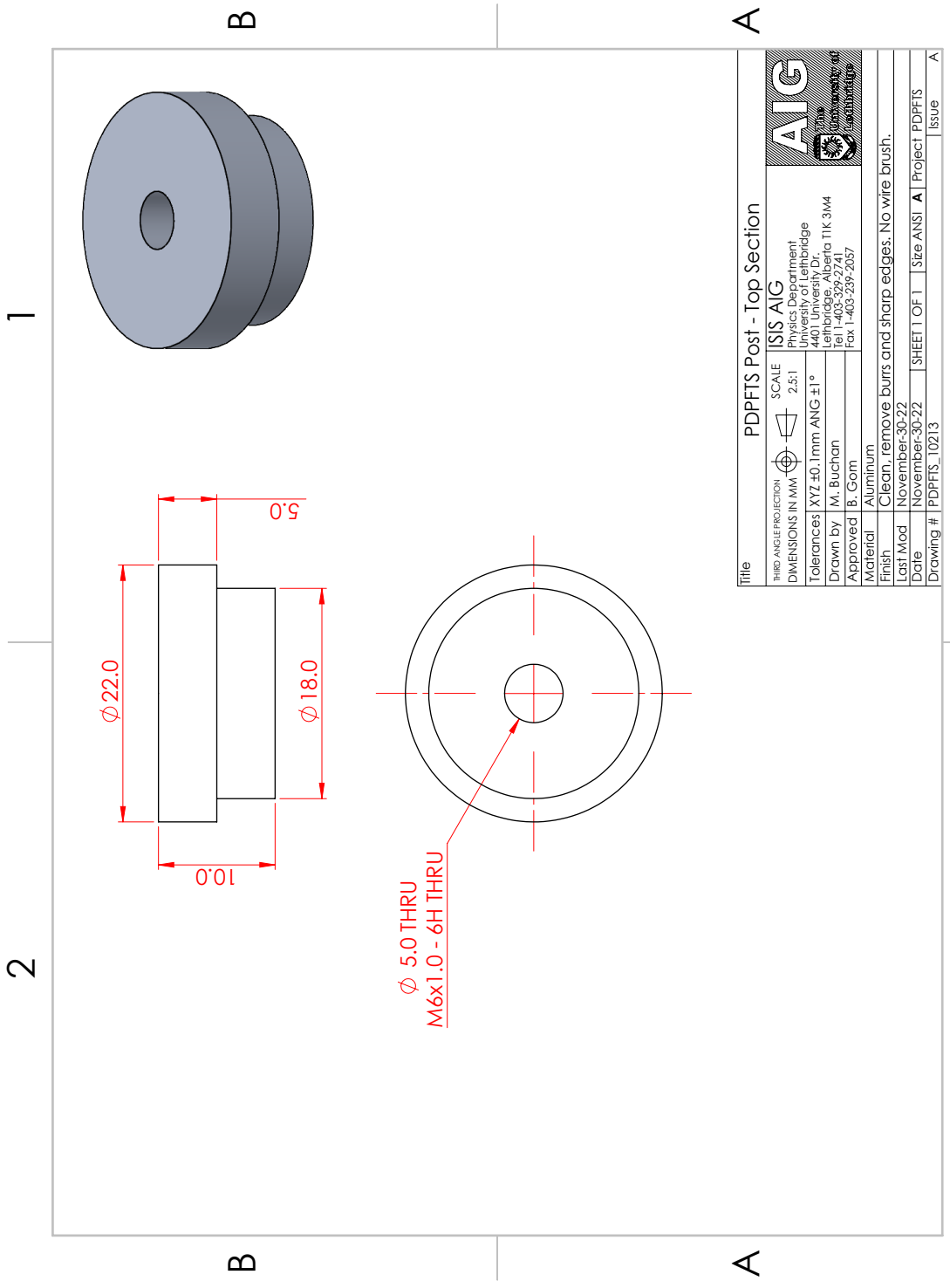
B
A
1
2
5.0
Ø22.0
Ø18.0
10.0
Ø 5.0 THRU
M6x1.0 - 6H THRU
Title
PDPFTS Post - Top Section
THIRD ANGLE PROJECTION
DIMENSIONS IN MM
SCALE 2.5:1
ISIS AIG
Physics Department
University of Lethbridge
4401 University Dr.
Lethbridge, Alberta T1K 3M4
Tel 1-403-329-2741
Fax 1-403-239-2057
AIG
The University of Lethbridge
Tolerances XYZ ±0.1mm ANG ±1°
Drawn by M. Buchan
Approved B. Gom
Material Aluminum
Finish Clean, remove burrs and sharp edges. No wire brush.
Last Mod November-30-22
Date November-30-22
SHEET 1 OF 1
Size ANSI A
Project PDPFTS
Drawing # PDPFTS_10213
Issue A

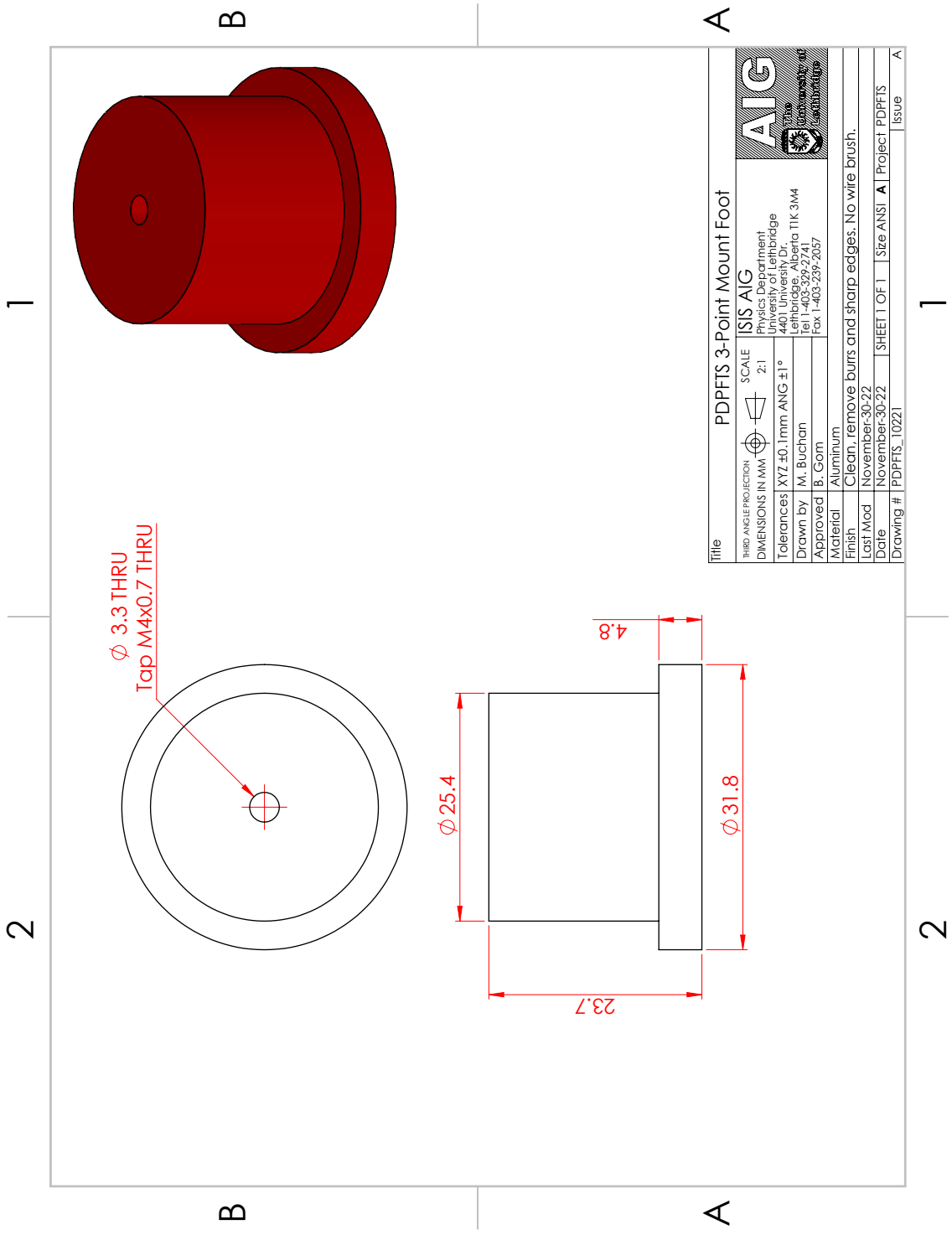
B
A
1
2
∅ 3.3 THRU
Tap M4x0.7 THRU
4.8
∅25.4
∅31.8
23.7
Title
PDPFTS 3-Point Mount Foot
THIRD ANGLE PROJECTION
DIMENSIONS IN MM
SCALE 2:1
ISIS AIG
Physics Department
University of Lethbridge
4401 University Dr.
Lethbridge, Alberta T1K 3M4
Tel 1-403-329-2741
Fax 1-403-239-2057
Tolerances XYZ ±0.1mm ANG ±1°
Drawn by M. Buchan
Approved B. Gom
Material Aluminum
Finish Clean, remove burrs and sharp edges. No wire brush.
Last Mod November-30-22
Date November-30-22
Drawing # PDPFTS_10221
SHEET 1 OF 1
Size ANSI A
Project PDPFTS
Issue A

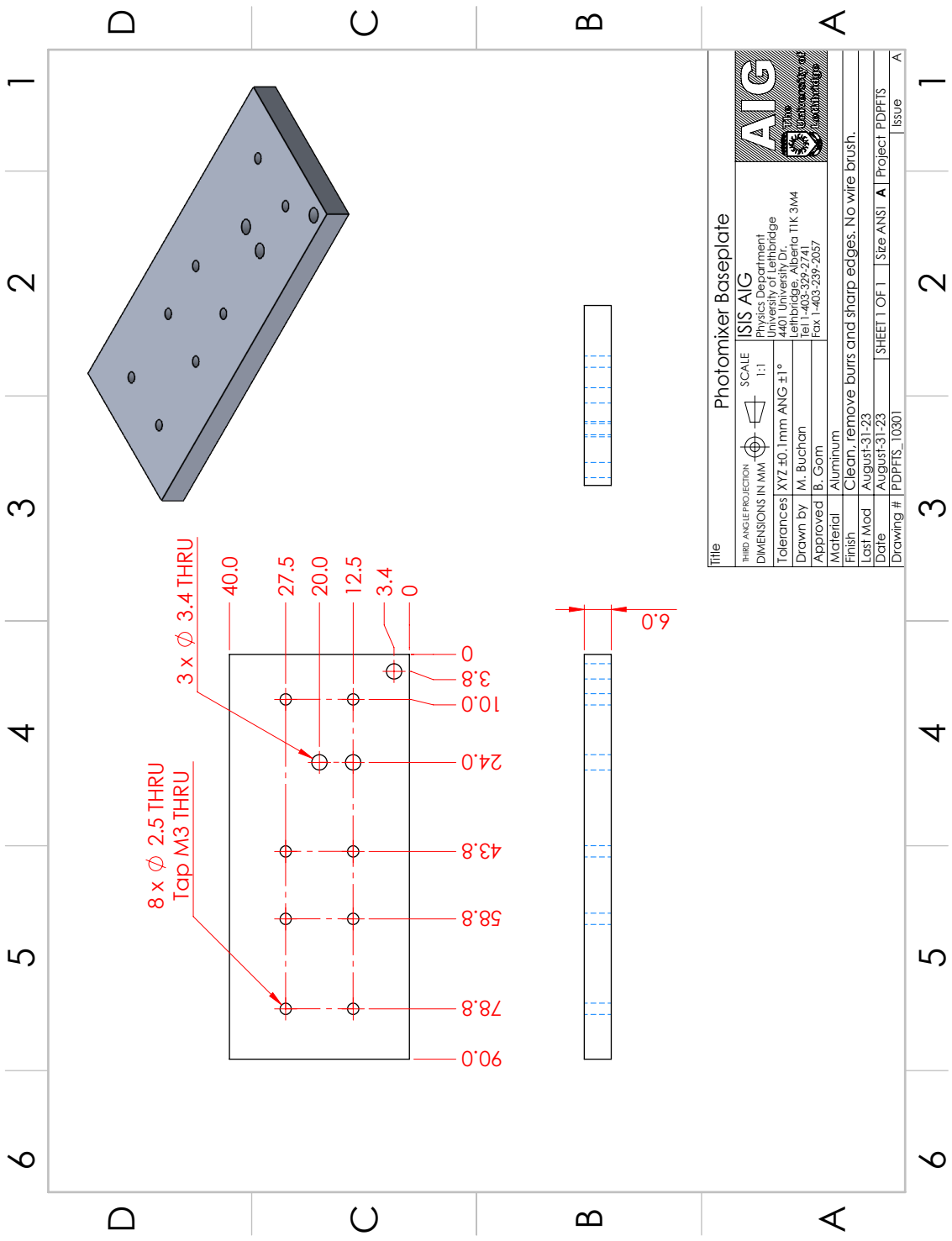
Photomixer Baseplate
ISIS AIG
Physics Department
University of Lethbridge
4401 University Dr.
Lethbridge, Alberta T1K 3M4
Tel 1-403-329-2741
Fax 1-403-239-2057
SCALE 1:1
THIRD ANGLE PROJECTION
DIMENSIONS IN MM
Tolerances XYZ ±0.1mm ANG ±1°
Drawn by M. Buchan
Approved B. Gom
Material Aluminum
Finish Clean, remove burrs and sharp edges. No wire brush.
Last Mod August-31-23
Date August-31-23
Drawing # PDPFTS_10301
SHEET 1 OF 1
Size ANSI A
Project PDPFTS
Issue A
3 x ∅ 3.4 THRU
8 x ∅ 2.5 THRU
Tap M3 THRU
40.0
27.5
20.0
12.5
3.4
0
3.8
10.0
24.0
43.8
58.8
78.8
90.0
6.0

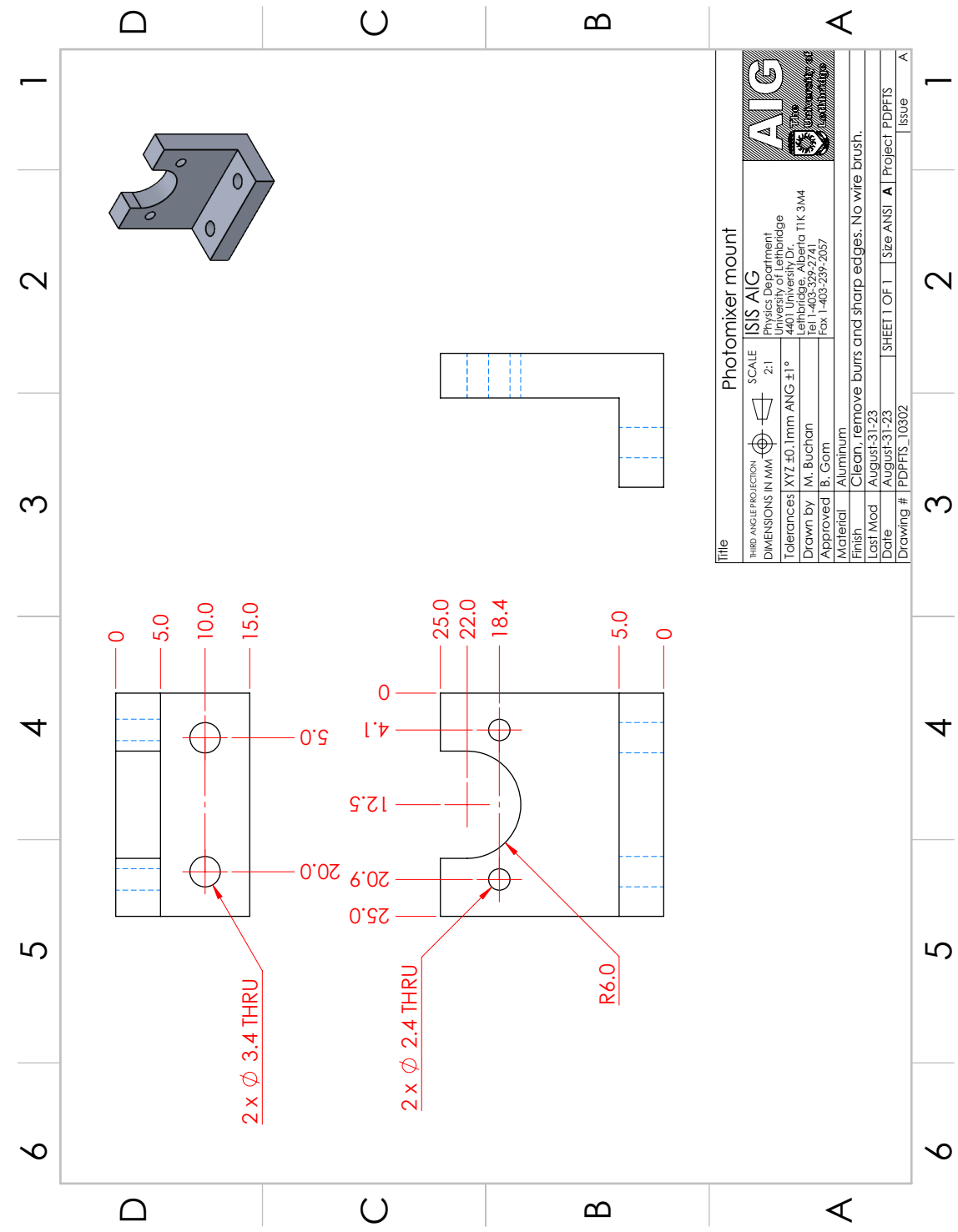
Photomixer mount
ISIS AIG
Physics Department
University of Lethbridge
4401 University Dr.
Lethbridge, Alberta T1K 3M4
Tel 1-403-329-2741
Fax 1-403-239-2057
THIRD ANGLE PROJECTION
DIMENSIONS IN MM
SCALE 2:1
Tolerances XYZ ±0.1mm ANG ±1°
Drawn by M. Buchan
Approved B. Gorn
Material Aluminum
Finish Clean, remove burrs and sharp edges. No wire brush.
Last Mod August-31-23
Date August-31-23
Drawing # PDPFTS_10302
SHEET 1 OF 1
Size ANSI A
Project PDPFTS
Issue A
0
5.0
10.0
15.0
5.0
20.0
2 x ∅ 3.4 THRU
0
4.1
12.5
20.9
25.0
25.0
22.0
18.4
5.0
0
2 x ∅ 2.4 THRU
R6.0

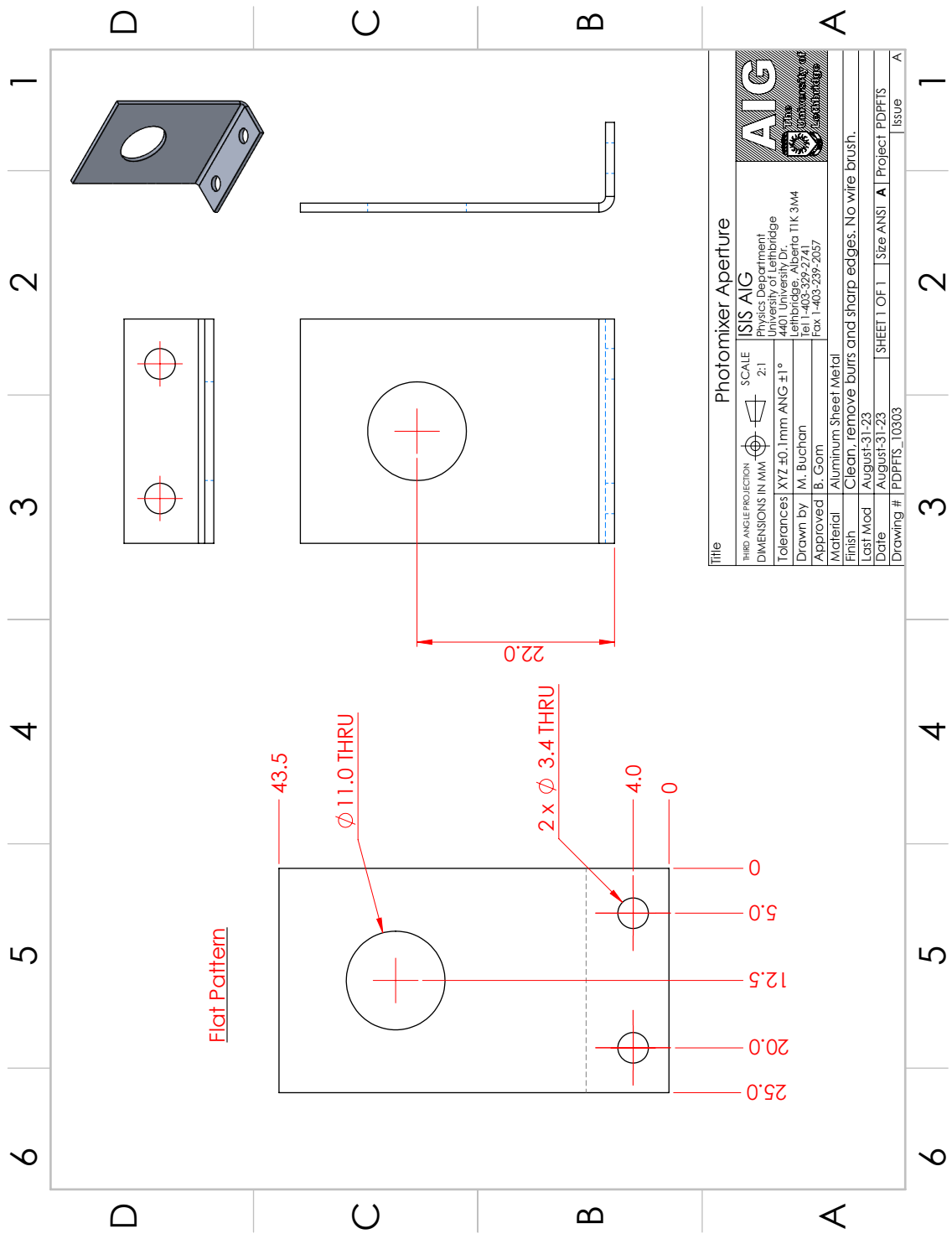
Photomixer Aperture
ISIS AIG
Physics Department
University of Lethbridge
4401 University Dr.
Lethbridge, Alberta T1K 3M4
Tel 1-403-329-2741
Fax 1-403-239-2057
THIRD ANGLE PROJECTION
DIMENSIONS IN MM
SCALE 2:1
Tolerances XYZ ±0.1mm ANG ±1°
Drawn by M. Buchan
Approved B. Gom
Material Aluminum Sheet Metal
Finish Clean, remove burrs and sharp edges. No wire brush.
Last Mod August-31-23
Date August-31-23
Drawing # PDPFTS_10303
SHEET 1 OF 1
Size ANSI A
Project PDPFTS
Issue A
Flat Pattern
43.5
Ø 11.0 THRU
2 x Ø 3.4 THRU
4.0
0
0
5.0
12.5
20.0
25.0
22.0

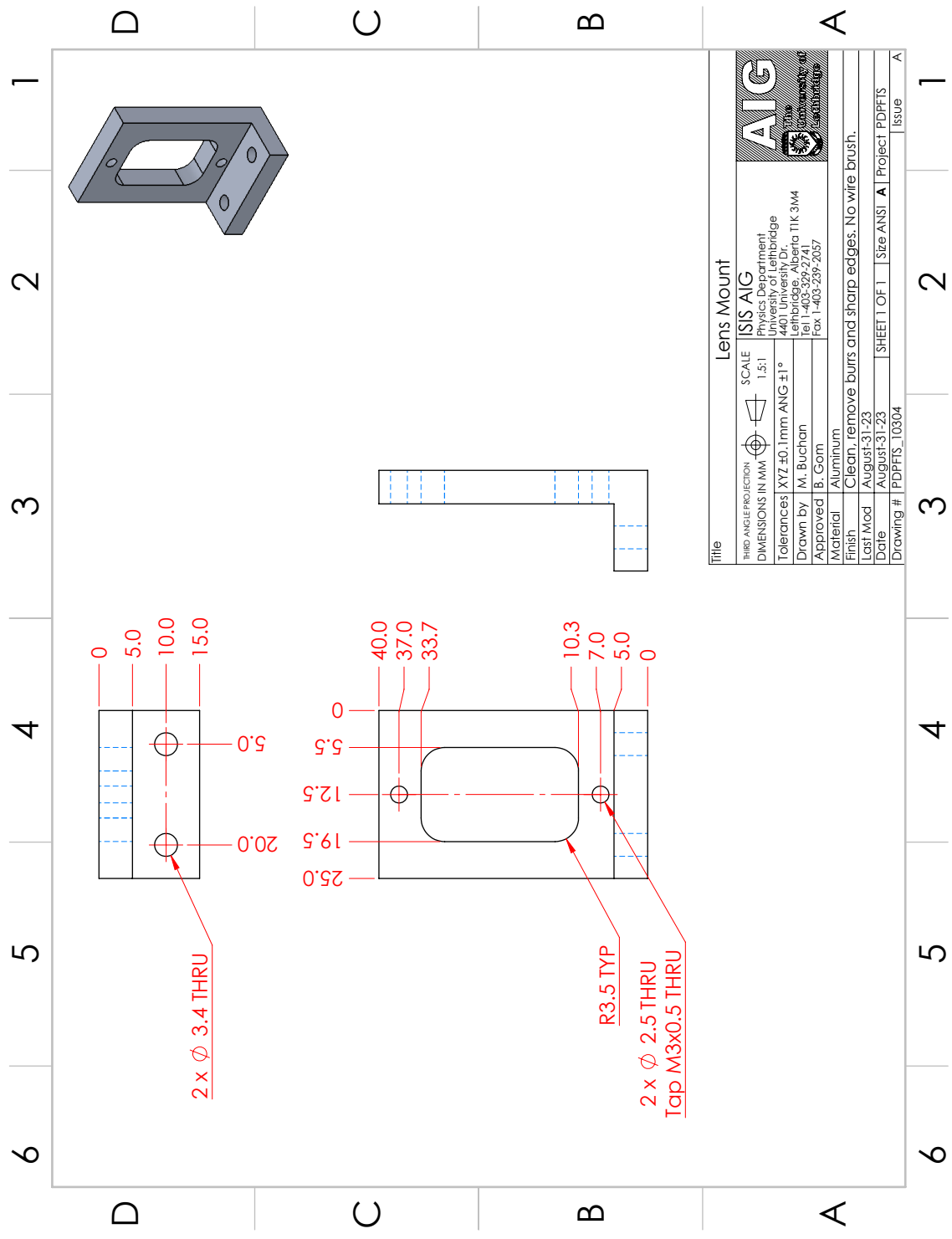
Lens Mount
THIRD ANGLE PROJECTION
DIMENSIONS IN MM
SCALE 1.5:1
ISIS AIG
Physics Department
University of Lethbridge
4401 University Dr.
Lethbridge, Alberta T1K 3M4
Tel 1-403-329-2741
Fax 1-403-239-2057
The University of Lethbridge
Tolerances XYZ ±0.1mm ANG ±1°
Drawn by M. Buchan
Approved B. Gorn
Material Aluminum
Finish Clean, remove burrs and sharp edges. No wire brush.
Last Mod August-31-23
Date August-31-23
SHEET 1 OF 1
Size ANSI A
Project PDPFTS
Drawing # PDPFTS_10304
Issue A
0
5.0
10.0
15.0
5.0
20.0
2 x ∅ 3.4 THRU
40.0
37.0
33.7
0
5.5
12.5
19.5
25.0
10.3
7.0
5.0
0
R3.5 TYP
2 x ∅ 2.5 THRU
Tap M3x0.5 THRU

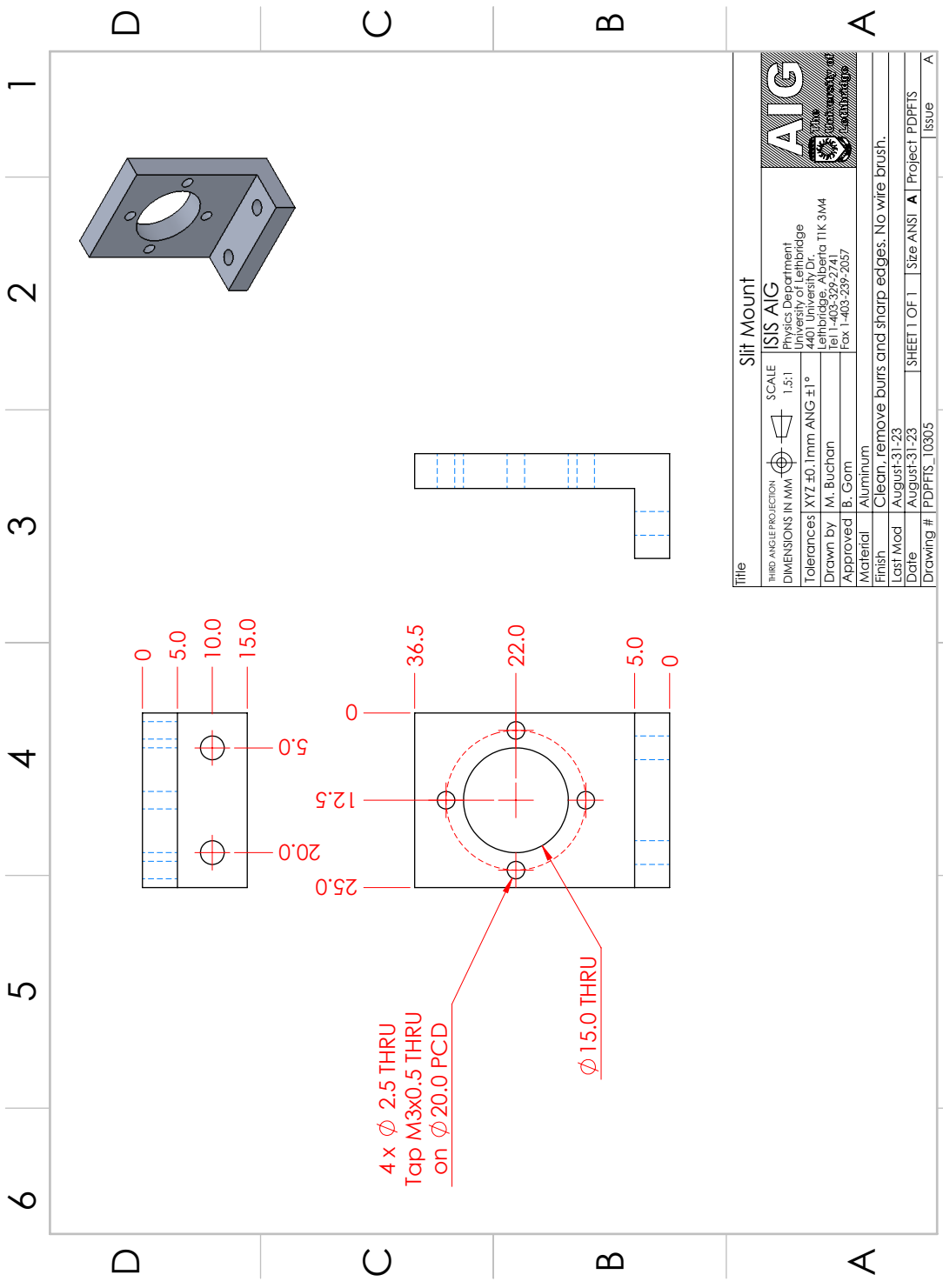
Title
Slit Mount
THIRD ANGLE PROJECTION
DIMENSIONS IN MM
SCALE 1.5:1
ISIS AIG
Physics Department
University of Lethbridge
4401 University Dr.
Lethbridge, Alberta T1K 3M4
Tel 1-403-329-2741
Fax 1-403-239-2057
The University of Lethbridge
Tolerances XYZ ±0.1mm ANG ±1°
Drawn by M. Buchan
Approved B. Gom
Material Aluminum
Finish Clean, remove burrs and sharp edges. No wire brush.
Last Mod August-31-23
Date August-31-23
SHEET 1 OF 1
Size ANSI A
Project PDPFTS
Drawing # PDPFTS_10305
Issue A
0
5.0
10.0
15.0
5.0
20.0
0
36.5
22.0
5.0
0
12.5
25.0
4 x ∅ 2.5 THRU
Tap M3x0.5 THRU
on ∅20.0 PCD
∅15.0 THRU

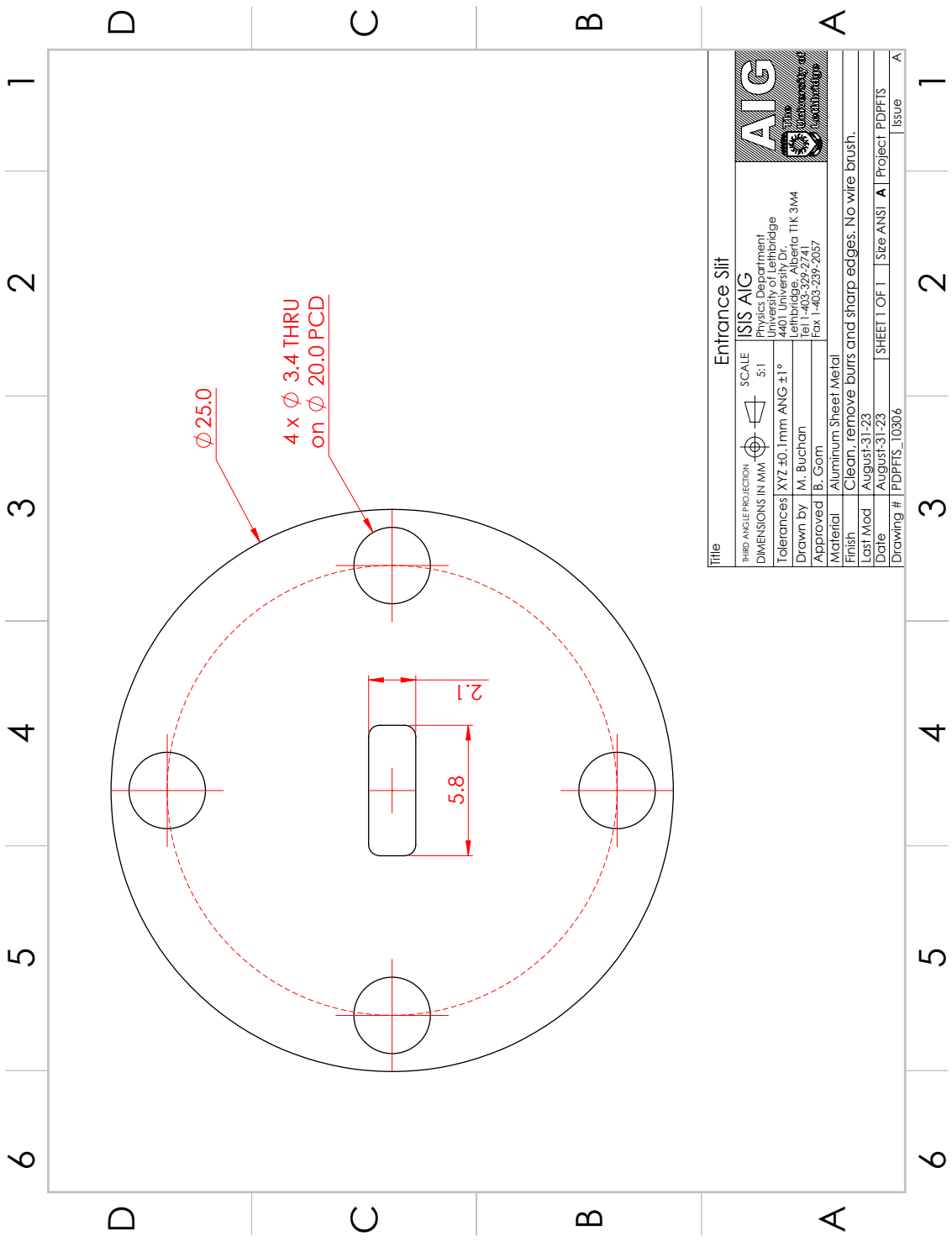
Ø25.0
4 x Ø 3.4 THRU
on Ø 20.0 PCD
2.1
5.8
Title
Entrance Slit
THIRD ANGLE PROJECTION
DIMENSIONS IN MM
SCALE 5:1
ISIS AIG
Physics Department
University of Lethbridge
4401 University Dr.
Lethbridge, Alberta T1K 3M4
Tel 1-403-329-2741
Fax 1-403-239-2057
AIG
The University of Lethbridge
Tolerances XYZ ±0.1mm ANG ±1°
Drawn by M. Buchan
Approved B. Gom
Material Aluminum Sheet Metal
Finish Clean, remove burrs and sharp edges. No wire brush.
Last Mod August-31-23
Date August-31-23
SHEET 1 OF 1
Size ANSI A
Project PDPFTS
Drawing # PDPFTS_10306
Issue A

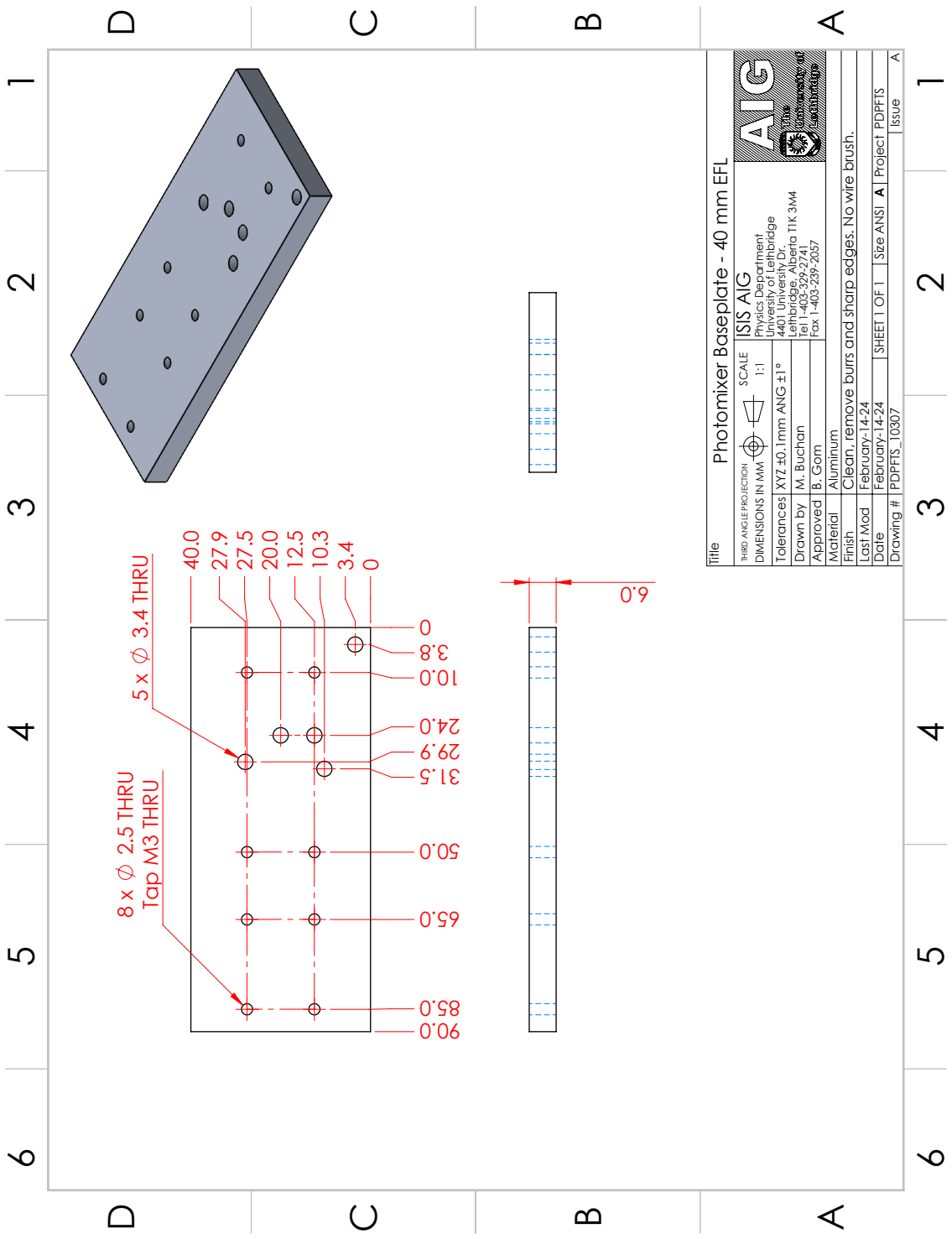
Photomixer Baseplate - 40 mm EFL
ISIS AIG
Physics Department
University of Lethbridge
4401 University Dr.
Lethbridge, Alberta T1K 3M4
Tel 1-403-329-2741
Fax 1-403-239-2057
THIRD ANGLE PROJECTION
DIMENSIONS IN MM
SCALE 1:1
Tolerances XYZ ±0.1mm ANG ±1°
Drawn by M. Buchan
Approved B. Gom
Material Aluminum
Finish Clean, remove burrs and sharp edges. No wire brush.
Last Mod February-14-24
Date February-14-24
Drawing # PDPFTS_10307
SHEET 1 OF 1
Size ANSI A
Project PDPFTS
Issue A
5 x ∅ 3.4 THRU
8 x ∅ 2.5 THRU
Tap M3 THRU
40.0
27.9
27.5
20.0
12.5
10.3
3.4
0
90.0
85.0
65.0
50.0
31.5
29.9
24.0
10.0
3.8
0
6.0

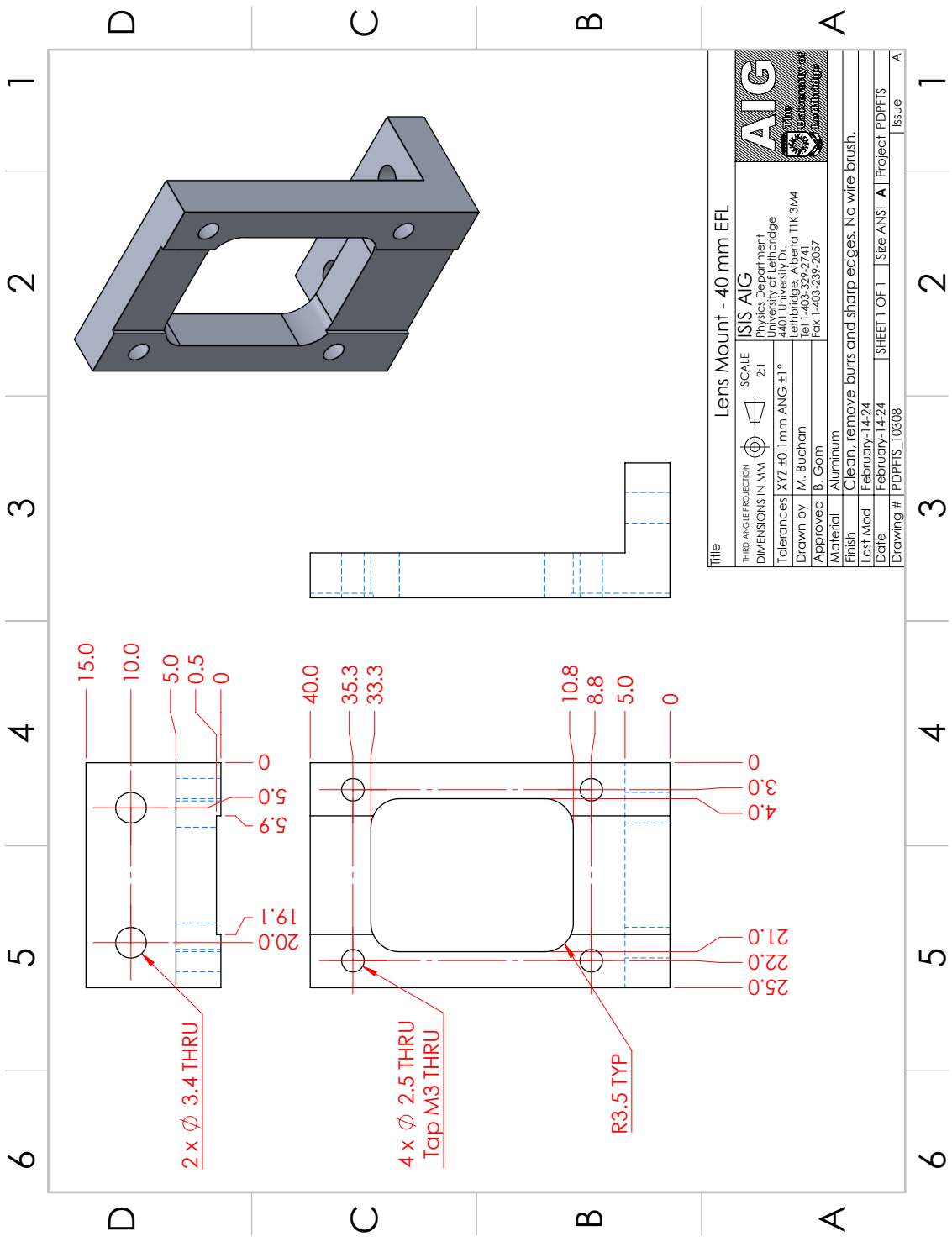
Lens Mount - 40 mm EFL
ISIS AIG
Physics Department
University of Lethbridge
4401 University Dr.
Lethbridge, Alberta T1K 3M4
Tel 1-403-329-2741
Fax 1-403-239-2057
THIRD ANGLE PROJECTION
DIMENSIONS IN MM
SCALE 2:1
Tolerances XYZ ±0.1mm ANG ±1°
Drawn by M. Buchan
Approved B. Gom
Material Aluminum
Finish Clean, remove burrs and sharp edges. No wire brush.
Last Mod February-14-24
Date February-14-24
Drawing # PDPFTS_10308
SHEET 1 OF 1
Size ANSI A
Project PDPFTS
Issue A
2 x ∅ 3.4 THRU
4 x ∅ 2.5 THRU
Tap M3 THRU
R3.5 TYP

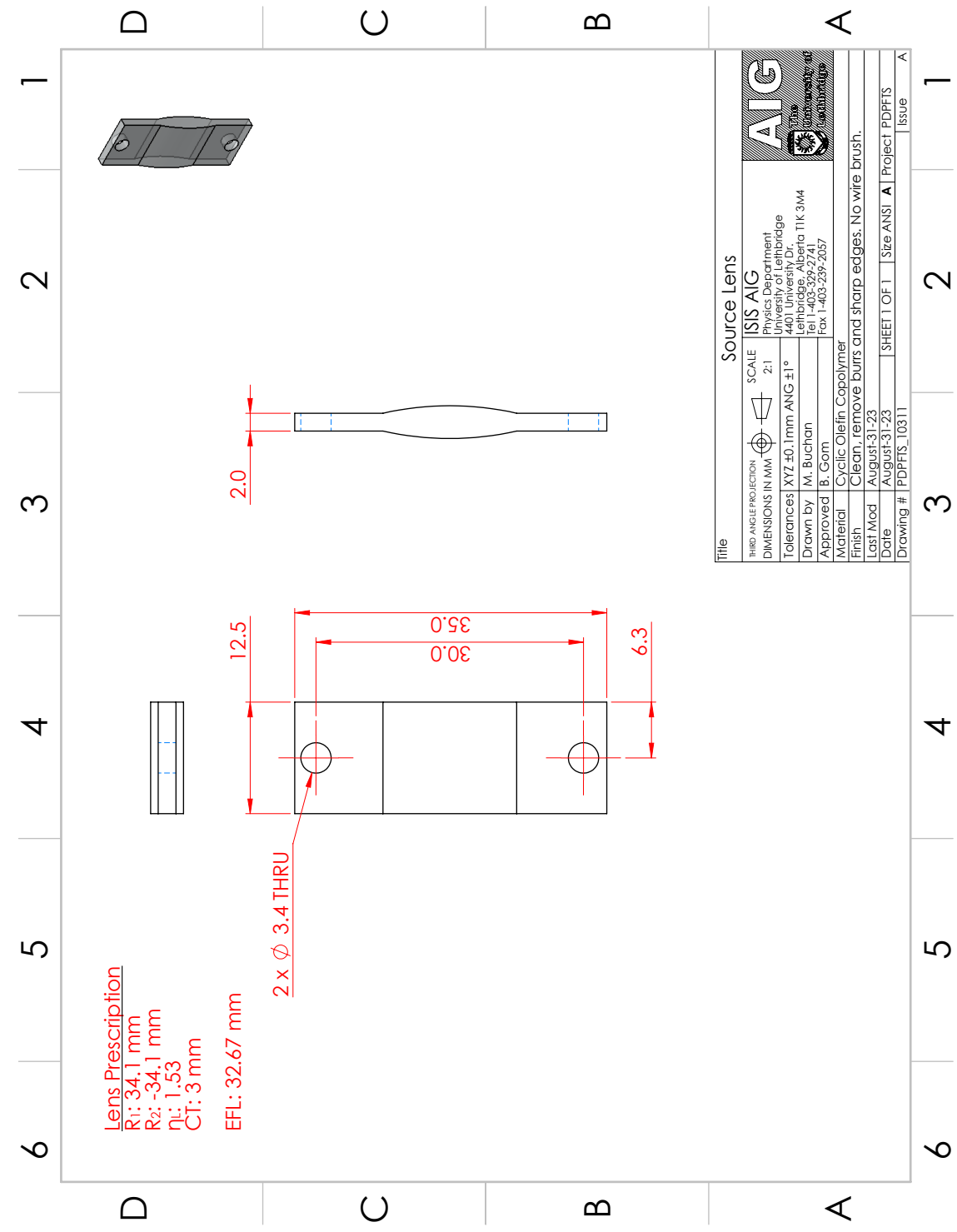
Lens Prescription
R1: 34.1 mm
R2: -34.1 mm
ηL: 1.53
CT: 3 mm
EFL: 32.67 mm
2 x ∅ 3.4 THRU
12.5
30.0
35.0
6.3
2.0
Title
Source Lens
THIRD ANGLE PROJECTION
DIMENSIONS IN MM
SCALE 2:1
ISIS AIG
Physics Department
University of Lethbridge
4401 University Dr.
Lethbridge, Alberta T1K 3M4
Tel 1-403-329-2741
Fax 1-403-239-2057
Tolerances XYZ ±0.1mm ANG ±1°
Drawn by M. Buchan
Approved B. Gorn
Material Cyclic Olefin Copolymer
Finish Clean, remove burrs and sharp edges. No wire brush.
Last Mod August-31-23
Date August-31-23
Drawing # PDPFTS_10311
SHEET 1 OF 1
Size ANSI A
Project PDPFTS
Issue A

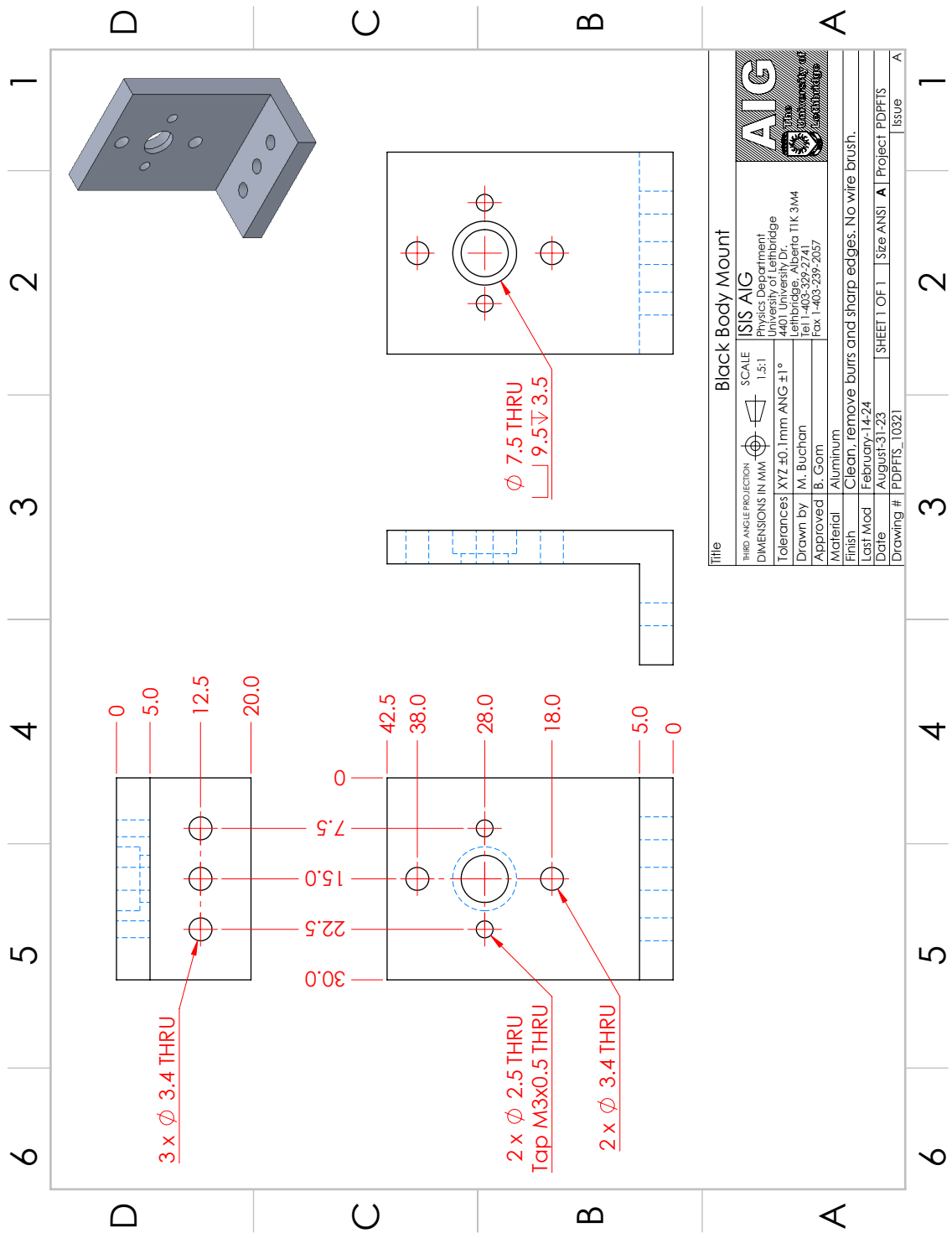
Black Body Mount
ISIS AIG
Physics Department
University of Lethbridge
4401 University Dr.
Lethbridge, Alberta T1K 3M4
Tel 1-403-329-2741
Fax 1-403-239-2057
SCALE 1.5:1
THIRD ANGLE PROJECTION
DIMENSIONS IN MM
Tolerances XYZ ±0.1mm ANG ±1°
Drawn by M. Buchan
Approved B. Gom
Material Aluminum
Finish Clean, remove burrs and sharp edges. No wire brush.
Last Mod February-14-24
Date August-31-23
Drawing # PDPFTS_10321
SHEET 1 OF 1
Size ANSI A
Project PDPFTS
Issue A
Ø 7.5 THRU
9.5▽ 3.5
3 x Ø 3.4 THRU
2 x Ø 2.5 THRU
Tap M3x0.5 THRU
2 x Ø 3.4 THRU
0
5.0
12.5
20.0
42.5
38.0
28.0
18.0
5.0
0
7.5
15.0
22.5
30.0

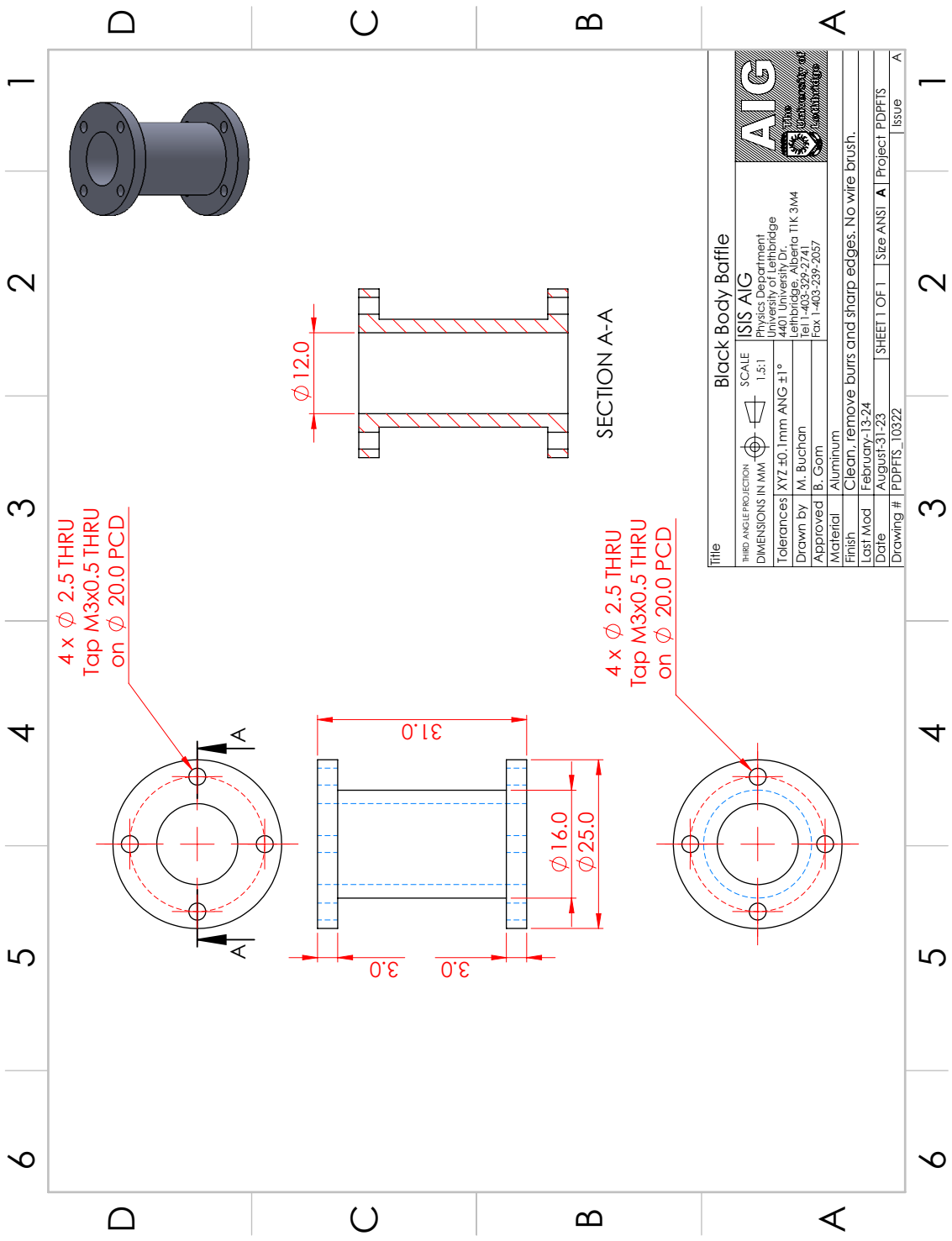
4 x ⌀ 2.5 THRU
Tap M3x0.5 THRU
on ⌀ 20.0 PCD
⌀12.0
SECTION A-A
31.0
⌀16.0
⌀25.0
3.0
3.0
A
A
4 x ⌀ 2.5 THRU
Tap M3x0.5 THRU
on ⌀ 20.0 PCD
Title
Black Body Baffle
THIRD ANGLE PROJECTION
DIMENSIONS IN MM
SCALE 1.5:1
ISIS AIG
Physics Department
University of Lethbridge
4401 University Dr.
Lethbridge, Alberta T1K 3M4
Tel 1-403-329-2741
Fax 1-403-239-2057
Tolerances XYZ ±0.1mm ANG ±1°
Drawn by M. Buchan
Approved B. Gom
Material Aluminum
Finish Clean, remove burrs and sharp edges. No wire brush.
Last Mod February-13-24
Date August-31-23
SHEET 1 OF 1
Size ANSI A
Project PDPFTS
Drawing # PDPFTS_10322
Issue A